Personalized Biomechanical Heart Modeling for Clinical Applications

Radomir Chabiniok

Modélisation biomécanique personnalisée du cœur et applications cliniques

THÈSE DE DOCTORAT

Présentée par

Radomir Chabiniok

pour obtenir le grade de

DOCTEUR DE
L'UNIVERSITÉ PIERRE ET MARIE CURIE - Paris VI

Spécialité : Mathématiques Appliquées

Soutenue publiquement le 24 Janvier 2011 devant le jury composé de :

Dominique Chapelle	Directeur de thèse
Leon Axel	Rapporteur
Annie Raoult	Rapporteur
Patrick Clarysse	Examinateur
Bijan Ghaleh	Examinateur
Frédéric Hecht	Examinateur
Philippe Moireau	Examinateur
Nic Smith	Examinateur

Thèse préparée au sein de l'équipe-projet MACS
Centre de Recherche INRIA Paris-Rocquencourt
Domaine de Voluceau, BP 105
78153 Le Chesnay CEDEX
France

To A.J., and everyone else who has never given up.

Acknowledgements

First and foremost, I would like to thank Dominique Chapelle, the head of the MACS team-project at INRIA Paris-Rocquencourt, under whose supervision I carried out my thesis. His supervision of this multidisciplinary work – between such distinct subjects as applied mathematics and medicine – was incredible. I am really glad that he decided to set out on this uncertain venture without any results being guaranteed beforehand. I greatly admire his style of work and his willingness to go back to the fundamentals in order to answer any questions while always bearing the final goals in mind. Each discussion with our clinical or experimental partners was followed by a detailed analysis of the problems we were facing followed by constructive conclusions, which gave direction both to the theoretical side of his work and to the applied medical side as well, which I had a unique chance to contribute to.

I am grateful that since the very beginning of my PhD, Dominique allowed me to take on considerable responsibility. In just the second month of my PhD I was sent to Sophia Antipolis where I collaborated with our colleagues during a 1-week stay. On several occasions – as for instance at some meetings with clinicians – I was the sole representative of the MACS team-project. At such events, we always discussed in detail the results that we obtained, the difficulties that we faced and also any additional information and tools which would help our work. I felt privileged to be given these opportunities to represent our team and gain greater confidence in my abilities. I also really appreciated the opportunity that Dominique gave me to work with young Master's students – Matthew Sinclair and Gregoire Lecourt, whose contributions I would like to acknowledge as well.

I would also like to thank Dominique for his help, especially during my first months in France. Although I could not speak French and I did not have any experience of living in a foreign country, I had the chance to fully enjoy life in Paris. Without his help, it would have been very difficult for me to get set up in France.

I would like to offer my greatest thanks to Philippe Moireau, a researcher in the MACS team-project. He provided me with many explanations related to modeling and estimation in our research. Together with Dominique he co-ordinated the part of the thesis related to the joint state-parameter estimation and acted effectively as an additional supervisor. I really appreciated having the chance to look into the state-of-the-art research in this domain and actually being a part of it. All computations were performed using the modeling

and estimation software HeartLab – of which Philippe is the main developer. Thanks to his careful development and a clever design of the code, the adaptation related to, for instance some particularities in the clinical data were possible, and we were able to perform simulations and estimations using such data. I believe our co-operation was greatly efficient and fruitful.

I would like to thank Jaroslav Tintera from the Institute for Clinical and Experimental Medicine (IKEM) Prague. He taught me both the basics of MRI and also some advanced methods – cardiac MRI in particular, which opened up a path for me to engage in profitable co-operations with medical specialists – radiologists and cardiologists. I tried to follow his example of care and diligence in acquiring all MRI data also in France. Together with him, we set up the MR sequences for the animal experiments in order for the acquired images to be of satisfactory quality. By testing some of those sequences directly at IKEM Prague and following long discussions regarding the MR settings when acquiring MR images of healthy volunteers, patients and animals in France, he acted as another supervisor – for the MR acquisition part.

Many thanks to the radiologists and cardiologists from the Henri Mondor Hospital in Créteil, namely to Jean-François Deux, Pierre-François Lesault, Jérôme Garot, Alain Rahmouni and Laurens Mitchell-Heggs, with whom we performed animal experiments. I appreciate the confidence that Jean-François Deux had in me during my evening's testing of MR sequences with healthy volunteers. The experiments themselves took place either during the nights or on week-ends. I felt guilty since everybody could have spent this time for instance with family or friends, instead of experimenting with animals. However, I am very glad that the experimental data obtained served a valuable purpose in various parts of my thesis and even now, new projects in the MACS team rely on these data.

I would like to thank Yves Lecarpentier and Jean-Louis Hébert from the Department of Cardiac and Respiratory Physiology, University Paris-Sud XI, Hospital Bicêtre, for data related to 1-dimensional simulations (contraction of a myocardial fiber) and for our discussions, which we tried to reflect in the modeling.

I would like to acknowledge researchers and clinicians at St. Thomas' hospital in London for data acquisition, processing of electrophysiological data and constructive discussions which moved the CRT modeling project closer to actual clinical applications. I would like to thank in particular Reza Razavi, Phani Chinchapatnam, Matt Ginks, Aldo Rinaldi, Pier Lambiase and Kawal Rhode with whom I worked directly, and Maxime Sermesant who co-ordinated the whole joint operation.

The creation of the geometrical models was dependent on the image segmentations using CardioViz3D software developed by the Asclepios team-project of INRIA Sophia Antipolis. I would like to especially thank Tommaso Mansi, with whom we segmented the hearts of the patients in the preclinical study performed in co-operation with King's College and St. Thomas' hospital in London. The computational meshes were created by using the meshing tools developed by the Gamma team-project of INRIA Paris-Rocquencourt.

During my PhD defense, I was honored by the presence of eight great researchers who

made up the examination committee. I appreciated their interest in reading the thesis, giving me constructive comments and questions. In particular I would like to thank the reviewers – Leon Axel and Annie Raoult – for a detailed reading of the whole thesis and for their invaluable feedback. Most of their comments were taken into account in the final version of the manuscript, which I believe greatly increased the readability of the thesis. I also want to thank all the people who read some parts of the thesis, providing me with their comments.

I really enjoyed the community of 'Bâtiment 16 et ses amis' at INRIA Rocquencourt. We were comprised of the youth from many parts of the world, each of us trying to speak French with a touch of our own accent and a vocabulary that was by default influenced by our mother tongues. At the same time as personalizing our models at work, French was successfully personalized in our everyday life. I will never forget the times that we spent together – lunches, breaks, trips, 'soirées'. As for the 'adults' of Bâtiment 16, they were always understanding of our activities and sometimes even attended them. I would like to apologize to my friends who spent hours in the MR scanner and who were awarded with just photos that I took for them. Did you recognize the people in the 'family album of Bâtiment 16', for instance in Figures 3.15, 3.28 or 4.5? Your participation in these test acquisitions was really irreplaceable for the whole experimental framework. Thanks both to the very interesting work I undertook and the nurturing work environment, I felt almost as if I was part of a family in Bâtiment 16. It became evident that working towards my PhD was the greatest, most fulfilling period of my studies to date.

During all my studies, I felt constant support from my family who tried to help me as much as they could in any situation. Děkuji svým rodičům, své sestře a její rodině za podporu, kterou mi po celou dobu dávali. Bez Vás by to také nešlo.

This work was funded by CardioSense3D – a large scope initiative of INRIA, and eu-Heart Project – European Community's Seventh Framework Program (FP7/2007-2013) under grant agreement number 224495.

Abstract

Personalized Biomechanical Heart Modeling for Clinical Applications

The objective of this thesis is the assessment of a biomechanical heart model using experimental data, and the investigation of clinical applications with patient-specific modeling.

At the 1D level we aimed at reproducing physiological experiments with myocardial fiber contraction. For the 3D validation we performed in co-operation with a clinical partner an experiment with animals (pigs) in order to obtain data in the healthy stage and after creating a myocardial infarct. We showed that our model can reproduce the pressures and motion of a healthy heart and that the infarct can be represented by changing only the parameters directly related to the pathology.

The objective of the first clinical application was to predict the short-term effect of the Cardiac Resynchronization Therapy (CRT) by means of an increase of 'max LV dp/dt'. The model personalization was performed using patients MRI and pressure data in the baseline condition – prior to CRT. Then we fixed the values of all parameters and applied electrical activation patterns according to the pacing modes considered. We obtained a very good prediction of max LV dp/dt using various pacing patterns in 3 clinical cases. This preliminary clinical validation shows that the modeling of CRT is a very promising approach as an assistance to therapy planning.

The second application is based on the adaptation of data assimilation methods developed in the MACS team at INRIA. We performed joint state-parameter estimation with real image data. We showed the effectiveness of these algorithms in automatic model personalization and that the estimated contractility values can serve as an indicator of the local heart function.

Modélisation biomécanique personnalisée du cœur et applications cliniques

L'objectif de cette thèse porte sur la validation d'un modèle biomécanique du cœur à base de mesures expérimentales, et sur des investigations concernant des applications cliniques en modélisation personnalisée.

Dans le cadre 1D, nous avons reproduit des expériences physiologiques de contraction d'une fibre cardiaque. Concernant la validation 3D, nous avons effectué dans une collaboration clinique une expérience avec des animaux (cochons), afin d'obtenir des données saines et après création d'infarctus. Nous avons démontré que notre modèle est capable de représenter le cœur sain, et que l'infarctus peut être correctement modélisé en modifiant uniquement les paramètres directement concernés par la pathologie.

Dans la première application clinique nous avons démontré que le modèle est prédictif sur l'effet immédiat d'une "Cardiac Resynchronization Therapy" (CRT), sur le critère du "max LV dp/dt". La personnalisation du modèle a été réalisée au moyen des données d'IRM et de pressions au stade 'baseline' (avant la CRT). Puis, tous les paramètres du modèle étant figés, nous avons appliqué les schémas d'activation électrique correspondant aux modes de CRT. Nous avons obtenu une prédiction très proche des indicateurs mesurés sur 3 patients avec plusieurs schémas d'activation. Cette étude clinique préliminaire montre que la modélisation de CRT est très prometteuse comme assistance à la planification thérapeutique.

Dans une deuxième application nous avons adapté des méthodes d'assimilation de données developpées dans l'Equipe-Projet MACS à l'INRIA, à des fins d'aide au diagnostic. Nous avons ainsi réalisé une estimation conjointe état-paramètres en utilisant des données réelles (IRM). Nous avons demontré l'efficacité de ces méthodes, et l'intérêt des paramètres de contractilité estimés comme indicateurs de la fonction du myocarde.

Contents

1 Introduction **12**
1.1 Cardiac modeling 12
1.2 Outline of the thesis 15
1.3 Personal publications related to the thesis 17

I Preparatory work **19**

2 Basic medical concepts **20**
2.1 Introduction 20
2.2 Basic cardiovascular anatomy 20
2.3 Basic cardiovascular physiology 23
2.3.1 Cardiac cycle 23
2.3.2 Contraction of the muscle fiber 26
2.3.3 Electrical activation of the heart 28
2.3.4 Coronary circulation 33
2.3.5 Regulation of the heart function 34
2.4 Cardiological remarks 37
2.4.1 Heart failure 37
2.4.2 Ischemic heart disease 39
2.4.3 Cardiomyopathies 40

3 Magnetic Resonance Imaging **43**
3.1 History 43
3.2 Basic principles of MRI 44
3.2.1 Tissue magnetization 44
3.2.2 Excitation and relaxation 46
3.3 Basic MR sequences 48
3.3.1 Spin ECHO 50
3.3.2 Turbo Spin ECHO 51
3.3.3 Inversion recovery 52

3.3.4 Gradient ECHO . . . 53
3.4 Concept of k-space . . . 56
3.4.1 Slice selection . . . 57
3.4.2 Reconstruction of the 2D image . . . 58
3.4.3 3D acquisition . . . 59
3.5 Fat suppression . . . 60
3.6 Image contrast and contrast agents . . . 62
3.6.1 Paramagnetic contrast agents . . . 62
3.6.2 Superparamagnetic contrast agents . . . 64
3.7 Acceleration techniques . . . 64
3.8 Hardware . . . 65
3.9 Image artifacts . . . 67
3.9.1 Artifacts coming from the MR system . . . 67
3.9.2 Artifacts caused by the examined subject . . . 69
3.9.3 Intrinsic MR artifacts . . . 70
3.10 Some special sequences used in cardiovascular MRI . . . 72
3.10.1 Cardiac MRI . . . 72
3.10.2 Phase contrast MRI . . . 84
3.10.3 MR angiography . . . 86
3.11 Appendix: Diffusion Tensor Imaging (DTI) . . . 89
3.12 Remarks about the experimental protocol . . . 90

4 Biomechanical model of the heart 93
4.1 Introduction . . . 93
4.2 Multiscale modeling for the heart model . . . 93
4.2.1 The active part (Bestel–Clément–Sorine model) . . . 94
4.2.2 Electrical activation . . . 95
4.2.3 The rheological model . . . 98
4.2.4 Coupling with systemic and pulmonary circulations . . . 98
4.2.5 Boundary conditions . . . 99
4.2.6 The full heart model . . . 103
4.3 Functional modulations in the model . . . 105
4.4 Model calibration . . . 106
4.4.1 Anatomical model . . . 106
4.4.2 Calibration of the model parameters . . . 111

II Applied modeling part 116

5 Myocardial fiber contraction 117
5.1 Introduction . . . 117

5.1.1 Basic physiological considerations of the muscle contraction 117
5.2 Methods 118
5.2.1 Experimental data 118
5.2.2 Biomechanical model 119
5.2.3 Various parameters in the model 121
5.2.4 Calibration for the high preload value 126
5.2.5 Adjustment of the Frank–Starling mechanism 126
5.3 Results 127
5.4 Discussion 127
5.5 Conclusions and perspectives 129
5.6 Appendix: Implementation of exponential law in 1D model 130
5.6.1 Mooney–Rivlin material 131
5.6.2 Exponential law 132

6 Validation of the model using animal experiments 134
6.1 Introduction 134
6.2 Experimental data 134
6.3 Biomechanical model 136
6.3.1 Model formulation 136
6.3.2 Anatomical model 136
6.3.3 Electrical activation of the model 136
6.3.4 Calibration of mechanical parameters of the model 137
6.3.5 Modeling of the infarct 137
6.3.6 Results 138
6.4 Discussion 142
6.5 Further perspectives 142
6.6 Conclusions 143

7 Planning of Cardiovascular Resynchronization Therapy 144
7.1 Cardiac Resynchronization Therapy (CRT) 144
7.2 Methods 147
7.2.1 Patient selection 147
7.2.2 Measured data 147
7.3 Creation of geometrical models 149
7.4 Biomechanical model 151
7.4.1 Electrical activation of the model 151
7.4.2 Calibration strategy 151
7.5 Analytical activation patterns 153
7.6 Ensite based patterns 157
7.6.1 Modeling of the patient-specific electrical activation based on the electrophysiological Ensite data 157

7.6.2 KCL009 . . . 158
7.6.3 KCL012 . . . 165
7.7 Discussion . . . 166
7.7.1 Measured pressure values . . . 166
7.7.2 Personalization of the biomechanical model . . . 172
7.7.3 Repolarization times . . . 172
7.7.4 Analytical activation patterns . . . 173
7.7.5 Patient-specific activation patterns . . . 173
7.7.6 Remark: Treppe (Bowditch) effect . . . 174
7.8 Conclusions and perspectives . . . 174

8 Estimation of Tissue Contractility from Cardiac Cine MRI Using the Biomechanical Heart Model 178
8.1 Experimental Data and Direct Modeling . . . 179
8.1.1 Experimental data . . . 179
8.1.2 Anatomical model . . . 179
8.1.3 Direct modeling . . . 180
8.2 Introduction to state and joint state-parameter estimations . . . 181
8.2.1 Formulation of the problem . . . 182
8.2.2 Observations and observation operator . . . 183
8.2.3 Classical assimilation techniques . . . 183
8.2.4 Physical filters . . . 185
8.3 State estimation . . . 189
8.4 Adjustment of the joint state-parameter estimator . . . 190
8.4.1 Estimation using synthetic observations . . . 193
8.4.2 Estimation using real MR images as observations . . . 195
8.5 Automatic contractility personalization and detection of hypokinetic regions 199
8.5.1 Subdivision of the myocardium . . . 199
8.5.2 Joint state-parameter estimation at baseline, T0+10 and T0+38 stages using a 6(+1)-region mesh subdivision . . . 201
8.6 Simulations with estimated values of contractility . . . 204
8.7 Electrical activation . . . 206
8.8 A contact boundary condition . . . 209
8.9 Discussion . . . 214
8.9.1 Modeling error . . . 214
8.9.2 Synthetic observations . . . 215
8.9.3 Cine MRI observations (the real data) . . . 216
8.10 Conclusions and perspectives . . . 217

9 Conclusions and perspectives **219**
9.1 Work realized . . . 219
9.2 Perspectives . . . 221
9.3 Final conclusions . . . 224

10 Appendix: Animal data acquisition **225**
10.1 Introduction . . . 225
10.2 Mathematical model . . . 226
10.3 Measured data . . . 227
10.3.1 Cardiac MRI . . . 227
10.3.2 Pressure data . . . 229
10.3.3 Electrocardiography and echocardiography . . . 230
10.4 Principal objectives . . . 230
10.4.1 Validation of the physiological heart model . . . 230
10.4.2 Direct simulations of the infarcted heart . . . 230
10.4.3 Remodeling of the heart . . . 231
10.5 Detailed protocol of the data acquisition . . . 231
10.5.1 Examination of healthy animals, creation of the infarct . . . 231
10.5.2 Follow-up of the animals . . . 231
10.5.3 Examination protocol . . . 231
10.6 Data processing . . . 234

Chapter 1

Introduction

1.1 Cardiac modeling

During the recent years, there has been an increasing impact of mathematics in medicine. The widespread *evidence based medicine* – according to which any new treatment must be proven to be more efficient that the previous ones – is based upon statistical methods applied in clinical studies. Population dynamics methods are applied for example in epidemiology. Especially in the end of the 20th century and in the beginning of the 21st century, the accessibility of heavy computations has increased thanks to a fast technological development. Medical imaging is a typical example where intensive computing is used both during data acquisition (especially in some imaging modalities as for instance magnetic resonance imaging – MRI) and then in image reconstruction and post-processing.

Applied mathematicians – usually engaged in the modeling of physical, mechanical or engineering problems – have become interested in the modeling of biological phenomena. However, the problems motivated by medicine are often very large and difficult to analyze and solve. We will hardly ever be able to create models that would represent all parts of the studied systems. We need to focus on a particular phenomenon and the ingredients of the model must be carefully balanced with the expected objectives. This is why detailed multi-disciplinary interactions are necessary in order to decide on the important parts of the models representing the living body.

The final goal of any modeling effort is to create models based on physiological and physical principles, that would represent the reality adequately in order to be predictive in some aspects. Such models could serve in pre-clinical research in clarifying some physiological phenomena or they could even replace experimenting with animals, in some studies. At the moment, biomechanical modeling is still not adequately recognized as a useful tool in most branches of clinical medicine. One exception are applications in orthopedics where the modeling has been used for instance for optimizing the design of new joint endoprosthesis. It is usually difficult to convince clinicians from other specialities, in which modeling (in

the sense referred to here) is not traditionally present, that a deep co-operation of mathematical and clinical groups can be fruitful. Nevertheless, there are clinical departments that are highly motivated in such a research, which is also reflected in the thesis.

The modeling of the cardiovascular system – and of the heart in particular – is a greatly challenging topic for the applied mathematics. The multi-scale complexity of the heart function involves muscle fiber contraction, electrical activation, nutrition of the myocardium by means of the coronary blood flow and myocardial perfusion, and numerous regulation circuits. The contraction itself can be studied at the microscopic level (interaction of contractile proteins inside the cells), mesoscopic level (shortening of myofibrils and of muscle cells) and at the macroscopic level (muscle fiber contraction or the contraction of the whole 3D organ). All these scales are involved in the biomechanical model of heartbeat developed at INRIA[1], as a part of the CardioSense3D[2] initiative.

When using mathematical models, we can consider general basic simulations, physiological, clinical and patient-specific simulations. There is no clear border between these levels. Some simulations can be called basic in the case of a simpler model but they could already be categorized as physiological in a more complex model. The following description is more likely related to the INRIA heart model.

The general (basic) simulations usually do not take into account detailed anatomical properties or measured values of input quantities. In our model, we often use an analytically prescribed ellipsoidal geometry representing the heart ventricle or even a simple 1D model of contracting fiber. Markedly lower computational costs make this type of simulations especially important in the testing and optimization of numerical schemes or implementation of new model features. These basic simulations with the INRIA heart model are presented for example in [95].

In the physiological simulations, we often use an accurate geometry representing the anatomy of the modeled tissue or organ. Although information about some model input quantities may be missing, we typically use common physiological values. Due to finer geometrical models (computational meshes), these simulations are more time demanding. Some instabilities – for instance related to the complex anatomy or to the realistic input numerical values – can arise. Such simulations with the INRIA heart model were performed in [23]. While the anatomical model in this work was obtained from real human image data, the pressure conditions and the electrical activation pattern were not available. When applying a physiological activation pattern, the model showed a physiological behavior with respect to some global indicators of heart function (for instance the pressure and volume changes during cardiac cycle). Furthermore, when the activation pattern was modified in order to represent some typical electrical activation disorders, the model output changed in the expected direction. This predictive aspect certainly qualifies the model in the next level – of clinical simulations.

[1] Institute National de Recherche en Informatique et en Automatique (French National Institute for Computer Science and Automatization), `http://www.inria.fr`

[2] `http://www-sop.inria.fr/CardioSense3D`

In order for models to serve clinical medicine, they need to fit patient data. *Patient-specific modeling* is the highest simulation level and we cannot achieve it before the model is validated at all the previous steps. Besides physiologists, also clinical physicians must be involved in the work and the approach is becoming even more inter-disciplinary. First of all, we need to decide about the expected clinical outcomes of a particular patient-specific model. Then, we need to take into account the availability of certain types of clinical data that could be used to create the model – including practical questions such as the invasivity of an acquisition procedure or the expected error in the data. Then, the setup of the model itself may be quite a delicate problem. It frequently includes post-processing of the measured data in order to obtain an input suitable for the model. Some other types of modeling can be involved in these procedures ([92], [96]).

Ideally, we would like a patient-specific model to satisfy all available results of clinical exams and measurements – that may be of various types. After such a personalization step, a good model may for example provide some missing information – such as a quantity non-measurable in the in vivo conditions but with a significant clinical impact. Some models could even predict future – natural or artificial, such as for various therapeutical scenarios – evolutions of the system, which may be of a great importance in therapy planning. Although manual adjustments can be useful in some specific situations, an automatization of the model personalization is a necessary step in patient-specific modeling. Data assimilation techniques – such as have been developed in the Team-project MACS[3] of INRIA in [80], [81] and [79] – are a very promising way.

There are large groups dealing with modeling of the heart function. We can recall for instance the laboratory of Peter Hunter in Auckland, New Zeland. Peter Hunter has been a leading person in cardiac modeling since the very beginning. He started mechanical modeling of the heart based on the continuum mechanics approach in the 1970s ([53]). His laboratory does not focus only on the heart mechanics but models various physiological functions of the body. The international 'Physiome Project' – of which he is one of the main representatives – includes modeling at any level starting from the gene expression (see [31]). The group of Nic Smith based in London, UK – another participant of the Physiome Project – is particularly interested in multi-scale modeling of coronary blood flow and heart perfusion ([100], [68]). The models of the cell microenvironment and for instance cell-matrix interactions in cardiac mechanical signaling of Andrew McCulloch's lab (San Diego, USA, [2]) have a clear macroscopical output – in the contraction of the muscle fiber, long-term hypertrophy or for instance in post-myocardial infarction remodeling.

Models developed by all these groups offer an insight into cardiac function – in the healthy and also diseased state. However, in the case of large and complex models it is very difficult to put them in the patient-specific framework. The MACS team follows a distinctive path by defining a model of a lower complexity than in the groups mentioned above, but at each modeled scale satisfying physical and physiological considerations, and

[3] `http://www-roc.inria.fr/MACS`

essential thermomechanical requirements. The physical character predisposes the model to predictivity. The mechanical character of the model enables using effective estimation techniques motivated by data assimilation methods developed in the field of structural mechanics. Indeed, the detailed personalization is a major advantage of the model. Clinical applications of this model including patient-specific simulations are the main topic of the thesis.

1.2 Outline of the thesis

This multi-disciplinary doctoral work – performed at INRIA Paris-Rocquencourt in the MACS team-project under the supervision of Dominique Chapelle – combines the methods of applied mathematics, cardiovascular physiology, cardiology and also of cardiovascular imaging. The main objective of the thesis is the validation of the biomechanical heart model developed at INRIA and its clinical applications in patient-specific modeling. The document is divided into two parts: the preparatory and the applied modeling parts.

Preparatory part

The first part consists of the basic concepts of cardiovascular physiology and clinical cardiology, magnetic resonance imaging and biomechanical modeling of the heart function.

In Chapter 2 we give basic medical aspects that are especially important for the model, in order to represent the function of a healthy heart adequately. Then, we discuss selected cardiac pathologies and diseases. We focus on the clinical states with which we are directly confronted in the applied modeling part.

All data used to set up the models in the thesis came either from human patients or specially designed animal experiments. An experiment with a big animal (a pig), with the objective to obtain rich data sets consisting of non-invasive and invasive data in the healthy stage and after creating a controlled myocardial infarction, was performed in a co-operation with the Radiological and the Cardiological departments of Henri Mondor Hospital in Créteil, France. We actively participated in the definition of the experimental protocol, the preparation of the imaging setup and in all stages of the experiments themselves. Chapter 3 explains the fundamental principles of magnetic resonance imaging, emphasizing typical issues arising with cardiac MR imaging, which we had to overcome in order to obtain image data of an adequate quality.

Finally, in Chapter 4, a description of the biomechanical heart model developed at INRIA is given. We particularly concentrate on the setup and calibration of the model using real clinical data sets, hence the patient-specific modeling.

Applied modeling part

The applied modeling part deals with the model validation at both 1D and 3D levels, and we engaged in two clinical applications – the first one in the field of therapy planning and the second one for computer assisted diagnosis.

The objective of Chapter 5 is to validate the model at the fiber level using physiological experiments of myocardial fiber contraction and to study in detail some parts of the model that are connected to phenomena well observable in the experiments. The experimental data were provided by Prof. Yves Lecarpenier, Physiological Department of Hospital Bicêtre, France.

In Chapter 6, we set up subject-specific models using the data sets acquired in the animal experiments mentioned above. Our first objective was to show that the model is able to represent a healthy heartbeat by means of the motion pattern and simulated cavity pressure values. Then, we explore a possibility of introducing a myocardial infarction in the model only by modifying the mechanical parameters directly connected to the type of pathology and only in the infarcted region. We aim at demonstrating the model predictivity with respect to the global indicator of the left ventricle volumes and also with respect to the local motion pattern for this frequent heart disease.

The first clinical application was performed in co-operation with St. Thomas' Hospital and King's College in London, UK and is described in Chapter 7. The patients involved in the study suffered from a severe chronic heart failure and were indicated for an implantation of a special bi-ventricular pacemaker – the so-called Cardiac Resynchronization Therapy (CRT). We set up patient-specific models using image and pressure data acquired by physicians at the hospital before CRT (the baseline stage). The electrical activation in the model was prescribed according to the invasive electrophysiological measurements that were post-processed by researchers in the Asclepios team-project of INRIA and at King's College London, or using a simplified approach taking into account the non-invasive data only. In this preclinical study, we aim at demonstrating the model predictivity of LV pressure and dp/dt changes, when using the model calibrated for the baseline stage and applying new electrical activation patterns according to the pacing modes tested during the CRT implantation.

Chapter 8 deals with an application of data assimilation methods developed in the MACS team. The main objective is to perform state and joint state-parameter estimation with observations coming from real image data – using once more the data sets obtained during the experimental animal campaign. The parameters of concern are the contractility parameters. We would like to illustrate the effectivity of these data-assimilation algorithms and show that the estimated contractility values can improve the model itself and that they can serve as an indicator of the local heart function, by means of a detection of hypokinetic or akinetic regions in the myocardial tissue as typically arises after a myocardial infarction.

In Chapter 9 we conclude the results obtained during the PhD study and suggest some perspectives of ongoing work related to the thesis.

As an Appendix, we add a protocol created during the planning of the animal experiments in order to validate the in vivo study by the Institutional Animal Care and Use Committee of 'Faculté de Créteil', France.

1.3 Personal publications related to the thesis

- [22]: Conference article presenting a validation of the 3D model of the healthy and infarcted heart using data coming from an animal experiment performed in co-operation with Henri Mondor Hospital, Créteil, France. This article is related to Chapter 6.
  R. Chabiniok, D. Chapelle, P.F. Lesault, A. Rahmouni, J.F. Deux: Validation of a biomechanical heart model using animal data with acute myocardial infarction, In CI2BM09 - MICCAI Workshop on Cardiovascular Interventional Imaging and Biophysical Modelling, London United Kingdom, 2009.

- [97]: Conference article presenting patient-specific modeling in the cardiac resynchronization therapy planning applied for the first patient, in co-operation with Team-project Asclepios of INRIA, St. Thomas Hospital and King's College in London, UK. This article is related to Chapter 7.
  M. Sermesant, F. Billet, R. Chabiniok, T. Mansi, P. Chinchapatnam, P. Moireau, J.M. Peyrat, K. Rhode, M. Ginks, P. Lambiase, S. Arridge, H. Delingette, M. Sorine, A. Rinaldi, D. Chapelle, R. Razavi, N. Ayache: Personalised electromechanical model of the heart for the prediction of the acute effect of cardiac resynchronisation therapy, Proceedings of Functional Imaging and Modeling of the Heart 2009, FIMH09, LNCS, vol. 5528, June 2009, pp. 239–248.

- [98]: Methodological article for patient-specific modeling in the cardiac resynchronization therapy planning, in co-operation with Team-project Asclepios of INRIA, St. Thomas Hospital and King's College in London, UK. This article is related to Chapter 7.
  M. Sermesant, R. Chabiniok, P. Chinchapatnam, T. Mansi, F. Billet, P. Moireau, J.-M. Peyrat, K.C.L. Wong, J. Relan, K. Rhode, M. Ginks, P. Lambiase, H. Delingette, M. Sorine, A. Rinaldi, D. Chapelle, R. Razavi, N. Ayache: Personalised Macroscopic Electromechanical Model of the Heart for the Prediction of the Acute Effects of Pacing in Cardiac Resynchronisation Therapy, in preparation.

- Article presenting an application of the state and joint state and contractility parameter estimation using real image data. Data come from the animal experiment performed in co-operation with Henri Mondor Hospital, Créteil, France. This article is related to Chapter 8.
  R. Chabiniok, P. Moireau, J.-F. Deux, P.F. Lesault, A. Rahmouni, D. Chapelle: Estimation of Tissue Contractility from Cardiac Cine MRI Using a Biomechanical Heart Model, in preparation.

- [112]: Article presenting a sensitivity analysis of a pro-active electromechanical model-based cardiac motion tracking framework, in co-operation with Team-project Asclepios of INRIA.
  K.C.L. Wong, F. Billet, T. Mansi, R. Chabiniok, M. Sermesant, H. Delingette, N. Ayache: Cardiac motion estimation using a proactive deformable model: Evaluation and sensitivity analysis, in STACOM MICCAI Workshop on Statistical Atlases and Computational Models of the Heart: Mapping Structure and Function, Beijing, China, 2010.

Part I

Preparatory work

Chapter 2

Basic medical concepts

2.1 Introduction

The main topic of the thesis are clinical applications of a biomechanical model of the heart function. In this preparatory chapter, we would like to give some basic introduction to the elements of cardiovascular physiology and cardiology directly related to the type of data used and the simulations performed in the thesis. Most of this information is inspired by textbooks of physiology [46] and cardiology [70].

2.2 Basic cardiovascular anatomy

The heart is a muscular organ situated in the thorax between the two lungs in a space called the mediastinum. The function of the heart is to pump the blood in the circulatory system.

A longitudinal septum divides the heart into the left and right part, see Figure 2.1. Each part consists of an atrium and a ventricle. The atrium and the ventricle of either side are separated by an atrioventricular (AV) valve. The AV valve consists of three cusps on the right side (the *tricuspidal valve*), and of two cusps on the left side (the *bicuspidal valve*, more often called the *mitral valve*). Fibrous structures called *chordae tendineae* prevents the cusps of the AV valves from folding into the atria during myocardial contraction when the AV valve are closed. The chordae are fixed to the ventricle wall by the *papillary muscles*. The two ventricle extremities are: the base (to which the atria and large vessels are attached) and the apex (the bottom part of the ventricle). The axis connecting the apex and the base of the ventricle is called the *long axis*. Planes perpendicular to the long axis are the *short axis planes*.

Histologically, the heart tissue has a direct correspondence with the vessel wall structure. It consists of the following three layers: the inner layer – the *endocardium* (a single layer epithelium with a thin subepithelial connective tissue, similar to the vessel wall en-

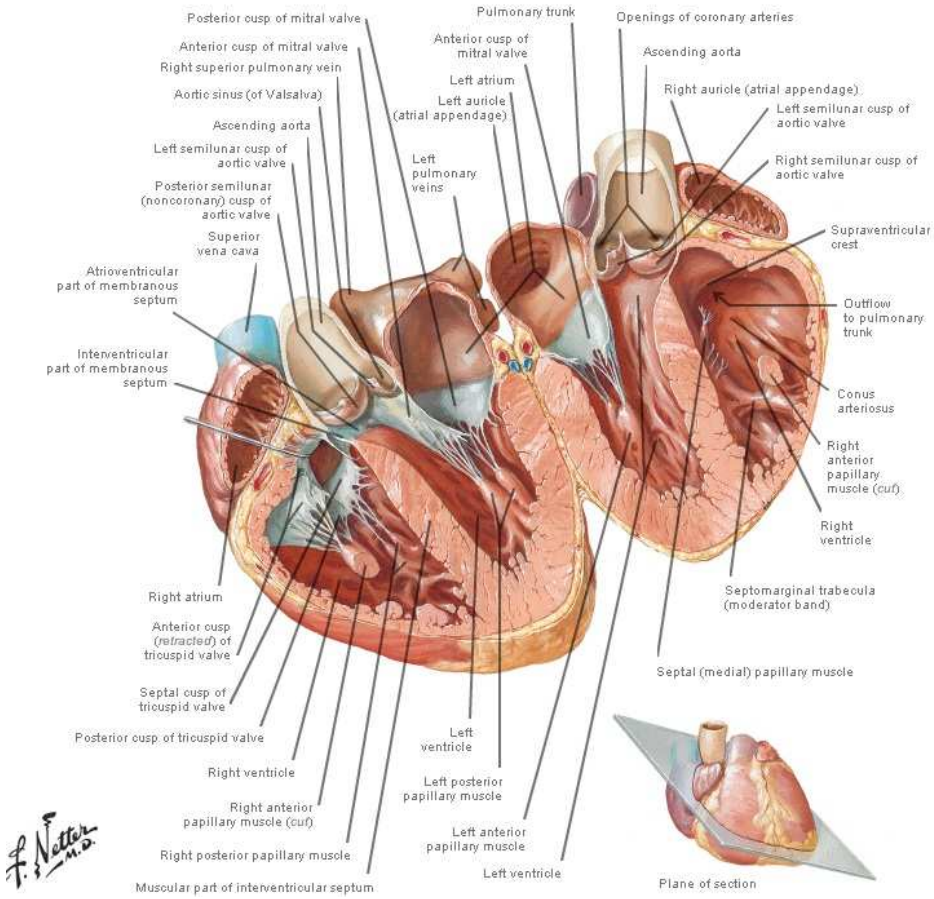

Figure 2.1: Anatomy of the heart, from [84].

dothelium), the thickest layer of cardiac muscle cells (the *myocardium*), and the outer layer made of two membranes (the *pericardium*). The first one is a serous membrane that is tightly attached to the myocardium (the visceral pericardium, *epicardium*) and the second – fibrous membrane – forms the pericardial sac (the parietal pericardium). There is a tiny space between the two pericardial membranes – the *pericardial cavity*. A small amount of pericardial fluid inside the cavity decreases the friction between the pericardial membranes. This friction can be augmented during some pathological states (e.g. inflammation of the pericardium, the *pericarditis*). The myocardium itself can be divided into three layers: the subendocardial third, the mid-third and the subepicardial third. Each of them has specific functional properties with respect to the blood supply and also for instance with respect to the duration of the contraction.

Atria are filled by blood from the veins and serve as a first-stage pump for the ventricles. The right atrium receives blood from the systemic veins (superior and inferior venae cavae), then the right ventricle pumps blood through the *pulmonary artery* to the lungs where the blood oxygenation takes place. The oxygenated blood returns via the *pulmonary veins* to the left atrium. The left ventricle ejects blood through the main systemic artery – the *aorta* – in the body (the systemic circulation). During ejection, the closed AV valves prevent blood from regurgitating back to the atria. During the period of ventricle filling, the AV valves are open and the ventricles are being filled by blood from the atria. Reverse blood flow from the large arteries to the ventricles is prevented by semilunar valves – the *aortic* and the *pulmonary valve*.

The heart is supplied with oxygen and nutrients by three main coronary arteries: The left anterior descending (LAD), the left circumflex[1] (LCx) and the right coronary artery (RCA). Although there is inter-subject variability, in general each artery supplies the following parts of the ventricles: the anterior wall of the LV and RV and the anterior part of the septum are supplied by the LAD, the lateral wall of the LV by the LCx and the inferior wall of both ventricles and the inferior part of the septum by the RCA. The main coronary arteries are located on the epicardium. Their smaller branches penetrate into the deeper layers of the myocardium and finally the vessels form the subendocardial capillary bed. After passing the capillary bed, blood is collected by the coronary veins. Most of the cardiac blood returns to the right ventricle via the *coronary sinus*. See Figure 2.2 with the anatomy of the coronary arteries and veins.

To assess local kinematical properties of the left ventricle (e.g. wall thickening during contraction) or to describe localization of several pathologies of the ventricles, the following recommendations of the American Heart Association (AHA) are applied: The left ventricle is divided into 3 parts with respect to the long axis: the basal third, the mid-cavity and the apical part. The basal and the mid-third are subdivided into 6 segments each, (segments #1–6 for the basal third and segments #7–12 for the mid-cavity). The apical third is subdivided into 4 segments (#13–16). The last segment of the left ventricle – the apex – is denoted as segment #17.

The segments of the left ventricle are schematically visualized using the so-called bull's eye view, see [21] and Figure 2.3. We will be using the subdivision of the LV into 17 regions. Each region will be called *AHA segment* with the corresponding number. The region around the valves is excluded from the subdivision since it would be difficult to assess e.g. the wall thickness in the vicinity of the valves.

[1] LAD and LCx are two different arteries, clinically speaking. Anatomically, both comes from the short common left coronary artery.

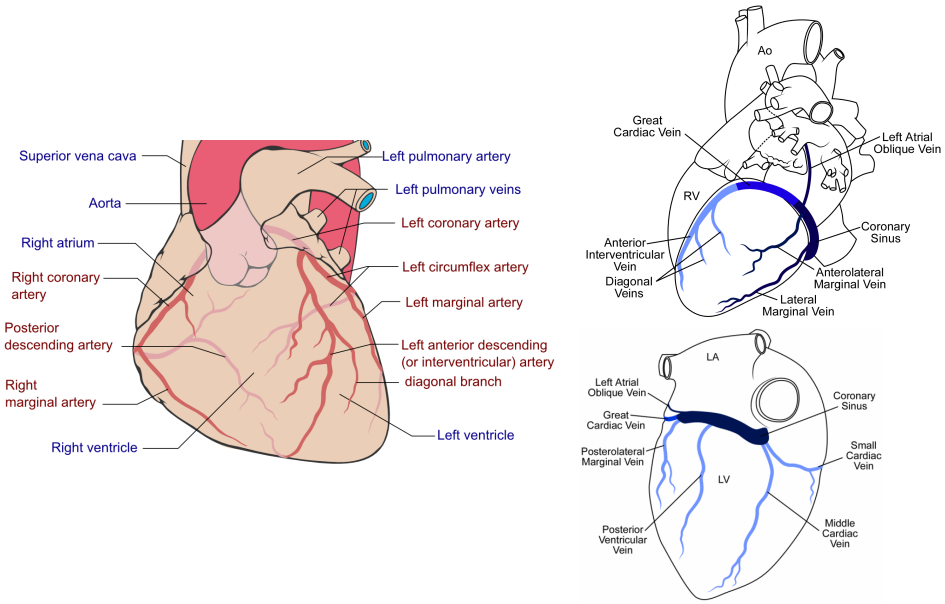

Figure 2.2: Coronary arteries from anterior view (left) and coronary veins from anterior view (right top) and posterior view (right bottom).

2.3 Basic cardiovascular physiology

2.3.1 Cardiac cycle

The period between two successive heartbeats is called the *cardiac cycle*. It consists of a period of ventricle contraction – *the systole*, and of ventricle relaxation – *the diastole*, see Figure 2.4. The duration of a normal cardiac cycle at rest is 0.75–1 sec which corresponds to a heart rate of 60–80 bpm (beats per minute). The diastole covers approximately two thirds of the cardiac cycle at rest. Although the heart rate increases during a physical activity, the length of the systole remains 250–330 ms and it is mostly the diastole that is getting shorter.

The volume of the left ventricle filled by the blood – the *end-diastolic volume (EDV)* – is about 130 mL. The minimum LV volume after ejection – the *end-systolic volume (ESV)* – is around 50–60 mL. It means that the relative ejected volume with respect to the end-diastolic volume of the ventricle – the *ejection fraction (EF)* – is around 50–60%.

The diastole consists of three parts of approximately same durations at rest: the period of rapid filling, the diasthasis and the atrial contraction (the atrial systole). The first part occurs immediately after the AV-valves opening. The ventricles are filled rapidly by blood from the atria. It accounts for the filling of the ventricles by approximately 70% of the stroke volume. While the blood flow from the atria follows the pressure gradient, and it

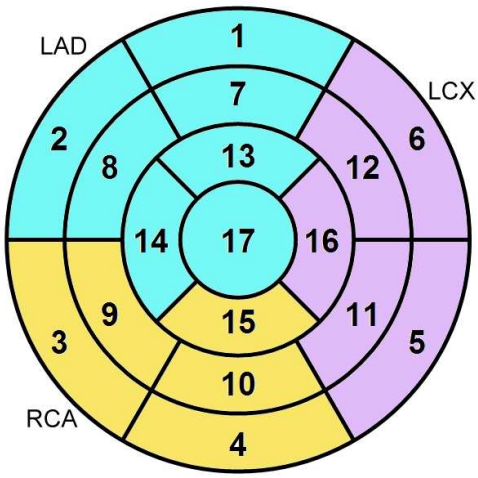

AHA #	Name of the segment
Basal third	
1	basal anterior
2	basal antero-septal
3	basal infero-septal
4	basal inferior-septal
5	basal infero-lateral
6	basal antero-lateral
Mid-third	
7	mid anterior
8	mid antero-septal
9	mid infero-septal
10	mid inferior-septal
11	mid infero-lateral
12	mid antero-lateral
Apical third	
13	apical anterior
14	apical septal
15	apical inferior
16	apical lateral
17	apex
not-referenced	region around the valves

Figure 2.3: Bull's eye view representing the AHA segments of the LV (from [21]). Each color represents the coronary artery by which the segment is supplied. The name of each segment is listed in the table.

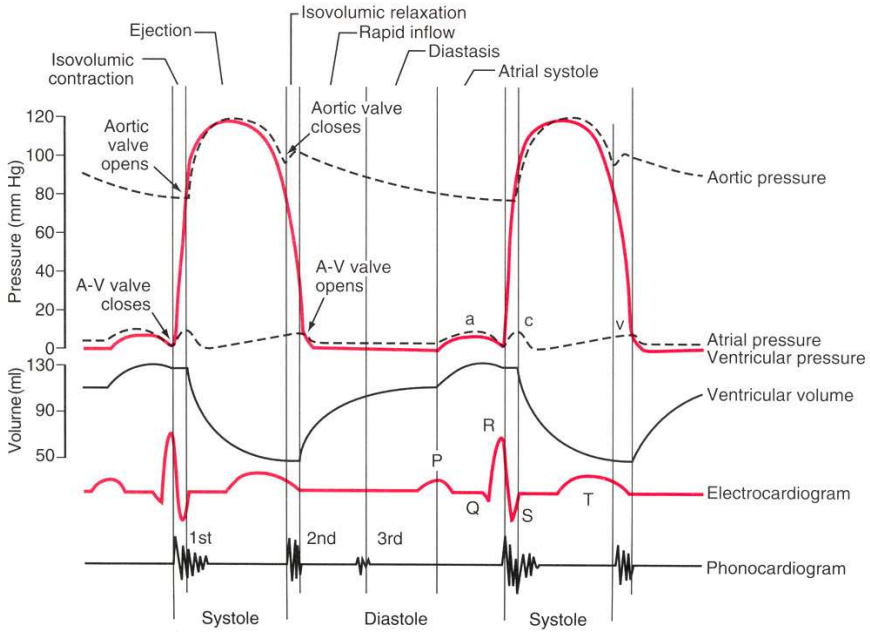

Figure 2.4: Cardiac cycle of the left ventricle (from [46]).

is therefore passive, the relaxation of the ventricle myocardium has an important active component, as discussed in Section 2.3.2. During the diasthasis, there is a minimal flow through the AV-valves. The diasthasis gets shorter if the heart rate increases. In the last third of the diastole, the atria contract and add the final 10–30% of the ventricle filling (the so-called atrial kick).

The right ventricle pumps blood against a mean pressure of 15 mmHg[2] (the low pressure – pulmonary circulation) and the left ventricle against a mean pressure of 100 mmHg (the high pressure – systemic circulation). These mechanical features of the circulatory system have an effect on the thickness of the ventricle walls and on the energetic needs of the ventricles. While the thickness of the wall of the right ventricle is approximately 3–4 millimeters, the thickness of the left ventricle is 12–15 millimeters and it has higher energetic needs. This also justifies why an ischemic heart disease (the disease caused by the lack of supply of the oxygen and nutrients in the myocardium, see Section 2.4.2) often affects the left ventricle.

The heart of an adult person (the left and right ventricle separately) has to pump approximately 5 liters of blood each minute, the so-called *minute heart volume* (MV). This value can increase sevenfold in a healthy person undergoing a physical activity (the

[2]Physicians usually represent the blood pressure as a height of mercury column, 1 mmHg corresponds approximately to 134 Pa.

heart rate can increase threefold and the myocardial contractility 2.5 folds). This so-called *cardiac reserve* is very limited in the diseased myocardium, which may lead to a symptomatic cardiac disease under stressful circumstances. The regulation of the heart function is discussed in detail in Section 2.3.5.

2.3.2 Contraction of the muscle fiber

Muscle contraction is based on an interaction of thick and thin filaments in a *sarcomere* – the functional unit of the muscle cell. Thin filaments consist of actin fibers and regulatory proteins such as tropomyosin and troponin. The main component of the thick filaments is a myosin protein. Tension created by repeatedly formed cross-bridges between the myosin heads and the binding sites of the actin can cause sliding of the myosin along the actin fibrils, which leads to the muscle fiber contraction, see [55] and [56].

Under resting conditions, the binding sites of the actin fibers are blocked by the troponin–tropomyosin complexes. Calcium ions (Ca^{2+}) cause conformational change of the complexes and the binding sites become uncovered. Immediately, myosin heads bind with a high affinity to the actin and form cross-bridges created under tension. The passive conformational change of the myosin molecule shifts the myosin head towards the centre of the sarcomere. The re-elongation of the myosin is an active process. It is an ATPase activity of the myosin head that provides the energy by lysing an adenosin triphosphate molecule (ATP). The cycle consisting of passive actin–myosin binding and the active myosin re-elongation is repeated as long as the myosin binding sites on actin are uncovered. The cytosolic Ca^{2+} ion concentration decrease to the initial low level is a necessary condition for the relaxation. See Figure 2.5 with description of the cardiac fiber and the functional unit of the fiber – the sarcomere – in particular.

Muscle cells have a well developed smooth endoplasmic reticulum, the so-called sarcoplasmic reticulum (SR). It serves as a storage of the Ca^{2+} ions. There are two main mechanisms in the rise of the cytosolic Ca^{2+} ion concentration after the generation of the membrane action potential. The first one is based on electrically activated slow reacting Ca^{2+} channels (the so-called dihydropyridine receptors, known also as L-Ca^{2+} channels) located in the cell membrane (*sarcolemma*), in particular in folds of the membrane called T-tubules. The second mechanism is the Ca^{2+} dependent release of the Ca^{2+} ions from the sarcoplasmic reticulum (the channel is part of a complex structure – the *ryanodine receptor*). The L-Ca^{2+} channels account for an increase of the cytosolic Ca^{2+} only by 10-20%. Nevertheless, this rise is very important for the consequent activation of the Ca^{2+} dependent release of Ca^{2+} which moves a high amount of the Ca^{2+} ions from the SR into the cytosol.

The main Ca^{2+} re-uptake mechanism is via an active transporter in the membrane of the SR (proteins from group SERCA[3]). Besides, there are other ways as for example the Na^{+} / Ca^{2+} antiport in the sarcolemma or the ATP-consuming sarcolemmal calcium pump

[3]SERCA stands for the smooth endoplasmic reticulum calcium re-uptake mechanism.

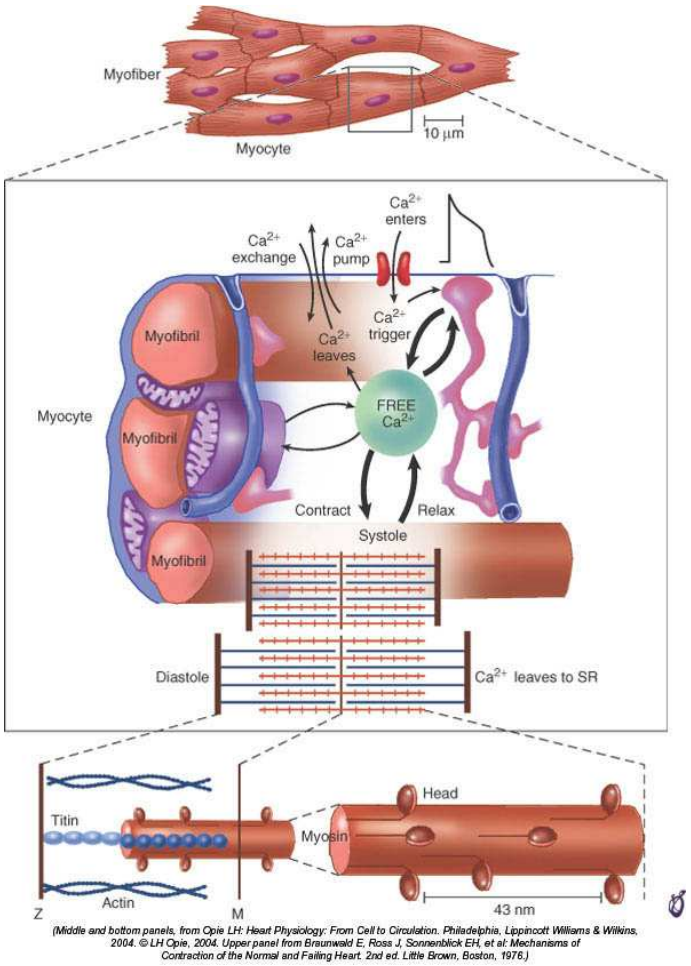

Figure 2.5: Myocardial fiber on macroscopical, microscopical and ultramicroscopical level. From [70].

(which carries Ca^{2+} from the intracellular to the extracellular compartment against the concentration gradient).

Preload and Afterload

Concerning muscle fiber contraction, the *preload* is defined as the tension in the fiber before contraction occurs. In a typical physiological experiment (as modeled in Chapter 5), the preload is given by the load that is attached to the fiber before the fiber is activated. Since the preload causes a passive extension of the fiber, it is often related to the degree of the passive extension.

By *afterload* we mean the tension generated by the fiber during the contraction. In the physiological experiment, the afterload is given by the weight of the load which is fixed to the fiber and that the fiber has to overcome. If we apply such an afterload value that the fiber is able to generate the active stress but it is not able to shorten (or raise the load), we talk about *isometric contraction*. If we fix the generated stress and let the fiber contract, we talk about *isotonic contraction*.

In the case of heart ventricle as a whole organ the most accurate definition of the preload and of the afterload would be the wall stress at the end-diastole or at the end-systole respectively. Since it is not possible to measure the wall stress in the myocardial tissue in vivo, the preload is usually represented either by the end-diastolic pressure in the ventricle or by the end-diastolic volume of the ventricle. The latter definition is related to the stretch of the myocardial fibers. The ventricle afterload is usually represented by the pressure against which the ventricle pumps the blood. In medical praxis, one usually takes the aortic pressure (or pulmonary artery pressure) as the afterload of the left (right) ventricle.

The part of the ventricle contraction (relaxation) when both the AV and the semilunar valves are closed and the ventricle volume is not changing is called the *isovolumic contraction*, respectively the *isovolumic relaxation*.

2.3.3 Electrical activation of the heart

Muscle cells (*myocytes*) belong to excitable cells, as for instance also neurons. The resting potential on the membrane[4] of the cardiac muscle cells (the *cardiomyocytes*) is around -90 mV. An action potential (AP) is generated when the membrane potential increases to a certain threshold, which is around -40 mV. The neighboring cardiomyocytes are electrically connected between each other and the action potential can propagate from one cell to the other. The resulting effect of the action potential is an increase of the Ca^{2+} ion concentration in the cytoplasm of the muscle cells (the *sarcoplasm*) which triggers the contraction, see Section 2.3.2.

[4]The so-called resting membrane (or transmembrane) potential.

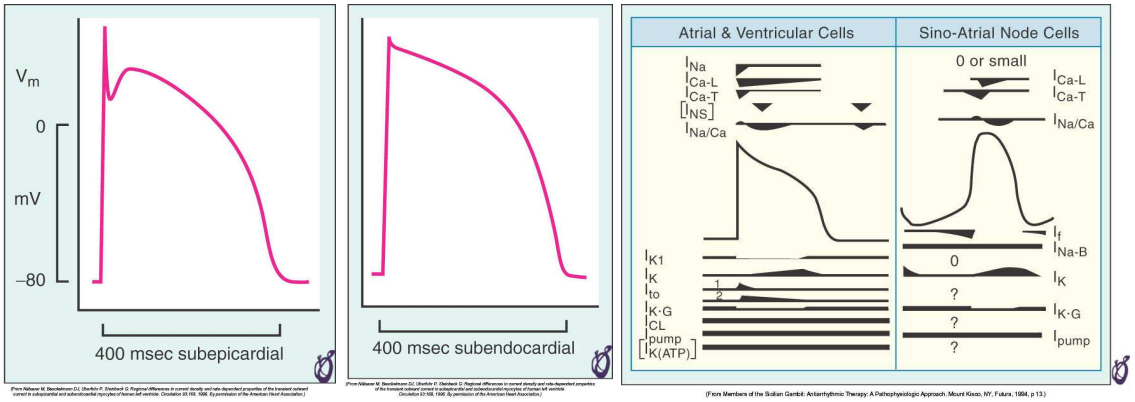

Figure 2.6: Typical action potentials in the myocardium of the ventricles and currents through each type of the ion channels involved in the generation of the action potential in a cardiomyocyte. From [70].

Resting and action membrane potential

Due to a distribution of ion channels in the cardiomyocyte membrane and due to active ion-transporting mechanisms (e.g. the Na–K ATPase that exchanges the intracellular Na^+ with the extracellular K^+) the resting potential on the cardiomyocyte membrane is negative in the intracellular medium with a value of around -90 mV. If the membrane potential rises to a certain threshold value (∼-40 mV), a rapid reaction with a positive feedback mechanism occurs: The higher the membrane potential is, the more fast voltage-gated Na^+ channels opens. The influx of Na^+ into the cell causes a sudden increase of the membrane potential which finally reaches slightly positive values (∼10–30 mV). We talk about *membrane depolarization*. The Na^+ channels do not remain active for more than a few milliseconds. At the time when their conductance ceases, another type of channels – the slow reacting Ca^{2+} channels – will open. The Ca^{2+} channels will keep the membrane in the depolarization stage for a period of another 200–400 ms. This part of the action potential is called the *plateau* and is entirely specific for the cardiomyocytes[5]. Finally, the efflux of the K^+ ions through potassium channels will bring the membrane potential back to its resting value – the so-called *repolarization*. In the following 250–300 ms a new action potential cannot be generated, which is the so-called *refractory period*. See Figure 2.6 for typical shapes of the action potential in the cardiomyocytes and for the conductances of each group of the ion channels during action potential generation.

[5]Neurons or skeletal muscle cells do not have the slow reacting Ca^{2+} channels, therefore the action potential does not contain the plateau. This is why the *action potential duration* (APD) is only 4–6 ms.

Excitation–contraction coupling

The electrically activated membrane Ca^{2+} channels cause an increase of the intracellular Ca^{2+} ion concentration in the cardiomyocyte. Consequently, the so-called Ca^{2+} activated Ca^{2+} channels will cause further – much higher – increase of the Ca^{2+} ion concentration, using reserves in the sarcoplasmic reticulum. The Ca^{2+} ions act directly in the sarcomere, where they suppress an inhibiting effect of the troponin–tropomyosin complexes and therefore they activate the contraction. For details see Section 2.3.2.

Conduction system of the heart

Cardiac muscle cells are electrically connected by the so-called *intercalated disks*, through which the electrical activation can propagate from one cell to the other, and the myocardial cells form a functional syncytium.[6] The propagation velocity in the working myocardium is around 0.3–0.5 m/s. There exist myocardial cells specialized for a fast transfer of the electrical signal, which form pathways of the *conduction system of the heart*. The propagation velocity through this dedicated system is up to 6 times higher than in the normal cardiomyocytes and can reach values of 1.5–4.0 m/s.

The primary electrical activation comes from another part of the conduction system – the so-called *pacemaker cells*. These are specialized muscle cells that are able to generate action potentials without any external activation. Their resting potential is higher than in the non-specialized cardiomyocytes with a value of around -55 mV, which is much closer to the threshold value for the AP generation. The membrane potential of the pacemaker cells slowly rises due to a moderate number of opened Na^{+} channels. When it reaches the threshold value, the action potential develops and spreads to the other cells. The pacemaker cells are located in the following parts of the heart (see Figure 2.7, left):

- sinoatrial node (or sinus node, SA node) – in the right atrium in the vicinity of the superior vena cava opening; the rate of AP self-generation is around 60–80 bpm
- atrioventricular node (AV node) – between the atria and the ventricles; the rate of AP self-generation is around 30–40 bpm
- cells of the conduction pathways – with a rate of AP self-generation of only 10–30 bpm

The SA node serves normally as a primary pacemaker, since it has the highest rate of spontaneous depolarization. The electrical signal generated in the SA node propagates to the AV node through the *internodal pathways* and activates the myocardium of the atria. Thanks to a relatively slow propagation in the AV node, the electrical activation is delayed by approximately 90 ms between the atria and the ventricles. The ventricles are electrically connected with the atria only by a single conductive network – the *bundle*

[6] A true syncytium is formed by cells that are fused together and share the same cytoplasm, plasma membrane etc. as in skeletal muscle.

of His (also called the AV bundle). It divides into the left and right branch that are located beneath the endocardium and follow the septum until the apex. The left branch divides into two main subbranches – the anterior and the posterior fascicles. The bundles progressively divide down to small branches (the so-called *Purkinje fibers*) that finally terminate directly on the myocardial cells in the subendocardial part of the heart. Thanks to this fast conductive system, the whole subendocardial region of the ventricles can be depolarized in a time period as low as 30 ms after the electrical signal crosses the AV node. Then, the electrical signal has to propagate from the subendocardial to the subepicardial region via the normal cardiac muscle cells. This is much slower and takes approximately the same time period as the activation of the whole subendocardial region ($\sim$ 30 ms). Therefore under normal conditions the whole ventricle myocardium is activated in about 60–70 ms.

ECG representation

An electrical activation of the heart can be recorded by placing electrodes on the surface of the body – the method called *electrocardiography* (ECG). The usual ECG consists of measuring electrical potentials between standard points on the body surface. It is a reproducible measurement that can show the progress of a cardiac disease or its current status. The complete ECG analysis is out of scope of this text, therefore we will only show some basic parts of a typical single derivative-ECG record taken in one cardiac cycle (see Figure 2.7, right):

- P wave: represents the depolarization of the atria
- QRS complex: represents the depolarization of the ventricles (the whole ventricle myocardium is activated during the period of time that corresponds to the duration of the QRS complex – QRSd, and is shorter than 120 ms in physiological activation)
- T wave: represents the repolarization of the ventricles

Cardiac Arrhythmias

States in which the electrical activation of the heart does not follow the physiological way described above are called cardiac arrhythmias. They can be caused by an abnormality on several levels of the electrical activation–conduction system:

1. abnormality of the pacemaker
2. block in various parts of the conduction system
3. spontaneous generation of electrical impulses in the myocardium

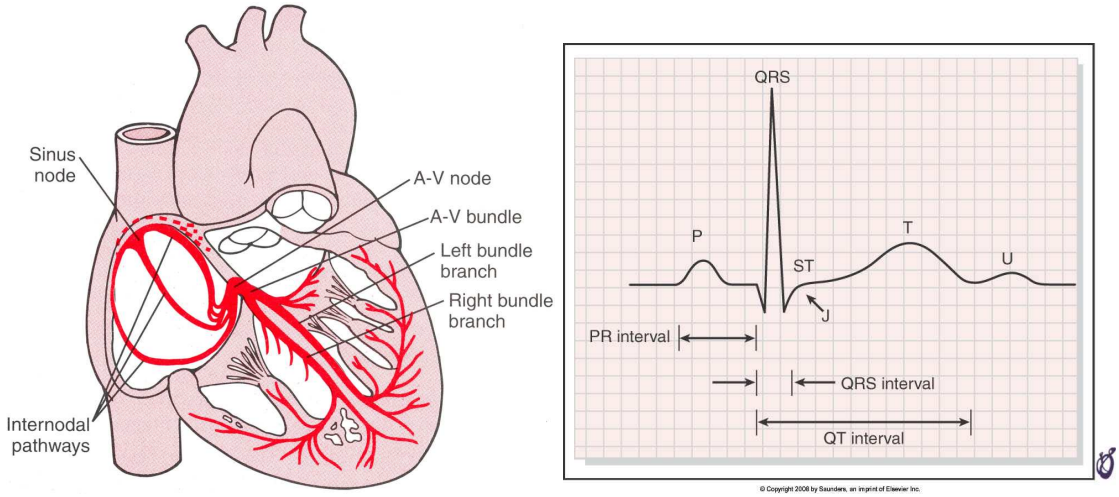

Figure 2.7: Left: Schematic of the conduction system of the heart (from [46]). Right: Typical ECG record from one cardiac cycle (from [70]).

Ad 1: Although the patient can have a normal sinus rhythm, the action may be either too fast (tachycardia) or too slow (bradycardia). If the SA node for some reasons fails, the pacemaker function is replaced by the AV node – but the heart rate will be considerably lower (∼30–40 bpm). If also the AV node fails, the cells of the conductive pathways in the ventricles may give the primary rhythm as well. The heart rate at this point would be very seriously decreased.

Ad 2: Conductivity in any part of the conduction system may be blocked. It may be caused e.g. by an ischemic necrosis of the tissue (myocardial infarction), by a dilatation of the heart chambers (e.g. in dilated cardiomyopathy), by an inflammation of the myocardium (myocarditis) or by some cardiac toxins (e.g. diphtheria toxin). The following list gives the localization of some blocks:

- *sinoatrial block* – between the SA node and the atrial myocardium (in this case, the AV node usually acts as the primary pacemaker).

- *atrioventricular block* – the block is located either in the AV node or in the bundle of His. The block can be uncomplete (of several grades) or complete (in which case the atria and ventricles contract independently). From a mechanical point of view, the effectivity of the ventricle filling may be reduced due to a limited effect of the atrial contraction. In the case of a complete AV block, the ventricle action is usually considerably slower. From the clinical point of view, the problem of AV blocks is very extended and complex.

- *block in the ventricle conduction* causes a dyssynchrony in the contraction of the ventricles and reduces the effectivity of the heart function. Typically, the left bundle branch may be blocked (the so-called left bundle branch block, LBBB). In the case of a right bundle blockage we talk about the right bundle branch block (RBBB). The left anterior fascicle block (LAFB) and the left posterior fascicle block (LPFB) represent common partial blocks of the left bundle. A characteristic sign in the ECG is an extended QRS complex with modified shape of each wave of the QRS. A more detailed description of the LBBB is given in Section 7.

Ad 3: In any part of the myocardium, a spontaneous action potential may be created. If the surrounding tissue is in the refractory period, the AP cannot propagate and it burns out. If the surrounding tissue is not in the refractory period, it can eventually activate the whole myocardium (the so-called *extrasystole*). The extrasystole may be of an atrial or ventricular type. The repetitive discharging of such a focus can cause a regular pattern – e.g. pairs of extrasystoles (*couplets*), successions of three extrasystoles (*triplets*) – or even an *extrasystolic tachycardia*. In some cases, the electrical signal may circulate along some atrial or ventricle pathways – the so-called *flutter* – or the trajectory may become completely chaotic – we then talk about atrial or ventricle *fibrillation*. Ventricular flutter and ventricle fibrillation cause minimal cardiac output and that is why we talk about malign arrhythmias, causing sudden cardiac death.

2.3.4 Coronary circulation

The heart is supplied by three main coronary arteries (LAD, LCx and RCA), as was described in Section 2.2. Now, we will give a few functional remarks about the coronary circulation.

The flow in the heart at rest is about 225 mL/min, which represents approximately 5% of the LV output. While the flow in the epicardial part of the heart is almost continuous, the flow in the subendocardial regions is intermittent. It is considerably reduced during systole, because of the mechanical squeezing of the subendocardial vessels, see Figure 2.8. Reducing the length of the diastole – typically by increasing the heart rate – decreases the blood supply, especially in the subendocardial regions. Therefore, the first symptoms of an ischemic heart disease often appear subendocardially. There are almost no collaterals between the main coronary arteries which has critical consequences if one of them becomes occluded. The tissue behind the occlusion undergoes an ischemic necrosis – the so-called myocardial infarction (see Section 2.4.2).

Most of the tissues in the body in resting conditions remove approximately 40% of the oxygen during the passage of the blood through the capillary bed. Therefore, the venous blood is usually still quite well saturated with oxygen. If there is a need for a higher oxygen supply, the oxygen uptake from the capillary blood may rise. However, situation differs in the coronary arteries where the myocardium removes 80–90% of the arterial oxygen even

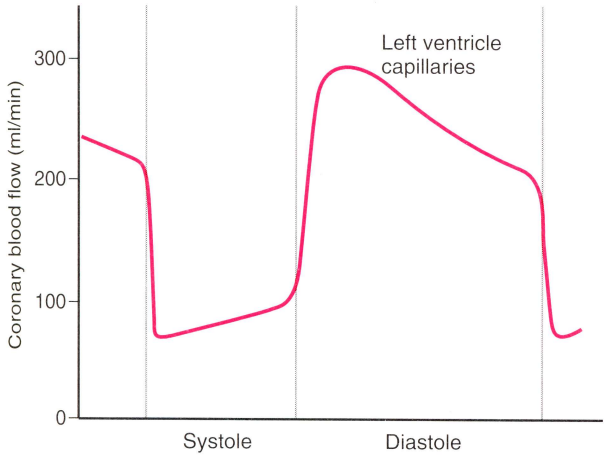

Figure 2.8: Intermittent coronary blood flow during a cardiac cycle with the lowest value in the systole. From [46].

at rest. Therefore, in any situation when the heart has higher oxygen demands (e.g. during any physical activity), the perfusion of the heart must increase.

2.3.5 Regulation of the heart function

The cardiac output is controlled by the peripheral tissues. Higher metabolic needs in the tissues cause their increased perfusion thanks to autoregulation mechanisms, which are controlled by the tissues themselves. The heart reacts immediately on an increased venous return by increasing the minute output by several mechanisms: The *heterotropic regulation* based on the *Frank–Starling mechanism* occurs during the first minutes of the venous return increase. Positively inotropic (an increased contractility of the ventricle), chronotropic (an increased heart rate), dromotopic (an increased conductivity in the conduction system of the heart) and positively lusitropic activation (an increased rate of the ventricle relaxation) account for the most important parts in the regulation of the cardiac output. The heart function can be regulated in a long-time scale (months–years) by hypertrophy of the myocardium.

Heterotropic regulation

A phenomenon of an increased stroke volume after increasing the end-diastolic volume of the ventricle, independently of the homeotropic, chronotropic or lusitropic regulations, was described already in the end of the 19$^{\text{th}}$ and beginning of the 20$^{\text{th}}$ century by Otto Frank

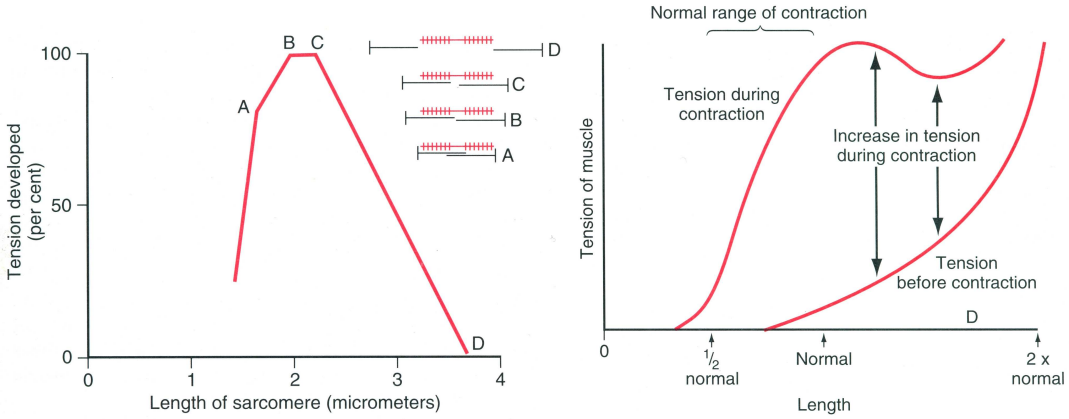

Figure 2.9: Left: Length–tension diagram for a single sarcomere with relative positions of the actin and myosin filaments depicted at the upper right. Note that the most effective contraction occurs for sarcomere length between the points B and C. Right: Length–tension diagram for the whole muscle, both before and during the activation. From [46].

and Ernest Starling.[7]

One possible explanation could be a better overlap between the actin and the myosin molecules when the fiber is stretched as is represented in Figure 2.9. It would lead to a higher number of actin–myosin cross-bridge formation, that would create an increased active stress in the fiber. Nowadays, it is known that the stretching of the muscle fiber causes an increased sarcomere Ca^{2+} sensitivity which increases the contractility. In [20] is shown that the increase of the contraction force is also related to the increase of the sarcomere passive tension rather than only to the sarcomere length. A molecule *titin* plays the role of an intermolecular sensor.

On an organ level, most of the physiological experiments demonstrating the Frank–Starling mechanism were performed on isolated heart–lungs preparates perfused by a certain solution (e.g. solution of albumin) and ventilated by a ventilator. In such experiments, the heart is extracted from the thorax of an animal without the pericardium. By increasing the filling pressure, we can directly increase the end-diastolic volume of the ventricle. Then, a stretching of the muscle cells induces a higher level of contraction via the Frank–Starling mechanism. The thick curve in Figure 2.10 on the left shows a typical cardiac output curve of the heart (the minute cardiac output depending on the right atrial pressure or equivalently on the end-diastolic ventricle filling) without any additional activation. We can see that the minute volume increases until a limit value is reached (∼12 L/min).

[7] Otto Frank (1885): *. . . the peak systolic pressure in the frog heart is directly related to resting diastolic fibre length.*
Ernest Starling (1914): *. . . cardiac output is directly related to the filling pressure.*

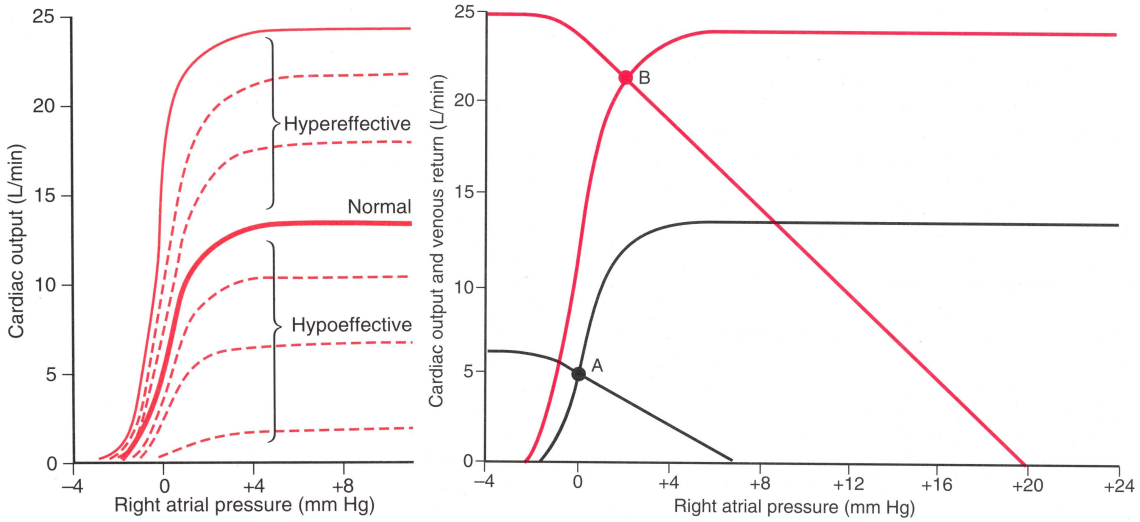

Figure 2.10: Left: Cardiac output curves (Frank–Starling curves) under basic conditions and for several positively inotropic activations (hypereffective hearts) and negatively inotropic regulations (hypoeffective hearts). Right: Cardiac output and venous returns curves at rest (in black) and during heavy exercise (in red). From [46].

It is difficult to obtain similar results in vivo for the following reasons: First, the heart is placed in the thoracic cage surrounded by the pericardium that prevents the ventricles from a higher level of dilatation. Secondly, by increasing the filling of the heart, the stress in the ventricle walls increases and the consecutive contraction is energetically very disadvantageous – especially for the failing heart. Nevertheless, the heterotropic regulation is present in vivo. We can observe it usually as a first reaction regulation – during the first minutes after increasing the venous return – before the other regulation mechanisms get activated. The Frank–Starling mechanism is especially important to equilibrate the left and right ventricle outputs.

Increased chronotropy

By increasing the heart filling, the right atrium is stretched, which leads to an activation of the vasomotoric centre in the brain stem and an increase of the heart rate (the so-called Bainbridge reflex). A stretch of the SA node itself increases the heart rate directly, with the elevation of an order of 20–25%. During physical activity, the main chronotropic activation is caused by stimulating the SA node by the sympathetic system. The heart rate can increase 2–3 folds.

Class	Objective Assessment
I	Patient with cardiac disease but without any limitations in physical activity
II	Comfortable at rest, ordinary physical activity results in fatigue, palpitations, dyspnea or anginal pain
III	Comfortable at rest, but less than ordinary physical activity results in fatigue, palpitations, dyspnea or anginal pain
IV	Symptoms of HF may be present even at rest

Table 2.1: New York heart association classification for the heart failure (NYHA).

Inotropic and lusitropic activation

The contractile properties of the myocardium (the strength of the contraction) can be increased by the inotropic activation. The ejection fraction of the ventricles is a clinically measurable indicator of the inotropic state. As an example of inotropic activation, there are mechanisms that increase the Ca^{2+} ion concentration in the cytosol (e.g. by increasing the ryanodine receptor sensitivity). The inotropic stimulation may also be achieved by increasing the myosin ATPase activity or directly by increasing the rate of cross-bridge formation, independently on the activity of the ATPase. Lusitropic activation is achieved by increasing the re-uptake rate of the Ca^{2+} ions from the sarcoplasm to the sarcoplasmic reticulum or to the extracellular compartment. These processes are often controlled by the state of phosphorylation / dephosphorylation of certain proteins initiated e.g. by the stress hormones epinephrin or norepinephrin. Hence the activation of the sympathetic system has positively chronotropic, inotropic, lusitropic and also dromotropic effects.

The increased or decreased effectivity of the contraction of the heart caused by the inotropic activation is depicted in Figure 2.10.

2.4 Cardiological remarks

2.4.1 Heart failure

Heart failure (HF) is a symptom by which the heart is not able to pump the amount of blood that returns via the venous system. The venous return is directly given by the metabolic needs of the tissues. That is why the heart failure may also be defined as a state in which the heart is not able to pump enough blood to supply the peripheral tissues with an adequate quantity of oxygenated blood. Due to the blood stagnation in front of the heart ventricles, the patient develops symptoms such as dyspnea and fatigue (typical of the left ventricle failure) or edemas. HF can be clinically evaluated using a global index as for instance the NYHA classes, see Table 2.1.

HF may be an acute disorder or the result of a long-term process (that finally leads to such a situation). Patients suffering from HF may be categorized into 2 groups (approxi-

mately of the same size): HF with a depressed ejection fraction (the *systolic heart failure*) or HF with a preserved ejection fraction (the *diastolic heart failure*).

Systolic heart failure

Systolic heart failure is characterized by a decreased ejection volume, while the diastolic ventricle filling is preserved. It can be caused by a decreased contractility either locally or globally in the whole ventricle. The former case is typically the result of myocardial infarction (see Section 2.4.2), in which a part of the myocardium becomes hypo– or akinetic. The latter case may arise from some diseases affecting the whole myocardium, as is the case for cardiomyopathies (see Section 2.4.3). A dyssynchronous heart contraction or a stenotic aortic valve are some other examples of diseases that may lead to a systolic heart failure.

Diastolic heart failure

During diastole, ventricles are relaxing and the pressure decreases from the systolic value back to the low diastolic value. As soon as it drops below the atrial pressure, the AV valves open and the blood flows along the pressure gradient to the ventricles. The relaxation of the myocardium has a passive and an active component.

The passive component of relaxation is given by an elastic recoil of the ventricle. It can be impaired if the myocardium becomes stiffer (e.g. in a hypertrophied heart with increased fibrosis). The active component of the relaxation is based on the re-uptake of the Ca^{2+} ions from the sarcoplasm. It is an ATP–dependent process and is especially important in the isovolumic phase of the relaxation. It can be altered in any situation when the heart supply is decreased.

In an early stage of the ischemic heart disease, the ejection fraction can still be normal thanks to compensation mechanisms that cause an increased contractility of the heart, but the diastolic phase may be already altered. Later, the diastolic heart failure can be followed by the systolic heart failure.

Compensated and decompensated heart failure

Under resting conditions, the heart has to provide the tissues with approximately 5 L/min of blood (cardiac output). In an acute heart failure the cardiac output drops immediately and the following compensatory mechanisms are activated (see Figure 2.11):

1. An increased sympathetic activation (and parasympathetic inhibition) during the first minutes.

2. Retention of body fluids by kidneys leading to an increased volume of the circulating blood (hours–days).

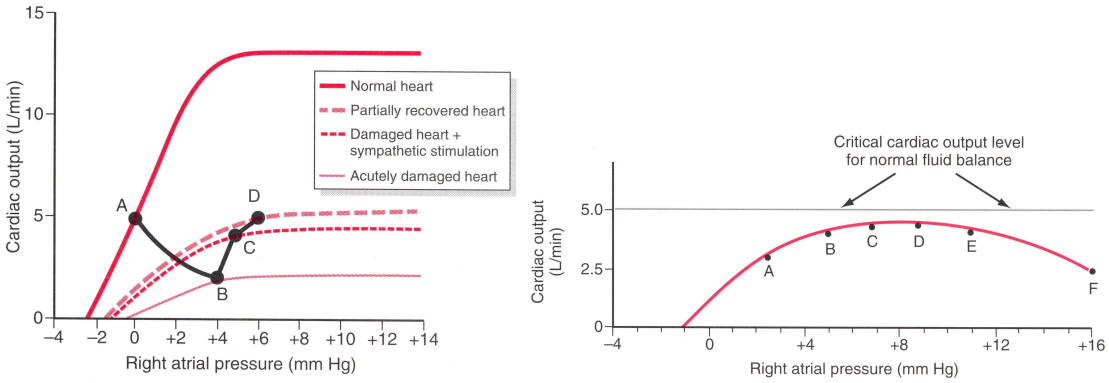

Figure 2.11: Left: Progressive changes (points A–D) in an acute compensated HF. Note that the partially recovered heart is able to pump 5 L/min but the cardiac reserve (the maximum cardiac output) has dropped significantly. Right: Vicious cycle in decompensated heart failure – the heart is not able to react to the progressive fluid retention over a period of days (points A–F). From [46].

3. Progressive recovery of the heart (months–years).

If the sympathetic response returns the cardiac output to a sufficient level and the heart is able to sustain an increased load due to the fluid retention by kidneys, we talk about *compensated heart failure*. On the contrary, if the heart function is so weak that it cannot reach the cardiac output of 5 L/min, the kidneys will be still acting in the fluid retention and a vicious cycle will be set. The heart will be getting still weaker, and the cardiac output will not be sufficient. This situation is called *decompensated heart failure*.

2.4.2 Ischemic heart disease

An ischemic heart disease (IHD) arises when there is an insufficient blood supply in a part of the myocardium. The most usual cause is the atherosclerosis in a coronary artery.

The atherosclerosis is a chronic inflammation in the intimal layer of the arterial wall caused by activated macrophages. The consequences of the atherosclerotic disease are either the stenosis of the artery, or the artery occlusion. It is a rupture of an atherosclerotic plaque followed by the blood coagulation and thrombus formation which actually occludes the arterial lumen. If the thrombus does not dissolve within a few minutes, the myocardial tissue behind the occlusion will undergo an ischemic necrosis (the *myocardial infarction*). The infarcted region affects the heart function mechanically, since it becomes hypo- or akinetic, and also electrically. In the first minutes to hours some arrhythmias may appear, among which ventricle flutter and fibrillation are the most threatening.

The following forms of IHD are recognized:

- Stable angina pectoris: a transient episode of myocardial ischemia caused by an increased need of the myocardium (for example due to physical activity) and an impossible increase of the coronary blood flow (e.g. due to stenosis of the supplying artery). The chest pain or discomfort are typical clinical symptoms. The pain relieves by itself in a few minutes or after application of nitroglycerin.

- Unstable angina pectoris: the angina symptoms occur either at rest or they evolve significantly and last for more than 10 minutes but the myocardium does not undergo ischemic necrosis. The cause of the symptoms may be an atherosclerotic plaque rupture (followed by a rapid thrombus dissolution), the spasm of a coronary artery (Prinzmetal's variant angina), an advanced and progressing stenosis of the coronary artery, or an increased myocardial oxygen demand (as for example in anemia or tachycardia).

- Myocardial infarction: The symptoms of the unstable angina pectoris are followed by an ischemic necrosis of the myocardium. The first affected regions are situated in the subendocardial zone because of the most sensitive coronary circulation in this myocardial part (see Section 2.3.4). The infarcted region may propagate in the epicardial direction, and can affect the whole myocardium (*transmural infarction*).

- Sudden cardiac death: Manifestation of the ischemic heart disease by a lethal arrhythmia. It typically occurs in the first minutes after a coronary artery occlusion, that may be in some cases given just by a reversible coronary spasm.

2.4.3 Cardiomyopathies

Cardiomyopathies (CMs) are diseases affecting primarily the myocardium and resulting in a cardiac dysfunction. Diseases of the pericardium, valves and coronaries (ischemic heart disease) as well as congenital heart diseases are excluded from the cardiomyopathies[8].

The main morphological types of CMs are listed below. Selected CMs visualized by magnetic resonance imaging (MRI[9]) are shown in Figure 2.12.

- Dilated (DCM): DCM is characterized by an increased internal diameter of the LV with wall thinning. Histologically, the wall is remodeled in the sense of an increased fibrosis and consequently an increased tissue stiffness. DCM often leads to systolic heart failure. The conduction system is often affected, which may lead to some atrio-ventricular, interventricular or intraventricular blocks (e.g. LBBB or RBBB). The dilated heart may cause a valve disease (e.g. a secondary mitral regurgitation). Regarding the etiology of the DCM, in some cases it is genetic (including single

[8]The so-called ischemic cardiomyopathy – an increased myocardial stiffness with fibrosis caused by the ischemic heart disease (and possibly multiple infarctions) – is not a cardiomyopathy in a right sense.

[9]Description of Cardiac MRI is given in Chapter 3.

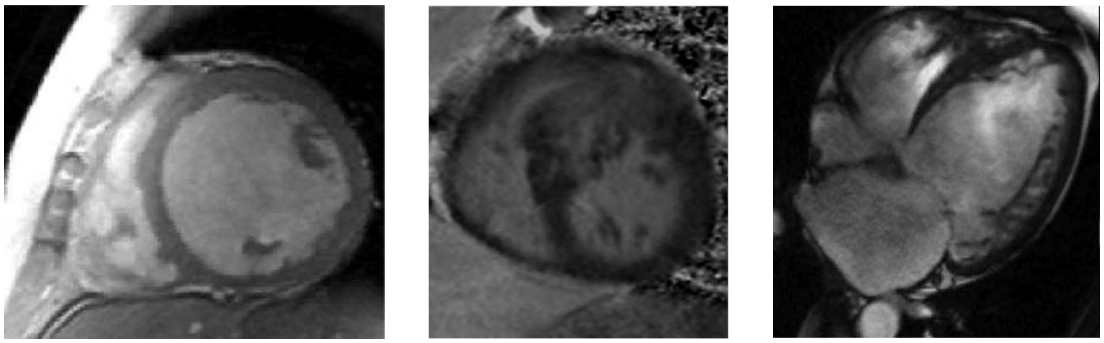

(a) Dilated cardiomyopathy (DCM)

(b) Hypertrophic cardiomyopathy (HCM) in the septum and LVOT

(c) Left ventricle non-compaction (LVNC)

Figure 2.12: Selected cardiomyopathies in MRI.

gene mutations as for instance in cytoskelet components, actin, etc.). DCM can follow a myocardial infection (viral myocarditis, it can be caused by diphtheric toxin, protozoal disease – the Chagas disease). There may occur a reversible reaction on an acute stress in a form of a balloon-like dilatation (Tako-Tsubo). DCM may also be induced by some toxic agents (e.g. alcohol abuse, anthracycline anticancer drugs). In many cases, the ethiology is unknown and the DCM is considered to be idiopathic.

- Hypertrophic (HCM): HCM is characterized macroscopically by an increase of the LV mass (asymmetric LV hypertrophy – especially in the septal area). The usual causes of the LV hypertrophy – as for instance the systemic hypertension or the aortic valve stenosis – are absent. The typical microscopic image shows disarranged myocardial fibers, which impairs the ventricle contractile function. The ventricle filling is severely affected, which leads to diastolic heart failure. The hypertrophy in the area of the LV outflow tract – as can be seen in Figure 2.12(b) – often creates a barrier for the blood ejection (a pressure gradient between the LV and the aorta). The most frequent cause of the mortality are malign cardiac arrhythmias.

- Restrictive (RCM): RCM is characterized by an increased stiffness of the subendocardial part of the myocardium, that prevents the ventricle from adequately filling. RCM therefore leads to diastolic heart failure. RCM develops often secondarily due to an infiltration of the myocardium e.g. by an amyloid protein (amyloidosis). An iron overload (as for instance in hemochromatosis or in β-thalasemia) or sarcoidosis are other causes of RCM.

- Arrhythmogenic right ventricle dysplasia (ARVD): ARVD is a degeneration of the wall of the RV (and sometimes also of the LV) by means of a fibro-fatty replacement

of the myocardial tissue. Thinning of the wall and formation of small aneurysms are the main morphological signs of ARVD, see Figure 3.10. ECG abnormalities, as for instance ventricle extrasystoles, are present. The most threatening consequences of ARVD are RV progressive failure and serious arrhythmias, including malign ventricle fibrillation.

- Left ventricle non-compaction (LVNC): LVNC is given by an arrest of the embryogenesis of the myocardium. The myocardium is formed by a spongy network of myocardial fibers with abundant recesses and sinusoids, as in the lateral LV wall in Figure 2.12(c). The disease may lead to chronic heart failure. The spongy tissue is often arrhythmogenic.

Chapter 3

Magnetic Resonance Imaging

Image data used in this thesis for personalization of the model were obtained by magnetic resonance imaging (MRI). The data were either acquired by specialists at hospitals or in case of an animal experiment we actively participated by suggesting the experimental setup, preparing the imaging sequences and performing the data acquisition. In this chapter we are going to explain the basis of MRI and discuss imaging of the cardiovascular system and of the heart in particular. The aim of this chapter is to finally describe a protocol for cardiac MR data acquisition during an animal experiment, performed during the PhD study.

This chapter is inspired by the course of MRI given by J. Tintera at Institute for Clinical and Experimental Medicine (IKEM), Prague, Czech Republic. The presented MR images were acquired either directly by J. Tintera or with his participation in the setup of MR sequences.

3.1 History

The first resonance experiments with magnetic properties of nuclei were performed by Isidor Isaac Rabi[1] in 1933. The phenomenon of nuclear magnetic resonance (NMR) was described independently by Felix Bloch and Edward Mills Purcell in 1946.[2] NMR became a valuable technique used for the chemical and physical analysis of molecules by means of the NMR spectroscopy. In such applications, the NMR signal is acquired from the entire volume of the chemical sample and the resulting analysis does not contain any spatially dependent information. In 1973 Paul Lauterbour and Peter Mansfield[3] proposed an idea

[1] I.I. Rabi was awarded by The Nobel Prize in Physics in 1944 "for his resonance method for recording the magnetic properties of atomic nuclei".

[2] F. Bloch and E.M. Purcell were awarded by The Nobel Prize in Physics in 1952 "for their development of new methods for nuclear magnetic precision measurements and discoveries in connection therewith".

[3] P. Lauterbour and P. Mansfield were awarded by The Nobel Prize in Physiology and Medicine in 2003 "for their discoveries concerning magnetic resonance imaging".

nucleus	concentration in living tissues (mMol)	gyromagnetic ratio (γ) ($s^{-1}T^{-1}$)
^{1}H	10^5	$2.6752 \cdot 10^8$
^{31}P	10^1	$1.0829 \cdot 10^8$
^{13}C	10^1	$6.7266 \cdot 10^7$

Table 3.1: Concentration and gyromagnetic ratio of selected nuclei.

to focus the acquisition of the NMR signal on small volumes by means of a subdivision of the imaging body into voxels ([64]). They constructed the first NMR tomograph.

In the second part of the 20th century, the word 'nuclear' was not well accepted by the public mainly because of the threats of the cold war. It is the reason why the name 'Nuclear Magnetic Resonance' (NMR) was replaced by the 'Magnetic Resonance Imaging' (MRI) in medical applications. The first commercial MR systems appeared in 1985. Since that time, the development went on in many aspects. One of the most visible progresses is in field of the acceleration of imaging protocols. While some types of acquisition could have taken more than 1 hour in the 1980s, it did not take more that a few minutes 10 years later. Thanks to this fact, the imaging of moving organs – as for the heart – has become available.

3.2 Basic principles of MRI

3.2.1 Tissue magnetization

Atomic nuclei with different numbers of protons and neutrons have a non-zero magnetic momentum. Typical examples of such nuclei in living tissues are ^{1}H, ^{31}P or ^{13}C, from which the nuclei ^{1}H are the easiest to detect by means of the NMR, thanks to their highest concentration and also due to the fact that they have the largest gyromagnetic ratio[4] γ, see Table 3.1. Therefore from now on we will be considering just the nuclei ^{1}H, each of them characterized by its magnetic momentum (spin) $\mathbf{m}_i$. Since the nuclei ^{1}H consist only of one proton and they do not have any neutrons, they are often called *'protons'*.

By net *tissue magnetization* $\mathbf{M}$ we mean the sum of all particular nuclear magnetic spins $\mathbf{m}_i$ in the imaging volume, hence $\mathbf{M} = \sum_i \mathbf{m}_i$. While we should use the quantum mechanics approach to describe the magnetic spins[5] $\mathbf{m_i}$, the tissue magnetization $\mathbf{M}$ is a macroscopic quantity for which the classical approach can be applied

[4]The ratio between the angular and magnetic momentum – a property characterizing each type of nucleus. Higher γ increases the sensitivity of the nucleus to the NMR effect.

[5] Since MRI is not the main topic of the thesis, we will be using classical mechanics (including to describe processes related to the nuclear spins $\mathbf{m}_i$) in order to simplify the explication of basic concepts. For the rigorous quantum approach see e.g. [69].

magnetic induction of $\mathbf{B_0}$	parallel orientation	antiparallel orientation
0.5 T	$10^6 + 3$	10^6
1.0 T	$10^6 + 6$	10^6
1.5 T	$10^6 + 9$	10^6
3.0 T	$10^6 + 18$	10^6

Table 3.2: Comparison of counts of ^{1}H nuclei in the parallel (the low-energy state) and in the antiparallel orientation with respect to the induction (strength) of the external homogenous magnetic field $\mathbf{B_0}$. Note that even for high magnetic fields, there is only a slight difference between the counts in the two configurations – hence the detectable tissue magnetization $\mathbf{M}$ is very low.

Under normal conditions, the orientation of all nuclear magnetic spins $\mathbf{m}_i$ is random and therefore there is a zero net tissue magnetization, $\mathbf{M} = \sum_i \mathbf{m}_i = \mathbf{0}$. However, if the tissue is placed in a strong homogenous magnetic field with a magnetic induction given by vector $\mathbf{B_0}$, the spins $\mathbf{m}_i$ will align either parallel to $\mathbf{B_0}$ or in an antiparallel way. The parallel orientation corresponds to the low-energy state, therefore there will be more nuclei in the parallel configuration than in the antiparallel one. Hence, the tissue magnetization will become a non-zero vector, $\mathbf{M} \neq \mathbf{0}$. The ratio of the spins in the parallel vs. antiparallel state depends on the magnitude of vector $\mathbf{B_0}$ that will be denoted by B_0 (the strength of the external magnetic field $\mathbf{B_0}$) and is larger in higher magnetic fields, see Table 3.2. Since the tissue magnetization $\mathbf{M}$ is a source of the NMR signal, we can obtain a higher signal for stronger external magnetic fields.

Remark:
The ratio of nuclei in the antiparallel vs. parallel configuration is governed by the Boltzman distribution: $\frac{N_{antiparallel}}{N_{parallel}} = e^{-\frac{\Delta E}{kT}}$, where k stands for the Boltzman constant, T is the thermodynamical temperature and ΔE represents the energetic difference between the parallel and antiparallel configuration.

Tissue magnetization $\mathbf{M}$ can be decomposed into two components: the *longitudinal magnetization* $\mathbf{M}_\parallel$, which is parallel to $\mathbf{B_0}$, and the *transverse magnetization* $\mathbf{M}_\perp$, which is perpendicular to $\mathbf{B_0}$. Hence, $\mathbf{M} = \mathbf{M}_\parallel + \mathbf{M}_\perp$. From the point of view of classical mechanics, the magnetic spins $\mathbf{m}_i$ (both in the parallel and antiparallel orientations) are aligned at a slight angle with respect to $\mathbf{B_0}$ and precess around the axis given by[6] $\mathbf{B_0}$, see Figure 3.1. The magnitude of the longitudinal component of the net tissue magnetization $M_\parallel = M_0 > 0$ due to the fact that there are more spins in the parallel configuration. The transverse component $\mathbf{M}_\perp = \mathbf{0}$ since the spin phases are random.

[6] According to Footnote 5 we point out that this argument is not true from the point of view of quantum mechanics since there are only two states for each spin and the spin precession does not have any sense if we do not sum a sufficient number of $\mathbf{m}_i$.

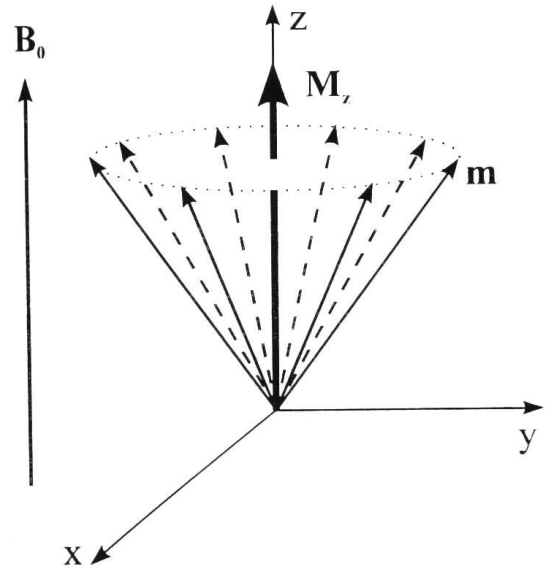

Figure 3.1: Vector of tissue magnetization $\mathbf{M}$ with contribution of all magnetic spins $\mathbf{m_i}$ precessing around the axis given by direction of $\mathbf{B_0}$. From [110].

3.2.2 Excitation and relaxation

The frequency of the precession motion of the magnetic spins is given by their gyromagnetic ratio γ and by the strength of magnetic field $\mathbf{B_0}$, the so-called *Larmor frequency*:

$$\omega_L = \gamma B_0. \tag{3.1}$$

Therefore for a given magnetic field $\mathbf{B_0}$ there is a specific – Larmor – frequency for each type of nucleus.

The system of spins precessing with the Larmor frequency ω_L is able to absorb an energy in the form of a radiofrequency pulse[7] (RF) of the same frequency – the process called *excitation*. Hence, the name of the method – *magnetic resonance* – comes from the fact that the energy exchange occurs when the RF pulse is 'in resonance' with the precession frequency of the spins.

After the excitation by the RF pulse of the Larmor frequency (ω_L), the full spin system will precess in phase and some of the spins will pass from the low-energy parallel configuration to the high-energy antiparallel state. This is why a transverse component of the tissue magnetization ($\mathbf{M}_\perp$) will appear and the longitudinal component ($\mathbf{M}_\parallel$) will decrease. While the longitudinal magnetization $\mathbf{M}_\parallel$ is undetectable, the transverse component induces a current of a few μA in the receiving coil due to electro-magnetic induction.

[7]The RF pulse is created by an oscillating magnetic field $\mathbf{B_1}$ perpendicular to $\mathbf{B_0}$.

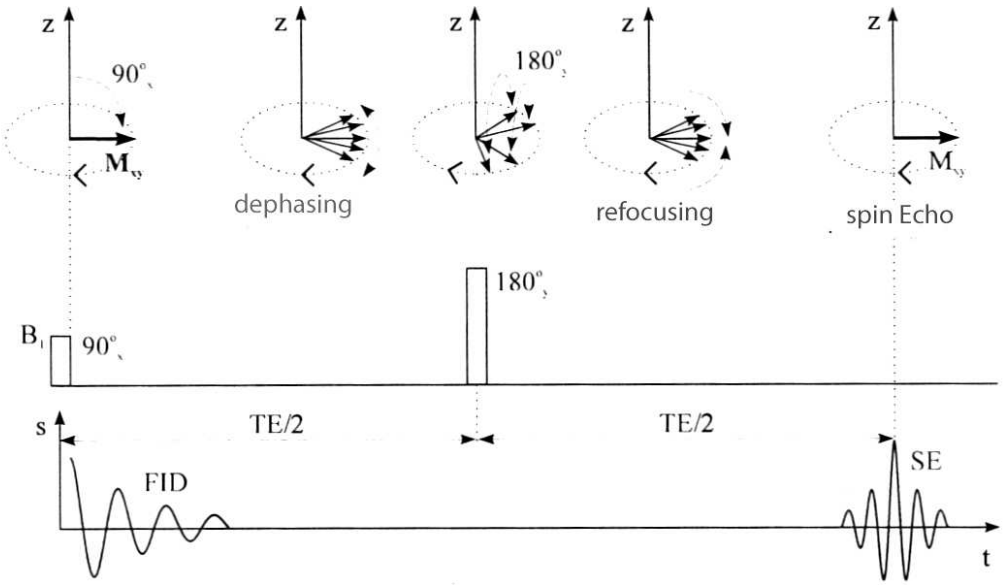

Figure 3.2: Excitation by 90 ° RF pulse tilts the magnetization vector in the transverse plane and brings the spin system into phase. This causes the signal FID to appear. The drop of FID amplitude is due to spin-spin interactions (T2 relaxation). The 180 ° RF pulse refocuses the spins and a signal in the form of echo re-appears (spin echo, SE). From [110].

The electrical current induced in the receiving coil – the MR signal – has a character of a damped sinusoid, the so-called *Free Induction Decay* (FID), see Figure 3.2. An amplitude decrease of the FID is caused by relaxation processes, which bring the magnetization back to the non-excited state.

The relaxation has two independent components: a recovery of the longitudinal relaxation – the *T1 relaxation* – and a decay of the transverse magnetization – the *T2 relaxation*. The relaxation rates are given by physical properties of the tissue and also by external effects (e.g. by the strength of the external magnetic field). Finally, the initial magnetization vector $\mathbf{M}$, with $M_{\parallel} = M_0$ and $M_{\perp} = 0$, will be recovered.

T1 relaxation

The exponential re-establishment of the longitudinal magnetization is caused by an energy transfer from the excited nuclei to the surrounding tissue (the lattice) in the form of heat. Therefore the T1 relaxation is also called the *spin–lattice relaxation*. The longitudinal relaxation is characterized by a time constant T1 and can be represented by the following equation:

$$M_{\parallel} = M_0(1 - e^{-\frac{t}{T1}}). \tag{3.2}$$

The T1 relaxation time constant is given by physical properties of the tissue and it also depends on the strength of the external field $\mathbf{B_0}$ – the T1 relaxation time increases at higher fields $\mathbf{B_0}$. The longitudinal relaxation of biological tissues is around 700–2000 ms, see Table 3.3.

T2 relaxation

The decay of the detected signal is caused by dephasing of the spins due to their interactions (*spin-spin interactions*, see Figure 3.2) and because of the local inhomogeneities of the magnetic field. The first component (the spin-spin interactions) stands for the true T2 relaxation and it is independent of the strength of $\mathbf{B_0}$. It causes an exponential decay of the transverse component of the magnetization (and therefore of the detected signal) with a time constant T2:

$$M_\perp = M_0 e^{-\frac{t}{T2}}. \tag{3.3}$$

The transverse T2 relaxation of biological tissues is around 80–200 ms, see Table 3.3.

In practice, the signal decay is always faster, which is caused by local inhomogeneities of the magnetic field $\mathbf{B_0}$. The transverse relaxation is given by an *effective relaxation time* T2*:

$$\frac{1}{T_2^*} = \frac{1}{T_2} + \gamma \Delta B, \tag{3.4}$$

where ΔB represents the inhomogeneities of $\mathbf{B_0}$. The larger ΔB is, the faster the T2* relaxation will be. A principle of fast dephasing and refocusing of the spins by a strong controlled $\mathbf{B_0}$ inhomogeneity is used in MR signal detection by the so-called *gradient echo technique*. This will be discussed in Section 3.3.4.

In Figure 3.3, we can see direct maps of T1 and T2 relaxation constants in a brain together with plots of T1 and T2 relaxation curves in grey and white matter. To obtain the T1 and T2 relaxation constants, we have to fit the exponential curves given by (3.2) and (3.3). Therefore, we have to perform several measurements and detect the MR signal in several points of the exponentials. It is rare to estimate directly the relaxation constants in clinical practice since the acquisition time would be very long. Instead, images with a contrast preferentially given e.g. by the T1, T2 or T2* relaxation rates are acquired just by one measurement. Such images are called *T1, T2* or *T2* weighted*.

3.3 Basic MR sequences

A sequence of tissue excitations by radio-frequency pulses (RF) and modifications of the external magnetic field, leading to an acquisition of a spatially encoded MR signal is called an *MR pulse sequence* (MR sequence, pulse sequence). In this section, we present basic types of pulse sequences. A detailed setup of the sequences can be found e.g. in [10]. The spatial encoding step is explained in Section 3.4.

tissue	T1 (ms) at $B_0 = 1.5$ T	T1 (ms) at $B_0 = 0.5$ T	T2 (ms)
skeletal muscle	870	600	50
liver	490	325	45
fat	260	215	85
white matter (cerebral)	790	540	90
grey matter (cerebral)	920	655	100
cerebrospinal fluid (liquor)	>4000	>4000	>2000

Table 3.3: Relaxation times of selected tissues. While T1 relaxation is longer at higher magnetic fields, the T2 relaxation is independent of B_0.

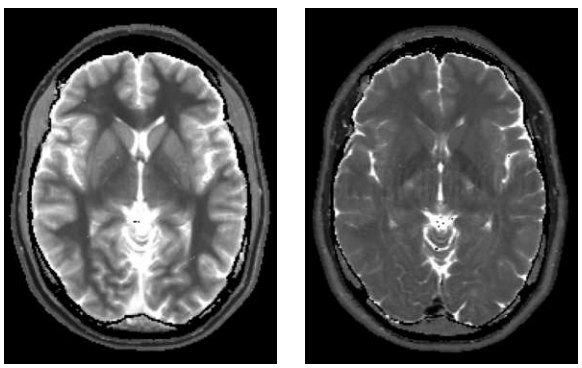

(a) T1 map

(b) T2 map

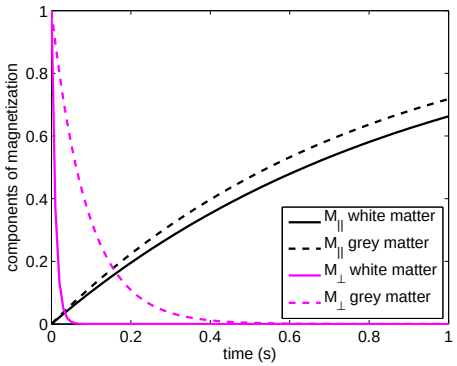

(c) T1 and T2 relaxation curves for white and grey matter in brain

Figure 3.3: Relaxation constants in brain (time constants of T1 and T2 relaxations).

3.3.1 Spin ECHO

Spin ECHO (SE) is the simplest imaging sequence. First, we apply an RF pulse of the Larmor frequency of the energy that exactly cancels the longitudinal magnetization ($M_{\parallel}$ will become zero). At the same, the the RF pulse brings the precessing spins into phase, which creates the non-zero transverse magnetization ($M_{\perp} > 0$). By a geometrical analogy, we say that the RF pulse has tilted the tissue magnetization vector $\mathbf{M}$ by a *flip angle* $\alpha = 90\,^{\circ}$ into the transverse plane. Therefore, such an RF pulse is called the *90° pulse*.

Immediately after the excitation by the 90 ° pulse, an MR signal in the form of a FID appears. We do not sample the signal at this time and it disappears soon due to spin-spin interactions and local magnetic field inhomogeneities (the T2* decay). The signal can re-appear after a period TE (*time echo*) by the following mechanism, illustrated in Figure 3.2: After a period of time TE/2 we apply an RF pulse of 180 ° that flips all the spins. The local magnetic field inhomogeneities will become exactly opposite with respect to the previous spin system and therefore the spins will get back into phase in another time period of TE/2. The 180 ° pulse is therefore called the *refocusing pulse*. At this time point, we register an MR signal – the *echo*. The amplitude of the signal will be lower than the amplitude of the original FID, since the spin-spin interactions (the effect of T2 relaxation) are irreversible and cannot be inverted by the 180 ° refocusing RF pulse. Hence, the peaks of the FID and of the detected echo lie on the T2 relaxation curve.

We can summarize that the SE is a pulse sequence of the 90 ° excitatory RF pulse, the 180 ° refocusing RF pulse and the detected echo: 90 ° – 180 ° – ECHO. The main parameters of the SE sequence are as follows: the *time echo* (TE) – the time period between the excitation by the 90 ° RF pulse and the echo creation, the *repetition time* (TR) – the time period between the two consecutive 90 ° pulses (the repetition time of the whole SE sequence).

By varying the parameters TR and TE of the SE sequence, we can obtain different types of images. The image contrast can be more dependent on the T1 relaxation times (the *T1 weighted images*) or the contrast can be mainly given by the T2 relaxation rates (the *T2 weighted images*). The image contrast in the so-called proton density weighted image (the *PD-weighted*) is given directly by the concentration of ^{1}H nuclei. Hence, three types of intrinsic[8] image contrasts can be easily obtained.

T1 weighted image

When using a short TR, the tissues with a long T1 relaxation will not have enough time to recover their longitudinal magnetization. After applying other 90 ° pulses, the signal from such tissues will become very low. However, the tissues with fast T1 relaxation can

[8] The image contrast is given directly by magnetic properties of the tissues themselves (namely by the T1, T2 relaxation times and concentration of ^{1}H). There is no modification, by means of an external contrast agent.

	short TE	long TE
short TR	**T1w** (TR = 400-600 ms, TE = 10–15 ms)	bad contrast
long TR	**PDw** (TR = 2000-5000 ms, TE = 10–15 ms)	**T2w** (TR = 2000-5000 ms, TE = 80–120ms)

Table 3.4: Typical parameters used in SE sequences in order to obtain T1, T2 or PD-weighted image.

recover almost their whole longitudinal magnetization even during a short time period TR and the signal will be high even after the successive excitations. The short TE at the same time will to some extent eliminate the influence of the T2 relaxation. Therefore the image contrast will be mainly given by differences in the T1 relaxation times and the resulting image is called the *T1 weighted image*. The signal will be high in the tissues with a short T1 relaxation and low in tissues with a long T1 relaxation. See Figure 3.4 with an example of the T1 weighted image on the left side. Note that the cerebrospinal fluid (CSF) is dark since the CSF has a long T1 relaxation (see Table 3.3).

T2 weighted image

The T2 weighted image can be acquired using a long TR and a long TE. Thanks to the long TR, the longitudinal magnetization will be almost fully re-established in all tissues before applying the next excitation 90 ° pulse. Therefore the resulting image will not be influenced by the T1 relaxation. The acquired signal will strongly depend on the T2 relaxation rate thanks to the long TE. The tissues with a fast T2 relaxation will not contribute to the detected signal as much as the tissues with a long T2 relaxation time. See Figure 3.4 (on the right) with an example of the *T2 weighted image*. Note that the cerebrospinal fluid (CSF) is the lightest part of the image, since the CSF has a long T2 relaxation (see Table 3.3).

Proton density (PD) weighted image

The proton density weighted image (*PD weighted image*) can be obtained by using a long TR and a short TE. Thanks to the long TR, the longitudinal component will always be re-established, as in the case of the T2 weighted images. The short TE will eliminate the influence of the T2 relaxation. Therefore, the image contrast will depend rather directly on the magnitude of the magnetization vector which is proportional to the ^{1}H concentration. An example of a PD weighted image is shown in the middle of Figure 3.4.

Parameters of typical SE sequences are summarized in Table 3.4.

3.3.2 Turbo Spin ECHO

The conventional SE sequence consists of the 90 ° RF pulse, 180 ° RF pulse and the signal in the form of echo is sampled afterwards. The time period between the echo and the

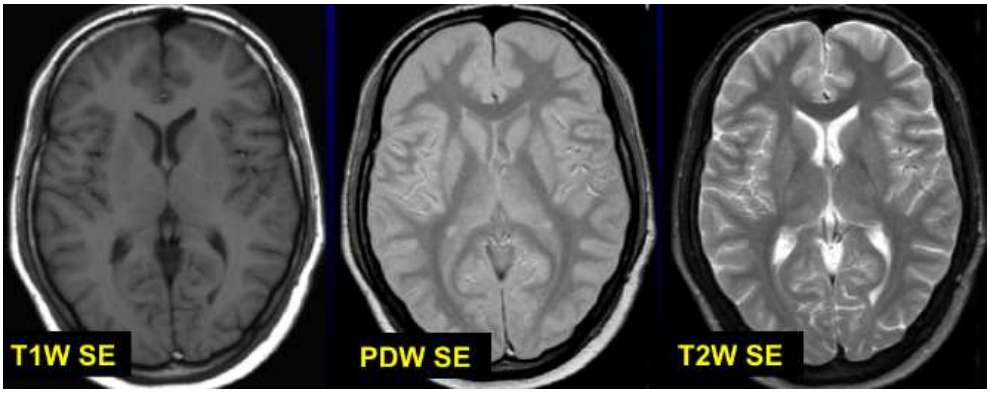

Figure 3.4: Spin ECHO sequence: examples of T1, PD and T2 weighted images.

following 90° excitation RF pulse is unused. Rather than waiting for the period TR to end, we can apply another 180° pulse and the signal of another echo can be sampled, see Figure 3.5. By this mechanism, we can obtain even more echos. Although the signal of the following echos is getting lower (due to the T2 relaxation), the level of the signal may be still acceptable. See Figure 3.5 for the sequence setup.

The number of echos obtained during one TR is called the *turbo factor* (TF) or the *echo train length* (ETL) and the SE sequence modified in such a way is called *Turbo Spin ECHO* (TSE). The turbo factor TF will accelerate the data acquisition TF-times.

3.3.3 Inversion recovery

Inversion recovery (IR) is another modification of the SE sequence. It can serve for a suppression of the MR signal in a particular type of tissue, or for increasing the image contrast in general. In principle, we apply a 180° RF pre-pulse before the excitation 90° pulse. The 180° pre-pulse inverts the tissue magnetization $\mathbf{M}$. Afterwards, $\mathbf{M}$ is returning back to the initial state with a rate depending on the tissue properties and on $\mathbf{B_0}$. If the 90° RF pulse is applied exactly at the moment when the magnetization of a particular tissue is crossing the transverse plain, the tissue signal will be very low. It is caused by the fact that the tissue cannot be excited when there is no longitudinal component of the magnetization. The time period between the 180° pre-pulse and the 90° pulse is called the *inversion time* (TI). By tuning the TI, we can for instance suppress the following tissues[9] :

- fat tissue – TI $\sim$ 170 ms, the so-called STIR (Short Tau Inversion Recovery)

[9]The values of TI are taken for a 1.5T MR system. Inversion times are longer at higher fields because of the longer T1 relaxation.

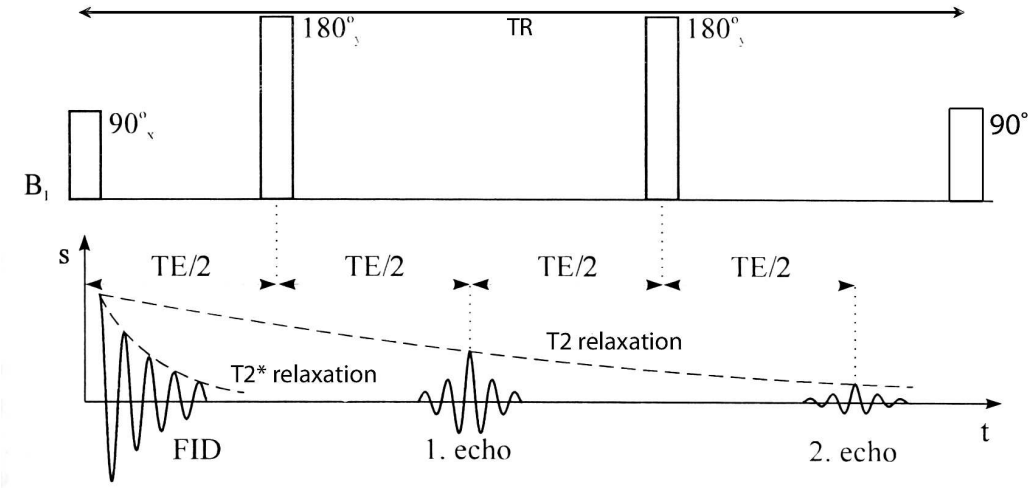

Figure 3.5: Turbo Spin ECHO (TSE) sequence with two generated echos. From [110].

- cerebrospinal fluid – TI $\sim$ 2000–2500 ms, the so-called FLAIR (FLuid Attenuated Inversion Recovery)
- myocardium – TI $\sim$ 200 ms – in combination with an extracellular contrast agent (see Section 3.6); we can obtain the so-called late enhancement images (LE), in which the signal in the myocardium is suppressed and the tissue with an entrapped contrast agent gives a high signal (see Section 3.10.1).

See Figure 3.6 for an example of IR TSE sequences with a different TI time.

3.3.4 Gradient ECHO

In the SE sequence, the 90 ° RF pulse brings the spins into phase, their dephasing is caused by the T2* relaxation and the refocusing is achieved by applying the 180 ° RF pulse. After excitation by the 90 ° RF pulse, we can accelerate the dephasing of the spins by applying an additional controlled magnetic field inhomogeneity – using gradient magnetic fields[10] (the so-called *gradients*). Switching on the gradient for a certain period of time will dephase the spins quickly. Then, by changing the gradient polarity, the spins will get into phase again and the MR signal in the form of an echo can be sampled. If we apply another pair of gradients of opposite polarities, we can recover the 2nd (or other) echos. Unlike the SE sequence, the peak signals in the GE sequence lie on the T2* curve instead of on the T2 curve, since the local field inhomogeneities are not compensated.

[10]Gradient magnetic fields cause linear variation of the external magnetic field $\mathbf{B_0}$, e.g. the gradient in the x-direction (G_x) will change the magnetic field strength to $B_0 + xG_x$.

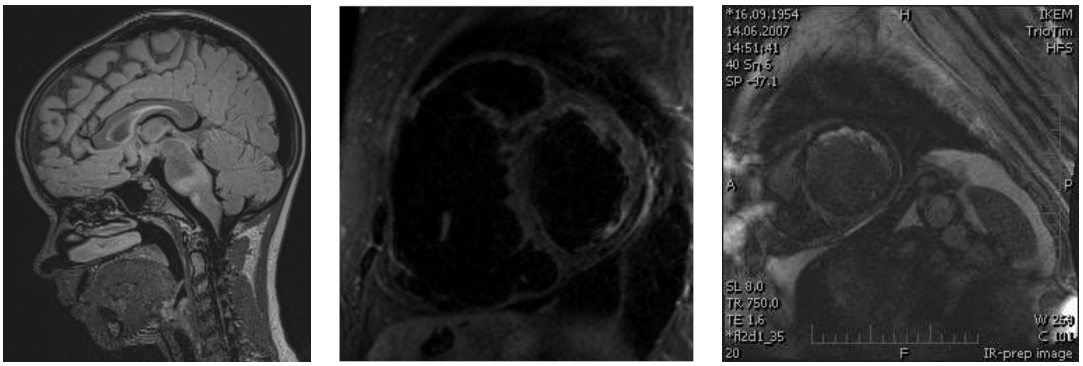

(a) Suppression of the cerebrospinal fluid (FLAIR)

(b) Suppression of the fat tissue (STIR)

(c) Suppression of the myocardium, after administering the contrast agent – late enhancement (LE) in the subendocardial part of the LV anterior and antero-lateral wall

Figure 3.6: Tissue suppression by inversion recovery (IR).

Instead of using the initial excitation 90 ° pulse, we use a lower *flip angle* α in the GE sequence. Thanks to such a settings, the longitudinal relaxation will become faster and we will be able to shorten the repetition time TR. Therefore the acquisition time will be shorter. For a basic setup of the GE sequence, see Figure 3.7.

In general, there are two groups of GE sequences: the coherent (steady state) and the non-coherent (spoiled).

Coherent GE sequences

The transverse component of the magnetization ($\mathbf{M}_\perp$) is kept at the end of each TR. All the phase-encoding[11] gradients are exactly balanced (symmetric). The resulting signal is T2/T1 weighted. There are some particular applications:

- Time of Flight (TOF) used in native MR angiography (see Section 3.10.3). Using a short TR, the static tissue is suppressed and the flowing blood has a high signal (the *GE inflow effect*). The parameters of a typical TOF sequence using the balanced GE sequence (e.g. FISP) are as follows: TR = 20–50 ms, TE set to the minimum value, α = 10–40 °.

- Balanced steady state free precession (bSSFP, trueFISP, FIESTA) – a very fast sequence (TR $\sim$ 1–5 ms). Although the ratio T2/T1 is quite uniform in the tissues, the

[11] The phase and frequency encoding directions are discussed in Section 3.4.

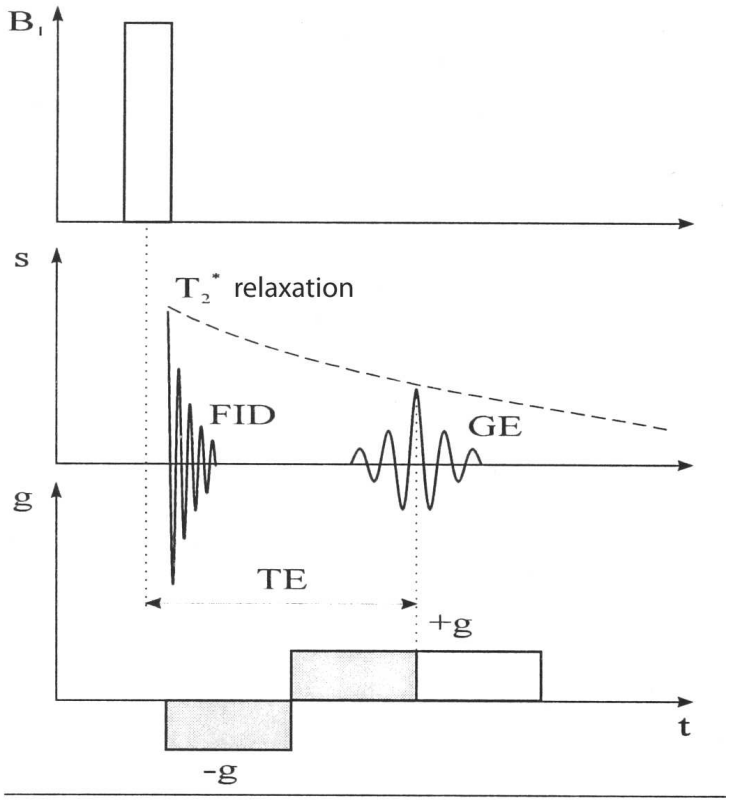

Figure 3.7: Settings of Gradient Echo sequence (GE). From [110].

T2/T1 ratio of blood is quite different from that of the adjacent muscle and vessel wall, leading to particularly valuable image contrast for cardiovascular applications (e.g. in native coronary angiography [44] or in cardiac Cine MRI, in which also the TOF effect plays a role).

Non-coherent GE sequences

The transverse component of the magnetization ($\mathbf{M}_\perp$) is canceled at the end of each TR either by gradient spoiling or by RF spoiling. The sequence does not depend on balancing the gradients, which is why it is not as sensitive to the $\mathbf{B_0}$ inhomogeneities as the balanced sequences. The resulting signal may be lower, especially if a low TR or high flip angle α is used. The sequence was published under the name FLASH = Fast Low Angle SHot (see [39], [40], [49]).

There are several typical applications of the non-coherent GE sequences in cardiac imaging (see Section 3.10.1 for a more detailed description):

- Cardiac Cine MRI – compared to the balance sequence (bSSFP), the GE sequence provides a lower signal and the acquisition time is longer; it is sensitive to flowing blood in the cavities (the signal drop may occur due to a loss of phase coherence, especially in turbulent flows) but without artifacts caused by the $\mathbf{B_0}$ inhomogeneities.
- Magnetization-prepared GE
  - Snapshot FLASH (see [47]) – a fast variant of FLASH with a low TR. The low tissue contrast (due to the short TR) is increased by applying a 90 ° or 180 ° IR pre-pulse (see Section 3.3.3). A single shot[12] sequence is used e.g. for cardiac perfusion (first pass of the contrast agent). FLASH with an IR pre-pulse not in the single shot version can be used in order to obtain high quality[13] late enhancement images of the myocardium (the images acquired approximately 10 minutes after administering a contrast agent).
  - SPAMM (SPatial modulation of the Magnetization, see [117], [5], [4]) – used for the tagged MR images (in Cardiac MRI).

3.4 Concept of k-space

In this section we will describe the reconstruction of a 2-dimensional image in magnetic resonance imaging (MRI). As in the previous part, only ^{1}H nuclei will be considered.

[12] The whole k-space is filled during one period TR.

[13] The balanced sequence is often used in this application – because of the acquisition speed-up. However, the spatial resolution is worse when using the bSSFP sequence and usage of such images is often limited only to detect an ischemic damage of the myocardium. The image quality is usually not sufficient to detect the late enhancement e.g. in some cardiomyopathies.

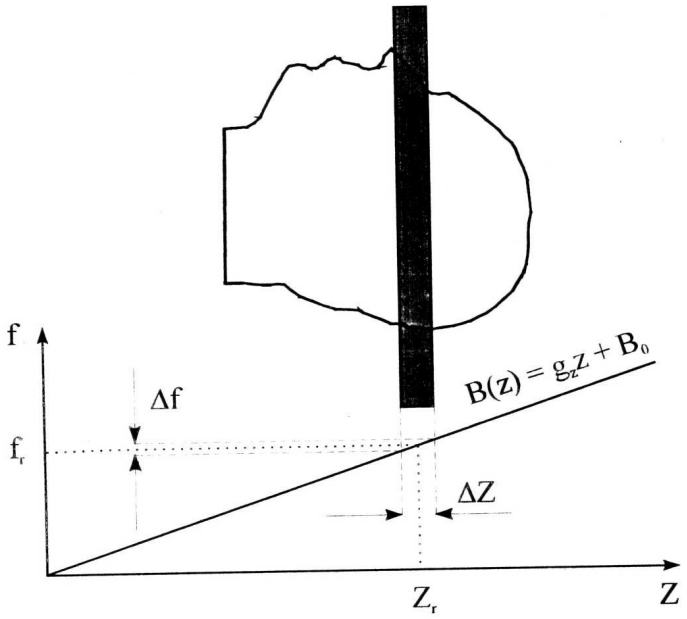

Figure 3.8: Slice selection using the additional slice selection gradient of the magnetic field G_z during the excitation by the 90 ° RF pulse. From [110].

3.4.1 Slice selection

As discussed in Section 3.2.2, the spin system is excited by applying an RF pulse of the Larmor frequency, which is given by the product of the gyromagnetic ratio of the nuclei and of the external magnetic field intensity, $\omega_L = \gamma B_0$. If we used only the static homogenous magnetic field $\mathbf{B_0}$, the RF pulse would excite all the ^{1}H nuclei inside the magnet. By varying the magnetic field $\mathbf{B_0}$ linearly along the direction perpendicular to the imaging slice (direction z) by the gradient G_z, the Larmor frequency ω_L will become slice-specific. The imaging slice will be given by the bandwidth of the RF pulse and the actual values of the magnetic field intensity:

$$\omega_L = \gamma(B_0 + zG_z). \tag{3.5}$$

As we can see in equation (3.5), a thin slice can be acquired either by using a very narrow bandwidth of the excitation pulse RF, or by using a very high value of the *slice selection gradient* G_z, see Figure 3.8. Adding the linear gradient magnetic fields in the NMR system was Paul Lauterbour and Peter Mansfield's idea for the spatial encoding of the MR signal which actually moved NMR from spectroscopy to imaging in the early 1970s.

3.4.2 Reconstruction of the 2D image

Assume that one particular slice was selected by using the slice selection gradient G_z during an application of the excitation RF pulse. The spins in this particular slice have got into phase. Each point of the slice is characterized by the MR signal S with an amplitude S_0, which is given by the magnitude of the transverse magnetization of the excited system ($M_\perp$). If we neglect the T2 relaxation, S_0 will be constant at each point during the data acquisition. Using the MR system, we need to estimate the values of S_0 at each point. These values will correspond to the intensity of the picture elements (pixels) in the final reconstructed image.

The MR system is able to measure the total signal in a selected volume Ω:

$$S_{total} = \int_\Omega S(x,y)d\Omega. \tag{3.6}$$

For a given amplitude S_0 the rotation of the spins with respect to a reference spin system, which is rotating with a frequency ω_{ref}, can be described by the following equation from classical mechanics:

$$S = S_0 e^{i(\omega-\omega_{ref})t}, \tag{3.7}$$

where t stands for the time variable and i is the imaginary unit. As a reference spin system, we consider the system where only the basic external magnetic field $\mathbf{B_0}$ is used, $\omega_{ref} = \omega_L = \gamma B_0$.

The angle velocity of the rotation can be changed by applying gradient magnetic fields – the *gradients* G_x or G_y – in the following manner:

$$\omega = \omega_{ref} + \gamma(xG_x + yG_y). \tag{3.8}$$

Let us assume that we switch on the gradient magnetic fields G_x and G_y for a period τ_x, respectively τ_y. The spin system will be rotating with the angle velocity given by (3.8). When the gradients are switched off, the spins will be rotating with the angle velocity ω_{ref} again but their phase will have changed. By substituting the angular velocity (3.8) to (3.7) and (3.7) to (3.6), we obtain the following signal with respect to the reference spin system:

$$S_{total} = \int_\Omega S_0(x,y)e^{i(\omega-\omega_{ref})t}d\Omega = \int_\Omega S_0(x,y)e^{i\gamma(xG_x\tau_x+yG_y\tau_y)}d\Omega. \tag{3.9}$$

The total signal (3.9) can be related to the Fourier transform of the image (the so-called *k-space*)

$$\hat{S}(k_x,k_y) = \int_\Omega S(\tilde{x},\tilde{y})e^{ik_x\tilde{x}}e^{ik_y\tilde{y}}d\tilde{x}d\tilde{y}, \tag{3.10}$$

k_x, k_y being variables in the k-space.

Hence, when choosing properly the parameters of the sequence, the measured signal will be exactly the Fourier transform of the image, and the image can be reconstructed just by applying the inverse Fourier transform on the acquired raw data.

Phase encoding

We can choose the appropriate values of k_x and k_y in the exponents of equation (3.10) by applying the gradients G_x and G_y for precisely defined combinations of periods τ_{x_m} and τ_{y_n}

$$\begin{aligned} k_x &= \gamma G_x \tau_{x_m}, \\ k_y &= \gamma G_y \tau_{y_n}, \end{aligned} \tag{3.11}$$

where $m,\ n = 0, \dots N-1$ represent the discrete k-space. The combinations of gradients are applied before the signal sampling and there will be one value of the discrete k-space related to each gradient combination. It means, that N^2 independent repetitions of the sequence must be performed to fill the whole discrete k-space of the size $N \times N$. In fact, this would be a very time demanding acquisition and such an approach is not used in MR imaging.

Phase and frequency encoding sequences

In this approach, we first apply the phase encoding gradient G_x using the appropriate value of τ_{x_m} as in (3.11). The data related to this particular phase encoding gradient will fill the line m of the k-space. Then, we switch on the gradient G_y and keep it on during the whole period of signal sampling. At the moment of acquisition of the n-th value in the line of the k-space corresponding to the gradient G_x, the gradient G_y has been switched on for the time period $n\xi$. The measured signal can be described by the following equation:

$$\hat{S}(kx, ky) = \int_\Omega S_0(\tilde{x}, \tilde{y}) e^{ik_x \tilde{x}} e^{ik_y \tilde{y}} d\tilde{x} d\tilde{y} = \int_\Omega S_0(\tilde{x}, \tilde{y}) e^{i\gamma G_x \tau_{x_m} \tilde{x}} e^{i\gamma G_y (n\xi) \tilde{y}} d\tilde{x} d\tilde{y}, \tag{3.12}$$

where $n = 0 \dots N-1$, $n\xi = \tau_{y_n}$ corresponds to n-th step in y-direction. Since the whole line of the k-space is acquired during one sequence repetition, we will have to repeat the sequence only N times in order to fill the k-space. Figure 3.9 shows a typical setup of a MR imaging sequence, with the *slice encoding gradient* G_s, the *phase encoding gradient* G_Φ and the *frequency encoding gradient* G_f, also called the *readout gradient*. Actually, such an approach is used in all MRI acquisitions.

By oversampling the acquired data in the frequency encoding direction, we do not nearly extend the acquisition time. However, each step in the phase encoding direction requires one complete repetition time of the MR sequence (TR). For this reason, we very often tend to undersample the data acquisition in the phase encoding direction. This can cause the so-called *wrap around artifact* discussed in Section 3.9.3, where also some remedies are suggested.

3.4.3 3D acquisition

The 2D MR image is acquired using the phase and the frequency encoding of the spatial information, as described above. By measuring several parallel 2D planes we can recon-

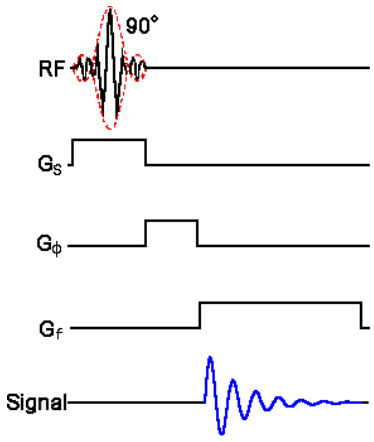

Figure 3.9: A spatial encoding in a single slice selected by the slice selection gradient G_S, which is applied together with the RF pulse. A line in the k-space is selected by the phase encoding gradient G_Φ. The frequency encoding (readout) gradient G_f is applied during the whole period of signal sampling, and the corresponding line in the k-space is filled.

struct the 3D object but it is still not a true 3D image. Acquiring a stack of parallel 2D images is called a *multiple 2D sequence* (M2D).

The idea of 3D encoding is quite simple: we keep the phase and frequency encoding gradients for directions x and y and we use an additional phase encoding gradient in the slice selection direction (z). Compared to the M2D approach, we can get much better spatial resolution in the z-direction and a higher signal-to-noise ratio (SNR). The major drawbacks of 3D sequences are long acquisition time and additional artifacts coming from the phase encoding (wrap around artifacts in both phase encoding directions, see Section 3.9.3).

3.5 Fat suppression

There are several possibilities to suppress fat tissues. We list the most usual ones and give a few comments. An example from cardiac imaging is shown in Figure 3.10.

- inversion recovery pre-pulse (STIR), discussed in Section 3.3.3.
- spectroscopic saturation of fat (FatSat, ChemSat, CHESS, see below)
- combination of IR and spectroscopic saturation (SPAIR)

The resonance (Larmor) frequency is given by the gyromagnetic ratio of nuclei but it is influenced also by the molecular structure. Therefore the resonance frequency of ^{1}H

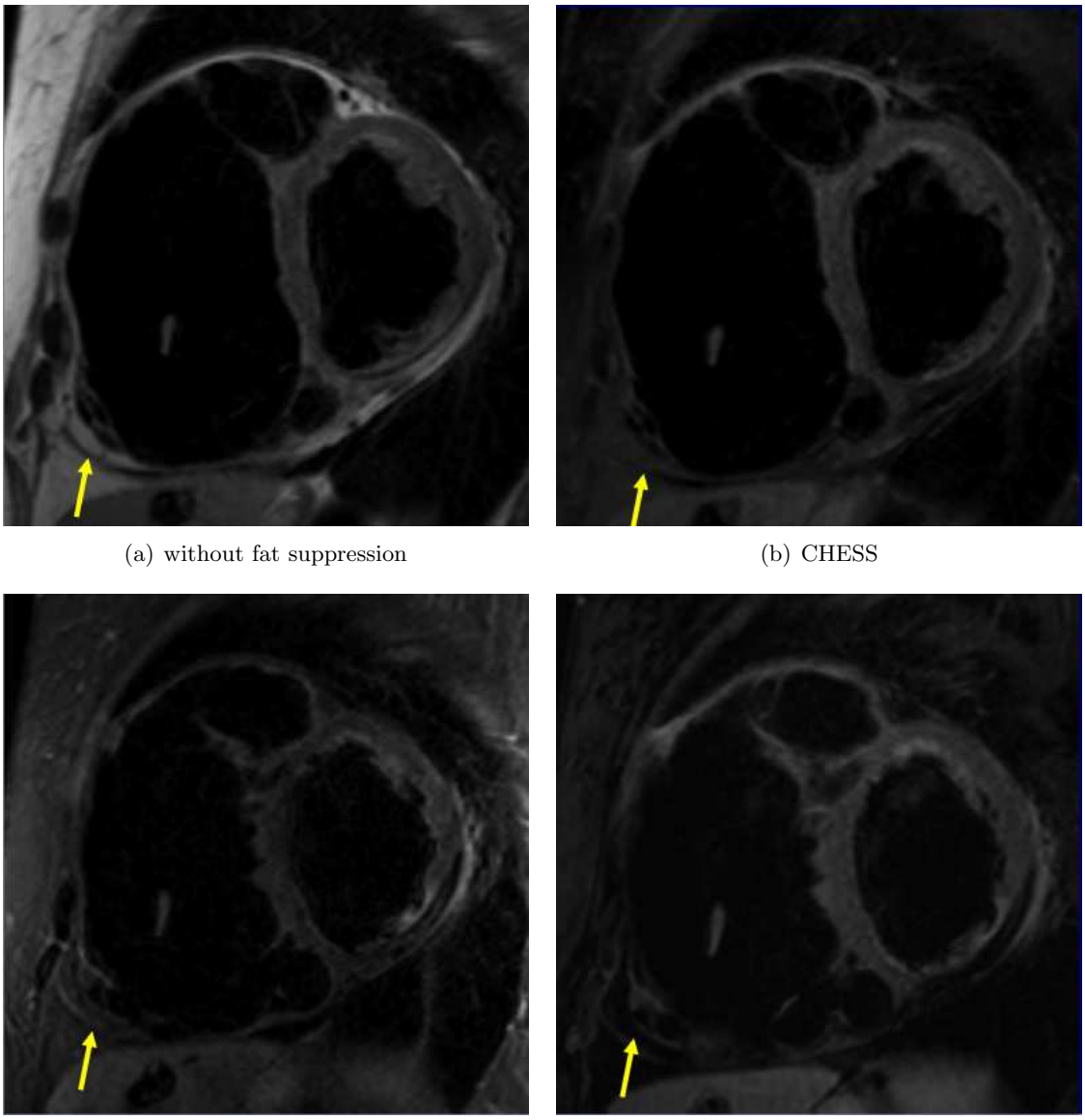

(a) without fat suppression

(b) CHESS

(c) STIR

(d) SPAIR

Figure 3.10: Fat suppression techniques, fat tissue in RV in patient with arrhythmogenic right ventricle dysplasia (ARVD).

in free water slightly differs from the resonance frequency of ^{1}H bound in lipids. This difference can be used for a selective suppression of the lipid tissue by means of a tissue specific spectroscopic saturation RF pre-pulse (sequence usually called FatSat, ChemSat or CHESS, see [51] and [48]). For an effective saturation, we need to have well distinguishable peaks of the free water and of the lipids in the MR spectroscopic image – therefore we need a strong $\mathbf{B_0}$. Then, the quality of the fat suppression will depend on the $\mathbf{B_0}$ homogeneity, which is a difficult issue for high magnetic fields.

The STIR technique is very robust and independent of $\mathbf{B_0}$ inhomogeneities. However, the IR pre-pulse extends the measurement and influences all the tissues, not only the fat.

The SPAIR technique uses a lipid specific (spectroscopic) IR pre-pulse. Compared with STIR, the SPAIR sequence is sensitive to the $\mathbf{B_0}$ inhomogeneities but the IR pre-pulse does not have an influence outside the fat tissues.

3.6 Image contrast and contrast agents

In the previous sections we gave some examples of tissue contrasts that create the MR image (e.g. the T1 or T2 tissue relaxation rates or density of ^{1}H nuclei). Some other examples can be for instance local magnetic field inhomogeneities caused e.g. by the degradation products of hemoglobin after an hemorrhage (the so-called tissue susceptibility effect) or the contrast given by flow or diffusivity of the spins (see Sections 3.10.3 and 3.11). Besides those intrinsic tissue contrasts, we can use some external agents that are able to modify the tissue magnetic properties in a way that they influence the rates of relaxation processes. Unlike the contrast agents used in X-ray imaging (or computerized tomography), we do not detect the contrast agent itself in MRI. It is the modification of the relaxation processes in the tissues that can enhance the signal in particular locations. In the following paragraphs, we are going to describe some contrast agents routinely used in clinical exams. Figure 3.11 shows several intrinsic MR image contrasts and one image acquired after the administration of an external contrast agent.

3.6.1 Paramagnetic contrast agents

Paramagnetic agents have no magnetic properties if they are outside the magnetic field. However, in the magnetic field $\mathbf{B_0}$ they partially arrange along the field and generate a magnetization. They mainly[14] shorten the T1 relaxation time and to some extent also the T2 relaxation time. Therefore, the paramagnetic contrast agents are especially efficient in the T1 weighted sequences. Typical examples of the paramagnetic agents are cations of metals, as for example Cr^{3+}, Mn^{3+}, Fe^{3+}, Ni^{3+}, Cu^{3+}, Gd^{3+}. All of them are toxic and potentially dangerous, therefore they have to be incorporated in a stable chelate complex,

[14] The level of shortening of the T1 and T2 relaxation times depends e.g. on the actual concentration of the contrast agent in the tissue.

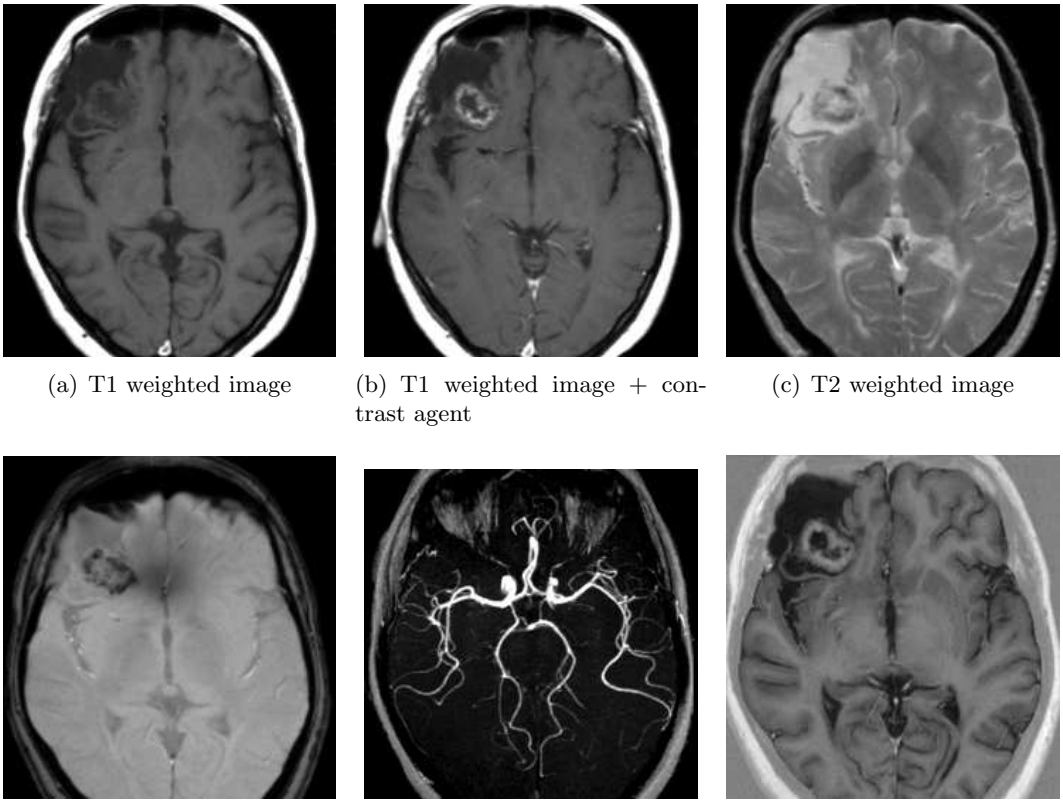

(a) T1 weighted image

(b) T1 weighted image + contrast agent

(c) T2 weighted image

(d) Magnetic field inhomogeneities

(e) Flow of the spins

(f) Inversion recovery T1

Figure 3.11: Examples of image contrasts in MRI. Only in the mid upper image, the external contrast agent (extracellular, Gd chelate) was administered.

e.g. EDTA-Gd. Nevertheless, in some patients with a kidney disease the so-called nephrogenic systemic fibrosis (NFS), possibly caused by a Gd intoxication, has been developed (see [45]). Paramagnetic contrast agents can be divided in 3 subgroups:

1. Without a bound on plasma proteins – the most usual, truly extracellular contrast agents. After first passage through the capillary bed, their blood concentration will be very low since they remain in the extracellular fluid. Typical examples are Magnevist (*gadopentetate*) or Gadovist (*gadobutrol*).

2. With a weak bound on plasma proteins (MultiHance – *gadobenate*). The weak bound with albumin slightly extends the effect of the contrast agent. The application is almost the same as for the group 1.

3. With a strong bound on plasma proteins – the so-called intravascular contrast agents (*vasovist*). Thanks to the strong bound on plasma proteins, they remain in blood and the signal in vessels can be detected for a long time (up to tens of minutes). They are used for some angiographic studies. One of their drawback is that after the first passage, they will be present in the arteries as well as in the veins, which can cause difficulties in distinguishing between the two types of vessels (see Figure 3.31(d)).

3.6.2 Superparamagnetic contrast agents

Superparamagnetic agents have a very high magnetic susceptibility and therefore they mainly shorten the T2 relaxation time (or more specifically, the $T2^*$ relaxation time). Typical examples are Fe^{3+} ions (*resovist*). They are used in imaging with a desired high T2 contrast (e.g. in some angiographic sequences, imaging of kidneys, liver or gastrointestinal tract).

3.7 Acceleration techniques

In Cardiac MRI, acquisition time is very limited due to heart and breathing motions. Therefore, we need to accelerate data acquisition. We have already given an example of acceleration by means of using sequences based on the gradient echo with low flip angle α and very short repetition time TR often used in turbo versions (FLASH, Snapshot FLASH, bSSFP, see Section 3.3.4). Here, we list some other possibilities.

- Non-cartesian trajectories in the k-space (either spiral or radial), in which the gradient system may work more efficiently and the k-space filling can be faster. Standard reconstruction algorithms first perform a step of re-gridding (filling of a usual rectangular k-space using an interpolation from the measured data) and the inverse Fourier transform is performed afterwards. Thanks to non-cartesian trajectories, we can use smaller field of view (FOV) while keeping the same voxel size (therefore we can use a

smaller acquisition matrix and obtain a better temporal resolution in dynamic time sequences). Unfortunately, associated artifacts are sometimes unpredictable.

- Ultra-fast acquisition sequences, as for exampe Echo Planar Imaging (EPI, see [75]). EPI is an example of the so-called single shot sequences, which can fill the whole k-space in a single TR period.

- Parallel techniques: Undersampling of the k-space leads to a typical wrap around artifact (see Section 3.9.3). However, by using a combination of several receiving coils with known sensitivities, we can reconstruct the missing lines of the k-space. The reconstruction can take place in the image space (SENsitivity Encoding = SENSE) or in the k-space (GRAPPA). The shortening of acquisition time is referred to as the *acceleration factor*.[15]

- kt-blast: Uses undersampling both in the spatial and in the temporal domain.

3.8 Hardware

In this section we give some remarks about MRI hardware, in particular with respect to the requirements of Cardiac MRI in order to obtain an adequate level of MR signal.

Static magnetic field $\mathbf{B_0}$

As explained in Section 3.2.1, we can obtain a higher MR signal for higher magnetic fields (see Table 3.2). Nowadays, MR systems can be subdivided into 3 groups according to the strength of the external magnetic field: low-field systems (< 0.5 T), high-field systems (1.5–3.0 T) and systems using ultra high-field (>3.0 T).

Low-field systems are not meant for cardiac imaging since the resulting spatial and temporal resolution with a reasonable signal-to-noise ratio (SNR) would be rather low. Ultra high-field systems are used mainly in MR spectroscopy (MRS) in order to obtain more distinct peaks in MR spectra, and in functional MRI (fMRI[16]) to obtain a higher BOLD signal. Some of the difficulties in heart imaging at very high fields would be related to the homogeneity of $\mathbf{B_0}$. Interfaces between different tissues in the thorax make the shimming[17] process less efficient. The very high-field systems would also make the ECG triggering difficult. First, the ECG measurement is always deteriorated by any strong

[15] For example SENSE factor 2 stands for: parallel techniques are on and the reconstruction takes place in the image space with the acquisition time reduction by a factor 2. SENSE factor 1 means that the acquisition is performed without any parallel techniques.

[16] A mapping of activated brain centers using the so-called Blood-Oxygen-Level Dependence effect (BOLD), see [86], [9].

[17] The system of additional shim coils is used to improve the homogeneity of $\mathbf{B_0}$. It is a part of each MR system. To guarantee a good $\mathbf{B_0}$ homogeneity at very high fields, we often need to perform a non-automatic (manual) shimming procedure, which is difficult and time demanding.

magnetic field (it is sometimes difficult to obtain an ECG signal suitable for the triggering at 3 T, and sometimes even in 1.5 T systems). Secondly, an electrical activity in the heart tissue is influenced by the strong magnetic field by means of the so-called magneto-hydrodynamic effect (MHD, see [62], [43]) that would have to be taken into account.

Finally, we list some properties of 3 T MR systems in comparison with 1.5 T systems:

- Longer T1 relaxation: It may be an advantage e.g. in cardiac MR tagged images (see Section 3.10.1), where the grid fading depends on the T1 relaxation rate. However, the slow T1 relaxation can be a disadvantage in some other applications (for example, we need to increase the repetition time TR in order to obtain a T2 weighted image).
- Stronger susceptibility artifacts (described in Section 3.9.1) due to a bad $\mathbf{B_0}$ homogeneity: Although higher susceptibility effects may be positive in diagnosis of some pathologies (e.g. an old hemorrhage), it is usually not the case for Cardiac MRI.
- The RF energy increases due to a higher Larmor frequency of the RF pulses. We can easily reach the level of maximum specific absorption rate for human (SAR). In such a case we have to re-adjust the parameters of the sequence, which often leads to a lower quality of the resulting image.
- Higher noise of the gradient system at 3 T fields.
- Higher price of 3 T systems.

Nowadays, 1.5 T MR systems seem to be optimal for most clinical applications in the field of Cardiac MRI. With 3 T systems, we could benefit from the higher signal in the diagnosis of some pathologies of the myocardial wall (possibly for some cardiomyopathies, e.g. ARVD, see Section 2.4.3), or we could obtain tagged MR images covering the whole cardiac cycle thanks to a longer T1 relaxation time. However in most cases, we would be fighting with stronger image artifacts and finally, we would not gain much from the higher signal.

Gradient coils

In order to use fast MR sequences, we need a powerful system of gradient coils that will be able to create a strong gradient of the magnetic field and will be able to switch on / off the gradient coils quickly. The gradient system is given by the following main parameters:

- Maximum amplitude – which gives the spatial resolution of the images. The usual values are 20–35mT/m and the best systems are equipped with gradients with a maximum amplitude of ∼45mT/m.
- Slew rate – which gives the measurement time by means of the shortest possible TR and TE. The usual values are 80–120mT/m/ms, the best systems have ∼ 200mT/m/ms.

- Duty cycle – continuous switching on of the gradient system (nowadays usually 100% for any MR system).

Transmitting coil

The transmitting coil in Cardiac MRI is usually represented by the basic body coil.

Receiving coil

Dedicated receiving coils are used for Cardiac MRI. The closer they fit the geometry (the thorax, in this case) the less noise they detect. Receiving coils usually consist of more elements used for parallel imaging (6–32), see Section 3.7.

3.9 Image artifacts

In the following section, we will focus on some typical artifacts in MR imaging. Thanks to a technical progress in MR systems on the one hand, many artifacts have almost disappeared – especially when considering 'classical sequences' that have been used for decades. On the other hand, by using faster sequences, higher magnetic fields, stronger and faster gradients we are obtaining new imaging possibilities but some 'old' artifacts may re-appear or some new ones can arise (see e.g. [66]). This section mainly aims at introducing some typical artifacts that may appear especially in Cardiac MRI, so that we would be aware of them and possibly, we would be able to avoid some of them.

3.9.1 Artifacts coming from the MR system

Many artifacts are due to an imperfection of various parts of the MR system. Usually, the user of the MR system does not have any possibility to correct them. The most common artifacts come from:

- RF instabilities – bad adjustment of RF pulses. In some multiple 2D acquisitions (M2D), the level of signal may vary in between the slices (e.g. in some cardiac Cine MR sequences).
- Gradient system
  - Nonlinear gradient can cause geometrical distortion, especially if a large Field Of View (FOV) is used.
  - Eddy currents induced by switching on and off the gradients causing an image distortion, see Figure 3.12(a).
  - Non-symmetry of the gradients (+G vs. -G) typically causes ghost artifacts, see Figure 3.12(b).

(a) Image distortion caused by the eddy currents (switch on / off of the gradients).

(b) $\frac{1}{2}$ ghost artifact caused by gradient non-symmetry.

Figure 3.12: Artifacts caused by the gradient system.

  - Time instability of the gradients.

- $\mathbf{B_0}$ inhomogeneities

  - the higher the static magnetic field, the more difficult it is to make it perfectly homogenous. A system of correction shimming coils is used. A bad shimming causes shorter FID and MR echos and therefore there is a lower level of signal in the resulting image.
  - susceptibility artifacts cause local $\mathbf{B_0}$ inhomogeneities and result in bright areas (misregistered signals) and dark areas (signal voids) nearby the tissue (material) with a high susceptibility. They can be caused e.g. by metal objects (such as orthopedic prosthesis, vascular stents or surgical clips) or intrinsic tissue components especially in sequences sensitive to the $\mathbf{B_0}$ inhomogeneities, see Figure 3.13.

A $\mathbf{B_0}$ inhomogeneity causes the gradients in coherent (balanced) GE sequences not to be perfectly symmetric, which leads to periodic bands of signal void and signal augmentation with a period $\sim$ 1 / TR (see Figure 3.18). A short TR available with current MR systems (as for example in the sequence bSSFP – trueFISP) decreases the periodicity of the artifacts and we are able to move them out of the field of view by adjusting a frequency offset ('delta offset frequency').

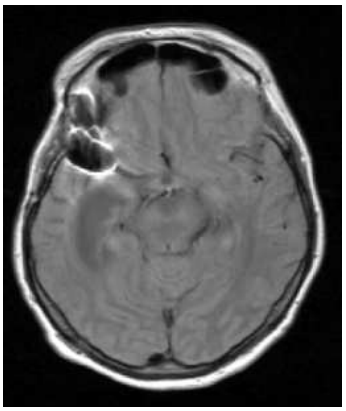

(a) Metal objects in a brain (a vessel clip) causes a signal void in the right temporal lobe. Part of the frontal lobe with missing signal due to an interface between brain tissue and air in the frontal bone sinuses.

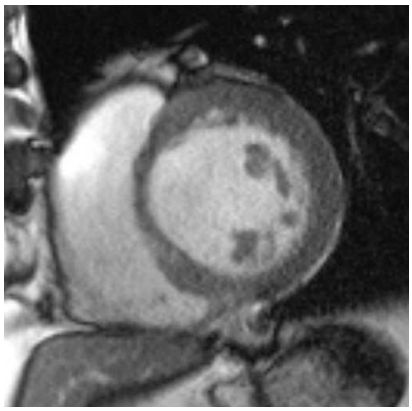

(b) A limited spatial resolution and susceptibility artifacts in bSSFP sequence caused by local field inhomogeneities at myocardium–fat interface make the thin wall of the right ventricle difficult to distinguish.

Figure 3.13: Susceptibility artifacts induced by local field inhomogeneities.

3.9.2 Artifacts caused by the examined subject

Typical artifacts are due to motion (either of the patient or of the imaging organ), due to blood flow, and to the so-called chemical shift.

- The motion causes an image blurring in the direction of phase encoding gradient, see Figure 3.14. It can be corrected by shortening the acquisition (using fast sequences), averaging over several measurements[18] (which leads to a long acquisition time), synchronization of the data acquisition with the organ motion (e.g. by ECG triggering in cardiac MRI), acquisition in a breath-hold period or synchronization with breathing motion (navigator echo technique). These possibilities will be discussed in cardiac imaging in Section 3.10.1.

- The in-plane flow causes an image blurring in the phase encoding direction (same principle as in the case of the motion of the patient). The through plane motion can amplify or suppress the signal of flowing blood – which can be productive in some angiographic sequences or counter-productive e.g. in some gradient echo kinematical images of the heart. Additional saturation pulses next to the imaging plane can solve the problem.

[18] Number of acquisitions is usually denoted by NEX.

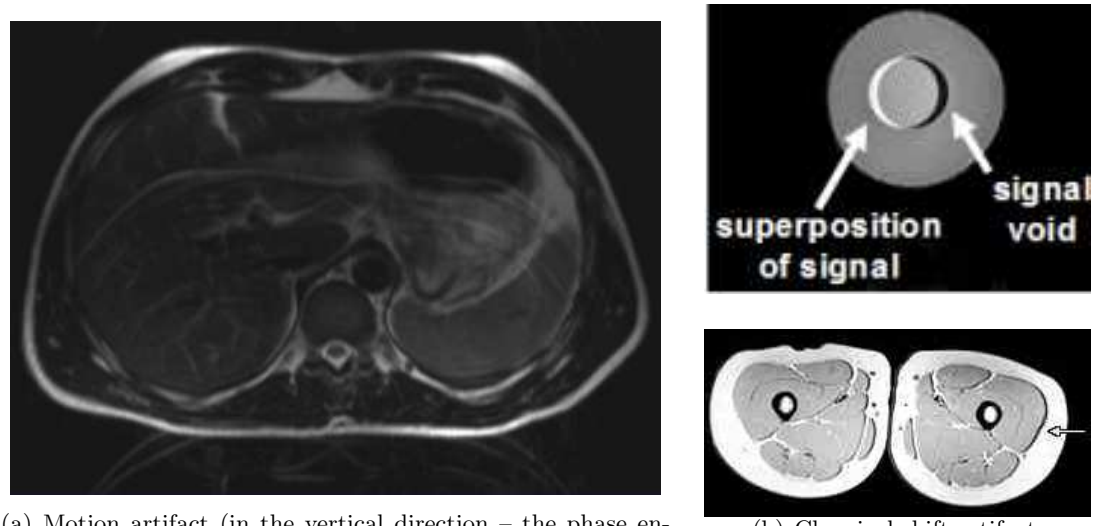

(a) Motion artifact (in the vertical direction – the phase encoding direction).

(b) Chemical shift artifact.

Figure 3.14: Motion and chemical shift artifacts.

- The resonance frequency of ^{1}H in free water and in fat tissue slightly differs due to molecular structures, as was discussed in Section 3.5. The shift of the resonance frequency (*chemical shift*) may interact with the frequency encoding step (see Section 3.4.2). The reconstruction algorithm cannot distinguish if the change of the resonance frequency is caused by the location of the tissue (frequency encoding) or by the chemical shift[19] and the tissue is shifted in the direction of the frequency encoding gradient. The chemical shift artifacts are stronger at higher fields. We can decrease the chemical shift by increasing the RF bandwidth (which on the other hand decreases SNR). See Figure 3.14 for a typical chemical shift artifact.

3.9.3 Intrinsic MR artifacts

We mention two artifacts entirely specific to the MRI spatial encoding process: the partial volume effect and the wrap around artifact.

- Partial volume effect is caused by signal averaging in a voxel that contains different types of tissues. A solution can be to decrease the voxel size, which would on the other hand lead to a lower SNR.

[19] For example, chemical shift between the water and fat at 1.5 T field is: $\Delta f = 3.5$ ppm $= 220$ Hz. If the bandwidth of the RF pulse is 60Hz / pixel, the actual shift is 3 pixels in the frequency encoding direction (ppm = particle per million).

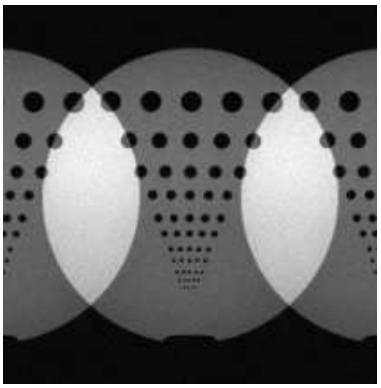

(a) Undersampling in the phase encoding direction

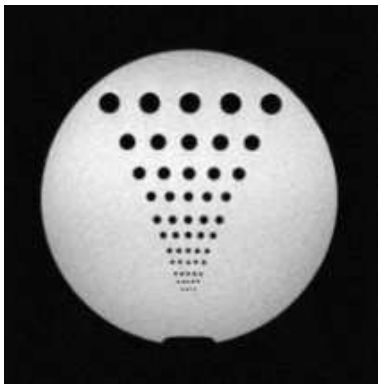

(b) Correct acquisition.

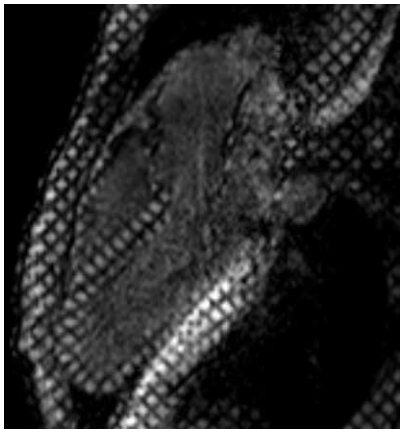

(c) Phase encoding in the vertical direction. Note the thorax is mirrored below the inferior wall of the heart.

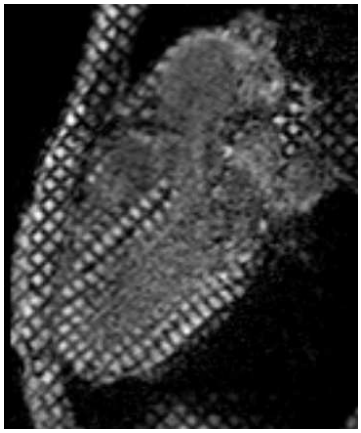

(d) Phase encoding in the horizontal direction without the wrap around artifact.

Figure 3.15: Wrap around artifact due to undersampling of data acquisition in the phase encoding direction.

- Wrap around artifact is caused by undersampling of the k-space. As we saw in Section 3.4.2, a 2D image is encoded using the phase encoding and the frequency encoding (readout) gradient. All the frequency encoding steps corresponding to one phase encoding gradient are acquired during one shot of the MR sequence. By oversampling in the frequency encoding direction, we nearly do not lengthen the measurement. However, each phase encoding step needs a single shot of the MR sequence that lasts one TR period (repetition time). To shorten the image acquisition time, we often decrease the number of phase encoding steps. At the same time, such an undersampling can create typical *wrap around artifacts* as shown in Figure 3.15. We can avoid them by:
  - Increasing the number of phase encoding steps (larger FOV), which however increases the acquisition time an the acquisition time is limited by a breath-hold period in Cardiac MRI.
  - Increasing the voxel size (at least in the phase encoding direction), which leads to a lower spatial resolution and an non-isometric voxel in directions x and y.
  - Using a rectangular acquisition matrix with shorter edge corresponding to the phase encoding direction. The rectangular FOV must correspond to the actual geometry of the scanned organ. The lower number of phase encoding steps reduces SNR but the acquisition time shortening is non-negligible (e.g. the rectangular FOV with a ratio 1:2 reduces the acquisition time by a factor 2).

3.10 Some special sequences used in cardiovascular MRI

3.10.1 Cardiac MRI

Cardiac MRI (CMR) is a highly specialized imaging technique to examine the heart. It can provide high quality images used to assess heart functional indicators or e.g. to diagnose some pathologies of the heart wall. See Figure 3.16 with the basic anatomy of the heart in a typical MR image. Compared to MR imaging of other organs, the following aspects need to be taken into account in Cardiac MRI: the motion of the heart, breathing motion and the blood flow in the heart cavities.

Heart motion

We use fast imaging sequences to deal with heart motion. The images are usually acquired over several heartbeats triggered by the patient's ECG.[20] There exist two main triggering strategies: prospective and retrospective gating.

[20] Some other types of triggering are also possible, e.g. using the peripheral pulse or acoustic signals from the heart. Nevertheless, the ECG is by far the most usual.

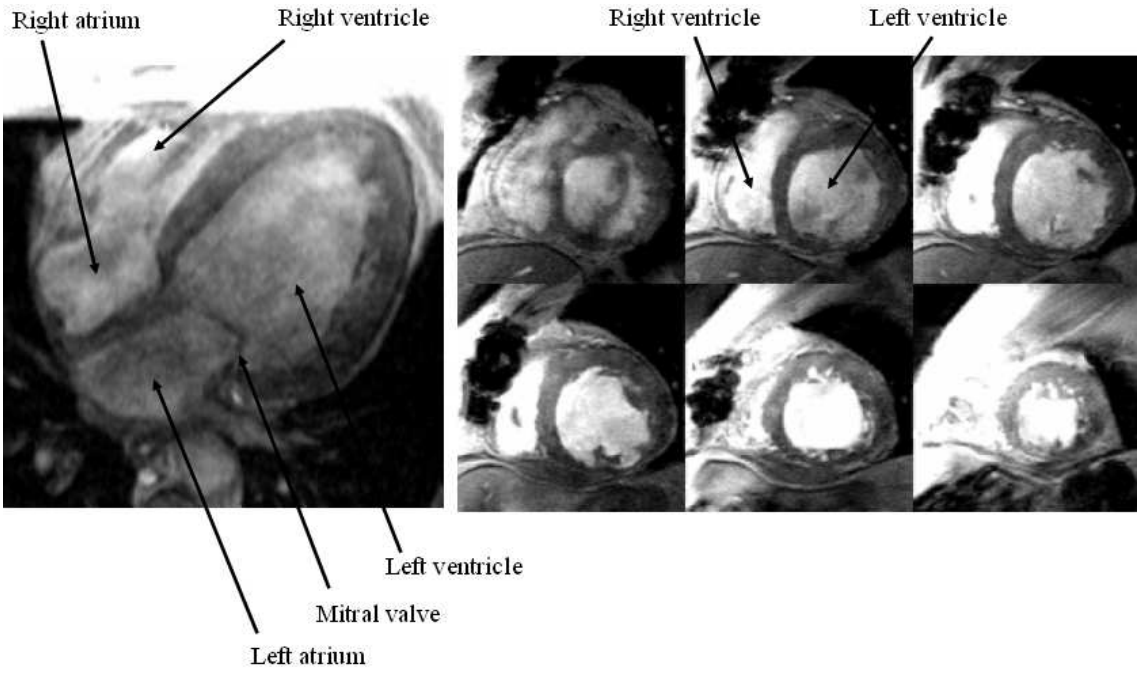

Figure 3.16: Basic heart anatomy in cardiac MRI. A 4-chamber view (on the left side) and short-axis projections (on the right side).

In prospective triggering, the imaging sequence is always launched when the R wave of the QRS complex[21] is detected. Then, the image data are acquired over the cardiac cycle at precisely defined time points. The acquired time frames are perfectly synchronized, assuming that the heart rhythm is regular. A difficulty may arise when the cardiac cycle becomes shorter than the imaging sequence. If such a situation occurs we have to re-launch the acquisition after shortening the sequence (e.g. by reducing the number of acquired time frame images, in case we are performing a dynamic imaging of the heart function).

Retrospective triggering is used only in the acquisition of dynamic sequences of images (Cine MRI, see later). The image data are acquired in a continuous way while the ECG signal is recorded. Both types of data are post-processed and each image data sample is assigned and interpolated to the proper time frame. This approach allows to cover the whole cardiac cycle – including the atrial contraction – however, interpolated images might be to some extent blurred. Thanks to non-intermittent data acquisition, tissue magnetization reaches steady state in the very beginning.

[21] The sequence itself can be delayed by a constant time period TD (*time delay*) which is measured starting from the detected QRS complex. For instance if we aim at obtaining a single diastolic image (e.g. a T1 or T2 weighted image), we need to apply an appropriate TD.

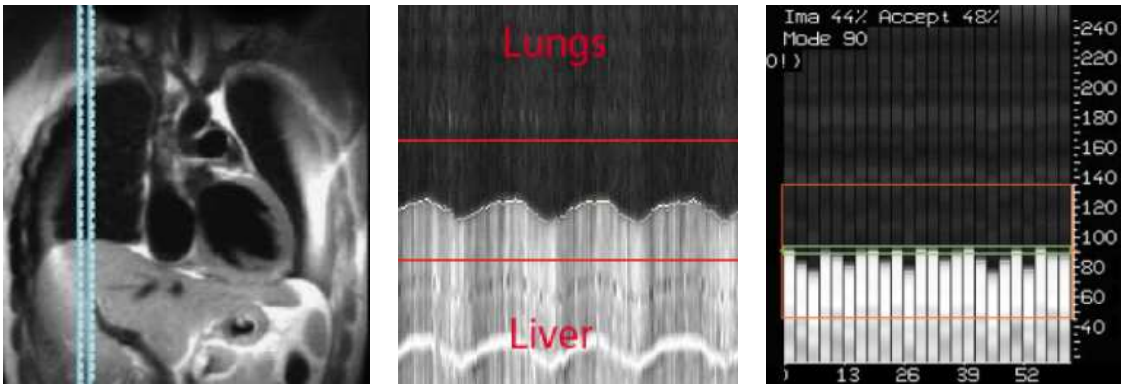

(a) Positioning of the navigator to track the diaphragm

(b) Motion of the diaphragm during free breathing

(c) The green box stands for the acceptable position of the diaphragm

Figure 3.17: Cardiac MRI in free breathing using breath navigator. Cardiac data are acquired if the position of the diaphragm is in the predefined location.

Using strategies that accelerate the image acquisition even further (e.g. a high parallel acquisition factor), we can acquire data in real time instead of over several cardiac cycles as in the previous triggering approaches. However, we will obtain a lower SNR and a worse spatial and temporal resolution. While the resolution of the cardiac gated sequence is[22] $\sim$ 2 x 2 x 8 mm x 30 ms, in real-time imaging we can obtain a resolution of $\sim$ 5 x 5 x 10 mm x 100 ms with a parallel acquisition factor often above 2.

Breathing motion

Breathing motion is dealt with either by acquisition in a breath-hold period (with strongest limitations in dyspneic patients), or by monitoring breath motion e.g. using a respiratory belt (that detects the movement of the thorax and abdomen) or by tracking the diaphragm using the MR navigator echo technique, see [76] and Figure 3.17. During acquisition in free breathing, image data are acquired only in a certain position of the diaphragm. The measurement is highly dependent on co-operation of the examined subject. The acquisition takes longer – especially if the breathing pattern is not regular – and the image obtained can sometimes be of low quality. Free breathing techniques are not suitable for continuous measurements, in particular for heart kinematics. However, using the free-breathing strategy with a well co-operating subject we can obtain truly 3D-morphological images (by means of Section 3.4.3) with a very good spatial resolution (e.g. 2 x 2 x 2 mm).

[22] A usually acquired (non-interpolated) resolution at 1.5 T.

Blood flow

Several strategies are used for blood flow deletion in the heart cavities. In general, the signal in the cavity can be enhanced (the *bright blood technique*) or suppressed (the *dark blood technique*).

Bright blood can be obtained by several procedures, a first instance being a GE sequence with a short TR. Due to the short TR, the signal is suppressed in the imaging slice (magnetic saturation effect). On the other hand, the blood flowing into the imaging slice is not saturated and gives a strong signal (GE inflow effect). If the blood flow is not perpendicular to the imaging slice (e.g. due to some turbulence), this effect does not occur homogeneously and some signal drops may appear in the cavity. A typical example of this sequence is FLASH triggered by the ECG (the so-called *segmented FLASH*[23]). A second MR sequence type used for bright blood imaging is a balanced sequence with a very short TR (TR $\sim$ 1–3 ms, the *balanced steady-state free precession* – bSSFP, trueFISP, FIESTA), see Section 3.3.4. Balanced sequences are flow-independent but extremely sensitive to the homogeneity of the magnetic field $\mathbf{B_0}$. Typical artifacts (signal voids) discussed in Section 3.9.1 arise especially in higher fields (3 T), see Figure 3.18. These artifacts may be avoided by adjusting a frequency offset (the so-called *delta offset frequency*). However, in some subjects the frequency offset needs to be re-adjusted – perhaps even several times – during examination, depending on the position of the imaging slice. It extends the examination and makes the usage of the bSSFP sequence in 3 T systems sometimes difficult.

The suppression of the blood signal in the cavity is achieved in the **dark blood technique** either by *gradient moment rephasing* (GMR, also called gradient moment nulling) or by double-suppression pre-pulse (see Figure 3.19). In principle, we obtain just a static 2D image of the heart either in diastole or in systole with a very good spatial resolution ($\sim$1.5 x 1.5 x 8 mm).

In the following sections we give some details about the Cardiac MRI sequences used in clinical practice. A detailed presentation is given for example in [13].

Cine MRI

Cine MRI refers to an examination of the heart kinematics. The heart is covered by 2D planes (M2D series) and the image data are usually acquired with a temporal resolution of 30–60ms. By a technique of echo sharing[24] the data may be reconstructed with a temporal resolution of about 20–40ms. The acquired spatial resolution is about 2 x 2 x 10 mm[25]. The ventricles can therefore be entirely covered by 10–15 slices, if no gap between the slices is imposed.

[23] Fast Low Angle SHot is a non-coherent GE sequence (see Section 3.3.4). 'Segmented' means that the image acquisition is divided into several cardiac cycles.

[24] The neighbouring time frame images share several lines of the k-space, which leads to some kind of interpolation along the time axis.

[25] Which is often automatically interpolated to a smaller voxel, e.g. 1.5 x 1.5 x 10 mm.

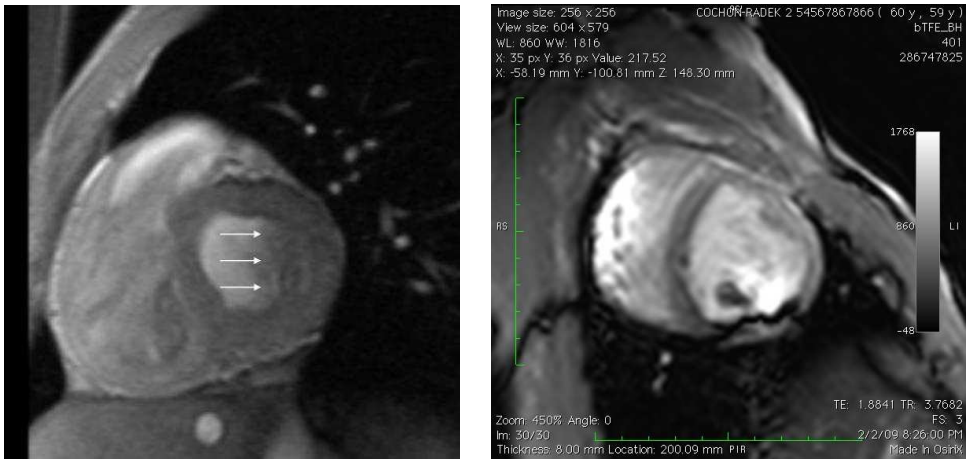

Figure 3.18: Left: Blurred LV lateral wall in the end-systole caused by the motion of the tissue and the blood flow in the segmented FLASH sequence. Right: A signal void in the LV inferior wall caused by the off-resonance frequency in the bSSFP sequence.

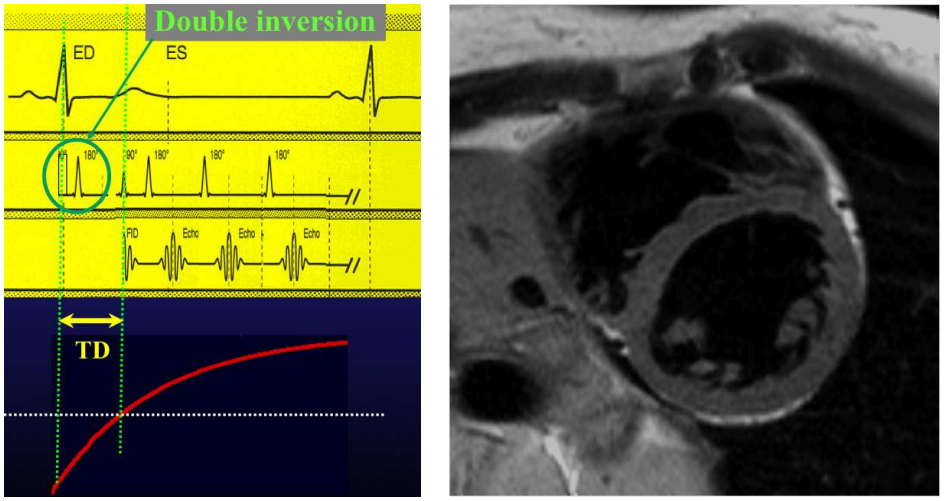

(a) Double inversion pulse

(b) T2 weighted image

Figure 3.19: Dark blood technique – double inversion pulse. If the blood changes in the imaging slice between a couple of 180 ° pulses, there will be a zero signal in the cavity (the dark blood). The static tissue will not be affected.

In Cine MRI we use bright blood techniques and the heart cavities are white whereas the myocardium is dark in the acquired images. The resolution for the myocardial wall is limited, but the cavity volumes can be measured very accurately. Typical sequences used for Cine MRI are balanced steady state free precession (bSSFP, trueFISP) and segmented FLASH.

The acquisition is performed in breath-hold periods. Each slice can be acquired in a single breath-hold, or we can perform the acquisition of multiple slices during one breath-hold. The latter approach is faster but it provides a lower spatial or temporal resolution. Since the breath-hold is not completely reproducible (especially if it is performed in an inspiration), we often have to deal with a spatial realignment of the slices acquired during different breath-holds. Retrospective triggering is preferred in clinical practice.

Tagged Cine MRI

Tagged Cine MRI is an example of magnetization-prepared GE sequences (see Section 3.3.4). An additional saturating pulse is applied before the standard Cine MRI sequence is launched. The pre-pulse saturates a part of the tissue, usually in the form of lines arranged e.g. in a parallel or radial pattern (the so-called SPAMM technique, SPAtial Modulation of Magnetization, [117], [5], [4]). The lines can form a rectangular grid as shown at the bottom of Figures 3.20 and 3.21. Since the saturation lines are imprinted in the tissue, they deform with the heart motion. The processed tagged images could directly provide a motion description in the Lagrangian formulation. However, the processing of tagged images is still very challenging and is not a part of standard cardiac packages available in MR systems.

The saturation pulse is strictly dependent on the triggering pulse and must be applied before each repetition of the MR sequence with exactly the same timing with respect to the cardiac cycle. This is why we have to use prospective triggering and therefore we do not usually observe atrial contraction in the acquired data. In order to avoid strong image artifacts, SPAMM is commonly used in combination with segmented FLASH.

The tissue magnetization becomes gradually less saturated during the cardiac cycle, which makes the tags fade. The desaturation is given by the T1 relaxation. In 1.5 T systems, the tags can usually only be clearly distinguished during the systolic part of the cardiac cycle. Longer T1 relaxation at higher fields provides longer lasting tags. Therefore, 3 T systems are more suitable for tagged Cine MRI data acquisition.

Dark blood technique

The dark blood technique (a suppression of blood in the heart cavity) is used for detailed studies of the heart wall morphology. We acquire T1 or T2 weighted images in short and long axis projections (usually 2D or M2D acquisition). We can combine blood suppression with some other pre-pulses, for instance in order to cancel the signal of fat (see Section 3.5).

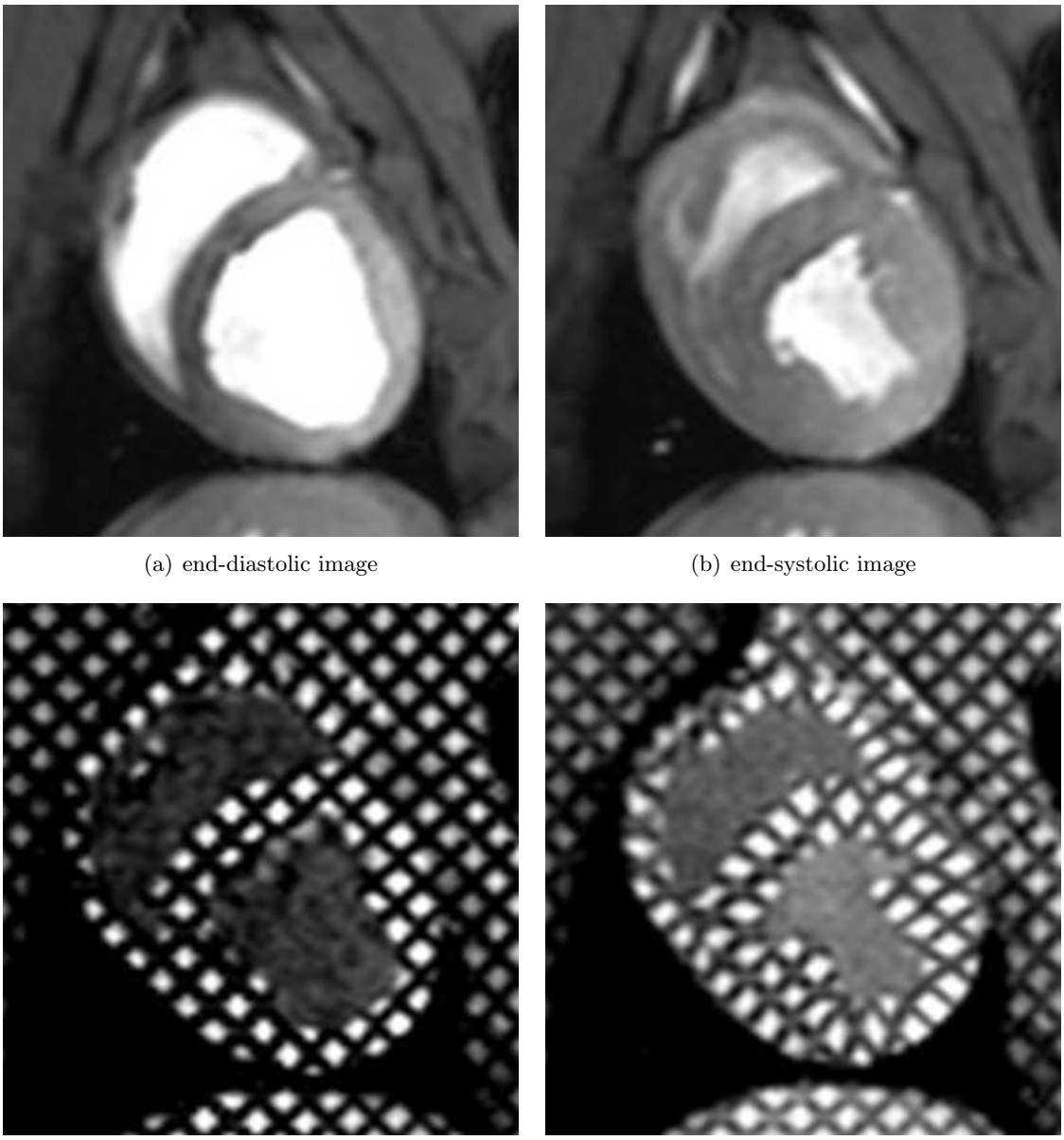

(a) end-diastolic image

(b) end-systolic image

(c) end-diastolic image

(d) end-systolic image

Figure 3.20: Short axis projection of the Cine MRI and tagged Cine MRI of a healthy subject.

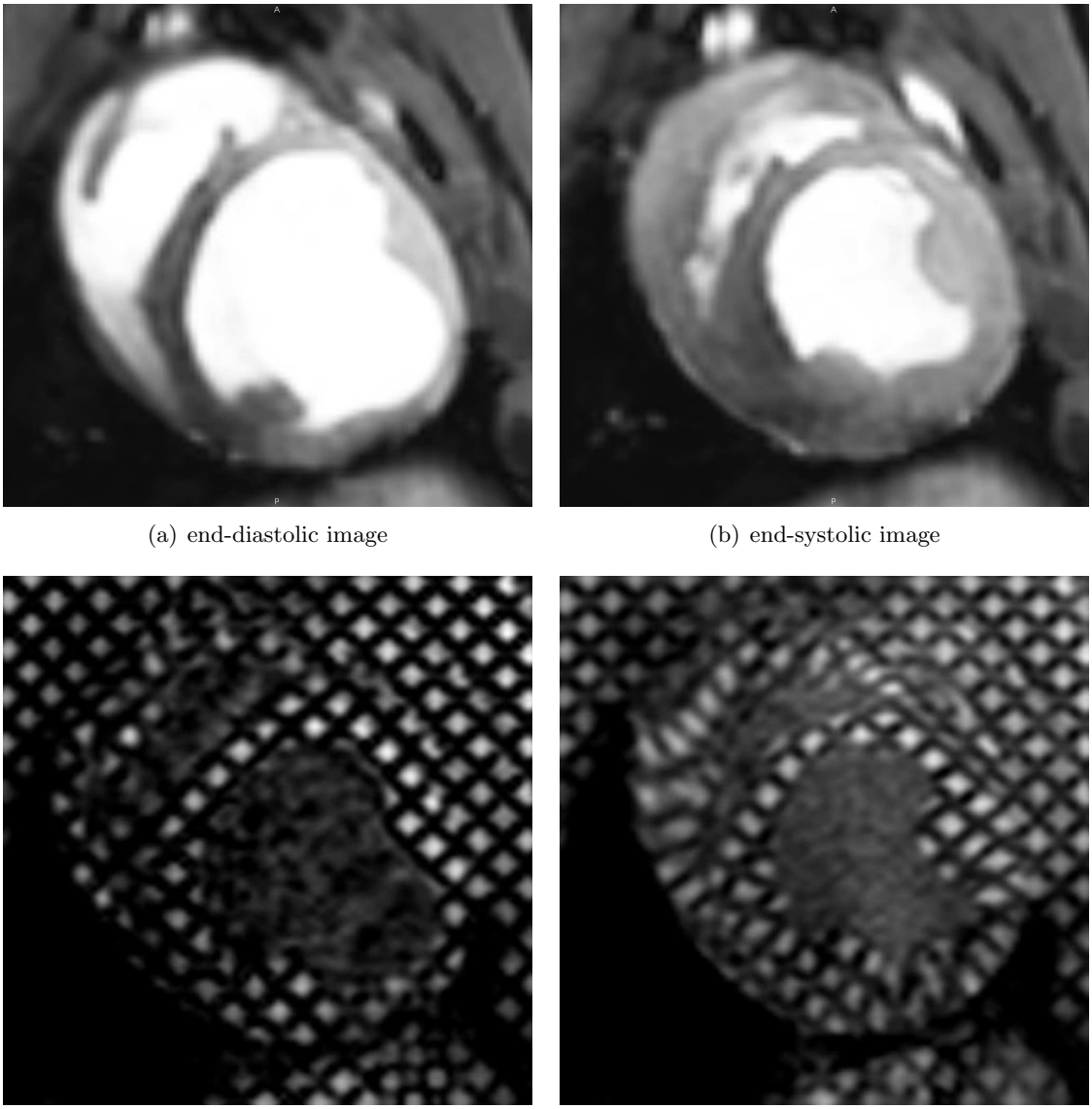

(a) end-diastolic image

(b) end-systolic image

(c) end-diastolic image

(d) end-systolic image

Figure 3.21: Short axis projection of the Cine MRI and tagged Cine MRI of a heart with an acute myocardial infarction in the LV antero-septal segment.

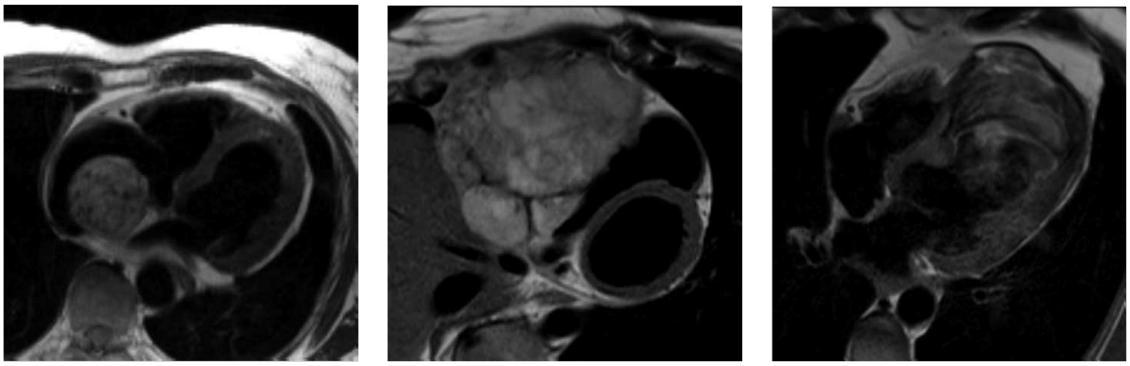

(a) Myxom in right atrium (b) Sarcom in right atrium (c) Thrombus in left ventricle ('pseudotumor')

Figure 3.22: Heart tumors in dark blood technique.

Myocardial tissue suppression by the IR pre-pulse is used in the so-called *late enhancement technique* (LE). T1 images with TI∼220 ms are acquired approximately 10 minutes after administering an extracellular contrast agent. The myocardial signal is suppressed and the regions with the entrapped contrast agent are clearly visible.

Dark blood images can be used to diagnose for instance the following pathologies and symptoms:

- Certain conditions of the pericardium (e.g. pericardial fibrosis, deposits, effusion, etc.).
- Fat deposits in the arrhythmogenic right ventricle dysplasia (ARVD, see Figure 3.10).
- Heart tumors or thrombi (see Figure 3.22).
- Nonviable myocardium (see [111]): the extracellular contrast agent will enter the hypoperfused part of the myocardium with a certain delay, which can be used to assess the perfusion defects during the first pass of the contrast agent. Then, the contrast agent will remain in the non-viable myocardium for a long time due to an altered wash-in / wash-out mechanism which creates the LE effect. Figure 3.23 illustrates the contrast agent pharmacokinetics.

  Using the LE technique, we can distinguish even small subendocardial post-infarcted scars, see Figure 3.24(b). The typical post-ischemic scar is located either in the subendocardial region or it propagates from the subendocardial region to the epicardial part. The entire wall thickness may be affected in a transmural infarction.

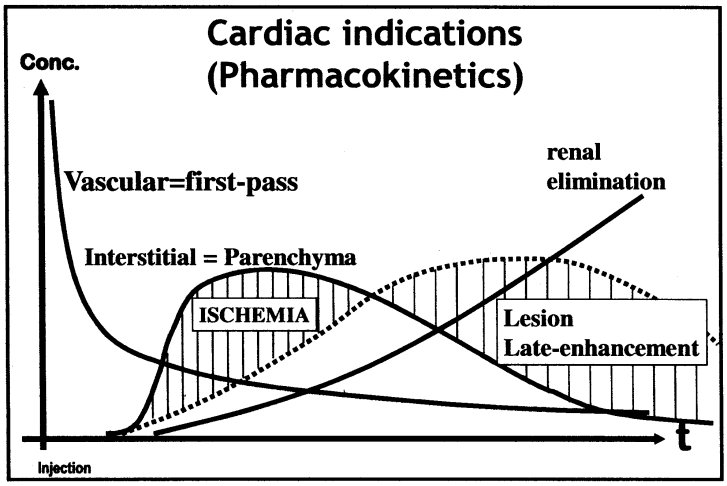

Figure 3.23: Fast perfusion and wash-out of the contrast agent in a healthy tissue (solid line). A non-viable tissue (dashed line) has a delayed perfusion and the contrast agent stays in the tissue for a long time period (late enhancement, LE). From presentation of J. Froehlich at ESMRMB School of MRI 2008 in Advanced Cardiac MRI.

- Cardiomyopathies[26] (HCM, some DCMs, non-compaction of the LV, ARVD), myocarditis, enzymatic diseases (e.g. Fabry's disease), infiltration of the myocardium (e.g. by amyloid, sarcoidosis) can cause LE which is usually not as intensive as in the case of infarction. Therefore we need LE images with a good spatial resolution and a high SNR. LE may be present in any part of the myocardium (e.g. only in the mid-myocardium or in the subepicardial layer), compared to the ischemic LE, which is always initiated in the subendocarial region. For examples of the non-ischemic LE, see Figure 3.25, LE in HCM is shown in Figure 2.12(b).
- Haemochromatosis – shortens the T2* relaxation (magnetic susceptibility effect).

3D acquisition

When using a breath navigator, a fully 3D approach is available (see Section 3.4.3). The resulting spatial resolution is as good as 2 x 2 x 2 mm. The acquisition time is about 15 minutes. 3D sequences can for instance be used for the examination of coronary arteries without any contrast agent (a native image, see [44]) or to obtain a 3D image of the infarcted scar using the late enhancement technique, see Figure 3.26. The 3D LE images with such a good spatial resolution are not routinely used in clinical practice, because of the

[26] See Section 2.4.3.

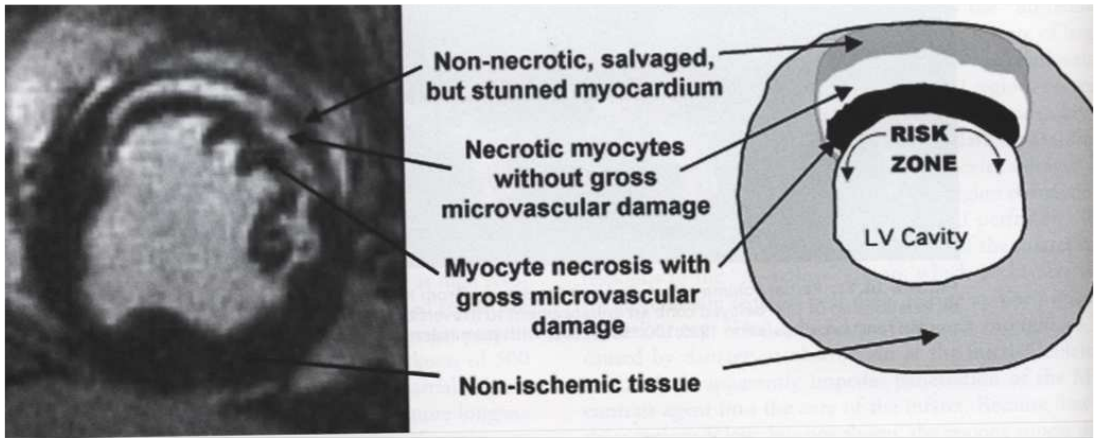

(a) Scheme of ischemic LE

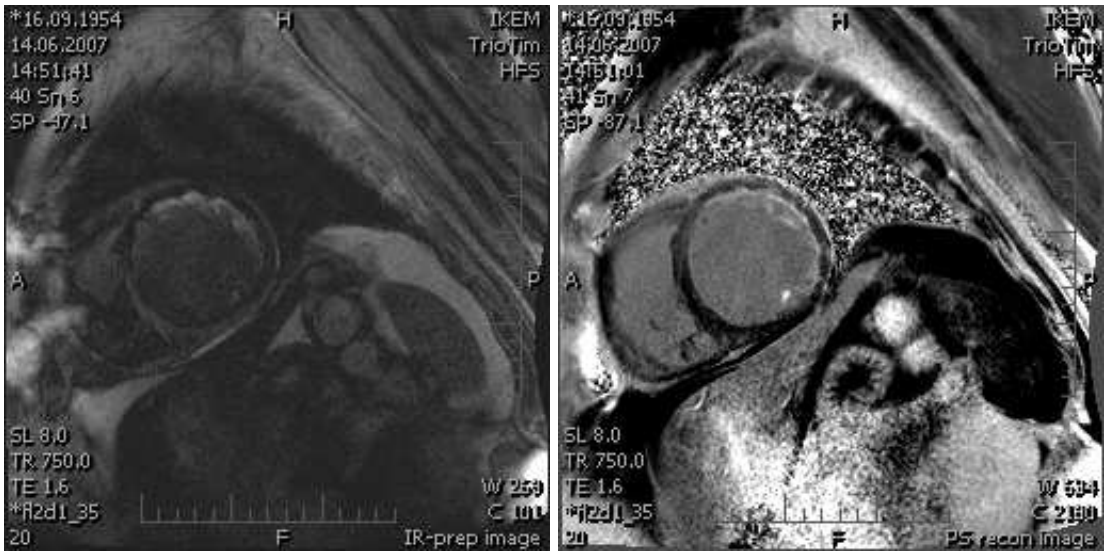

(b) LE in the subendocardial region of the LV anterior wall (an infarct scar). Magnitude image (left) and phase sensitive (right) image reconstruction.

Figure 3.24: Ischemic late enhancement.

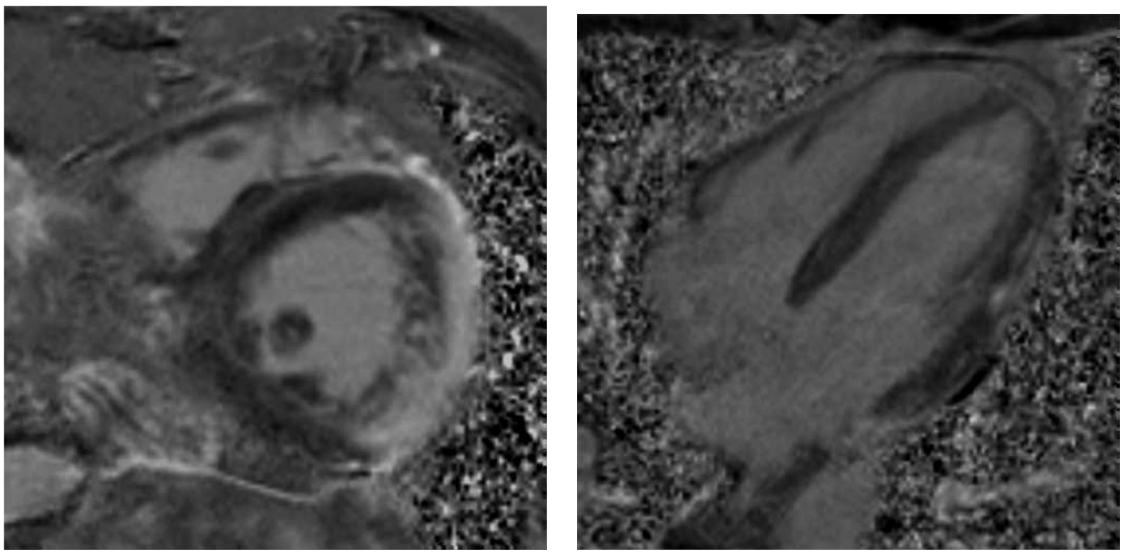

(a) Sarcoidosis

(b) Myocarditis

Figure 3.25: Examples of non-ischemic late enhancement.

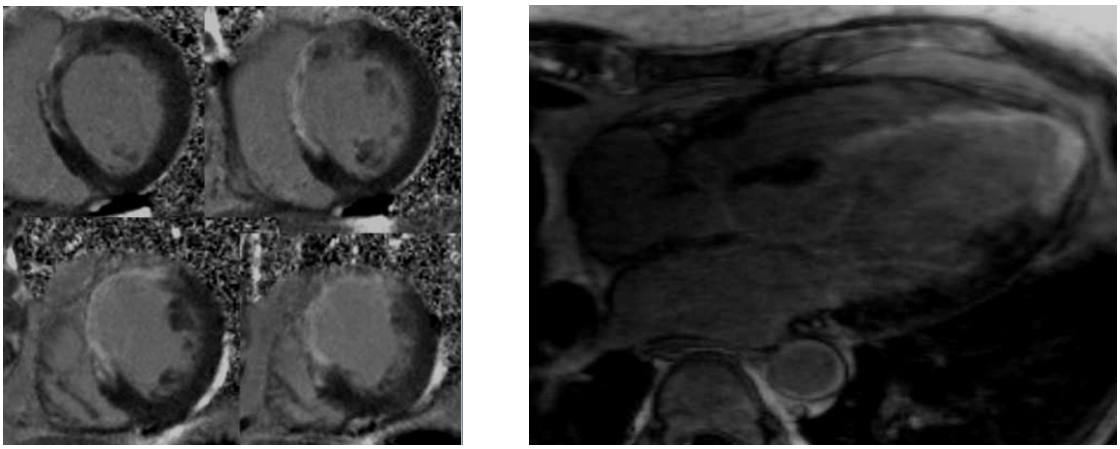

(a) 2D acquisition (segmented FLASH, phase sensitive reconstruction) in breath-holds, voxel size 2 x 2 x 10 mm.

(b) 3D acquisition (bSSFP, trueFISP) with breath navigator, voxel size 2 x 2 x 2 mm.

Figure 3.26: Late enhancement in the LV atero-septal segments and in the apex due to myocardial infarction.

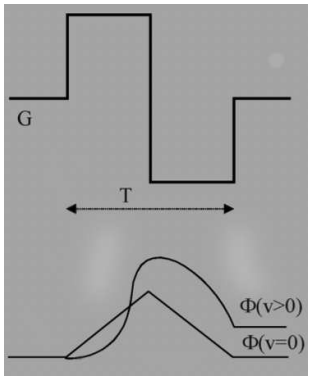

(a)

Figure 3.27: A bipolar gradient applied in phase contrast imaging causes phase shift of the moving spins.

long acquisition time and since the 2D LE images are suitable for estimating myocardial viability.

3.10.2 Phase contrast MRI

Applying a bipolar gradient causes a phase change of the moving spins, which can be used to measure the velocity of the flow by *phase contrast imaging* (PCI). The phase change Φ depends linearly on the component of velocity parallel to the applied gradient:

$$\Phi = \gamma T G v, \tag{3.13}$$

where T represents the duration of the gradient and G the gradient strength, see Figure 3.27. The variable γ stands for a gyromagnetic ratio of the nuclei concerned, and v is the velocity in the direction given by the gradient G. The signal phase Φ lies in the range $[-\pi, \pi]$ and is zero for the static spins. Before performing PCI, we need to adjust the multiplication factor of the velocity v in Equation (3.13) – given by the strength and duration of the gradient – according to the expected maximum velocity. An aliasing of the phase shift may occur when the factor γTG is large. On the other hand, a low factor γTG would reduce the accuracy of the velocity measurement.

In PCI, the acquired data consist of the signal amplitude (as in standard MRI), and in addition of the signal phase. We can reconstruct both types of images: the amplitude image (see Figures 3.28(b) and 3.29(a)) and the phase image (see Figures 3.28(c) and 3.29(b)). By post-processing the 2D phase contrast images, we can for example visualize the velocity profile through the imaging plane (see Figure 3.29(c)). Figure 3.30 shows a computed flow through the mitral and aortic valves during a cardiac cycle.

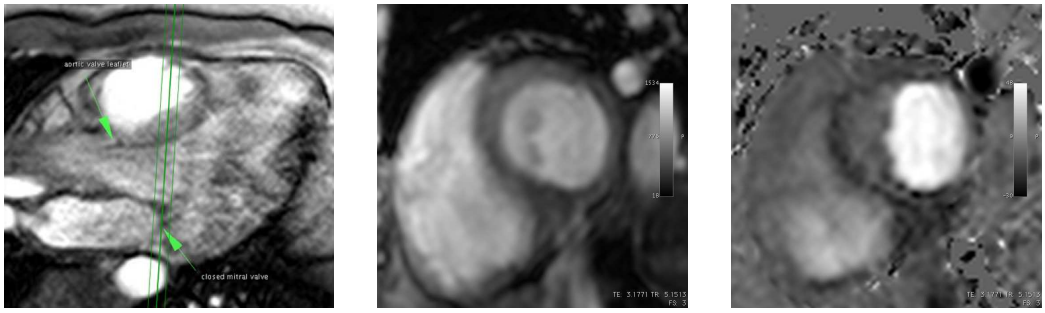

(a) Acquisition planning.

(b) Amplitude image.

(c) Phase image encoding the velocity information. Tones of white color encodes the velocity towards the LV.

Figure 3.28: Measurement of the velocity component perpendicular to the mitral valve using PCI.

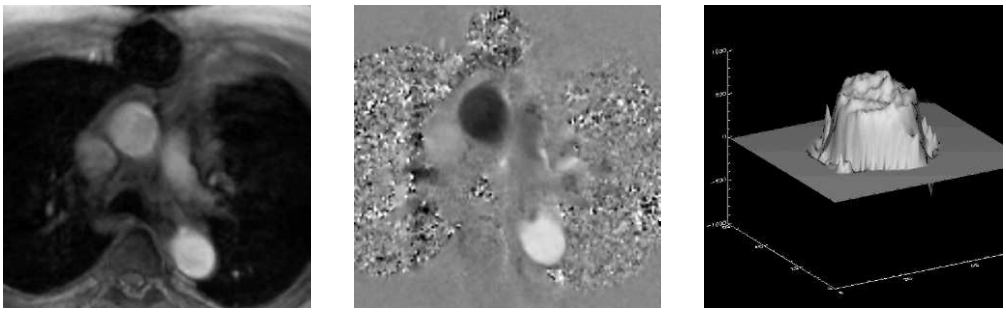

(a) Amplitude image.

(b) Phase image encoding the velocity information. Tones of black color encode the velocity outwards from the LV.

(c) Visualization of the aortic flow profile.

Figure 3.29: Measurement of the velocity component perpendicular to the aortic valve using PCI.

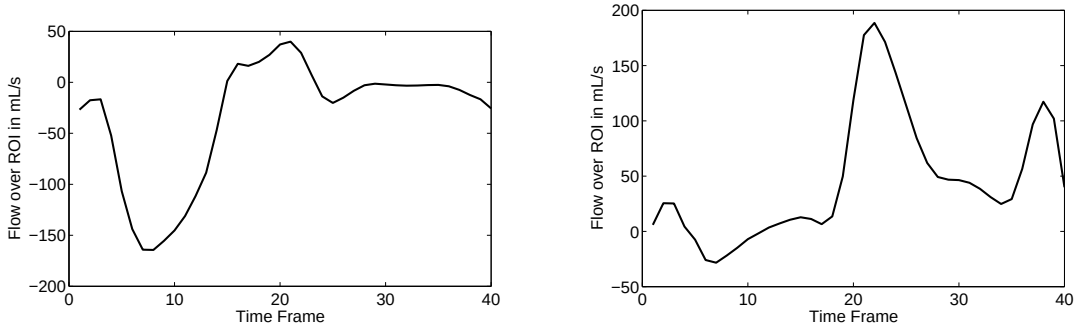

(a) Flow through left ventricle outflow tract.

(b) Flow through mitral valve.

Figure 3.30: Plots of outflow and inflow of the LV obtained by post-processing phase contrast images. Note that the opposing directions of the flows through the mitral and aortic valve are respectively represented by different signs of the flow.

The PCI sequence as described above produces a single velocity component in a 2D imaging slice. The acquisition is performed in a breath-hold period. Such a type of sequence is implemented in any clinical MR system and can be routinely used for instance to evaluate the function of heart valves (stenosis, regurgitation) or to diagnose septal defects. To obtain the full velocity vector using this type of sequence, we need to perform three measurements with three perpendicular bipolar gradients representing the components of the velocity. The spatial registration is necessary since the images representing each velocity component are acquired in other breath-holds.

Nowadays, measurements of the full 3D vector in a 3D volume are becoming available, when using a breath-navigator (see [109], [85]). It is a long acquisition which is still difficult to perform on patients. By using a tripolar gradient, we can encode and visualize the acceleration of the flow (see [34], [105], [19], [6]).

3.10.3 MR angiography

Using MRI, we are able to examine and obtain data of a vascular system (the so-called *MR angiography*, MRA). The vascular system may be visualized when using a contrast agent, but there exist also completely non-invasive methods without any contrast agent administered in the patient (a native MRA). In the following paragraphs, we briefly list the main principles of MRA. A detailed description can be found e.g. in [93].

Signal void in SE

The first method – although it is not strictly speaking an angiographic method – can provide information about the vessels using a simple principle of the spin echo sequence (SE, see Section 3.3.1). The spins in the blood flowing in the direction perpendicular to the imaging slice are first excited by the 90 ° RF pulse. If the spins flow out from the imaging slice before the 180 ° refocusing pulse is applied, there will be no signal at this location (the new inflowing spins – although influenced by the 180 ° pulse – were not excited by the 90 ° pulse beforehand). The phenomenon is called *flow void*, see Figure 3.31(b).

Time of flight

Time of flight (TOF) is based on the GE inflow effect (GE signal enhancement), which was discussed in Section 3.10.1 (a part related to the bright blood techniques in Cardiac MRI). In principle, when using a GE sequence with a short TR, the static tissue in the imaging slice will become saturated and will not give a sufficient MR signal (magnetic saturation effect). Nevertheless, the inflowing blood – not influenced by the previous excitations – will give a strong signal.

A short[27] TR (TR = 20–50 ms) can be used in coherent GE sequences (FISP), as described in Section 3.3.4. According to the principle of TOF, the imaging slices need to be perpendicular to the blood flow. TOF is suitable also for 3D acquisition with a reasonable acquisition time. See Figure 3.31(a) for an example of 3D TOF.

Phase contrast angiography

Phase contract MR angiography (PC-MRA) is based on phase contrast imaging as described in Section 3.10.2. We need to perform measurements of 3 components of the velocity vector, together with the so-called gradient moment nulling measurement (GMN), in which the flow is compensated. By the simple subtraction $\sqrt{v_x^2 + v_y^2 + v_z^2} - GMN$ we eliminate the static tissue and obtain an MRA image that is independent of the flow direction with respect to the measurement slice. Using the PC-MRA we can obtain 3D images of high quality but the measurement time is rather long. See Figure 3.31(c) for an example of 3D PC-MRA.

Contrast agent angiography

A bolus of contrast agent in the blood shortens the T1 relaxation time and the vessels give a strong signal in T1 weighted images. The static tissue is subtracted using a measurement performed beforehand without the contrast agent. We need to adjust the timing of

[27] An appropriate TR depends on many factors, e.g. on the velocity of the flow. Although a very short TR could even better suppress the static tissue, it may also saturate to some extent blood if the flow is not fast enough.

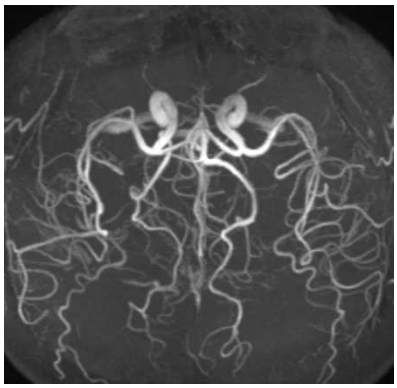

(a) Time Of Flight (in the brain).

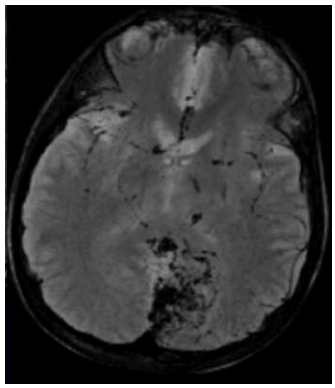

(b) Flow void in the vessels perpendicular to the imaging slice in SE sequence (black dots in the brain).

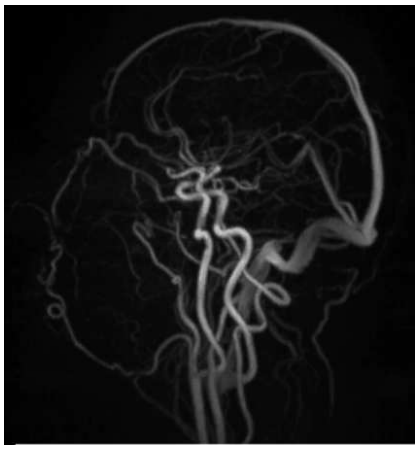

(c) Phase contrast MRA (PC-MRA, in the brain).

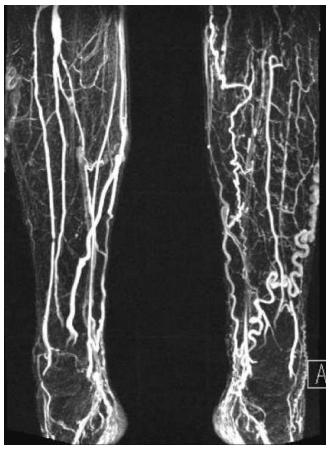

(d) Intravascular contrast agent (vasovist) – the contrast agent is present both in arteries and veins of crus.

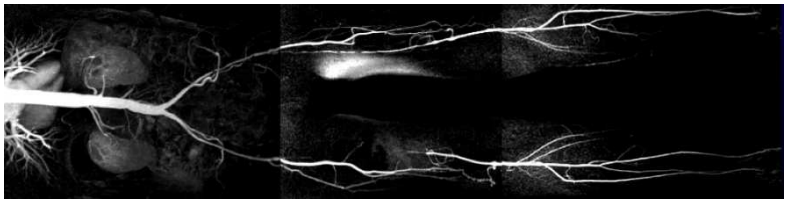

(e) Contrast agent MRA – arterial part (using extracellular contrast agent and bolus timing).

Figure 3.31: Examples of MRA images.

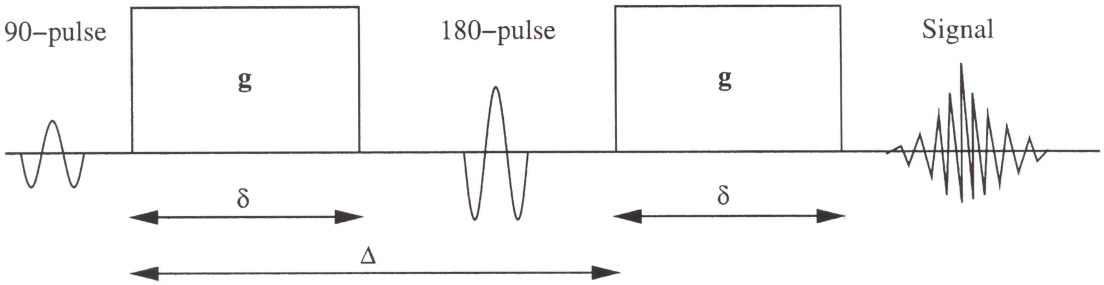

Figure 3.32: Diffusion weighted sequence with a couple of strong gradients. The gradients have either opposite polarity or a 180 ° RF pulse is placed between them (as in this case).

acquisition to the period when the bolus is present in the part of the vascular system of interest. See Figure 3.31(e) where the arterial part only is well visualized. Intravascular contrast agent ('vasovist', see Section 3.6) can recirculate through the circulatory systems several times and therefore this is suitable for some MRA applications. However, we have to distinguish between the arterial and venous component of the system, when using this type of contrast agent (see Figure 3.31(d)).

Advantages of the contrast agent MRA is are high image quality and a fast acquisition time. Some disadvantages are mainly related to the application of the contrast agent (contraindications e.g. in patients with kidney failure, price of the contrast agent).

3.11 Appendix: Diffusion Tensor Imaging (DTI)

The measurement of diffusion by magnetic resonance was described by Stejskal et Tanner already in 1965 (see [102]). When applying a strong bipolar gradient, the signal will be dependent on the spin diffusion. The first gradient will dephase all the spins and the second gradient will refocus the static ones. The spins that changed the position will not be refocused and therefore they will not give any signal. The signal decay can be described by the following equation:

$$S = S_0 e^{-bD}, \tag{3.14}$$

with $b = \gamma^2 \delta^2 (\Delta - \frac{\delta}{3}) |g|^2$ being the so-called diffusion weighting factor b (see [65]). The value of b is given by the parameters of the sequence (timing and strength of the diffusion gradients, see Figure 3.32). The variable D represents a tissue diffusivity. Diffusion in biological tissues with a fiber structure (for example in a brain white matter or a muscle tissue) is highly anisotropic. Therefore, the diffusivity D is represented by a tensor.

The tensor D is antisymmetric and is characterized by 6 values. To assess D by means of Equation (3.14) using MRI we need to perform measurements with 6 different gradient

directions, and in addition a measurement without diffusion weighting usually denoted as *B0 image*. The principal eigenvalue of tensor D gives the preferential diffusion direction, which occurs in the direction of fibers. The reconstruction of the fibers using the principal eigenvalues of D is called *Diffusion Tensor Imaging* (DTI, see [83]).

DTI has become a valuable examination in the brain. It used in neurosciences in order to assess neural connections between brain centers, or in clinical practice in order to visualize e.g. the relation of neural tracts with an epileptic focus or a brain tumor, see Figure 3.33. However, if performing DTI in the muscle tissue (and in particular in myocardium), some additional issues need to be taken into account:

- Homogeneity of $\mathbf{B_0}$ – it is more difficult to obtain a homogeneous field in the thorax than in the brain.
- Due to shorter T2 relaxation time in muscle than in brain (see Table 3.3) we would like to shorten TE in the case of muscle imaging. For technical limitations, we are usually not able to shorten TE to the optimal value.
- Possibly a lower anisotropy in the muscle than in the white matter of the brain.
- In the case of the in vivo DTI of myocardium, the most challenging issue arises from the heart motion.

DTI of the myocardium can provide information about the distribution of myocardial fiber directions for the heart model. This will be discussed in Section 4.4.1.

3.12 Remarks about the experimental protocol

A detailed experimental protocol suggested for the animal experiments performed during the thesis is in Appendix 10. Here we sum up some basic requirements on the type of data.

Cine MRI

We used the Cine MRI data to build anatomical models. To avoid the bSSFP offset-frequency artifacts, we decided to use a segmented FLASH sequence. In order to get the best spatial and temporal resolution, each slice was acquired in a single breath-hold period. The acquisition was performed in the expiration of animal, controlled by a respirator. The breath-holds were perfectly reproducible and we did not need to solve the problem of slice realignment. By using retrospective ECG triggering we covered the whole cardiac cycle, including the atrial contraction. See Figure 3.20 for the Cine MR images of a healthy subject and Figure 3.21 with a hypokinetic part of the left ventricle caused by the myocardial infarction created during the experiment.

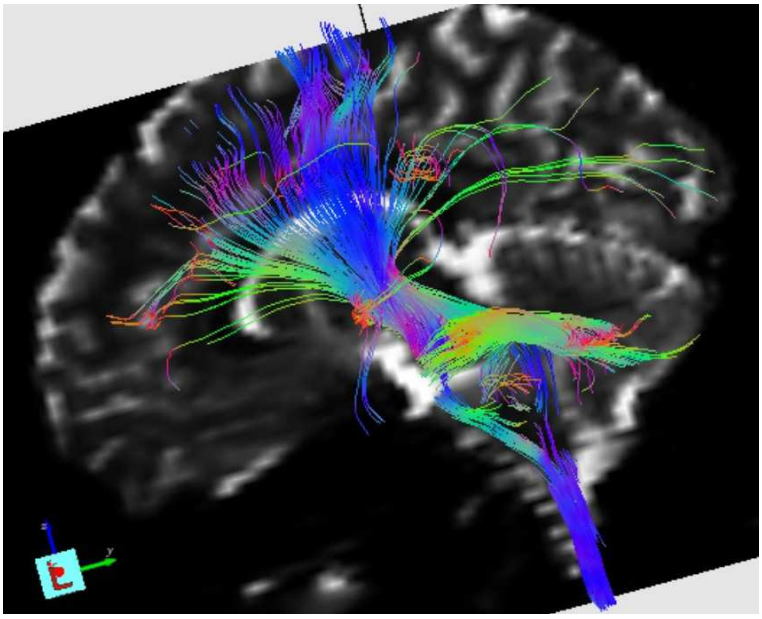

Figure 3.33: Reconstruction of the neural fibers in the white matter of brain using DTI.

Thanks to the small size of the animal, we were able to use adequately small acquisition matrices and we obtained a better temporal resolution. The radial or spiral k-space trajectory was considered but at the time of the experiments, the sequence was not available in the MR system. We did not use parallel techniques in order not to decrease SNR.

Tagged Cine MRI

We used a standard segmented FLASH sequence with SPAMM. The geometry (and acquisition matrices) were given by the Cine MR acquisitions. We decreased the RF bandwidth to the minimum value (equivalently, we increased the water-fat shift to the maximum value) in order to increase SNR. The temporal resolution was still acceptable and the noise in the images decreased significantly. In Figures 3.20 and 3.21 we can also see the tagged images of the healthy and of the diseased animal.

A good quality of the tagged images was the main objective for performing the image acquisition in a 3 T MR system.

Dark blood technique

We used the STIR technique to acquire the T2 weighted images with a fat suppression. The spectroscopic fat saturation (CHESS) was not effective enough due an inadequate

shimming of the static magnetic field $\mathbf{B_0}$.

Late enhancement images

We acquired 2D LE images with both types of reconstructions – the magnitude and the phase sensitive. We did not perform acquisition of 3D data in free breathing because of the time limitations in the experiment.

Phase contrast imaging

We acquired a single component of the velocity vector parallel to the heart valves. Since we did not perform any particular calibration of the MR system, the quantitative values could not be taken as the 'ground truth'. However, the post-processed data provided at least an exact timing for each part of the cardiac cycle (opening and closure of the valves, period of fast ventricle filling, atrial contraction).

Chapter 4

Biomechanical model of the heart

4.1 Introduction

The biomechanical model of the heart developed at INRIA is based on physiological considerations and is consistent with essential thermomechanical requirements (energy balances in particular). The model is described in detail in [95] and [25]. We aim at performing clinical simulations using real medical data and a model inversion by means of estimating some of the parameters of the model. In this chapter, we will first summarize the main ingredients of the model. Then, we will deal with the problem of model setup and calibration, using medical data of healthy and pathological hearts.

In principle, we could model the whole 4-chamber organ (with 2 atria and 2 ventricles). However, it is quite difficult to obtain reasonable anatomical models of the atria and our main interest is in modeling the behavior of the ventricles. Therefore, the geometrical models used for the simulations consist only of 2 ventricles.

4.2 Multiscale modeling for the heart model

The heart is modeled as a visco-elastic material with an active component that enables the contraction. The blood flow pattern plays an important role in some pathologies as for instance in valve diseases or some congenital heart defects. In such cases, simulating possible treatment strategies could help in the therapy planning. However the patients included in the work related to the thesis suffered from other types of diseases, in which a detailed description of the flow would not change any clinical decisions. This is why, although it would be possible to perform a full fluid-structure interaction as presented e.g. in [38], we model just the solid part and the internal pressure in each ventricle is represented by a single lumped value[1] P_V.

[1] All pressure variables used in the model are vectors of a size given by the number of cavities. In our case for instance $P_V = (P_{V_{LV}}, P_{V_{RV}})$, with $P_{V_{LV}}$ and $P_{V_{RV}}$ being the LV and RV pressures.

The heart is coupled with systemic and pulmonary circulations, that are represented by Windkessel models (see [74], [103]). Hence, the main unknowns of the problem are the displacements of the myocardium ($\underline{y}$), the ventricle pressures (P_V) and the pressures in large arteries just behind the semilunar valves (the aortic and the pulmonary artery pressures, denoted by P_{ar}). The atrial pressures (P_{at}) are considered as measured values (the input data). Internal variables[2] related to the active part of the model (namely the strain, active stress and active stiffness in a sarcomere denoted by e_c, τ_c, k_c) will be discussed in the following section.

4.2.1 The active part (Bestel–Clément–Sorine model)

The active part of the model is based on the modeling of interaction of contractile proteins – the actin and myosin molecules – in a sarcomere, the functional unit of the muscle cells (see Section 2.3.2). The model is derived from the Huxley model, see [54]:

$$\begin{aligned} \frac{\partial n(\xi,t)}{\partial t} + \dot{e}_c \frac{\partial n(\xi,t)}{\partial \xi} &= (1-n(\xi,t))f(\xi,t) + n(\xi,t)g(\xi,t), \\ n(\xi,0) &= n_0(\xi)\ \forall \xi, \end{aligned} \tag{4.1}$$

where $n(\xi,t)$ represents the number of actin-myosin cross-bridges with extension ξ at time t and e_c is the active strain of the sarcomere. The functions $f(\xi,t)$ and $g(\xi,t)$ represent the rates of creation and destruction of the cross-bridges, respectively. A new cross-bridge may be formed if the myosin head is near the actin binding site and if the binding site is not covered by troponin-tropomyosin complex. The second assumption is satisfied in the in vivo conditions if the intracellular Ca^{2+} concentration reaches a certain threshold C. On the other hand, the cross-bridge may be released if the Ca^{2+} concentration falls below the threshold C or if the bridge extension or the contraction rate are excessive. A detailed analysis of the problem was introduced by Bestel, Clément and Sorine in [12], where the following prescriptions for functions f and g are proposed:

$$\begin{aligned} f(\xi,t) &= k_{ATP}\mathbf{1}_{\xi\in[0,1]}\mathbf{1}_{Ca^{2+}\geq C}, \\ g(\xi,t) &= \alpha|\dot{e}_c| + k_{SR}\mathbf{1}_{Ca^{2+}<C} + k_{ATP}\mathbf{1}_{Ca^{2+}\geq C}\mathbf{1}_{\xi\notin[0,1]}, \end{aligned} \tag{4.2}$$

with k_{ATP} being the rate of the myosin ATPase activity (the contraction rate), k_{SR} being the rate of sarcoplasmic reticulum calcium re-uptake mechanisms and α is a constant related to the cross-bridge release due to a high contraction rate.

We can introduce the unique control variable u:

$$u = k_{ATP}\mathbf{1}_{Ca^{2+}\geq C} - k_{SR}\mathbf{1}_{Ca^{2+}<C}, \tag{4.3}$$

[2] By internal variables, we mean the unknown variables with no spatial derivatives present in the resulting system of equations. These variables are governed just by ordinary differential equations.

the electrical activation u being positive during contraction and non-positive during relaxation. The function u can be regularized in order to avoid numerical difficulties. A typical profile used in the simulations is depicted in Figure 7.5.

Using moment scaling techniques (see [116] and [25]), we can obtain the following constitutive equations for the active part (the Bestel–Clément–Sorine model):

$$\begin{cases} \dot{k}_c = -(|u| + \alpha|\dot{e}_c|)k_c + k_0|u|_+, \\ \dot{\tau}_c = -(|u| + \alpha|\dot{e}_c|)\tau_c + \dot{e}_c k_c + \sigma_0|u|_+, \\ \sigma_c = d(e_c)\tau_c + \mu_c\dot{e}_c, \end{cases} \tag{4.4}$$

where τ_c represents the active stress that can be developed in the tissue and k_c the active tissue stiffness. If the Frank–Starling mechanism is taken into account (see Section 2.3.5), the final active stress σ_c will also depend on the actual strain e_c of the sarcomere by means of the function d in the last equation of (4.4) which will be discussed in Section 4.3. The parameter μ_c represents a viscosity in the active element.

4.2.2 Electrical activation

Electrical activation is considered as a model input and it is given by the function u prescribed by (4.3) at each part of the myocardium. It represents a concentration of the cytosolic TroponinC–Ca^{2+} complexes (TnC–Ca), which trigger the fiber contraction as discussed in Section 2.3.2. In general, the electrical activation should be modeled on a cellular level by means of modeling the transmembrane potential and intracellular TnC–Ca dynamics, and on an organ level by modeling the propagation wave of the activation in 3D anatomical models. In this section we will briefly sum up several possibilities for modeling these phenomena. The electrical activation modeling is worked up in monographs [94], [90], [104].

The cytosolic TnC–Ca concentration in cardiac muscle cells depends on Ca^{2+} ionic flows between the extracellular space, the sarcoplasmic reticulum and the sarcoplasm. The inflow of the Ca^{2+} ions into the sarcoplasm is induced by the opening of the cellular membrane L-Ca^{2+} channels triggered by the action potential generated on the membrane, and by Ca^{2+} channels in the membrane of the sarcoplasmic reticulum being opened thanks to an increased sarcoplasmic Ca^{2+} concentration ('Ca^{2+} dependent release of Ca^{2+} ions'). Therefore we would ideally like the 0D cellular model to be able to represent the resting membrane potential, the ionic flows (I_{ion}) during an action potential that cause an increase of the intracellular Ca^{2+} concentration, and the creation of TnC–Ca complexes. The following electrophysiological models of various levels of complexity can be considered:

1. A fully biophysical approach that models the transmembrane potential using systems of ordinary differential equations (ODEs), taking into account various types of ionic channels and ionic flows. Some examples of these models are: Beeler–Reuter 1977

([8]), Luo–Rudy LR1 1991 ([72]), Luo–Rudy LR2 1994 ([73]), ten Tusscher 2004 ([106]). Then, the intracellular Ca^{2+} dynamics can be modeled e.g according to [32].

2. Simplified models analogous to 1. that can typically represent the transmembrane potential but do not take into account the full complexity of the membrane. Some examples of these so-called *phenomenological models* are: FitzHugh–Nagumo 1961 ([37]), Aliev–Panfilov 1996 ([3]), Fenton–Karma 1998 ([36]), Bernus 2002 ([11]), Mitchell–Schaffer 2003 ([77]). Due to similar profile of the propagating waves of the transmembrane potential and the cytosolic TnC–Ca concentration as obtained with the more complex model of [32], we can directly rescale the transmembrane potential to obtain the activation function u of the biomechanical heart model. This approach was used in [23].

3. An ad-hoc prescription of the function u with a profile corresponding to the physiological models.

The phenomenological models can capture important physiological features. The full biophysical cellular models should in theory improve the results. Unfortunately, these complex models are rather computationally intensive and difficult to tune, hence we often do not obtain such encouraging results as with the phenomenological ones.

Although the approach 3. is the simplest one, it can represent the heart contraction correctly if the timing of the activation onset in each part of the myocardium is well prescribed.[3] However, if we have no information about the tissue repolarization, the activation based on the uniform function u cannot accurately represent heart relaxation.

Now, we will discuss the following possibilities of modeling the activation propagation in the 3D tissue:

1. Bidomain models

2. Monodomain models

3. Eikonal equation

4. Analytical prescription

ad 1. At the 3D tissue and organ level, the propagation wave is modeled using reaction-diffusion systems of partial differential equations (PDEs), that are coupled with ODEs modeling the ionic currents I_{ion} flowing through the membrane (as described above). The so-called *bidomain* models (see [104], [16], [35]) consider the intracellular and extracellular compartments, each of them characterized by its electrical potential u_i and u_e, with the transmembrane potential given by $v = u_i - u_e$. The ion concentration is denoted by c. A gating variable w represents the state of the ionic channels (either 'opened' or 'closed',

[3]The activation is given by depolarization times that offset the function u.

and in some types of channels may in addition also feature an 'inactivated' state). The following system of reaction-diffusion equations with the unknowns u_i, u_e and c needs to be solved:

$$\begin{cases} \rho C_m \frac{\partial(u_i-u_e)}{\partial t} - \operatorname{div}(D_i \nabla u_i) + \rho I_{ion}(v,w,c) = I^i_{app} \ \text{ in } \Omega \times (0,T), \\ -\rho C_m \frac{\partial(u_i-u_e)}{\partial t} - \operatorname{div}(D_e \nabla u_e) - \rho I_{ion}(v,w,c) = I^e_{app} \ \text{ in } \Omega \times (0,T), \\ \frac{\partial w}{\partial t} = R(v,w) \ \text{ in } \Omega \times (0,T), \\ \frac{\partial c}{\partial t} = S(v,w,c) \ \text{ in } \Omega \times (0,T), \end{cases} \tag{4.5}$$

with ρ being the ratio of membrane area to tissue volume, C_m the membrane capacitance, I^i_{app} and I^e_{app} are applied currents. The tensors D_i and D_e represent the intracellular and extracellular conductivities.

ad 2. The main difficulty in using the bidomain equation (4.5) is that we need a very fine spatial discretization in order to capture the phenomena that occur between the extracellular and intracellular compartments. Using some additional assumptions, as for instance an equal anisotropy ratio of the conductivity tensors $D_e = \lambda D_i$ (see [104]), we can simplify (4.5) and obtain a single reaction-diffusion equation for the transmembrane potential v. This equation is called the *monodomain* equation and it has the following form:

$$\begin{cases} \rho C_m \frac{\partial v}{\partial t} - \operatorname{div}(D \nabla v) + \rho I_{ion}(v,w,c) = I_{app} \ \text{ in } \Omega \times (0,T), \\ \frac{\partial w}{\partial t} = R(v,w) \ \text{ in } \Omega \times (0,T), \\ \frac{\partial c}{\partial t} = S(v,w,c) \ \text{ in } \Omega \times (0,T). \end{cases} \tag{4.6}$$

The phenomenological model proposed by Mitchell and Schaffer ([77]) coupled either with the bi– or monodomain reaction-diffusion equation is used e.g. in [14] and [15]. The same electrophysiological model is used in [23] for a weak electromechanical coupling with our biomechanical model.

ad 3. The Eikonal equation is a static non-linear partial differential equation derived from more complex models of the electrical activation discussed above (see [60], [30]). The following form of the Eikonal equation can be used:

$$c_0 \sqrt{\nabla T_d^T D \nabla T_d} - \operatorname{div}(D \nabla T_d) = \tau \ \text{ in } \Omega \times (0,T), \tag{4.7}$$

where c_0 is a dimensionless constant related to the cell membrane, τ is the cell membrane time constant, D is a tensor related to the myocardial fiber directions. The unknown variable T_d represents depolarization times of the myocardial tissue.

ad 4. An analytical prescription of the depolarization times T_d can be given by a traveling planar or spherical wave which in a physiological activation propagates from the heart apex to the base (as shown in Figures 6.2 and 7.7). We may adjust the propagation velocity, so that the activation period corresponds to the physiological timing, or the period of activation may be given by the measured data (QRS duration in ECG that will be

denoted by QRSd). We can apply a more complex yet still analytical prescription by giving a fast propagation velocity for the activation of the endocardial part and a slow transmural propagation, as depicted in Figure 8.18. In Section 8.7 we show that both types of analytical prescriptions give almost identical results including in a joint state-parameter estimation, supposing that the propagation velocities are well adjusted.

In most of the simulations performed in the thesis, we use a simple analytical prescription of the electrical activation – with the timing of propagation corresponding to the measured QRSd. In Chapter 7 we use in addition a prescription of the depolarization times based on the Eikonal equation (4.7) and measured electro-physiological data.

4.2.3 The rheological model

The myocardial tissue is modeled as a material of Hill–Maxwell type (see [52]) with two branches, depicted in Figure 4.1: the active series branch and the passive parallel branch. The active part is modeled by the Bestel-Clément-Sorine component. It creates the active contraction in the privileged direction given by the direction of myocardial fibers $\underline{n}$. The parallel passive branch is 3-dimensional and is modeled as a viscoelastic material, with a Mooney–Rivlin based hyperelastic potential (Ciarlet–Geymonat material, see [27])

$$W^e = \kappa_1(J_1 - 3) + \kappa_2(J_2 - 3) + \kappa(J_3 - 1) + \kappa(\ln J_3), \tag{4.8}$$

with κ_1, κ_2, κ being the material parameters (the passive tissue stiffness) and J_1, J_2, J_3 being the reduced invariants of the Cauchy–Green tensor $\underline{\underline{C}} = \underline{\underline{F}}^T \cdot \underline{\underline{F}}$ with $\underline{\underline{F}} = \underline{\underline{1}} + \underline{\underline{\nabla y}}$ (see [67]), and with the viscoelastic pseudopotential

$$W^\eta = \frac{\eta}{2} tr(\underline{\underline{\dot{e}}}^2), \tag{4.9}$$

where the parameter η represents a viscosity in the passive branch.

The variable e_{1D} stands for the strain in the active branch and it combines e_c (the strain in the Bestel–Clément–Sorine unit) and e_s (the strain related to the passive elastic element E_s, see Figure 4.1), and σ_{1D} is the corresponding stress. The strain in the passive branch coincides with the Green–Lagrange strain in the Hill–Maxwell unit denoted by $\underline{\underline{e}}$. Finally, we can write the constitutive equation for the 2$^{\text{nd}}$ Piola–Kirchhoff stress of the whole material:

$$\underline{\underline{\Sigma}} = \frac{\partial W^e}{\partial \underline{\underline{e}}} + \frac{\partial W^\eta}{\partial \underline{\underline{\dot{e}}}} + \sigma_{1D}(e_{1D}, e_c)\underline{n} \otimes \underline{n}. \tag{4.10}$$

4.2.4 Coupling with systemic and pulmonary circulations

A cardiac cycle can be divided into 2 non-isovolumetric phases (ventricle filling and ejection) and 2 isovolumetric phases (isovolumetric contraction and relaxation). Let $V(t)$ denote the ventricle volume at time t. Then the blood flow leaving the ventricle is given by $Q = -\dot{V}(t)$.

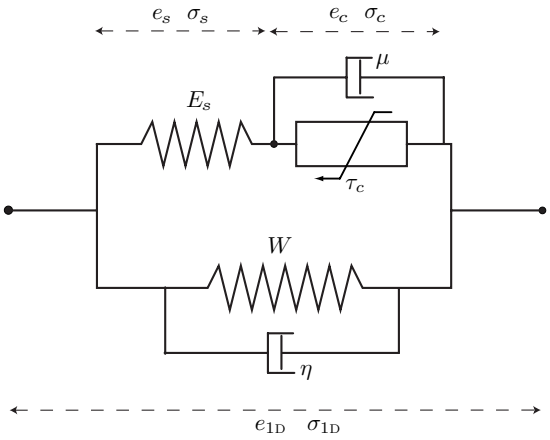

Figure 4.1: Rheological model of Hill–Maxwell type with 1D-active branch (Bestel–Clément–Sorine model) and 3D passive branch. From [25].

During the isovolumetric phases, the tissue displacements need to satisfy the constraint $Q = 0$. The value of the ventricle pressure P_V then corresponds to the Lagrange multiplier of this constraint. In the non-isovolumetric phases, we have either a condition $P_V = P_{at}$ in the filling phase, or $P_V = P_{ar}$ during the ejection. The former equation says that the ventricle pressure is prescribed during the filling phase (P_{at} is a part of the given data) and the latter equation couples the heart with the circulatory systems.

The systemic and pulmonary circulations are represented by Windkessel models with resistances and capacitances R_p and C_p in the proximal part of the system (just behind the ventricle outflow tracts), and C_d and R_d in the distal part of the circulation. The Windkessel model – depicted in Figure 4.2 – is given by the following set of equations:

$$\begin{cases} C_p \dot{P}_{ar} + \frac{P_{ar} - P_d}{R_p} = Q, \\ C_d \dot{P}_d + \frac{P_d - P_{sv}}{R_d} = \frac{P_{ar} - P_d}{R_p}, \end{cases} \tag{4.11}$$

where the variable P_d represents the blood pressure in the distal part of the circulation and P_{sv} stands for the venous pressure.

4.2.5 Boundary conditions

In order to complete the system of equations governing the biomechanical model, we need to prescribe boundary conditions. We would like the boundary conditions to reflect the following constraints that can be observed in the image data:

- The base of the heart (the valves) will follow the movement along the long axis according to the image data.

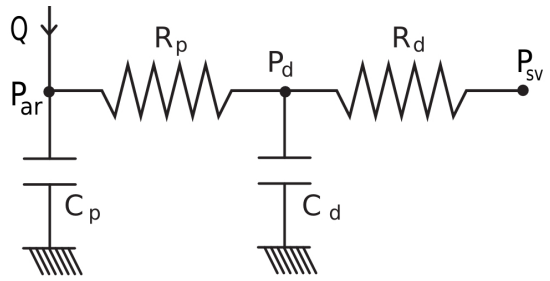

Figure 4.2: Scheme of the Windkessel model. From [78].

- The heart apex will be nearly fixed.
- The boundary conditions will represent a contact of the myocardium with surrounding structures – in particular with the thoracic cage and diaphragm.

The simplest would be to fix (or prescribe displacements on) a part of the heart surface $\mathcal{B}$ using the Dirichlet boundary conditions:

$$\underline{y} = 0 \text{ on } \mathcal{B}. \tag{4.12}$$

We can apply Dirichlet boundary conditions on the base of the heart (areas around the valves, see Figure 4.3(a)) and as a post-processing of the results we can subtract the simulated displacement of the apex from the modeled displacement vector $\underline{y}$. Although we can obtain a good model even with such a simple approach (see Figure 4.4), we rather consider the following more physiological types of boundary conditions.

We replace the Dirichlet boundary condition by visco-elastic boundary conditions prescribed on the heart base and on the area around the heart apex. The force associated with the boundary condition applied on the surface $\mathcal{B}$ is given by the following variational formulation (see [82]):

$$\mathcal{P}^{ext}(\delta\underline{v}) = -\int_{\mathcal{B}} (a(x)\underline{y} + b(x)\dot{\underline{y}}) \cdot \delta\underline{v} dS \quad \forall \delta\underline{v} \in V, \tag{4.13}$$

where the functions $a(x)$ and $b(x)$ represent elastic and viscous moduli. They are adjusted so as to preserve the motion of the base of the heart, as seen in the long axis projections of Cine MRI, and to prevent the apex from displacing. Therefore the stiffness of the boundary conditions applied on the apex needs to be higher than for the boundary conditions applied on the base.

A contact between the heart and the surrounding structures – as for instance the thoracic cage or diaphragm (see Figures 4.3(b), 4.3(c) and 4.5) – can be represented by additional visco-elastic boundary conditions with stiffnesses approximately of the same order

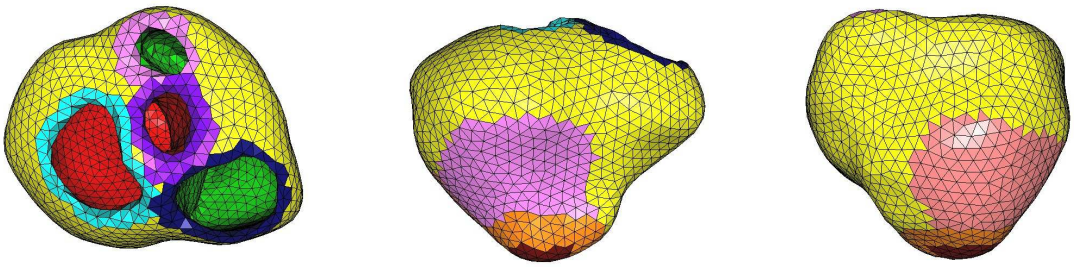

(a) View of the heart base: Light and dark blue, pink and purple areas around the valves designated for the boundary conditions.

(b) Inferior-wall view: Purple area for a contact with the diaphragm; orange and brown regions for fixation of apex.

(c) Anterior-wall view: Red area for a contact with the thoracic cage.

Figure 4.3: Prescription of the boundary conditions on the base of the heart, the apex and the epicaridal surface adjacent to the thoracic cage and diaphragm.

as for the apex. Such boundary conditions prevent the ventricle wall from the movements that are constrained by the surrounding anatomical structures but to some extent also prevent the myocardial wall from contracting because of the partial fixation of the adjacent epicardium.

To avoid this drawback, we can use another type of boundary conditions that directly represent the contact between the heart wall and the surrounding structures by penalizing the distance between them. A representation of the distances between the surfaces uses the same approach as in [81], where distances of surfaces of the model from observations (the reference surfaces) were computed in order to correct the model. The variational form prescribing the force associated with the boundary condition is as follows:

$$\mathcal{P}(\delta \underline{v}) = \mathcal{K} \int_{\mathcal{B}} |\operatorname{dist}(x, S_{\text{ref}})|_{-} \underline{\nu} \cdot \delta \underline{v} dS, \tag{4.14}$$

where S_{ref} is the pericardial surface designated for the sliding boundary condition, $\operatorname{dist}(x, S_{\text{ref}})$ stands for the signed distance of x to the surface S_{ref} and

$$|\operatorname{dist}(x, S_{\text{ref}})|_{-} = \begin{cases} \operatorname{dist}(x, S_{\text{ref}}) & \text{if } x \text{ is inside } S_{\text{ref}}, \\ 0, & \text{otherwise.} \end{cases} \tag{4.15}$$

The variable $\underline{\nu}$ stands for an outward unit normal vector to $\mathcal{B}$ and $\mathcal{K}$ is a large penalization coefficient. By using the boundary conditions given by (4.14), we can observe more physiological wall thickening and the epicardial surface may slide on the pericardium, as in the

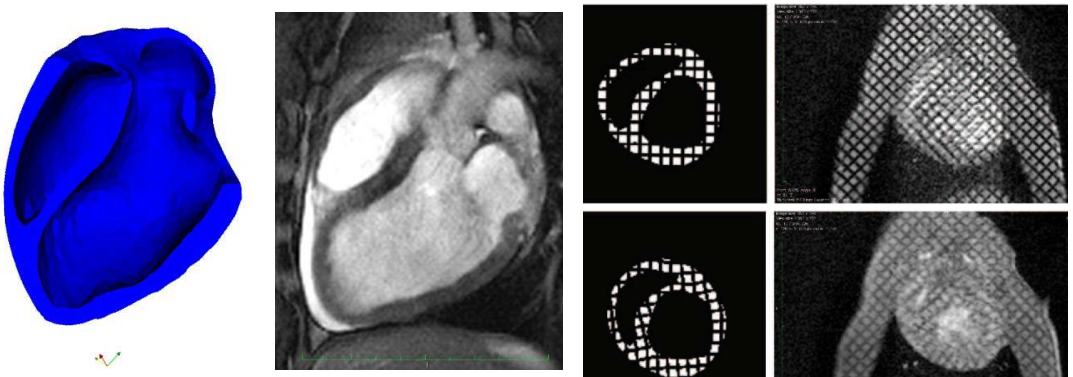

(a) Diastole, blue color represents non-activated model

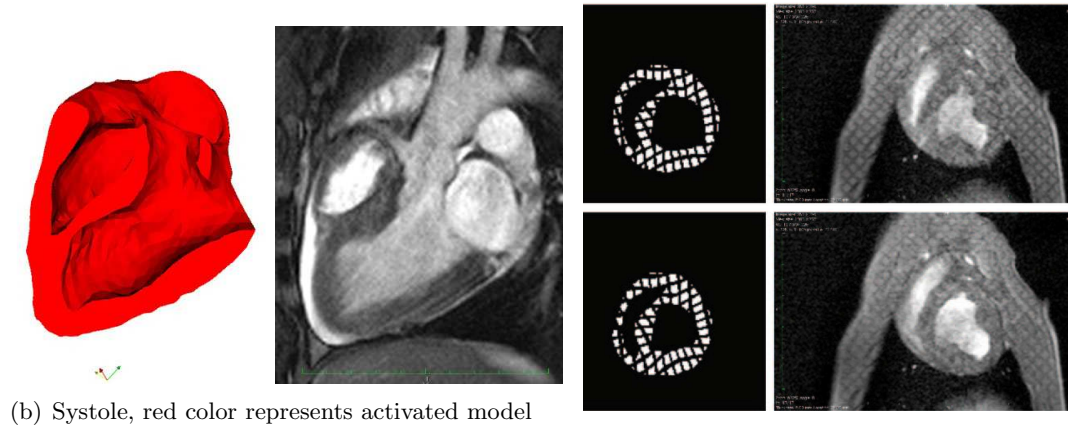

(b) Systole, red color represents activated model

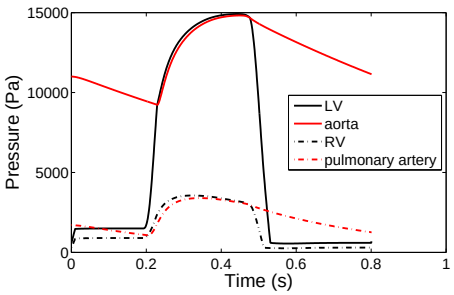

Simulated pressures

Location	End-systole (mmHg / Pa)	End-diastole (mmHg / Pa)	Mean pressure (mmHg / Pa)
LV	115 / 15200	14 / 1850	40 / 5400
aorta	115 / 15200	70 / 9400	95 / 12700

Measured pressure values

Figure 4.4: Example of the resulting model of healthy heart: The anatomical model is based on Cardiac CT data. Dirichlet boundary conditions are applied on the heart base and the simulated displacement of the apex is subtracted from $\underline{y}$. Comparison of the simulation (long axis projection of the mesh or synthetic tagged images in short axis) with measured MR images. The simulated pressures are comparable with the measured values.

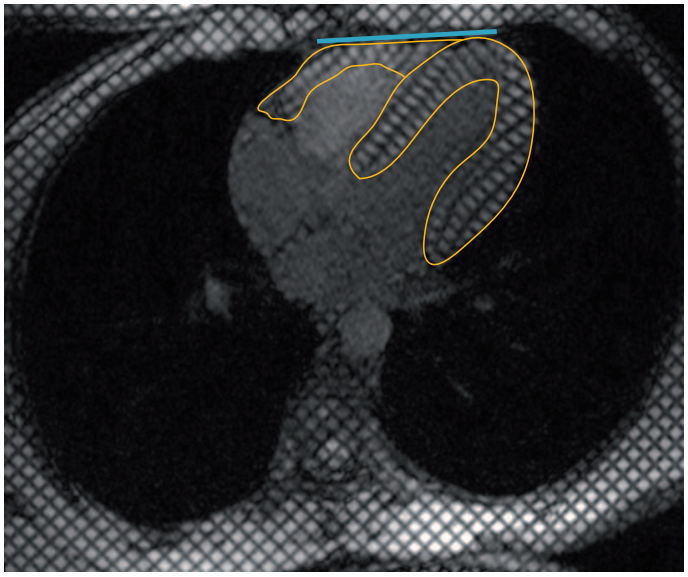

Figure 4.5: Surfaces designated for the contact boundary conditions are obtained using Cine MRI (or tagged Cine MRI, as in this case).

real situation. In practice, we need to create the complementary – pericardial – surface S_{ref} and both surfaces involved in the sliding boundary conditions need to be smooth without large surface irregularities.

Most of the models in the thesis are calibrated using the visco-elastic boundary conditions (4.13) applied on the base, apex and on the epicardial surfaces adjacent to the thoracic cage and the diaphragm. In Chapter 8, some preliminary simulations are performed with the sliding boundary conditions (4.14). Direct comparisons between the two types of the boundary conditions are shown in Figures 8.21 and 8.22.

4.2.6 The full heart model

The variational formulation of the model taking into account the equations (4.3), (4.4), (4.8) – (4.11) and the boundary conditions presented above can be written according to the principal of virtual work (PVW, [7]):

$$\int_{\Omega_0} \rho \ddot{\underline{y}} \cdot \delta \underline{v} d\Omega_0 + \int_{\Omega_0} \underline{\underline{\Sigma}} : \delta \underline{\underline{e}} d\Omega_0 + \int_{\Gamma} P_V \underline{\nu} \cdot \underline{\underline{F}}^{-1} \cdot \delta \underline{v} J d\Gamma = 0 \quad \forall \delta \underline{v} \in V. \tag{4.16}$$

We recall that $\underline{y}$ and P_V are the main unknowns of the problem – the displacement field, and the left and right ventricle pressures. The symbol Ω_0 denotes the reference domain corresponding to the cardiac tissue, and Γ represents the left and right ventricle endocardial surfaces with outward unit normal vector $\underline{\nu}$.

The model given by Equation (4.16) is discretized in space using P1-Lagrange finite elements and in time using a mid-point Newmark scheme, see [95] and [25]. We introduce the following matrix-form notation according to [78]. Let $\underline{y}_h \in V_h$ denote the discretized displacement vector $\underline{y}$ and $\underline{\dot{y}}_h$ is the associated velocity. The degrees of freedom (DOFs) of our problem consist of 3 components of the displacement $\underline{y}_h$ for each node of the computational mesh which is not fixed by the Dirichlet boundary condition. Let Y, $\dot{Y}$ are displacement and velocity vectors associated with the DOFs stored in columns. The problem of linear elasticity would be to find Y such that

$$\begin{cases} M\ddot{Y} + C\dot{Y} + KY + \Sigma_{PS}(t) = F^e(t), \\ Y(0) = Y_0, \\ \dot{Y}(0) = \dot{Y}_0, \end{cases} \tag{4.17}$$

with M, C, K being the mass, damping and stiffness matrices of the linear problem. The variable $\Sigma_{PS}(t)$ represents an imposed active stress in time t (the *prestress*) and F^e is an external force.

We can re-write equation (4.17) for a non-linear case, still with the prescribed prestress:

$$\begin{cases} M\ddot{Y} + C(\dot{Y}) + K(Y,t) + \Sigma_{PS}(t) = F^e(t), \\ Y(0) = Y_0, \\ \dot{Y}(0) = \dot{Y}_0. \end{cases} \tag{4.18}$$

The active stress in our heart model is not imposed from the 'outside' as in systems (4.17) and (4.18), but it is created by the tissue itself thanks to the actin-myosin interactions in sarcomeres with an activation given be the function u. Hence, the full model can be written in the following form:

$$\begin{cases} M\ddot{Y} + C(\dot{Y}) + K(Y,u(t)) = F^e(t), \\ Y(0) = Y_0, \\ \dot{Y}(0) = \dot{Y}_0. \end{cases} \tag{4.19}$$

The time discretization for the mid-point between the time steps n and $n+1$ has the following form (Newmark scheme):

$$\begin{aligned} Y_{n+1/2} &\approx \frac{Y_{n+1} + Y_n}{2}, \\ \dot{Y}_{n+1/2} &\approx \frac{\dot{Y}_{n+1} + \dot{Y}_n}{2} = \frac{Y_{n+1} - Y_n}{\Delta t}, \\ \ddot{Y}_{n+1/2} &\approx \frac{\ddot{Y}_{n+1} + \ddot{Y}_n}{2} = \frac{\dot{Y}_{n+1} - \dot{Y}_n}{\Delta t}. \end{aligned} \tag{4.20}$$

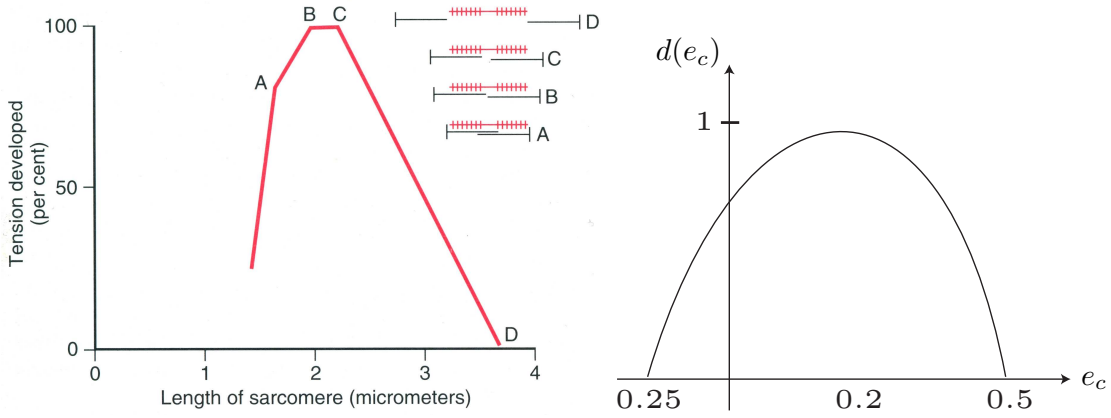

Figure 4.6: Maximum active stress depending on the sarcomere length in an experiment (left) with relative positions of the actin and myosin filaments depicted at the upper right corner (from [46]), and function d representing the same phenomenon in the model (right).

4.3 Functional modulations in the model

Basic physiological mechanisms of the regulation of heart function were discussed in Section 2.3.5. These mechanisms are included in the model and can be modulated in the following ways.

The contractility level of the model is given by the product of the parameters k_{ATP} (the maximum value of the electrical activation function u) and σ_0 (the tissue active contractility) in Equations (4.3) and (4.4). By increasing (decreasing) either of them, we will achieve the positive (negative) inotropic stimulation. The lusitropic activation (the relaxation rate level) is given by the parameter k_{SR} (the minimum value of the electrical activation function u) in (4.3). The dromotopic stimulation (an increased conductivity in the heart conduction system) can be modulated directly by the propagation velocity of the electrical activation wave, if some simple analytically prescribed activation pattern is used.

The heterotropic regulation (the Frank–Starling mechanism) is modeled by means of the function d in (4.4). It modifies the active stress τ_c according to the actual strain of the sarcomere (e_c). The function $d \in [0, 1]$, and $d = 1$ for the optimum sarcomere length and decreases to 0 for either an overextension of the sarcomere or if the sarcomere shortens below a certain threshold, see Figure 4.6.

4.4 Model calibration

In this section, we will describe a basic strategy in setting up the subject-specific[4] heart models. The clinical data used in creating the models consist of image data and pressure data measured in the heart cavities and large vessels. The calibrated models need to correctly represent both the motion pattern according to the image data and the pressure values according to the measured pressure curves.

4.4.1 Anatomical model

Image modalities

The subject-specific anatomical models are created by segmenting image data acquired by Cardiac MRI or Cardiac CT.

Cardiac MRI was discussed in detail in Section 3.10.1. It can provide a static 3D image with a spatial resolution as good as 2 x 2 x 2 mm or kinematical Cine images with a spatial resolution of about 2 x 2 x 10 mm and with a temporal resolution of about 30 ms.

The 3D static images are acquired in free-breathing. Due to a long data acquisition[5] and a non-uniform data quality, they are often not available. The Cine MRI data are acquired during several breath-hold periods of the examined subject. Since the breath-holds are not exactly reproducible (especially in patients in whom the data are acquired usually during inspiration), we often need to re-align the 2D image data to obtain the correct 3D geometry. In subjects with a myocardial infarction, Cardiac MRI can visualize the infarct scar by means of the late-enhancement technique. The scar can be directly projected in the mesh without any major registration issues[6]. As for the morphological images, the late-enhancement data can be either acquired in breath-hold periods with a non-isotropic voxel of about 2 x 2 x 10 mm – a quite limited resolution for an accurate 3D definition of the scar in the anatomical model – or using the true 3D approach in free-breathing with a spatial resolution of around 2 x 2 x 2 mm but with all the difficulties of the 3D morphological data (i.e. long acquisition time and unpredictable image quality).

A disadvantage of Cardiac MRI data is that current commonly available image segmentation software is not efficient enough to create anatomical models automatically from patients' data of usual resolution and quality, and we need to use either some semi-automatic or fully manual approaches.

Cardiac CT can provide data of a better spatial resolution compared to MR images and

[4] By subject, we mean either a human healthy volunteer, patient or animal during an animal experiment.

[5] It is an additional approximately 15-mins acquisition after an usual 30–60 min Cardiac MRI examination. The resulting image is usually not crucial for patient's diagnosis (except if we aim for instance at native MR coronarography).

[6] Supposing that the subject did not move between the acquisition of the morphological and the late-enhancement data.

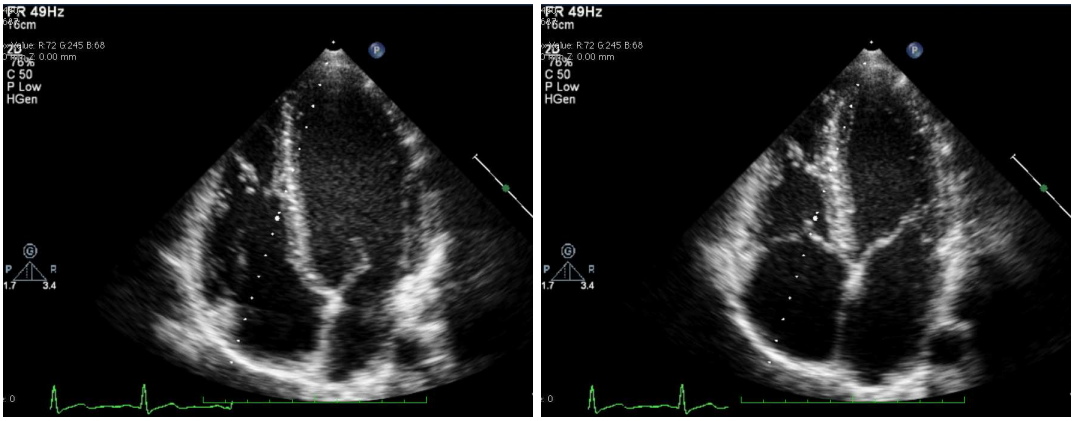

Figure 4.7: A 4-chamber projection using 2D echocardiography can give an approximate value of the LV ejection fraction (left: end-diastole, right: end-systole).

of better image quality.[7] It is easier to create accurate anatomical models thanks to already existing robust algorithms for image segmentation. As drawbacks of Cardiac CT we should mention a lower temporal resolution (we acquire either just a static image or a dynamic sequence with a temporal resolution of about 100 ms), registration issues if we aim at using also some other imaging modalities (e.g. Cine MRI with a better temporal resolution, tagged MRI, late-enhancement MR images or FDG–PET[8]). Significant radiational doses prevent us from performing cardiac CT on purpose only for creating the models (e.g. in healthy volunteers). In fact, only one of the anatomical models used in the thesis was created from the Cardiac CT data – the model presented in Figure 4.4. All other subject-specific anatomies were created using the Cine MRI data.

Finally, we can discuss the role of echocardiography[9] in setting up the models. Current 3D-echocardiography can provide a reasonable geometry but the data quality depends on many additional non-cardiac factors (e.g. patient's level of obesity). Creating anatomical models is a long procedure, which is the reason why we prefer using data of a quality as high as possible. Therefore we use Cardiac MRI or CT data. Nevertheless, echocardiographic data can be used e.g. in measuring some functional indicators, as for instance the LV ejection fraction (see Figure 4.7) or a flow through the valves using the Doppler technique (see Figure 4.8). This can serve as complementary information to set up the biomechanical

[7] The acquisition is limited to the time period when the bolus of the contrast agent is present in the heart (period of 10–20 secs). Then, depending on many factors such as the number of detectors or the energy of X–rays, we may obtain a spatial resolution of about 0.5 x 0.5 x 0.5 mm.

[8] Positron Emission Tomography using ^{18}fluor-deoxy-glucose is in some countries considered as a gold standard for assessing the myocardial viability. See [114] for a review of non-invasive imaging of the viability.

[9] Echocardiography is an ultrasound examination of the heart and is described e.g. in [87].

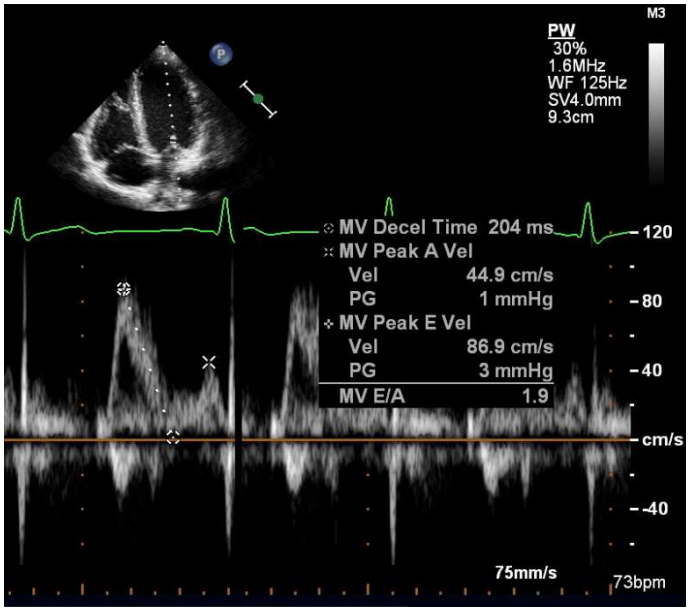

Figure 4.8: Analysis of flow through mitral valve using pulse Doppler measurement.

model. Some easily measured indicators could be used in follow-ups of patients in order to develop models representing some long-term processes (e.g. tissue remodeling).

Segmentation

The LV and RV endocardial and the epicardial surfaces are segmented manually using the software CardioViz3D, see [107]. We exclude the atria from the geometrical models due to difficulties in their segmentation. Therefore we truncate the models slightly above the atrio-ventricular and semilunar valves. We cannot obtain a very accurate geometry of the myocardium in the vicinity of the valves because of the low image spatial resolution and anatomical complexity. Nevertheless, we try to obtain reasonable surfaces in this part of the myocardium as well, in order to preserve the full ventricle volumes. We exclude papillary muscles and trabeculae from the segmentation of endocardia. The segmentation of each surface has its own specificity.

The ellipsoidal shape of the LV endocardium facilitates the segmentation. The most difficult task is to exclude the papillary muscles and the trabeculae (see Figure 4.9) because of inter-subject variability. The complex shape of the RV endocardium and the thin RV wall – which is often not clearly visible in MR images obtained by the bSSFP (trueFISP) sequence due to susceptibility artifacts[10] – make the RV segmentation rather difficult. The

[10]The magnetic field inhomogeneities are caused by epicardial fat. The thin RV wall is hidden in the

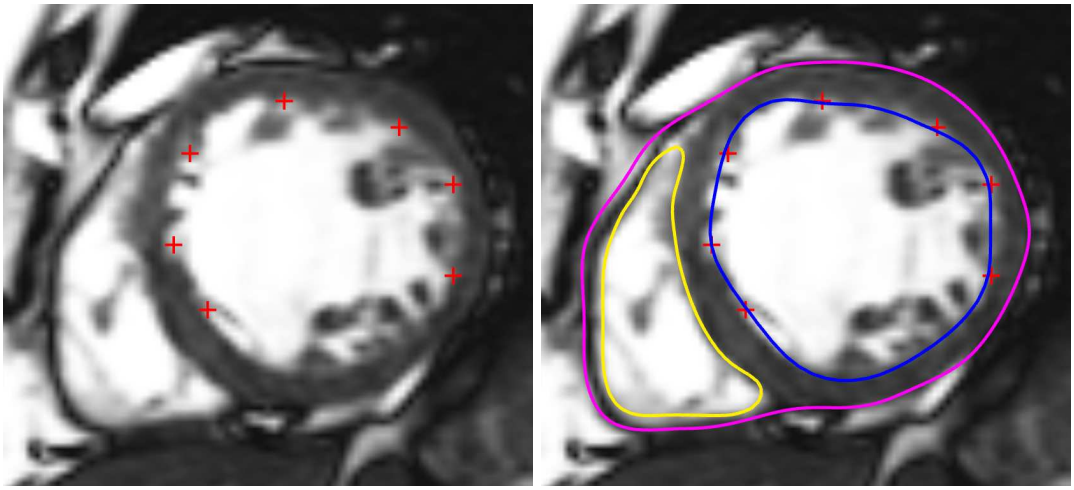

Figure 4.9: Surface segmentation using CardioViz3D software. We try to exclude the papillary muscles and the trabeculae in the LV (blue contour) and RV (yellow contour). Note also a difficult segmentation of the RV wall (partially invisible due to limited spatial resolution and susceptibility artifacts), and a complicated segmentation of the inferior wall epicardium due to close connection with diaphragm and liver.

epicardium of the inferior wall is in a direct contact with the diaphragm and hepatic tissue. In some cases, the epicardial contour is undistinguishable in a single time frame image. If this occurs we have to carefully watch the whole Cine loop, to reconstruct the epicardial surface adequately. Some difficulties in segmenting the RV and the epicardium can also be seen in Figure 4.9.

Mesh creation

The surfaces exported from CardioViz3D usually need to be regularized in the valve regions, where the geometry is the most complex. For this task, we can use for instance the commercial software 3-Matic[11]. Then, we create computational tetrahedral meshes using the Yams and GHS3D meshing tools developed by Team-project Gamma at INRIA, see [41].

In subjects with post-infarcted scars, the regions of non-viable tissue are segmented from the late-enhancement MR images and projected into the computational meshes (see Figure 6.3). The volumic meshes of the LV are subdivided into 17 segments according to

black line of the signal void as in Figure 4.9. For an explanation of the susceptibility artifact see Section 3.9.

[11] `http://www.materialise.com/BiomedicalRnD/3-matic`

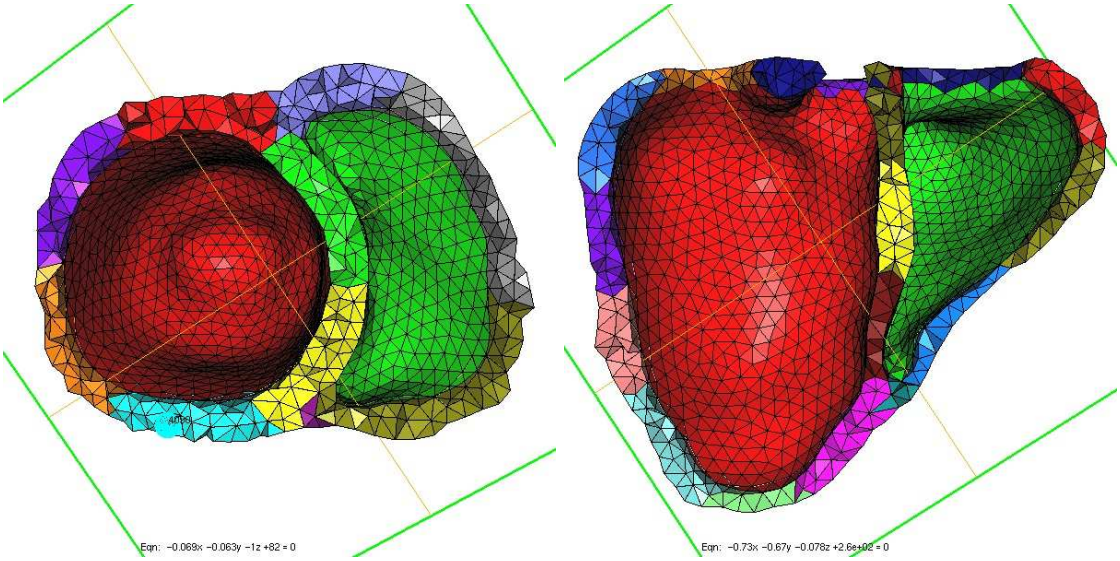

Figure 4.10: A 17-segment subdivision of the LV proposed by AHA in [21] (the *AHA segments*).

the American Heart Association (AHA) recommendations (see [21], Section 2.2 and Figure 4.10).

Myocardial fibers

The direction of the active contraction in the model is given by the myocardial fiber directions. Their prescription may be performed using an ex-vivo MR-DTI study[12] (see e.g. [113] where an analysis of a postinfarct porcine ex-vivo myocardium is perfomed, or [88] where an atlas of ex-vivo canine hearts is used to prescribe the fibers). There are some promising results in the in vivo MR-DTI measurements on the beating heart (see e.g. [115] and [108]) but these methods are still at the research stage.

In our models, we use an analytical prescription of the fibers based on anatomical knowledge (see e.g. [101]). The procedure is fully described in [78] and it was also used in [23]. The angles between the fibers and the short axis plane are prescribed on the epicardial and endocardial surfaces (both for the LV and RV). Inside the myocardium, the fibers are linearly interpolated. The directions corresponding the best with [88] are -60/60 degrees in the LV and -50/50 degrees in the RV, from the epicardium to the endocardium (see [78]). Thanks to the automatic analytical prescription, we can guarantee that we use the same approach for all subjects involved, either in validation studies (see [22]) or in clinical

[12] For an explanation of Magnetic Resonance Diffusion Tensor Imaging (MR-DTI), see Section 3.11.

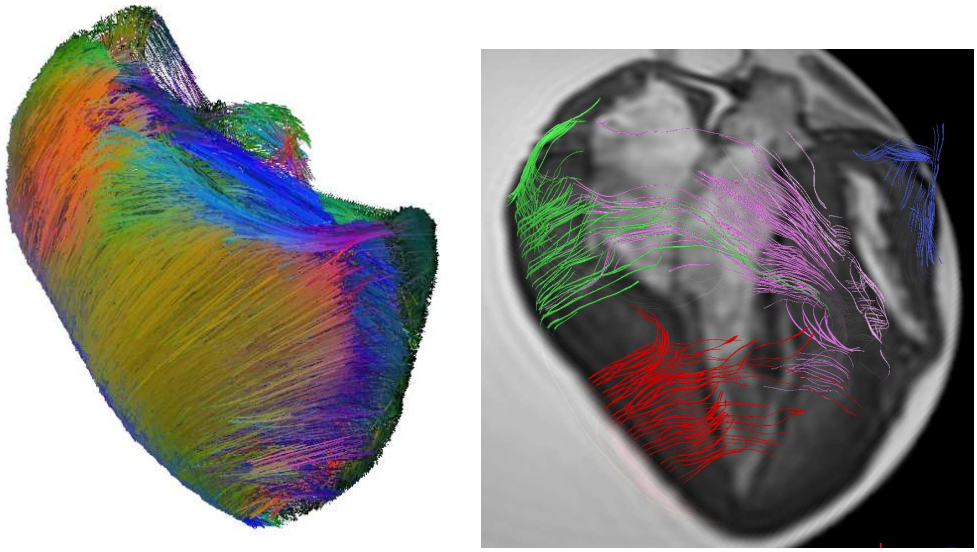

Figure 4.11: Analytical prescription of myocardial fibers in porcine geometry (left) compared with ex-vivo MR-DTI study of the same heart (right). This is the heart model that was used for the simulation presented in Figure 4.4. Visualization using MedINRIA software developed by Team-project Asclepios at INRIA.

applications (see [97]). See Figures 4.11 and 6.1 for examples of myocardial fibers created in this manner. The epicardial and endocardial fiber directions are considered as additional parameters of the model, as was used in [112].

4.4.2 Calibration of the model parameters

By adjusting the boundary conditions, the passive material properties (passive tissue stiffness) and the active properties (tissue contractility), we would like the motion pattern and the simulated pressures to correspond to the measured data. The simulated pressure values in the ventricles and in the large arteries are modulated by the contractility of the ventricles and by the Windkessel models. In a calibration of the tissue mechanical parameters, first we will be using constant values over the whole myocardium. Later on, we can take into account local variations of these values, e.g. in between the AHA segments. Indeed, this is necessary especially for pathological hearts in which the values may vary significantly throughout the myocardium. The model calibration is usually performed using a simple electrical activation, e.g. an analytical prescription of the depolarization wave starting in the apex and propagating along the long axis. The calibration consists of the following steps.

First we would like to adjust the fiber directions for both ventricles. We fix the base of the heart by applying Dirichlet boundary conditions. At this stage, we do not aim at a precise adjustment of the mechanical parameters of the passive tissue stiffness and contractility. Yet, we need to use some meaningful values of these parameters, so that the simulation can be in agreement with the measured data (e.g. by means of an approximate value of the LV ejection fraction). We test several combinations of the fiber directions. We usually start with the values -60/60 degrees in the LV and -50/50 degrees in the RV, from the epicardium to the endocardium. Then we can try to make the fibers more horizontal or vertical by 10–15 degrees. Excessively horizontal fibers make the contraction mainly circumferential without any longitudinal shortening. Even more, a longitudinal extension could appear. The other extreme would be just a longitudinal contraction with a low circumferential component. A choice of fiber directions in a compromise between these two extreme positions leads to reasonable resulting simulations.

In the second step, we adjust the visco-elastic boundary conditions applied on the heart base and apex. The concerned surfaces around the valves can be created automatically using the borders between the LV and RV endocardial and epicardial surfaces. The apex reference surface is registered from the image data. We adjust the stiffnesses of the boundary conditions applied on the base so that the longitudinal movement of the base of the heart is preserved. To that purpose we usually compare with the motion of aortic and mitral valves in the long axis projections of Cine MRI. Unlike the base of the heart, we would like the apex to be nearly fixed. This is why the boundary conditions applied on the apex are stiffer than the ones applied on the base (by a factor 10–50).

In some cases, the model may tend to bulge – especially in thin parts of the myocardium if there is a high pressure in the ventricle (see the orange contour of the model in Figure 4.12). The bulging of the real heart is to some extent prevented by a contact with the surrounding structures such as the thoracic cage, diaphragm or a stiff pericardial sac. We represent such a contact in the model by applying additional boundary conditions on parts of the epicardial surfaces designated using the image data (the green surface in Figure 4.12). Then, the stiffness of these boundary conditions – usually of the same order as in the case of the boundary condition applied on the apex – has to be adjusted (see the blue contour in Figure 4.12 with not adequately stiff boundary condition and the red contour with the stiffness high enough).

The third step consists of an adjustment of the passive tissue properties. Supposing that the passive tissue stiffness is uniform throughout each ventricle and assuming we have accurately measured atrial pressure and ventricle volume changes, we can calibrate the passive tissue stiffness using the part of the cardiac cycle corresponding to the atrial contraction. The atrial pressures can be replaced by measured flows through the atrioventricular valves.

Next, using information about the ejection fraction we can adjust the tissue contractility. For this task, we fix the arterial pressure to the measured end-systolic value. In non-pathological hearts, we can obtain an adequate local motion pattern just by using a uniform contractility value. In pathological hearts, we often need to modify the contrac-

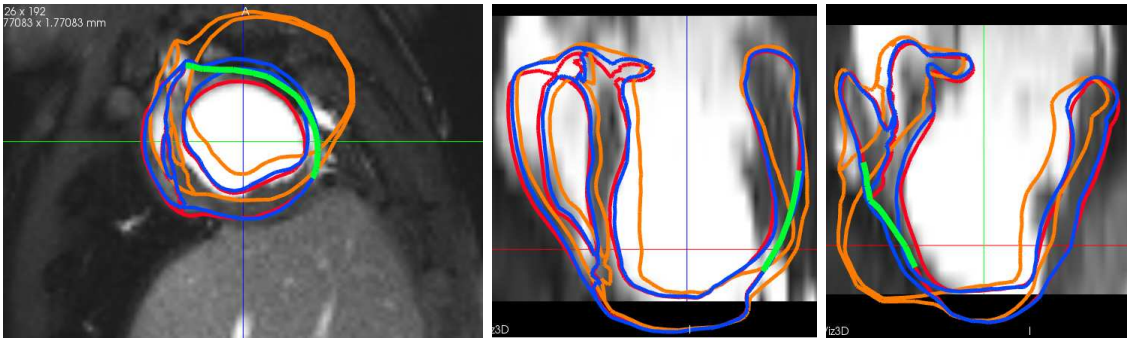

Figure 4.12: Visco-elastic boundary conditions (BCs) applied on the part of epicardium in contact with the thoracic cage (the green surface). The myocardium of this particular subject is very thin at this location due to post-infarction LV apical aneurysm formation. An extreme wall bulging occurs if no BC is applied (the orange contour). The blue color represents the model with unsufficiently stiff BC and the red color represents properly calibrated BC.

tility values locally. A manual approach of the contractility adjustment is used in Chapter 7, while an automatic approach by means of data assimilation techniques is applied in Chapter 8.

The adjustment of the Windkessel models is the last calibration step. The Windkessel models given by (4.11) consist of two components: The proximal part representing the beginning of the large arteries (aorta and pulmonary artery) is characterized by a resistance R_p and a capacitance C_p. The distal part has a resistance R_d and a capacitance C_d, see Figure 4.2. The values of resistance and capacitance in the distal part are larger than in the proximal part: $R_d > R_p$, $C_d > C_p$. The adjustment of the parameters of the Windkessel models follows the scheme:

1. Adjusting of R_d according to the systolic increase of the distal pressure P_d (given measured data).

2. Adjusting of C_d so that the arterial pressure can be periodic between the cardiac cycles (time constant $\tau_d = R_d C_d \sim 1$ s).

3. Adjusting of R_p according to the systolic increase of the arterial pressure P_a and of the ventricle pressure P_V (given measured data).

4. Adjusting of C_p so that the time constant or the proximal part of the Windkessel model would be $\tau_p = R_p C_p \sim 1$ ms.

A high increase of the resistance in the Windkessel models would prevent the ventricles from ejecting an appropriate volume. For this reason, we perform the fine adjustment of

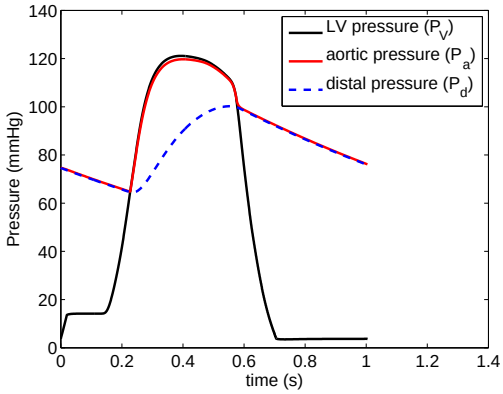

Figure 4.13: Example of simulated pressure curves for the left ventricle using a well calibrated Windkessel model (4.11).

the contractility values and of the Windkessel models simultaneously. Finally we obtain both accurate ejection volumes and correct pressure characteristics. An example of the simulated pressures with a well calibrated Windkessel model is shown in Figure 4.13.

Difficulties

- The visco-elastic boundary conditions (4.13) representing the contact of the myocardium with the surrounding structures prevent the wall from an adequate systolic thickening. The sliding boundary conditions given by (4.14) have better properties in this respect but their adjustment is more difficult. We need to designate complementary epicardial and pericardial surfaces which should be smooth without large irregularities, so that they do not prevent the surfaces from sliding freely on each other.
- The calibration of the passive properties is a very difficult part for the following reasons:
  - In a fast heart action, the atrial contraction cannot be completely separated from the other parts of ventricle filling. Therefore, it is not possible to accurately assess the pressure and volume increases that correspond to the atrial contraction.
  - In practice, it is difficult to measure atrial pressures since the absolute values and also the variations during a cardiac cycle are very low. In fact, a direct measurement of the left atrial (LA) pressure during the catheterization is difficult.[13] We

[13]Typically, we would have to enter the left atrium from the right atrium by crossing the atrial septum.

usually replace the LA pressure by measuring the pulmonary capillary wedged pressure (PCWP, see chapter 19 in [70]), which more likely mirrors the mean LA pressure over the cardiac cycle and can give information about the global LA pressure rather than the accurate pressure variations. This is why we cannot easily apply the adjustment procedure of the tissue properties according to the atrial pressure and ventricle volume changes during the atrial contraction.

  - Although we may substitute measured atrial pressures by measured AV flows, we would still need an absolute value of the initial pressure. Moreover, the Doppler measurement provides velocities and not flows and the accuracy of Doppler echocardiography and of phase contrast MRI[14] measurements is a difficult issue.
  - The LV wall thickness may vary significantly in between the LV regions, especially in pathological hearts. The passive properties may vary from less stiff values in a normal tissue to very stiff in thin remodeled parts of the myocardium (due to an increased tissue fibrosis).

- Some missing data (e.g. the measured aortic pressure) especially in patient-specific models make the adjustment of the Windkessel models more difficult.

[14] For an explanation of phase contrast MRI see Section 3.10.2.

Part II

Applied modeling part

Chapter 5

Myocardial fiber contraction

5.1 Introduction

A 1D implementation of the cardiac model described in Chapter 4 will be used for the model validation using experimental data coming from the contraction of individual muscle fibers. The aim of this chapter is to show that the 1D model is able to represent the myocardial fiber contraction for several preload and afterload values according to the experiment. Thanks to the experimental data, we will be able to study in detail some aspects of the model, as for example material laws, some model parameters, or the implementation of the Frank–Starling mechanism.

5.1.1 Basic physiological considerations of the muscle contraction

We refer to Section 2.3.2 for the physiological basis of muscle contraction. The heterotropic regulation (the Frank–Starling mechanism) was discussed in Section 2.3.5. Here we sum up some basic physiological facts.

Muscle contraction is based on an interaction of thick and thin filaments in a sarcomere – the functional unit of the muscle cell (see Figure 2.5). The thin filaments consist of actin fibers and regulatory proteins such as tropomyosin and troponin. The main component of the thick filaments is a myosin protein.

The *preload* is defined as the tension in the fiber before contraction occurs. In a typical physiological experiment (as depicted in Figure 5.1(a)), the preload is given by the load that is attached to the fiber before the fiber is activated. Since the preload causes a passive extension of the fiber, it is often related to the degree of passive extension.

By *afterload* we mean the tension generated by the fiber during contraction. In the physiological experiment, it is given by the weight of the load which is fixed to the fiber and that the fiber must overcome. If we apply such an afterload value that the fiber is not able to shorten (or raise the load) despite the active stress, we talk about *isometric*

contraction. By fixing the generated stress during the fiber contraction we obtain *isotonic contraction*.

An increased preload causes an increased force of the contraction according to the *Frank–Starling mechanism*. One possible explanation of this phenomenon is due to a better overlap between the actin and myosin molecules when the fiber is stretched. This leads to a higher number of actin–myosin cross-bridge formation and to the subsequent increase of the active stress in the fiber. If the applied preload exceeds the maximum in the Frank–Starling curve (the point D in Figure 2.9, left), the contraction force will drop. It is a reversible effect in the case of skeletal fiber – by decreasing the preload we would get again onto the increasing part of the Frank–Starling curve. However, for the cardiac fiber the effect is irreversible. Getting to the decreasing part of the curve would damage the cardiac fiber and it would not show the usual fiber contractile properties anymore, even after releasing the preload.

5.2 Methods

5.2.1 Experimental data

In the experiment settings, the papillary muscle from a laboratory rat with acromegaly was used as a cardiac fiber[1]. The animal was of an excessive growth but the heart was almost of a normal size. The initial length of the papillary muscle was approximately 4–4.5 mm and the cross-section area approximately 1.2 mm^2. The fiber was stretched passively by applying a preload. Then, the muscle was stimulated electrically to induce contraction against an afterload, see Figure 5.1(a). In the isotonic case, the expected shortening was of an order of 20–25% with respect to the configuration of the extended fiber.

The following two preload values were used: a high value – corresponding to the preload supposedly giving the optimal properties with respect to the Frank–Starling mechanism – and a lower value. The initial passive extension of the fiber after applying the preload was not measured. The expected value for the high preload was of the order of 20%–30%.

During the experiment, the displacement of the lower end of the muscle and the force created by the fiber were measured simultaneously with the sampling rate of 0.5 ms. For an easy comparison between the experiments and the corresponding simulations, the data were postprocessed, so that we could use the following indicators independent of the fiber geometry:

- The fiber extension defined as the measured displacement divided by the length of the unloaded fiber, which is taken as a reference configuration. By fiber shortening we mean the negative extension.

[1]Experimental data were provided by Prof. Yves Lecarpentier, Department of Physiology, University Paris-Sud XI, Hospital Bicêtre.

- The stress indicator defined as the measured force divided by the cross-section area of the unloaded fiber.
- The strain rate as a difference of the subsequent extensions: $(extension_i - extension_{i-1})/time\ step$. We used basic filtering techniques to decrease noise in the strain rate data.

Both the experimental data and the simulated results will be rescaled accordingly to these indicators. The loads applied on the fiber (the preload and the afterload) will also be transformed in the stress formulation by dividing the force by the cross-section area. See Figure 5.1 for the measured experimental data.

5.2.2 Biomechanical model

The myocardial fiber is modeled as a viscoelastic material with an active component representing the contraction as described in Chapter 4. Here, we will recall the main model ingredients that will be used in the 1D simulation setup.

The activation of the contraction is given by the electrical activation function u representing the cytosolic TroponinC–Ca^{2+} concentration:

$$u = k_{ATP}\mathbf{1}_{Ca^{2+}\geq C} - k_{SR}\mathbf{1}_{Ca^{2+}<C}. \tag{5.1}$$

The electrical activation function u is positive during contraction and non-positive during relaxation. The maximum and minimum values of u are given by the parameters k_{ATP} and k_{SR} respectively. These parameters represent the contraction and relaxation rates.

The active part of the model is governed by the constitutive equations in the following form (Bestel–Clément–Sorine model, [12]):

$$\begin{cases} \dot{k}_c = -(|u| + \alpha\dot{e}_c)k_c + k_0 u_+, \\ \dot{\tau}_c = -(|u| + \alpha\dot{e}_c)\tau_c + |\dot{e}_c|k_c + \sigma_0|u|_+, \\ \sigma_c = d(e_c)(\tau_c + k_c\xi_0) + \mu_c\dot{e}_c, \end{cases} \tag{5.2}$$

where τ_c represents the active stress that can be developed by the tissue and k_c the active tissue stiffness. If the Frank–Starling mechanism is taken into account, the final active stress σ_c will also depend on the actual strain e_c of the sarcomere by means of the function d. A typical example of the function d is depicted in Figure 4.6. The parameter μ_c represents a viscosity in the active element.

By analyzing equations (5.1) and (5.2), we can see that during the fiber activation the active fiber stress rises to the limit value given by σ_0 with the time constant $1/k_{ATP}$. The time constant for the relaxation is given by $1/k_{SR}$. By varying the parameter σ_0 we can modulate the inotropic state of the fiber (an increase or decrease of the fiber contractility) and by varying k_{ATP} we can vary the contraction rate. The parameter k_{SR} controls the lusitropic state of the myocardial fiber (the relaxation rate).

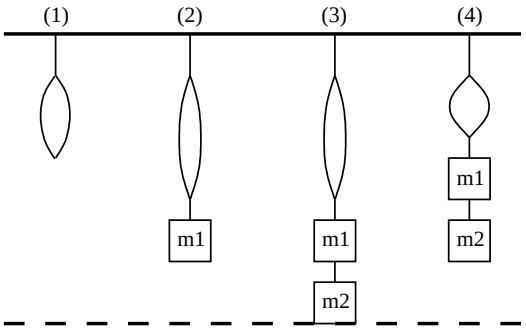

(a) Experiment settings. Reference configuration (1), passive extension by preload m1 (2), activation of contraction against afterload m1+m2 (3), contracted fiber (4).

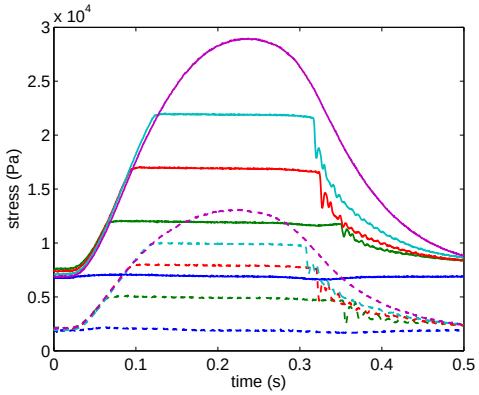

(b) Stress vs. time plots. Maxima of the stresses characterize afterload values. The purple color represents the isometric contraction and the dark blue color the contraction against the preload alone.

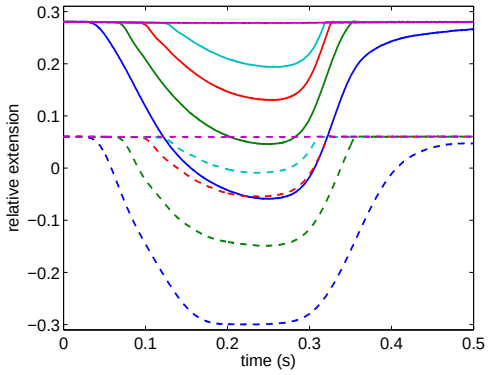

(c) Relative extension vs. time plots.

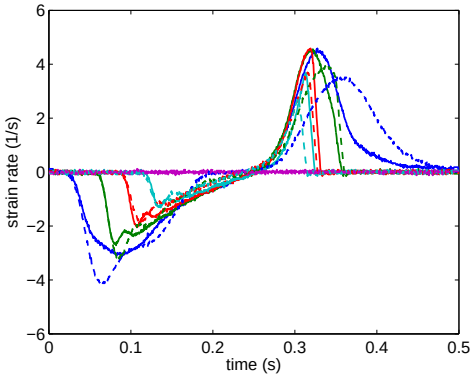

(d) Strain rate vs. time plots.

Figure 5.1: Example of the measured and scaled data. Solid lines represent experiments with the high preload value (optimal fiber extension with respect to the Frank–Starling mechanism), dashed lines represent experiments where the lower preload was applied.

The myocardial tissue is modeled as a material of Hill–Maxwell type with two branches, depicted in Figure 4.1: the active series branch and the passive parallel branch. The active part is modeled by the Bestel–Clément–Sorine component and the parallel part is modeled as a viscoelastic material. The type of hyperelastic potential used in the simulation will be discussed in Section 5.2.3. The viscous part uses a viscoelastic pseudopotential

$$W^{\eta} = \frac{\eta}{2} tr(\underline{\underline{\dot{e}}}^2), \tag{5.3}$$

where the parameter η represents a viscosity in the passive branch.

5.2.3 Various parameters in the model

In the following section, we will study some model parameters. We will be using the high preload value and the corresponding afterload values – the solid lines in the plots in Figure 5.1. In these preliminary tests, the Frank–Starling mechanism will not influence the simulations – the function d in (5.2) will be set to the constant value $d = 1$.

Viscosity

There are two viscosity elements included in the model: one in the passive branch (η) and one in the active branch (μ_c). The active viscosity is larger than the passive one. A high viscosity in the model causes a phenomenon of delayed relaxation – especially for low afterload values. Since we do not observe it in the experimental data (see Figure 5.1(b)), we need to decrease the viscosity.

Figure 5.2 shows a few tests when modifying the viscosity values. By decreasing the active viscosity, we obtain stress curves more similar to the experimental data. The passive viscosity is already low and even when decreasing it the simulation does not change (see Figure 5.2(e)). Figures 5.2(c) and 5.2(f) show nearly the same behavior and the stress curves are comparable with the shape of the experimental data. In the following parts, we will be using the viscosity values according to Figure 5.2(c).

Time constant of the Bestel–Clément–Sorine model

The whole contraction–relaxation cycle in the experiment lasts less than 400 ms and we assume that in the period ∼200 ms the fiber reaches its asymptotic shortening value. Indeed, in the experimental data in Figure 5.1(c) the shortening does not seem to be limited by the duration of the activation. By decreasing the viscosity in the model we already shortened to some extent the period of activation necessary to reach this asymptotic value. However, we will have to control this period directly by the time constant of the Bestel–Clément–Sorine active component, which is given by $1/k_{ATP}$.

Figure 5.3 shows simulations with three values of k_{ATP}, either with a very long activation (action potential duration APD = 1000 ms) – in order to obtain the value of

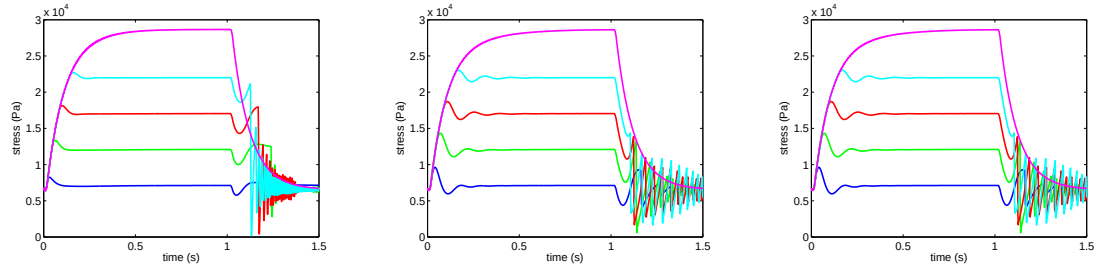

(a) Original values $\eta^0 = 68$ Pa.s, $\mu_c^0 = 2700$ Pa.s

(b) $\eta = \eta^0$, $\mu_c = \mu_c^0/5$

(c) $\eta = \eta^0$, $\mu_c = \mu_c^0/10$

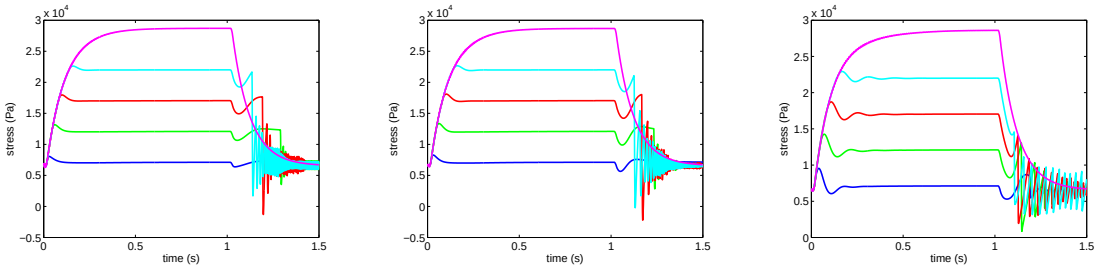

(d) $\eta = \eta^0 * 10$, $\mu_c = \mu_c^0$

(e) $\eta = \eta^0/100$, $\mu_c = \mu_c^0$

(f) $\eta = \eta^0 * 5$, $\mu_c = \mu_c^0/10$

Figure 5.2: Simulated stresses using various viscosity values. Note that if the fiber contracts against a low load and the viscosity is set to a high value, the relaxation is delayed. This effect is not present in the experimental data in Figure 5.1(c). Note the 'overshoot' and 'undershoot' in the curves shortly after the onset of contraction and relaxation, caused by the inertia effects, and the oscillations during the relaxation due to the 1D model implementation of contact conditions. We mention these issues in the discussion.

asymptotic shortening – and with APD corresponding to the experiment (APD = 200 ms). We can see that when using the value $k_{ATP} = 40$, the timing of the contraction–relaxation cycle is close to the experiment.

Material laws

For the parallel passive branch of the model we tested the following hyperelastic potentials.

- A polynomial potential (the Mooney-Rivlin material):

$$W^e = \kappa_1(J_1 - 3) + \kappa_2(J_2 - 3), \tag{5.4}$$

- An exponential material:

$$W^e = \kappa_1(J_1 - 3) + \kappa_2(J_2 - 3) + c_0 e^{c_1(J_1-3)^2}, \tag{5.5}$$

with κ_1, κ_2, c_0, c_1 being the material parameters and J_1, J_2, J_3 being the reduced invariants of the Cauchy–Green strain tensor $\underline{\underline{C}}$. For an implementation of the material laws in the 1D model see Appendix 5.6.

In Figure 5.4, we plotted several stress–strain laws using either the Mooney–Rivlin material (5.4) or the exponential material (5.5), with material parameters listed in Table 5.1. All of them were calibrated for an initial extension of 28% after application of the high preload. As we can see in the experimental data, when using the high preload the fiber is extended 28% above the initial (reference) length and during the contraction against the lowest afterload the shortening level is around 8% – namely a difference of 36% (see solid lines in Figure 5.1(c)). For this reason, we need our stress–strain law to be rather soft in the contraction part.

The exponential material is more flexible and we can adjust it, so that it is flatter in the contraction part (material denoted by 'epx1c' in Figure 5.4). It means that for low stress variations (afterload values), we can obtain larger variations of the shortening. However, when the shortening gets above 25% of the initial length, the stress increases very steeply – especially in the exponential material – no matter what material parameters are used. Moreover, the exponential material is quite symmetric in the contraction and the passive extension parts. If we adjust the material law to be flat in the contraction part (in order to reproduce the experiment), the passive part will become flat as well. In fact, we would need a material law in which the contractile and the passive extension parts could be adjusted more independently. For these reasons, we finally used the simpler Mooney–Rivlin material (5.4), which seems to be a good compromise both for the contraction and for the passive extension parts.

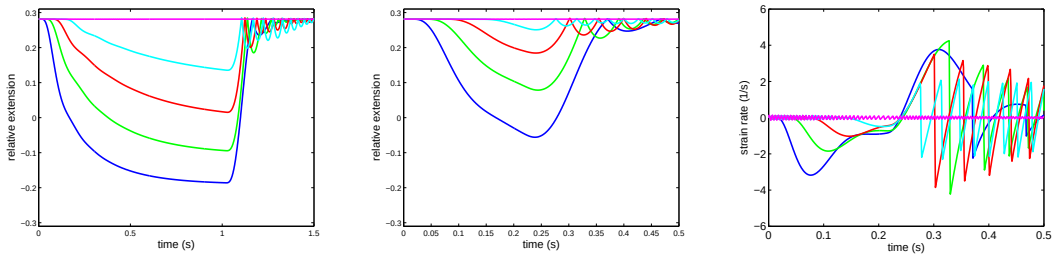

(a) $k_{ATP} = 10$

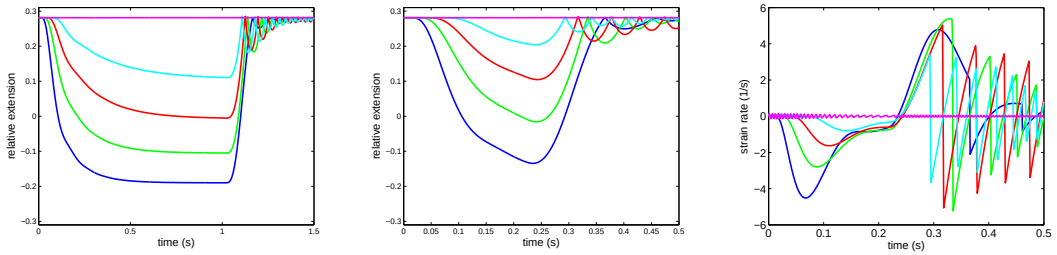

(b) $k_{ATP} = 20$

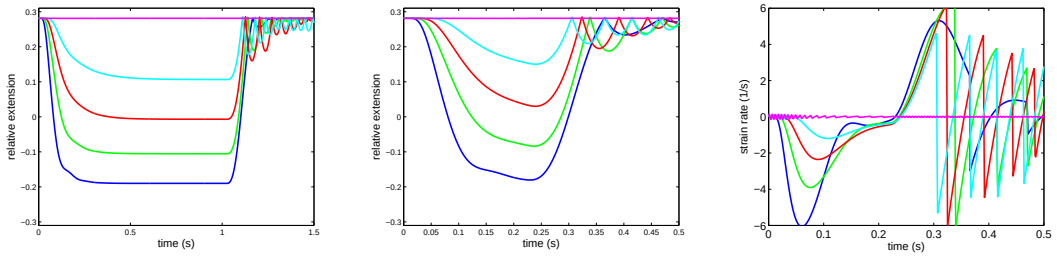

(c) $k_{ATP} = 40$

Figure 5.3: Relative extension for various values of k_{ATP}. Left column represents the simulations with long activation (APD = 1000 ms), in which the asymptotic shortening level can be estimated. Timing in the middle column is according to the experiment (APD = 200 ms). Note that maximum contraction strain rate increases with increasing k_{ATP} (right column).

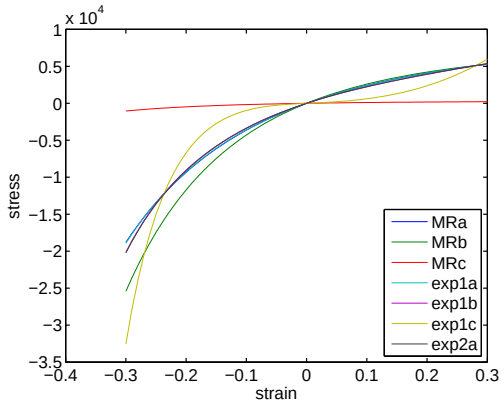

Figure 5.4: Examples of stress–strain curves for several material laws. Note, that the exponential material has a softer response for small strains. The parameters of the materials are in Table 5.1.

label	κ_1 (Pa)	κ_2 (Pa)	c_0 (Pa)	c_1
MRa	5000*0.96	80*0.96	0	0
MRb	5000*0.55	5000*0.55	0	0
MRc	80*1.22	5000*1.22	0	0
exp1a	5000*0.95	80*0.95	10	10
exp1b	5000*0.875	80*0.875	100	10
exp1c	5000*0.13	80*0.13	1000	10
exp2a	5000*0.88	80*0.88	10	100

Table 5.1: Parameters of materials plotted in Figure 5.4. 'MR' stands for the material of the Mooney–Rivlin type, 'exp' for the exponential material.

5.2.4 Calibration for the high preload value

For the model calibration, we used the experimental data of the isometric and isotonic contraction when the high preload was applied with the following constraints:

1. The passive elongation of the fiber is of an order 25–30%.
2. When applying the maximum afterload value used in the experiment together with the high preload, we will obtain an isometric contraction.
3. The duration of the contraction corresponds to the experiment and the fiber will reach the asymptotic shortening during this period. The maximum simulated strain rate in the isotonic contraction with the lowest afterload corresponds to the measured value.
4. When applying the minimum afterload value used in the experiment together with the high preload, we will obtain the isotonic contraction with the level of shortening corresponding to the data.

The condition 1. gives us information about the passive tissue stiffness. Thanks to the assumption 2. we are able to calibrate the active tissue contractility. The time constant of the simulated contraction is governed by the condition 3., which was discussed in Section 5.2.3. To obtain the level of shortening in the isotonic case according to the experiment – condition 4. – we will have to use the right material law.

5.2.5 Adjustment of the Frank–Starling mechanism

In order to adjust the Frank–Starling mechanism by means of the dependence of the maximum generated stress on the length of the fiber, we will be using the experimental data from the isometric contractions both with the high and the low preload. The function $d(e_c)$ in equation (5.2) needs to be adjusted so that the simulations with the adequate combinations of preload and afterload values lead to the isometric contractions.

The high preload gives maximum properties with respect to the Frank–Starling mechanism. Therefore, $d(e_c) = 1$ for $e_c = 0.28$ (the extension using the high preload). When using the lower preload, the fiber extension is around 7% and the maximum generated stress corresponds approximately to half of the stress values generated using the high preload. Therefore, $d(e_c) \sim 0.5$ for $e_c = 0.07$.

In fact, the function d of a shape in agreement with the curve in Figure 2.9 (left) and with the quantitative properties listed above would be very steep for negative values of e_c, hence the fiber would hardly shorten below the initial length. We decided not to modify the implementation of the Frank–Starling mechanism at the moment and rather make the function d constant when the fiber length is below the value obtained with the low preload passive extension, as is illustrated in Figure 5.5.

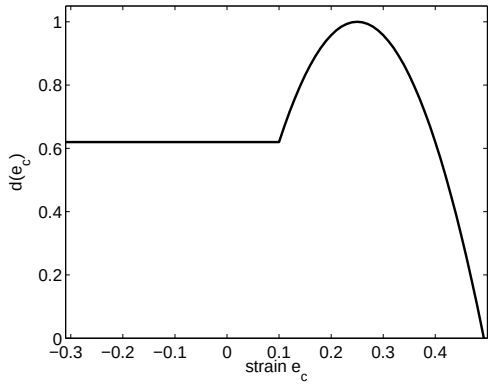

Figure 5.5: Frank–Starling curve applied in the model.

5.3 Results

We performed the model calibration according to Sections 5.2.4 and 5.2.5. The model parameters were adjusted so that we obtain isometric contractions for both the high and the low preload values and the corresponding afterloads, and the isotonic contraction with a given shortening level for the high preload.

To simulate all the remaining curves to be compared with the measured data, we fixed the model parameters and input the combinations of the preload / afterload values as used in the experiment. The measured data and the simulations are plotted in Figure 5.6.

As we can see, the simulated extension curves are directly comparable with the experimental values for the high preload. We managed to adjust the Frank–Starling mechanism so that the shortening with the low preload is also quite accurate, except for the case in which the fiber is contracting against the preload itself.

5.4 Discussion

During the experiment, the level of initial fiber extension was not measured. It is probably due to the fact that the error in measuring the non-extended fiber would be very high. In the simulation setup, we used the unstretched fiber as a reference configuration and we assumed that the fiber extension was 28% for the high preload value. In a more detailed study, we should explore the possibilities of measurement of this value.

We adjusted the material viscosity so that the fiber would not stay in the contracted state after the end of activation. This phenomenon is pronounced for low values of afterloads, if the viscosity is high. We set up the parameter k_{ATP} so that the timing of the simulated contraction–relaxation cycle corresponds to the experiment. By this approach,

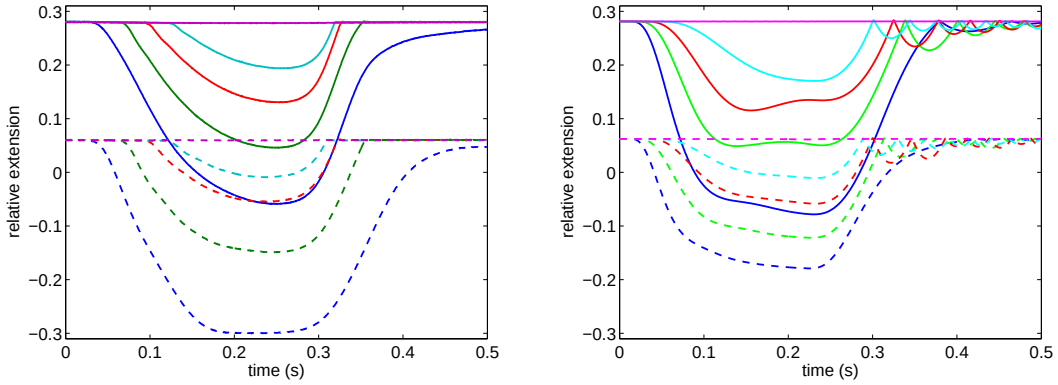

(a) Relative extension vs. time plots.

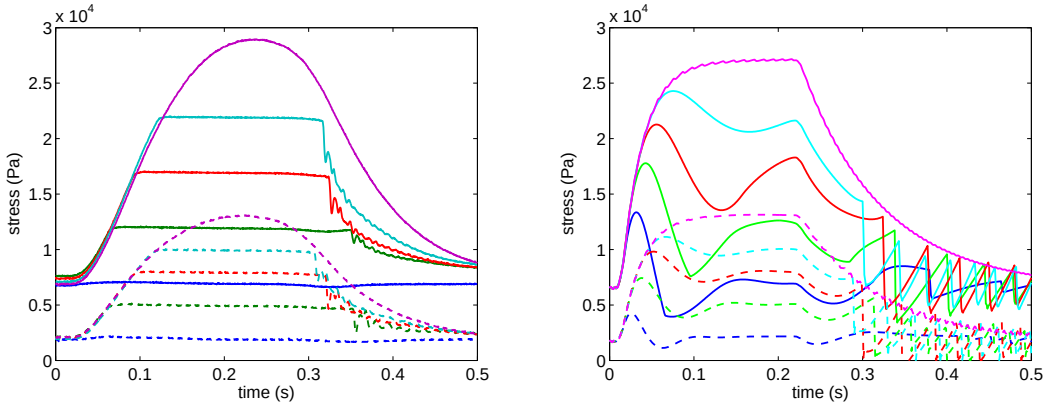

(b) Stress vs. time plots. Maxima of the stresses characterize afterload values.

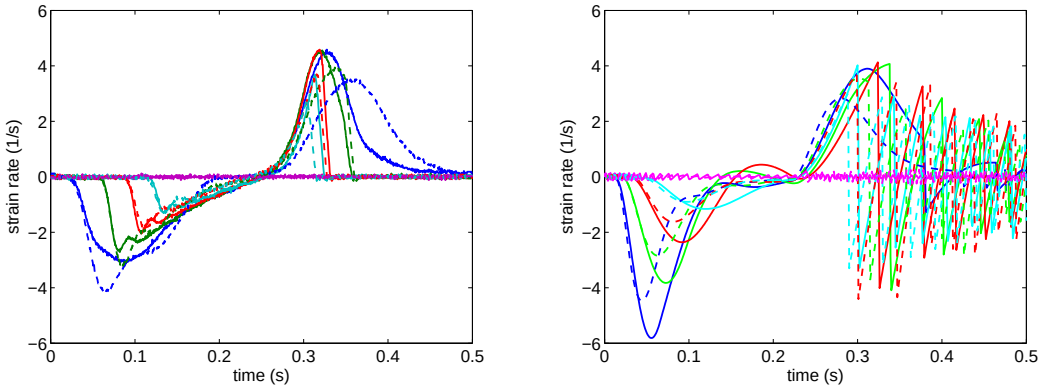

(c) Strain rate vs. time plots.

Figure 5.6: Experimental data (left column) and simulations (right column). The contractions with the high preload are plotted with solid lines, the contractions with the low preload with dashed lines.

we obtained the correct duration of the activation. The maximum simulated strain rate was higher in the simulation than in the experiment. To treat this issue, we would need to perform further – more detailed – analyses taking into account both the viscous elements and the time constant of the active part.

The exponential law is more suitable for adjustments of the stress–strain law in the contraction part. Unfortunately, we would need the relation to be quite flat in the contraction part and steeper in the relaxation part. This is not possible using the standard exponential law, since the behavior is quite symmetric. We would need a law in which the two parts can be adjusted separately.

The contraction with the low preload is prevented by the Frank–Starling mechanism. Our implementation of the Frank–Starling mechanism is based on the modification of the active stress according to the actual strain. We managed to obtain the isometric contraction for adequate afterload values for both preloads. However, Figure 5.5 shows that the Frank–Starling curve used in the model – although it gives reasonable levels of shortening compared with our experimental data – does not correspond to the typical Frank–Starling curve for low strain levels (see Figure 2.9). We may consider the mechanism not to be dependent only on the actual strain level but also on the stress in the fiber, as was shown in [20].

The simulated shortening levels corresponded to the experimental data except for the contraction against the low preload. When the low preload was applied and the fiber was contracting against the preload alone, the measured shortening was $\sim$30% while the simulated only $\sim$20%. To improve this aspect, we should investigate some other material laws and also revise the implementation of the Frank–Starling property. We should also consider that there could have been a measurement error for this particular combination of the loads and try to reproduce some other data sets.

The shape of the simulated stress curves is deteriorated by the mass effect (the 'overshoot' in the beginning of the contraction and 'undershoot' in the beginning of the relaxation. We think that it is possible that this effect is present also in the experiment but filtered in the measured stress curves. Secondly, oscillations in simulations during relaxation are caused by the 1D model implementation (contact problem between the fiber and the surface on which the fiber tip with the load lands). We can consider some damping property in this contact boundary condition in order to prevent these oscillations.

5.5 Conclusions and perspectives

In this Chapter, we showed that the model is able to represent the physiologic contraction of the myocardial fiber – and we can obtain shortening levels corresponding to the simulations. We observed some non-physiological phenomena related to the parameters used in the model and we were able to avoid them to some extent by adjusting parameter values directly related to these effects. We can further explore the passive properties of the model

in order to obtain results even closer to the simulations. For the Frank–Starling mechanism implementations, we would like to use data sets with more preload values in order to obtain more reference points of the curve given by the function d.

The 1D model is a fast way to test some model situations, new implementations or effect of some regulations on the local level. In the future, we may keep using the 1D setup for validating certain properties of the model which would be difficult to observe in the full 3D case.

5.6 Appendix: Implementation of exponential law in 1D model

The right Cauchy–Green tensor $\underline{\underline{C}} = \underline{\underline{F}}^T \underline{\underline{F}}$, where deformation gradient is given by $\underline{\underline{F}} = \underline{\underline{1}} + \underline{\underline{\nabla}}_{\xi} \underline{y}$ (gradient with respect to the reference configuration) is given by:

$$\underline{\underline{C}} = \begin{pmatrix} C & 0 & 0 \\ 0 & C^{-1/2} & 0 \\ 0 & 0 & C^{-1/2} \end{pmatrix}.$$

.

The strain tensor $\underline{\underline{C}}$ represents deformation in the longitudinal direction with incompressibility assumption taken into account ($\det \underline{\underline{C}} = 1$).

The invariants of the tensor $\underline{\underline{C}}$ are:

$$\begin{aligned} I_1 &= \mathrm{tr}\underline{\underline{C}} = C + 2C^{-1/2}, \\ I_2 &= \frac{1}{2}((\mathrm{tr}\underline{\underline{C}})^2 - \mathrm{tr}\underline{\underline{C}}^2) = 2C^{1/2} + C^{-1}, \\ I_3 &= \det \underline{\underline{C}} = 1. \end{aligned} \tag{5.6}$$

We introduce reduced invariants defined by the following formulas: $J_1 = I_1 I_3^{-1/3}, J_2 = I_2 I_3^{-2/3}, J_3 = I_3^{1/2}$. For the derivative of the reduced invariant J_1 we have:

$$\frac{\partial J_1}{\partial \underline{\underline{C}}} = \frac{\partial I_1 I_3^{-1/3}}{\partial \underline{\underline{C}}} = \frac{\partial I_1}{\partial \underline{\underline{C}}} - \frac{1}{3} I_3^{-4/3} I_1 \frac{\partial I_3}{\partial \underline{\underline{C}}} = 1 - \frac{1}{3}(C + 2C^{-1/2}) C_{ij}^{-1},$$

since $\frac{\partial I_1}{\partial C_{ij}} = \delta_{ij}$, $I_3 = 1$, $\frac{\partial I_3}{\partial C_{ij}} = I_3 C_{ij}^{-1} = C_{ij}^{-1}$, where $\underline{\underline{C}}^{-1}$ stands for inverse matrix of $(C)_{ij}$.

Then the longitudinal component of the derivative is

$$\left(\frac{\partial J_1}{\partial \underline{\underline{C}}} \right)_{xx} = \frac{2}{3}(1 - C^{-3/2}),$$

and the transverse component

$$\left(\frac{\partial J_1}{\partial \underline{\underline{C}}}\right)_{rr} = \frac{1}{3}(1 - C^{3/2}).$$

The derivative of the invariant J_2 is

$$\frac{\partial J_2}{\partial \underline{\underline{C}}} = \frac{\partial I_2 I_3^{-2/3}}{\partial \underline{\underline{C}}} = \frac{\partial I_2}{\partial \underline{\underline{C}}} - \frac{2}{3} I_3^{-5/3} I_2 \frac{\partial I_3}{\partial \underline{\underline{C}}}.$$

Since $\frac{\partial I_2}{\partial C_{ij}} = \delta_{ij} I_1 - C_{ij}$, we have:

$$\left(\frac{\partial J_2}{\partial \underline{\underline{C}}}\right)_{xx} = (C + 2C^{-1/2}) - C - \frac{2}{3}(2C^{1/2} + C^{-1})C^{-1} = \frac{2}{3}(C^{-1/2} - C^{-2}),$$

and

$$\left(\frac{\partial J_2}{\partial \underline{\underline{C}}}\right)_{rr} = (C + 2C^{-1/2}) - C^{-1/2} - \frac{2}{3}(2C^{1/2} + C^{-1})C^{1/2} = \frac{1}{3}(C^{-1/2} - C).$$

The second Piolla-Kirchhoff stress tensor is given by

$$\underline{\underline{\Sigma}} = \frac{\partial W}{\partial \underline{\underline{E}}} - p\underline{\underline{C}}^{-1}.$$

W is a hyperelastic potential characterizing the type of material against the Green–Lagrange strain tensor $\underline{\underline{E}} = \frac{1}{2}(\underline{\underline{C}} - 1)$. The second term is associated with the incompressibility condition. We assume that the radial stress is zero since there is no loading applied around the fiber, namely we have $\Sigma_{rr} = 0$, and therefore $p = C^{-1/2}\left(\frac{\partial W}{\partial \underline{\underline{E}}}\right)_{rr}$. The formulation for the 2nd Piola-Kirchhoff stress tensor in the longitudinal direction is then

$$\left(\underline{\underline{\Sigma}}\right)_{xx} = \left(\frac{\partial W}{\partial \underline{\underline{E}}}\right)_{xx} - C^{-3/2}\left(\frac{\partial W}{\partial \underline{\underline{E}}}\right)_{rr}. \tag{5.7}$$

5.6.1 Mooney–Rivlin material

The hyperelastic potential is given by the following formula:

$$W = \kappa_1(J_1 - 3) + \kappa_2(J_2 - 3), \tag{5.8}$$

where the constants κ_1 and κ_2 characterize the material stiffness. By substituting (5.9) in (5.7), we obtain:

$$
\begin{aligned}
\left(\underline{\underline{\Sigma}}\right)_{xx} &= 2\left(\frac{\partial W}{\partial \underline{\underline{C}}}\right)_{xx} - 2C^{-3/2}\left(\frac{\partial W}{\partial \underline{\underline{C}}}\right)_{rr}. \\
&= 2\kappa_1\left(\frac{\partial J_1}{\partial \underline{\underline{C}}}\right)_{xx} + 2\kappa_2\left(\frac{\partial J_2}{\partial \underline{\underline{C}}}\right)_{xx} - 2C^{-3/2}\kappa_1\left(\frac{\partial J_1}{\partial \underline{\underline{C}}}\right)_{rr} - 2C^{-3/2}\kappa_2\left(\frac{\partial J_2}{\partial \underline{\underline{C}}}\right)_{rr} \\
&= 2\kappa_1(\frac{2}{3}(1-C^{-3/2}) - \frac{1}{3}C^{-3/2}(1-C^{3/2})) \\
&= \frac{2\kappa_1}{3}(2(1-C^{-3/2}) - C^{-3/2}(1-C^{3/2})) + \frac{2\kappa_2}{3}(2(C^{-1/2}-C^{-2})) - C^{-3/2}(C^{-1/2}-C)) \\
&= 2(1-C^{-3/2})(\kappa_1 + C^{-1/2}\kappa_2).
\end{aligned}
$$

Since $C = (1+y_x)^2$ we can write:

$$\left(\underline{\underline{\Sigma}}\right)_{xx} = 2(\kappa_1 + \kappa_2(1+y_x)^{-1})(1-(1+y_x)^{-3}\kappa_2).$$

Consequently, the derivative with respect to y_x is

$$\frac{\partial \Sigma_{xx}}{\partial y_x} = 2(\kappa_1 + \kappa_2(1+y_x)^{-1}(-3(1+y_x)^{-4})) + 2\kappa_2(-1)(1+y_x)^{-2}(1-(1+y_x)^{-3}).$$

5.6.2 Exponential law

The hyperelastic potential include the same terms as the the Mooney–Rivlin material and additionally the exponential term:

$$W = W_{MR} + W_{exp} = \kappa_1(J_1-3) + \kappa_2(J_2-3) + c_0 e^{c_1(J_1-3)^2}. \tag{5.9}$$

The 2nd Piola-Kirchhoff stress along longitudinal direction is given by (5.7) and can be split into the part corresponding to Mooney–Rivlin terms and to the part given by the exponential term ($(\Sigma_{exp})_{xx}$). In order to compute the exponential part we will need the following derivatives:

$$
\begin{aligned}
\left(\frac{\partial W_{exp}}{\partial \underline{\underline{E}}}\right)_{xx} &= 2c_0\left(\frac{\partial e^{c_1(J_1-3)^2}}{\partial \underline{\underline{C}}}\right)_{xx} \\
&= 2c_0 e^{c_1(J_1-3)^2} 2C_1(J_1-3)\left(\frac{\partial J_1}{\partial C}\right)_{xx},
\end{aligned}
$$

and

$$
\begin{aligned}
\left(\frac{\partial W_{exp}}{\partial \underline{\underline{E}}}\right)_{rr} &= 2c_0\left(\frac{\partial e^{c_1(J_1-3)^2}}{\partial \underline{\underline{C}}}\right)_{rr} \\
&= 2c_0 e^{c_1(J_1-3)^2} 2C_1(J_1-3)\left(\frac{\partial J_1}{\partial C}\right)_{rr},
\end{aligned}
$$

where $J_1 = I_1 I_3^{-1/3} = I_1 = C + 2C^{-1/2}$, since $I_3 = 1$ is an incompressibility assumption.

Finally,

$$\begin{aligned}
\Sigma_{xx} &= \Sigma_{MR} + \Sigma_{exp} = \\
&= \Sigma_{MR} + \left(\frac{\partial W_{exp}}{\partial \underline{\underline{E}}} \right)_{xx} - C^{-3/2} \left(\frac{\partial W_{exp}}{\partial \underline{\underline{E}}} \right)_{rr} \\
&= \Sigma_{MR} + 4c_0 c_1 e^{c_1 (I_1 - 3)^2} (I_1 - 3)(1 - C^{-3/2}).
\end{aligned}$$

The derivative with respect to x_y will be:

$$\frac{\partial \Sigma_{xx}}{\partial x_y} = \frac{\partial \Sigma_{xx}^{MR}}{\partial x_y} + \frac{\partial \Sigma_{xx}^{exp}}{\partial x_y}, \tag{5.10}$$

where

$$\begin{aligned}
\frac{1}{4c_0 c_1} \frac{\partial \Sigma_{xx}^{exp}}{\partial x_y} &= e^{c_1 (J_1 - 3)^2} \left(4c_1 (J_1 - 3)^2 (1 - C^{-3/2})^2 C^{1/2} + 2(1 - C^{-3/2})^2 C^{1/2} + 3(J_1 - 3) C^{-2} \right) \\
&= e^{c_1 (J_1 - 3)^2} \left(2C^{1/2} (1 - C^{3/2})^2 \left(2c_1 (J1 - 3)^2 + 1 \right) + 3C^{-2} (J1 - 3) \right).
\end{aligned}$$

Chapter 6

Validation of the model using animal experiments

This chapter is adapted from [22].

6.1 Introduction

Personalized – or patient-specific – biomechanical modeling of the heart represents a tremendous challenge for clinical applications [99]. In such endeavors, the predictive capabilities of the model – namely, its ability to adequately simulate the various phenomena of concern in a given clinical application once the relevant parameters have been calibrated – is crucial, not only to represent normal behavior, but also pathologies, since personalized modeling aims at diagnosis and prognosis assistance.

The present work pertains to the clinical assessment of a biomechanical heart model used to represent the effect of acute myocardial infarction, with animal data providing a controlled infarct condition with a follow-up over several weeks. First, we set up the personalized model using data coming from the healthy animal. We will show that the model simulations compare quite accurately with the measured data, both for the tissue motion and for the blood pressures. The second part deals with the modeling of an acute myocardial infarction using the same biomechanical model with locally modified material properties, with a detailed assessment of the simulated indicators.

6.2 Experimental data

The experimental data[1] consisted of animal data obtained with a farm pig of 25kg. The in vivo study was approved by the Institutional Animal Care and Use Committee of 'Fac-

[1] For the *Experimental protocol* proposed during the planning of the animal experiments, see Appendix 10.

ulté de Créteil', France. The animal was housed and cared according to European Union Standards. Before each data acquisition, the subject was premedicated with intramuscular Ketamin (15 mg/kg), anesthetized with Propofol (0.35 mg/kg intravenous bolus and 0.05 mg/kg/min continuous infusion), intubated and ventilated, see [42] for the details. The subject was examined and data acquired once in a baseline condition (physiological heartbeat).

Then, antero-septal myocardial infarction was induced by a 120-min occlusion of the mid-left anterior descending coronary artery, using a balloon catheter, followed by reflow. Such an occlusion led to an extended myocardial infarction, as was proven in the follow-up by the late-enhancement MR images. The animal was re-examined 10 and 38 days after the infarct creation. The corresponding stages are referred to as baseline, T0+10 and T0+38 in the sequel. The T0+10 data acquisition corresponds to the acute stage (edematous necrotic tissue with only slightly diminished wall thickness), while at T0+38 we could already expect – and indeed observed – thinning of the LV wall (caused by resorption of the necrosis and tissue remodeling).

In each of the studied stages (baseline, T0+10 and T0+38), non-invasive MR image data were acquired and pressures in the heart cavities and large vessels were measured.

The image data were acquired using a Philips Achieva 3 T MR system (200 mT/m/ms slew rate, maximal gradient strength 80 mT/m, 32-channel phased-array cardiac coil). The following types of MR data were were obtained:

- kinematics of the heart in the short and long axis views
  - Cine in retrospective ECG gating (segmented FLASH, flip angle 15 °, TR∼6 ms, TE∼3.5 ms, turbo factor 5, SENSE 1, acq. matrix 210 x 160, voxel size 1.5 x 1.7 x 8 mm, 40 time frames / cardiac cycle)
  - tagged Cine data in prospective ECG gating (segmented FLASH with SPAMM, flip angle 10 °, TR∼8 ms, TE∼4.5 ms, turbo factor 4, SENSE 1, acquisition matrix 200 x 150, voxel size 1.3 x 1.4 x 7 mm, tag spacing 7 mm, 19 time frames / cardiac cycle without echo sharing)
- visualization of the infarct by means of the late-enhancement technique (gadolinium chelate contrast agent – gadoterate dimeglumine, Dotarem, 0.2 mmol/kg, T1 weighted gradient echo, 3D acquisition, flip angle 15 °, TR∼5.0 ms, TE∼2.4 ms, TI ∼ 220 ms, turbo factor 32, SENSE 2, acquisition matrix 175 x 175 x 15, voxel size 1.5 x 1.5 x 5 mm, magnitude and phase sensitive reconstructions)
- visualization of the infarct and the tissue edema using T2-weighted images with an inversion recovery to suppress the fat (TR∼1700 ms, TE∼60 ms, TI∼180 ms, turbo factor 20, acq. matrix 200 x 160, voxel size 1.8 x 1.8 x 8 mm)
- 2D flow through the aortic and mitral valve (phase contrast imaging in retrospective

ECG gating, flip angle 10 °, TR∼6.0 ms, TE∼3.5 ms, turbo factor 2, SENSE 1, acq. matrix 160 x 160, voxel size 2 x 2 x 8 mm, 40 time frames / cardiac cycle)

The pressures were measured invasively by means of retrograde catheterization (aortic and left ventricle pressure) and by antegrade catheterization (right atrium, right ventricle, pulmonary artery and pulmonary capillary wedged pressure).

6.3 Biomechanical model

6.3.1 Model formulation

The biomechanical model used here – described in Chapter 4 and detailed in [95] – is based on physiological considerations and is consistent with essential thermomechanical requirements (energy balances in particular), preserved from the continuous dynamical equations to the discrete versions used for numerical simulations. We also refer to [23] for another example of some physiological simulations performed within the same modeling framework.

The heart tissue is modeled as an active 3D viscoelastic material. It contains a 1D active component in the direction of the myocardial fibers, modeled according to [12]. The external blood circulations are represented by Windkessel models [74].

6.3.2 Anatomical model

The cardiac anatomy was obtained by segmenting a diastolic time frame of the Cine MR images preceding the atrial contraction, a state considered as a reference (stress-free) configuration of the heart. Segmentation of the left and right heart ventricles in this particular time frame image was performed manually using the CardioViz3D software [107]. Thanks to the anesthesia of animal, the position of each slice of Cine MRI was very reproducible and we did not need to perform any spatial registration.

Then a computational mesh was built in the segmented geometry using the Yams and GHS3D meshing tools [41], see the resulting mesh in Fig. 6.1.

Fiber directions – needed in the biomechanical model as privileged directions of contraction – were prescribed in the same anatomical model based on general anatomical knowledge [101]: -60/60 degrees in LV, -50/50 degrees in RV, from epicardium to endocardium, see Fig. 6.1.

6.3.3 Electrical activation of the model

In all simulations we used a simple electrical activation pattern in which the depolarization times were prescribed analytically by a planar wave propagating from the apex to the base of the heart along the long axis, see Figure 6.2. The propagation velocity was adjusted so that the whole myocardium would be activated in a time period corresponding to the

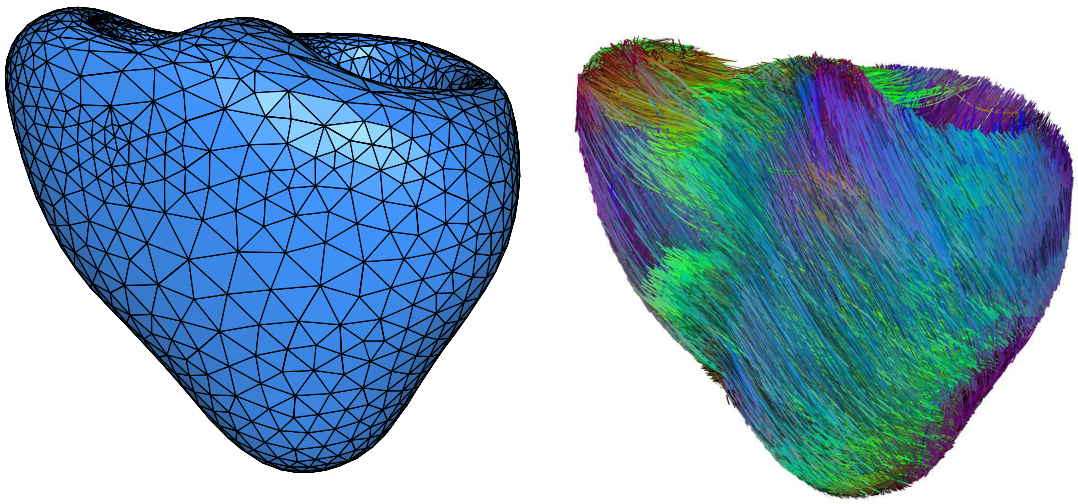

Figure 6.1: Computational mesh for baseline (left) and generic fibers prescribed in the mesh (right).

measured QRS duration (QRSd). The action potential duration in the simulation was kept constant over the whole myocardium, and was adjusted according to the Cine MRI data.

6.3.4 Calibration of mechanical parameters of the model

The model parameters were calibrated for the baseline condition, namely, in the healthy heart. Tissue contractility and passive tissue stiffness were calibrated to obtain good adequacy of the ventricular pressures and global motion compared to the measured data, including the LV pressure time derivative dp/dt and the ejection fractions. Correct peak ventricular pressure and the pressures in large arteries (aorta and pulmonary artery) were obtained by calibrating capacitances and resistances of the Windkessel models.

6.3.5 Modeling of the infarct

For each of the post-infarct stages, a new anatomical model was created by segmenting MR images in the same way as for the baseline condition. Additionally, we segmented the infarcted tissue using late enhancement images and projected it in the mesh (see Fig. 6.3). The initial aortic pressure and values of atrial pressures were taken from the measurements. The heart rate and duration of the heart contraction were adjusted to the MR image data. In order to represent the impact of the infarct on the tissue, we decreased the contractility

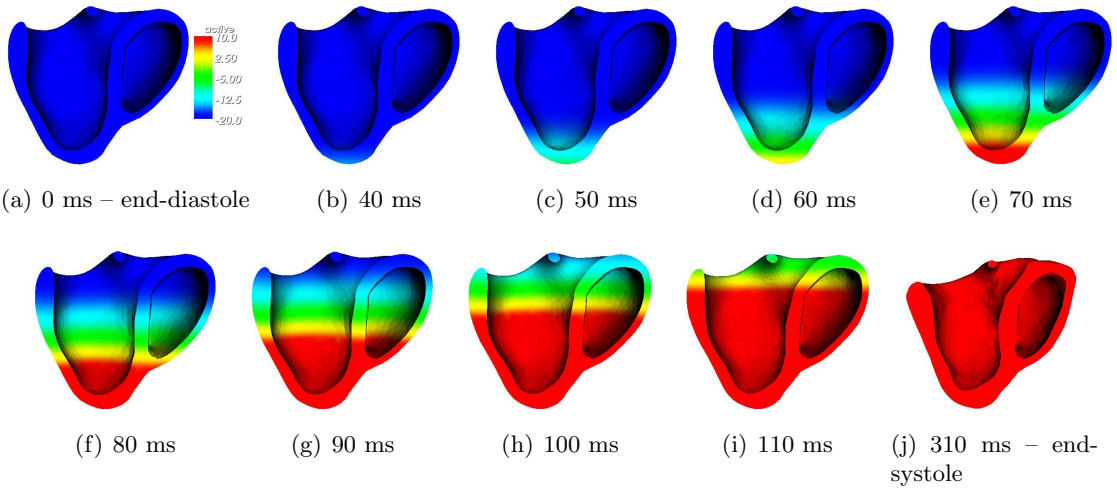

(a) 0 ms – end-diastole (b) 40 ms (c) 50 ms (d) 60 ms (e) 70 ms

(f) 80 ms (g) 90 ms (h) 100 ms (i) 110 ms (j) 310 ms – end-systole

Figure 6.2: Analytical prescription of the electrical activation at the baseline stage: the red activation planar wave propagates from the apex to the base. The activation offset between the apex and the base corresponds to the measured QRSd.

Parameter	Baseline	T0+10	T0+38
contractility	σ_0	$\sigma_0/5$ (infarcted region)	$\sigma_0/5$ (infarcted region)
stiffness	κ_1	$\kappa_1 * 10$ (infarcted region)	$\kappa_1 * 10$ (infarcted region)
minimum aortic pressure	73 mmHg	53 mmHg	89 mmHg
activation duration	220 ms	275 ms	246 ms
left atrial pressure	12 mmHg	12 mmHg	20 mmHg

Table 6.1: Parameter values modified in infarction model.

and increased the passive stiffness in the regions concerned, as segmented from the late-enhancement MR images. All other parameters of the model were kept exactly as in the baseline simulation. We summarize the parameter variations in Table 6.1.

6.3.6 Results

In Figure 6.4 we compare the simulated and measured pressures and volumes in the main compartments, for each of the three stages.

The heart motion is more accurately confronted with experimental data by plotting the model contours within MR images, see Figs. 6.5, 6.6 and 6.7. We also produced synthetic tagged images from the model simulations, which are compared with experimental ones in Fig. 6.8.

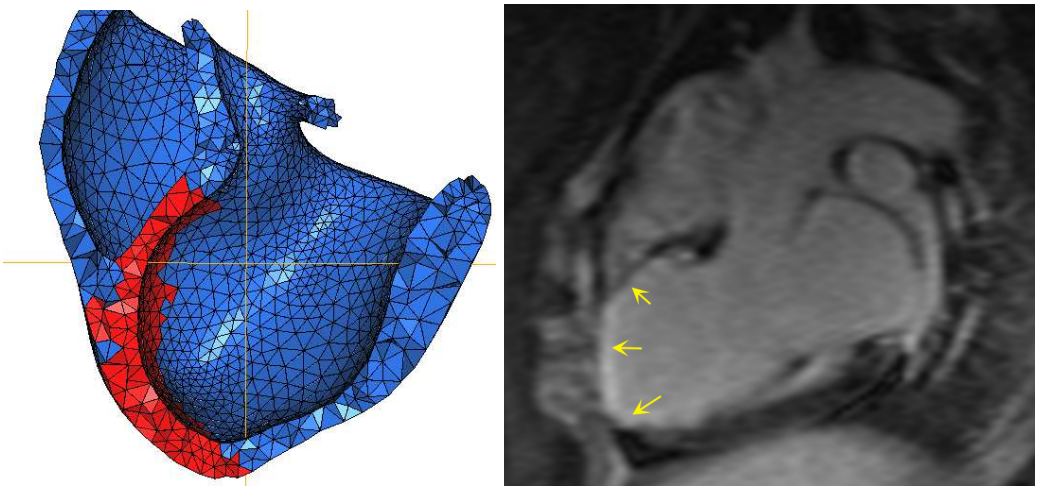

Figure 6.3: Infarct at T0+38: in the mesh (left, in red) as segmented from the late enhancement MR images (right, yellow arrows).

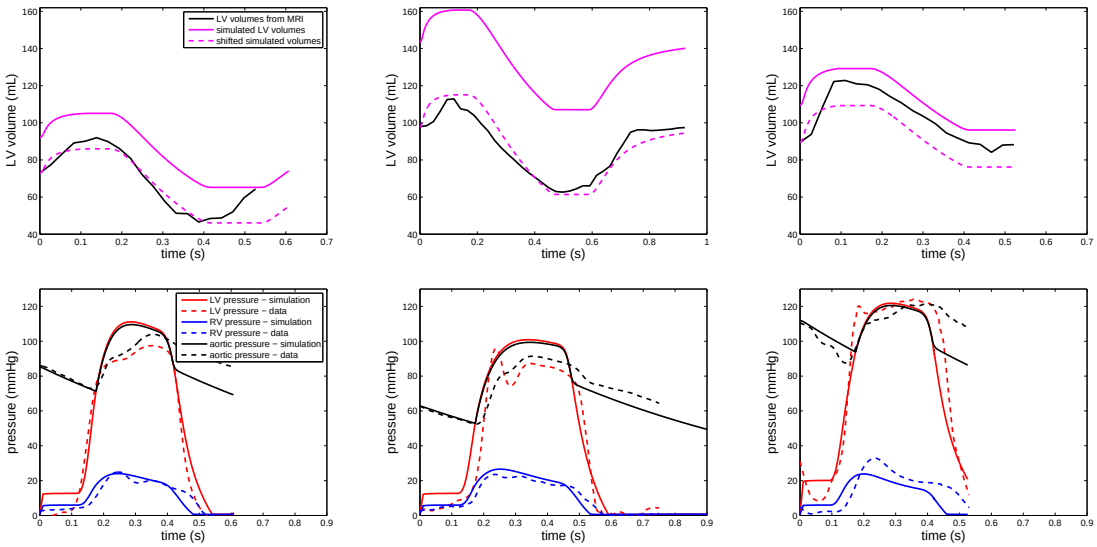

Figure 6.4: Volumes and pressures: baseline (left), T0+10 (in the middle), T0+38 (right).

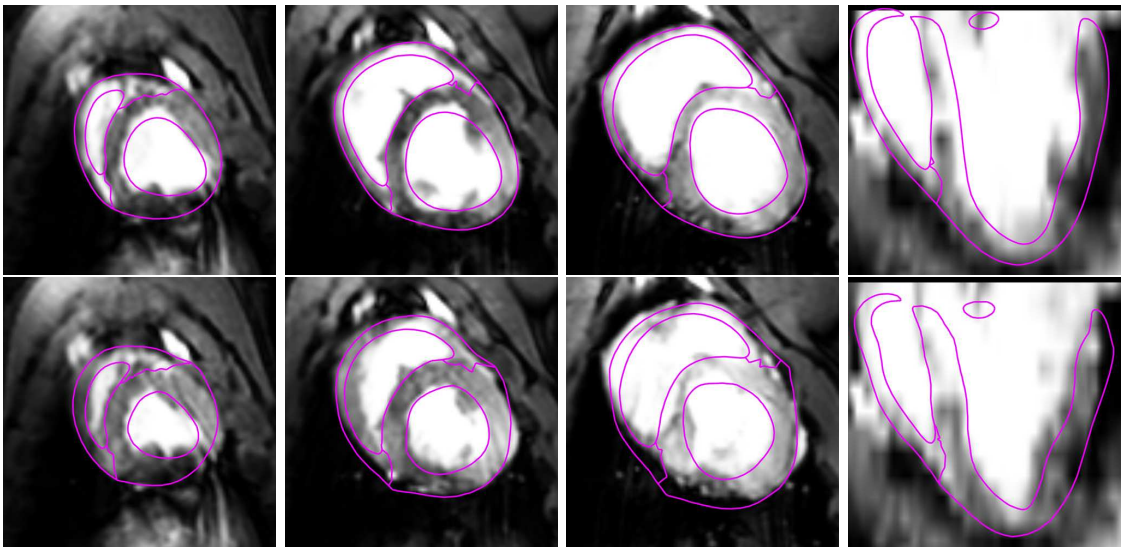

Figure 6.5: Baseline: Initial configuration (top) and end-systolic time frame (bottom), with model contours in purple.

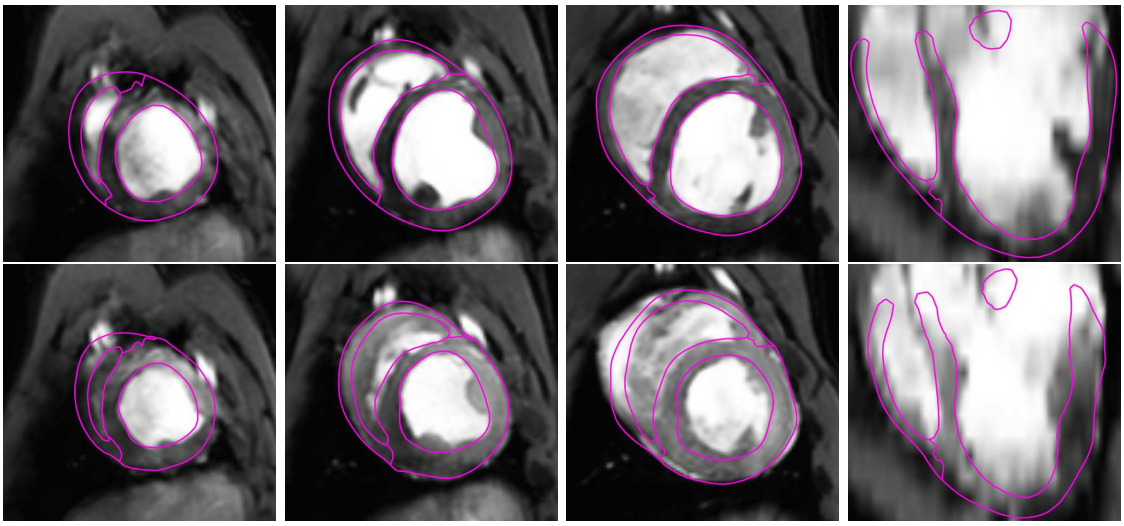

Figure 6.6: T0+10: Initial configuration (top) and end-systolic time frame (bottom), with model contours in purple.

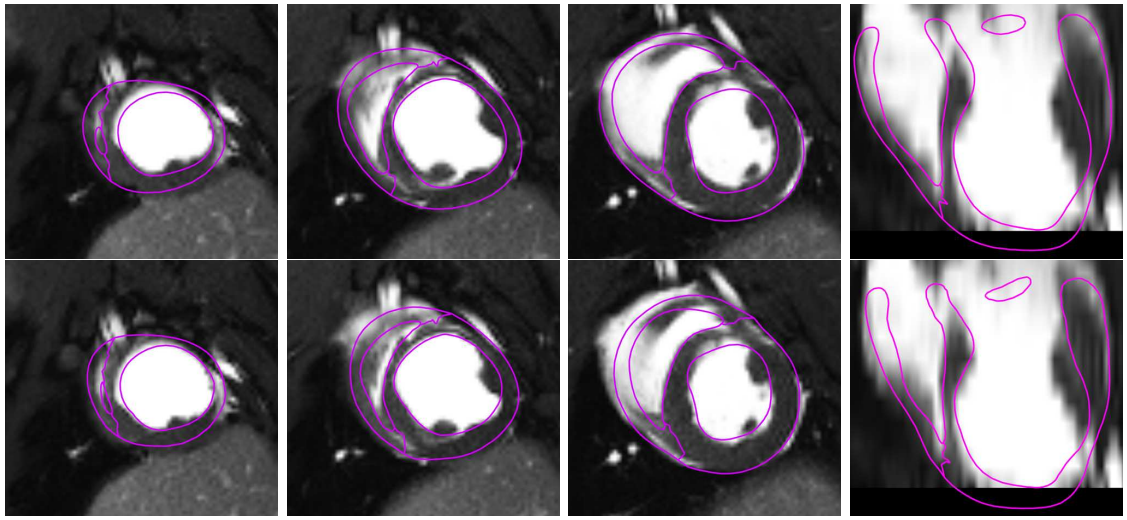

Figure 6.7: T0+38: Initial configuration (top) and end-systolic time frame (bottom), with model contours in purple.

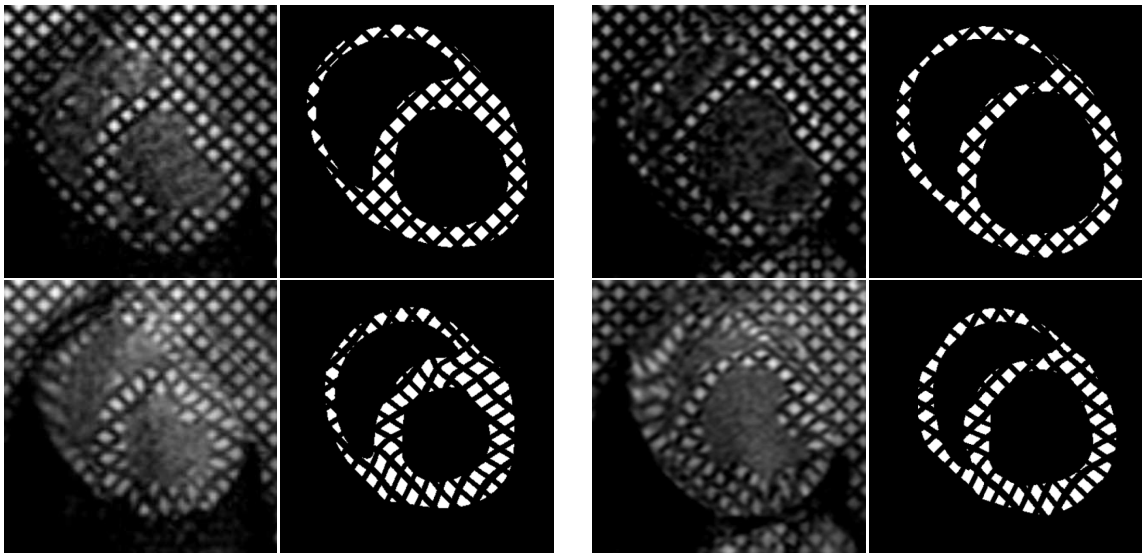

Figure 6.8: Comparison of MR and synthetic tagged images for baseline (left four images) and T0+10 stage (right four images). End-diastolic time frames are displayed in the upper row, end-systolic time frames in the lower row.

6.4 Discussion

There were no signs of dyssynchrony of the heart contraction in the Cine MRI at any stage of the experiment and the width of the QRS complex was physiological as well. Therefore we used the same electrical activation pattern – analytically prescribed representing the physiological activation – for all the stages.

Left ventricular volumes plotted in Fig. 6.4 are not directly accurate. This is mainly due to the fact that simulated and measured volumes are not computed based on the same regions. Simulated volumes take into account the model cavities approximately up to the valve plane, whereas measured volumes are taken in a truncated anatomy between two fixed sections in the image space. Hence, in Figure 6.4 we also show a shifted simulated volume to account for this difference. Nevertheless, these curves are mainly to be considered to assess the timings of the cardiac cycle, as detailed motions are directly assessed by comparing images and model contours.

The simulated and measured pressure values are found to be in very good overall agreement at the three stages. We note that the systolic pressure increase rate (dp/dt) is somewhat underestimated in the simulations at the infarcted stages. This may be due to an increase in the contractility resulting from growth combined with an adaptation mechanism of the cardiovascular system. In a larger study a mini-pig should be used (instead of a young subject) to avoid the influence of growth and young age specificities in the post-infarct follow-up.

The comparison of model contours with image also demonstrates a very good adequacy of the simulated motion. The main discrepancy is to be observed near the base, which is due to artificial boundary conditions which must be imposed in this region to account for the truncated part of the anatomy. The akinetic region (in the anterior and antero-septal apical and mid-cavity segments) is clearly visible – both in the images and in the model – and is even more pronounced at T0+38.

The synthetic tagged images in the baseline clearly show that the simulation of the healthy heart is very accurate in all segments of the left ventricle. The akinetic region seen in the T0+10 clinical tagged images is also well captured in the synthetic tagged images, although the anterior segment shows some slight thickening in the simulation. This is likely to be due to the difficulty of accurately assessing the extension of the infarcted region in the acute stage with the late enhancement images.

Therefore, according to the various indicators considered, by changing just a few relevant physiological parameters we obtain a very good adequacy between simulations and experimental data.

6.5 Further perspectives

This infarct model was considered in a case without any other co-morbidity factor. For a real patient, other factors (e.g. electrical activation pathologies) should be taken into ac-

count in the model. In addition, other artificial infarct protocols may be used, in particular since reversible occlusion may have a limited impact (tissue stunning, see [63]). From the follow-up of the animal in the present case, we can see that the tissue was really massively infarcted. Furthermore, we prefer reversible occlusion since it is more usual in patients in today's treatments of the myocardial infarction.

We emphasize that other physical variables can be obtained from the model simulations, such as stresses which may be essential to better understand some physiological phenomena involved in tissue remodeling, in particular.

A detailed study of the influence of the key physical parameters – namely, contractility and tissue stiffness – should be undertaken. This may be automatized by performing estimation of these parameters [99]. The experimental data can also be used in a global estimation procedure to correct the various model variables, hence to obtain improved motion fields and pressures, see [80]. This is in fact necessary to obtain a correct estimation of the parameters.

6.6 Conclusions

We showed that our biomechanical model of the heart can be personalized and calibrated to accurately reproduce the pressures and motion measured in a healthy animal subject. Then, we demonstrated that we can also adequately represent the behavior of the acutely infarcted heart by changing only the parameters directly related to the pathology (contractility and stiffness in the infarcted area) and to the physiological state of the subject during the exam (atrial and aortic blood pressure, heart rythm).

Of course, a more extensive validation – with numerous animal and human data-sets – is required to show that this personalized modeling strategy can be valuable in clinical applications. Further perspectives include automated estimation of the relevant physiological parameters, and the modeling of other types of pathologies, including with multiple co-morbidity factors.

Chapter 7

Planning of Cardiovascular Resynchronization Therapy

7.1 Cardiac Resynchronization Therapy (CRT)

Cardiac Resynchronization Therapy (CRT), also called biventricular pacing, is a non-pharmacological therapy for patients with an advanced heart failure. Such patients very often have an abnormal electrical conduction in the heart, such as an atrio–ventricular block or an intraventricular conduction delay. The latter is often manifested as a left bundle branch block (LBBB). In an LBBB, the lateral wall of the left ventricle (LV) may start to contract with a delay of as much as 100 ms with respect to the initiation of the septum contraction. The physiological offset between the activation of the septum and of the LV lateral wall is less than 40ms[1], see Figure 7.1 on the left.

The period of depolarization of the ventricles is directly mirrored by the QRS complex of the electrocardiogram (ECG). A typical ECG sign of prolonged ventricle activation is an extended QRS complex with a modified configuration of each wave. A QRS duration (QRSd) greater than 120 ms is considered to be non-physiological but it is a non-specific sign. Indeed, we cannot distinguish e.g. between an inter–ventricular conduction delay (a delay between the LV and RV activation) or an intraventricular delay (in which a conduction block is localized in the LV) just from the QRSd. Some typical QRS complex deformations and diagnostic criteria for LBBB and RBBB are depicted on the right side of Figure 7.1 and can be summarized as follows ([70, Chap. 12]):

LBBB

- QRSd $\geq$ 120ms

[1]The whole endocardial portion of the myocardium is activated in about 30 ms thanks to the fast conduction system of Purkinje fibers, see Section 2.3.3 and [46].

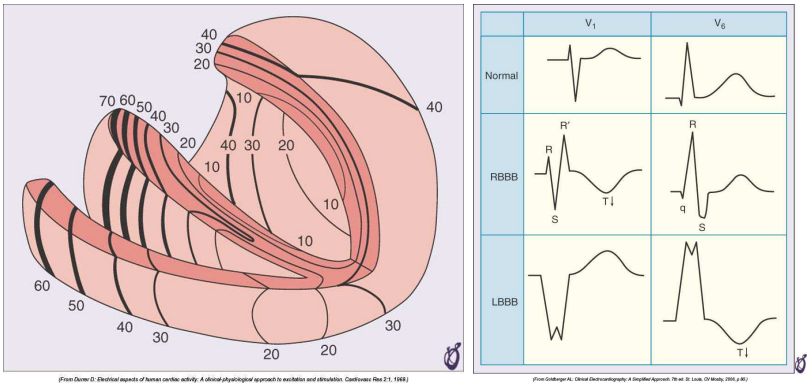

Figure 7.1: Left: Isochrones of activation times (in ms) for the heart ventricles in physiological case. Right: Typical ECG signs of RBBB and LBBB. From [70].

- Broad **R** waves in lateral precordial leads (V_5 and V_6) and usually also in leads I, avL
- Small or absent initial **r** waves in right precordial leads (V_1 and V_2) followed by deep **S** waves

RBBB

- QRSd $\geq$ 120ms
- Broad **R** waves (rsr', rsR', or rSR' patterns) in right precordial leads (V_1 and V_2)
- Wide and deep **S** waves in left precordial leads (V_5 and V_6)

The echocardiographic or Cine MR image of the LBBB often includes the so-called septal flash. It consists of a rapid septal movement towards the LV cavity at the very beginning of the systole when the septum is being activated. As soon as the LV lateral wall becomes activated and contracts, the resulting pressure increase pushes the septum back towards the right ventricle. The time period of the septal flash can serve as an indicator of the offset between the activation of the septum and LV lateral wall.

CRT is based on cardiac pacing in the right and in the left ventricle. Therefore it may decrease the dyssynchrony of the ventricle contraction. The pacing leads are usually placed in the right atrium (RA), right ventricle (as in the usual DDD pacing[2]), and an additional lead is placed in a lateral branch of the coronary sinus[3]. While the RV lead

[2]The first 'D' stands for a dual pacing (RA and RV), the second 'D' – dual sensing (RA and RV), the third 'D' – the sensed event can both inhibit or activate the stimulation.

[3]For the coronary vein anatomy we refer to Figure 2.2.

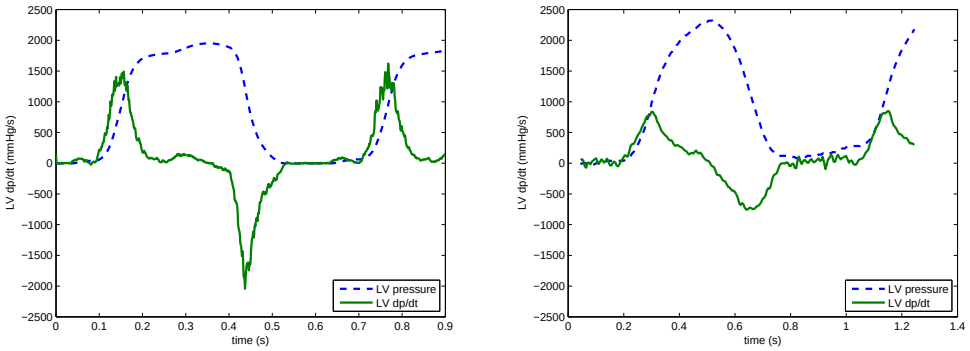

Figure 7.2: Left: Physiological LV pressure curve (in blue) and its time derivative dp/dt (in green). Right: LV pressure and LV dp/dt in LBBB. Note that the maximum value of the LV dp/dt in the physiological activation is $\sim$ 1500 mmHg/s, while it is less than 1000 mmHg/s in this particular example of the LBBB.

paces in the RV endocardium, the coronary sinus lead stimulates the epicardial part of the LV. Combinations of more than 3 pacing leads may be used, and the offset between each of them can be adjusted.

A long term pacing on the LV endocardium surface is technically more complicated. The lead needs to cross the inter-atrial septum from the RA to the LA and eventually reach the endocardial part of the LV via the mitral valve. The implantation issue is definitely not invincible and for example mathematical modeling could give some objective motivations for launching a large study comparing LV epicardial / LV endocardial pacing strategies.

Several clinical studies have shown that patients may profit from the CRT. Among them for instance the MIRACLE study (started in 1998, [1]), COMPANION study (started in 2000, [18]) or CARE–HF study (started in 2001, [28]). Nevertheless, up to 30% of the indicated patients turn out to be non-responders ([57]). All those facts raise many questions about CRT optimization, as for example: 'What would be the best number of the pacing leads, which position would be optimal and what would be the optimal offset for each pacing lead?' The final goal of any modeling effort would be to determine whether a particular patient could benefit from the CRT and what would be the best set up of the CRT in his (her) case.

An immediate effect of the CRT can be assessed by measuring the left ventricle pressure and its time derivative (LV dp/dt). The maximum value of LV dp/dt quantifies the ability of the ventricle to build up the pressure. While the normal value of the max LV dp/dt is 1500–2500 mmHg/s, the value can be even lower than 500 mmHg/s in a dyssynchronous heart contraction, see Figure 7.2. The value of max LV dp/dt may also be decreased in a synchronous contraction due to decreased contractility.

In this study[4], we would like to set up patient-specific biomechanical models that would be able to represent the baseline situation (LBBB) by means of the motion pattern and of the simulated and measured LV pressures and LV dp/dt. Once the model is adjusted properly, we will fix all the model parameters. By varying the electrical activation according to the CRT pacing patterns, we would like to show that the model is able to predict the changes of the LV dp/dt according to the measurements.

In the first part, analytical prescriptions of the electrical activation will be used. The objective will be to show that by using relatively simple activation patterns calibrated according to some typical motion signs visible in the Cine MRI, we can represent the baseline stage. Then, by making the artificial electrical activation more synchronous, we would like the value of the max LV dp/dt to increase.

In the second part, we will be using patient-specific electrical activation patterns obtained by post-processing data from an electrophysiological (EP) study, both for the baseline stage and for all the pacing modes. We will directly compare the results of the simulated values of max LV dp/dt with the measured values. The aim of this study is to assess the model predictivity with respect to this particular indicator of the LV function.

7.2 Methods

7.2.1 Patient selection

The patients included in this study suffered from an advanced heart failure (NYHA[5] III-IV) and a dyssynchronous heart contraction with the LBBB pattern and were indicated for the CRT. The etiology of the heart failure (HF) was either an ischemic heart disease (IHD) or a dilated cardiomyopathy (DCM). The patients are listed in Table 7.1.

7.2.2 Measured data

The measured data consist of the non-invasive cardiac magnetic resonance imaging data (CMR) acquired in the baseline condition and of the invasively measured electrophysiological data and LV pressures in the baseline and for each CRT pacing pattern.

Cardiac MRI

Cardiac MR (CMR) data were acquired in the baseline condition using the MR system Philips Achieva 1.5 T. The CMR consisted of the standard Cine MRI sequences (to ob-

[4]The work was performed in co-operation with King's College London, St. Thomas' Hospital in London (where also all clinical data were acquired) and Team-Project Asclepios of INRIA, Sophia Antipolis. People involved in the project are listed in [97].

[5]NYHA classes stand for the stages of heart failure according to the New York Heart Association, see Table 2.1 in Section 2.4.1. Patients with NYHA III are comfortable at rest but any other activity causes fatigue, palpitation, or dyspnea. Class IV patients may suffer from these symptoms even at rest.

Patient	Etiology of HF	Simulations with analytical act. patterns	simulations with patient-specific act. patterns
KCL003	DCM	baseline	no
KCL006	DCM	baseline	no
KCL008	DCM	baseline	no
KCL009	DCM / IHD	yes	yes
KCL010	DCM	baseline	no
KCL011	IHD	baseline	no
	(LE not segmented yet)		
KCL012	DCM	yes	yes
KCL014	IHD	yes	no

Table 7.1: Patients included in the study. Note: Only electrophysiological data of KCL009 and KCL012 were processed at KCL. In other cases, analytical prescriptions of electrical activation were used and usually only preliminary calibration of the baseline activation (the LBBB pattern) was performed. KCL009 is a patient with DCM and some not very extended nonviable postischemic regions.

tain the heart morphology and kinematics) and of late-enhancement images (acquired 10 minutes after administering an extracellular paramagnetic contrast agent – a gadolinium chelate). The late-enhancement images were used to assess the non-viable myocardial tissue and possibly to visualize a non-specific late-enhancement in some dilated cardiomyopahies. Additional 3D morphological sequences in free breathing (using the breath-navigator) were performed to obtain 3D diastolic images with high spatial resolution. The sequence parameters are as follows:

- **Cine MRI** in retrospective ECG gating (bSSFP, flip angle 60 °, TR $\sim$ 3.3 ms, TE $\sim$ 1.6 ms, turbo factor 14, acq. matrix 224 x 168, voxel size 1.8 x 2.4 x 10 mm, 30–40 time frames / cardiac cycle)
- **LE images** – bSSFP with IR pre-pulse, flip angle 15 °, TR $\sim$ 4.9 ms, TE $\sim$ 1.9 ms, TI $\sim$ 220 ms, turbo factor 30, acq. matrix 300 x 280, voxel size 1.45 x 1.45 x 10 mm
- **3D morphology in free breathing** – bSSFP, 3D acquisition, flip angle 90 °, TR $\sim$ 4.7 ms, TE $\sim$ 2.4 ms, turbo factor 20, acq. matrix 230 x 230 x 230, voxel size 1.4 x 1.4 x 1.5 mm

Electrophysiological data

A non-contact mapping study was performed using an Ensite 3000 multi-electrode array catheter system (St Jude, Sylmar, CA). The electrophysiological (EP) potentials were measured by electrodes mounted on an 8 mm balloon. They were automatically projected

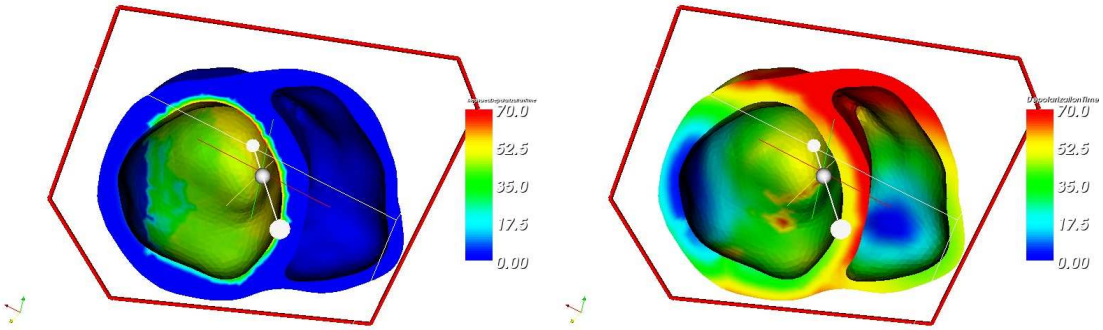

Figure 7.3: Left: Measured isochrones on the LV endocardium. Right: Estimated isochrones in the whole myocardium according to Section 7.6.

on the LV endocardial surface, where both isopotential and isochronal maps were reconstructed (see Figure 7.3). Such non-contact multi-electrode approach can provide the EP potentials from the whole LV endocardium surface taken during a single cardiac cycle. Hence the measurement of the EP potentials is fast and can be performed for each electrical activation pattern.

The EP data were registered to the MR data by XMR fusion (see [91]). For the registered 3D geometries see Figure 7.4.

LV pressure data

In addition to measuring the EP potentials on the LV surface, the LV pressure was measured using a high fidelity pressure sensor for each electrical activation pattern. The pressure data were automatically processed and the time derivative of the LV pressure (LV dp/dt) was obtained. Both curves – the LV pressure and the LV dp/dt – were recorded over several cardiac cycles.

7.3 Creation of geometrical models

For each patient, the short axis Cine MRI (multiple 2D series, M2D) covering the whole ventricle volumes were available with a spatial resolution of (2 x 2 x 10) mm. Some patients had also 3D morphological data taken in diastole with a spatial resolution of $\sim$ (1.5 x 1.5 x 1.5) mm. M2D Cine data are not the best option for creating the geometrical models because of the misalignment between the slices acquired in the different breath-hold periods and a limited resolution in the slice-selection direction. Unfortunately, the 3D morphological data were of limited quality. That is why we built the geometrical models of all patients from the Cine MRI data.

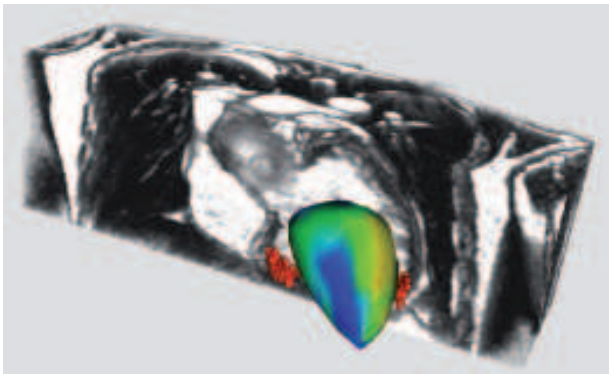

Figure 7.4: Fusion of late-enhancement derived scars (red surfaces), anatomical MR (volume rendering) and Ensite isochronal map (colored surface). From [98].

The models of the left and right ventricles[6] were obtained by manually segmenting the diastolic time frame image of the Cine MRI preceding the atrial contraction, using the CardioViz3D software, see [107]. Computational tetrahedral meshes were created using Yams and GHS3D, see [41]. The volumic mesh of the LV was subdivided into 17 segments according to the American Heart Association (AHA) recommendations, see [21]. In patients with an IHD and post-infarcted scars, the infarcted tissue was visualized by means of the MR late-enhancement, and it was projected into the computational mesh.

The direction of the active contraction in the model is given by the myocardial fiber directions. This is a reason why the prescription of fiber directions in the geometrical model is important. We tested two possibilities:

- Myocardial fibers coming from an atlas of ex vivo canine hearts (see [88]), registered into the actual geometry.
- Geometrical fiber prescription according to anatomical knowledge, see e.g. [101].

Although the fibers coming from the analysis of group of a animal hearts is a interesting approach, the resulting fibers turned out to be very horizontal and there was no longitudinal shortening observed in the full 3D heart model. Instead, we saw some longitudinal elongation. On the other hand, the geometrically prescribed fibers with usual orientation on the endocardial and epicardial surfaces and the fibers linearly interpolated inside the myocardium gave very good results.

[6]The atria were excluded from the geometrical models due to the difficulty of their segmentation, and since we are primarily interested in the modeling of the heart ventricles. Therefore, the models were truncated slightly above the atrio-ventricular and semilunar valves, and full ventricle volumes were preserved.

Parameter of function u	Value
Minimum of u	-5
Maximum of u	10
$t_{fastDepol}$	40 ms
t_{repol}	150 ms

Table 7.2: Parameters of the electrical activation function u used for each patient.

7.4 Biomechanical model

The biomechanical heart model was described in Chapter 4. The objective of this study is to apply several electrical activation patterns, representing either the baseline case (the LBBB) or the CRT pacing modes. The electrical activation pattern will therefore serve as an important input of the model. In the following paragraphs we will give some details about the model activation, and about the calibration strategy.

7.4.1 Electrical activation of the model

The electrical activation of each node of the model is given by the function u, see (4.3) in Section 4.2. The electrical activation u consists of the fast depolarization part (u increases from u_{min} to u_{max} during a very short period $t_{fastDepol}$), of the plateau ($u = u_{max}$ during a time period $t_{plateau}$) and of the repolarization phase (u drops back to u_{min} during a period t_{repol}). We used a function u of the same profile for each part of the heart muscle[7], which means that we did not vary neither u_{min}, u_{max}, nor the duration of fast depolarization, plateau or of the repolarization phase over the model geometry. The plateau duration was adapted to the duration of the systole observed in the Cine MR image data. See Figure 7.5 with a profile of the electrical activation u used in the model of a patient denoted as KCL009 and Table 7.2 with the actual values of the parameters of the function u.

The offset of the function u between each node of the computational mesh is given by depolarization times T_d. They are either prescribed analytically or obtained by post-processing the electrophysiological data. The two approaches will be discussed in Sections 7.5 and 7.6.

7.4.2 Calibration strategy

The calibration was performed using the MR image data and the LV pressure and LV dp/dt measurements at the baseline. In the first steps, we did not apply the patient-specific electrical activation patterns yet. Instead, we used the analytical prescription

[7]Except if the duration of the plateau or repolarization times were estimated from the EP data.

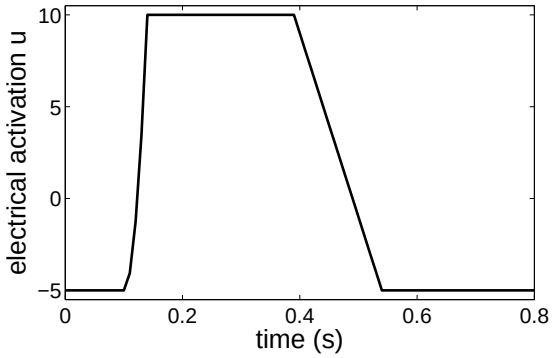

Figure 7.5: KCL009, electrical activation function u with parameters according to Table 7.2 and with plateau duration of 250 ms.

of the activation discussed in detail in Section 7.5. At this stage, we adjusted the visco-elastic boundary conditions and the approximate values of the main mechanical parameters of the model – in particular of the passive tissue stiffness and of the tissue contractility – according to the measured global functional indicators, e.g. the LV ejection fraction. These parameters were kept constant over the whole myocardial tissue, at the moment.

In the second step, we modified the contractility and the passive tissue stiffness in the infarcted region (for the patients after the myocardial infarction), according to the strategy of Chapter 6 – the contractility in the infarcted region was decreased by a factor 5 and the passive tissue stiffness was increased by a factor 10.

To personalize the model at the local level we analyzed in detail the Cine MRI data. We focused in particular on the wall thickening during the contraction and on the end-diastolic wall thickness in each AHA segment. Then, we adjusted the contractility values according to the observed hypokinetic zones. Assuming that the pathologically thin parts of the myocardial wall have undergone fibrous remodeling would justify increasing the passive tissue stiffness in the concerned AHA segments. In fact, the thinned region is not necessarily fibrous and may also be hibernating or stunned (see [63]), but by increasing the passive tissue stiffness by a factor 1.5–2.0 we prevent to some extent the thin wall from bulging – which is normally achieved by the surrounding tissues. The handling of the boundary conditions setup is a very difficult modeling issue – see Section 4.2.5) – and by increasing the tissue stiffness in the thin-wall zones we obtained a reasonable model behavior compared with the image data. Some detailed information on the local parameter values will be given in Section 7.6, which deals with the patient-specific activation patterns.

The adjustment of the Windkessel models was the last step in the model calibration. Since the aortic, pulmonary artery and RV pressures were not measured, we had to adjust the diastolic arterial pressures to meaningful values with respect to the measured LV end-

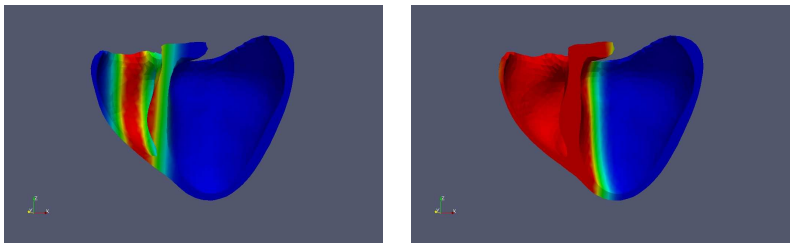

(a) time t = 150ms (b) time t = 200ms

(c) time t = 250ms (d) time t = 300ms

Figure 7.6: KCL014 using the analytical prescription of the LBBB-like pattern. The blue part of the mesh represents the non-activated tissue, the red is the activated myocardium.

systolic pressure and according to the type of pathology.

When applying the patient-specific activation patterns, there was usually no need for further corrections of the model. As soon as the simulated motion pattern was close enough to the measured image data, and the simulated LV pressure and LV dp/dt corresponded to the baseline activation, we fixed all the parameters of the model. The model was said to be calibrated at the baseline conditions.

7.5 Analytical activation patterns

The initiation T_d of the electrical activation (the depolarization time) for each node of the computational domain is given by an analytical prescription of a planar traveling wave starting either in the LV apex or in the septum. The propagation velocity is denoted by v and the propagation direction is given by the vector $\mathbf{w}$, which points either from the septum to the lateral ventricle wall (simulating the LBBB-like pattern, see Figure 7.6) or $\mathbf{w}$ is directly given by the LV long axis, see Figure 7.7.

We analyzed in detail 3 patients with the following sets of data: KCL009 and KCL012 with the known QRSd[8] and the measured LV pressures in the baseline and in

[8]Therefore the duration of the period during which the whole ventricle myocardium is activated is a

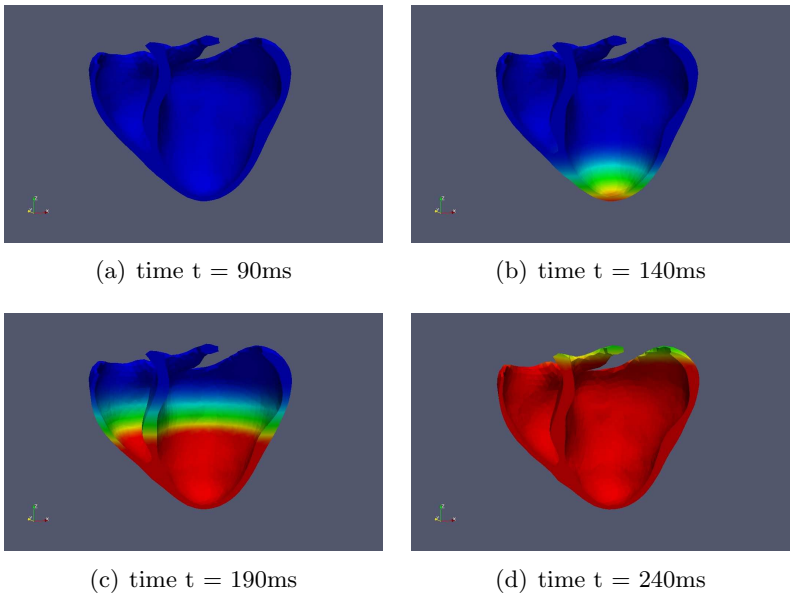

(a) time t = 90ms (b) time t = 140ms

(c) time t = 190ms (d) time t = 240ms

Figure 7.7: KCL014 using the analytical prescription of the synchronous activation pattern. The blue part of the mesh represents the non-activated tissue, the red is the activated myocardium.

activation pattern	velocity of V propagation (m/s)	simulated QRSd (ms)	simulated LV dp/dt (mmHg/s)
LBBB-like	**0.55**	**170**	**950**
LBBB-like	0.7	140	1080
apex–base	*1.5*	*100*	*1540*

Table 7.3: Analytical activation patterns for patient KCL009. The measured max LV dp/dt at baseline was **890 mmHg/s** with **QRSd∼170 ms** and the measured max LV dp/dt in the most synchronous case ('p1TRIV pattern') was *1450 mmHg/s* with *QRSd∼120ms*. The analytical activation corresponding best to the measured patterns are in **boldface** and in *italics*.

re-synchronized stages; the third patient was KCL014 for whom only the baseline pressure values were available.

Each patient has an LBBB pattern with a septal flash visible in the Cine MRI. This is why we used the LBBB-like analytical pattern. The propagation velocity of the activation wave along the direction septum–lateral wall was adjusted, so that the timing of the activation in the model would induce the septal flash corresponding to the measured data. We observed that such a propagation velocity will also activate the whole ventricle myocardium in the time period comparable to the measured QRSd. We calibrated the mechanical parameters of the models according to Section 7.4.2. The resulting max LV dp/dt of the simulations, when applying the propagation velocities adjusted with respect to the septal flash timing, correspond to **boldface** lines in Tables 7.3, 7.4 and 7.5.

After obtaining satisfactory results for the LBBB-like patterns, we set out make the analytical prescription of the electrical activation more synchronous. We either increased the propagation velocity of the activation wave or we varied its direction and onset. Typically, we used the activation wave starting in the apex and propagating along the long axis, instead of the LBBB-like pattern. The more synchronous the activation was, the higher increase of the simulated max LV dp/dt was obtained. When the period of activation in the model corresponded approximately to the QRSd of the CRT re-synchronized case, the increase of the maximum of LV dp/dt was close to the measured data (see the lines in *italics* in Tables 7.3, 7.4 and 7.5).

At this stage, we showed that the model can represent the LBBB pattern using a very simple prescription of the electrical activation and that the simulated max LV dp/dt is comparable to the measured value. The model is able to capture the phenomenon of the increase of max LV dp/dt when the electrical activation becomes more synchronous, see Figure 7.8. If the propagation direction and velocity are adjusted according to the measured QRSd of the re-synchronzed activation pattern, the change of the max LV dp/dt

known value.

activation pattern	velocity of V propagation (m/s)	simulated QRSd (ms)	simulated LV dp/dt (mmHg/s)
LBBB-like	**0.5**	**200**	**585**
LBBB-like	0.75	130	750
LBBB-like	1.0	100	910
LBBB-like	1.4	70	1000
LBBB-like	3.0	50	1130
apex–base	1.0	135	840
apex–base	*1.4*	*100*	*960*
apex–base	*1.5*	*90*	*990*
apex–base	3.0	65	1200

Table 7.4: Analytical activation patterns for patients KCL012. The measured max LV dp/dt at baseline was **640 mmHg/s** with **QRSd∼205 ms** and the measured max LV dp/dt in the most synchronous case ('p2DDDLV pattern') was *960 mmHg/s* with *QRSd∼115ms*. The analytical activation corresponding best to the measured patterns are in **boldface** and in *italics*.

activation pattern	velocity of V propagation (m/s)	simulated QRSd (ms)	simulated LV dp/dt (mmHg/s)
LBBB-like	**0.5**	**180**	**750**
apex–base	*1.0*	105	*940*
apex–base	3.0	65	1200

Table 7.5: Analytical activation patterns for patients KCL014. The measured max LV dp/dt at baseline was **720 mmHg/s** with **QRSd∼180ms**.

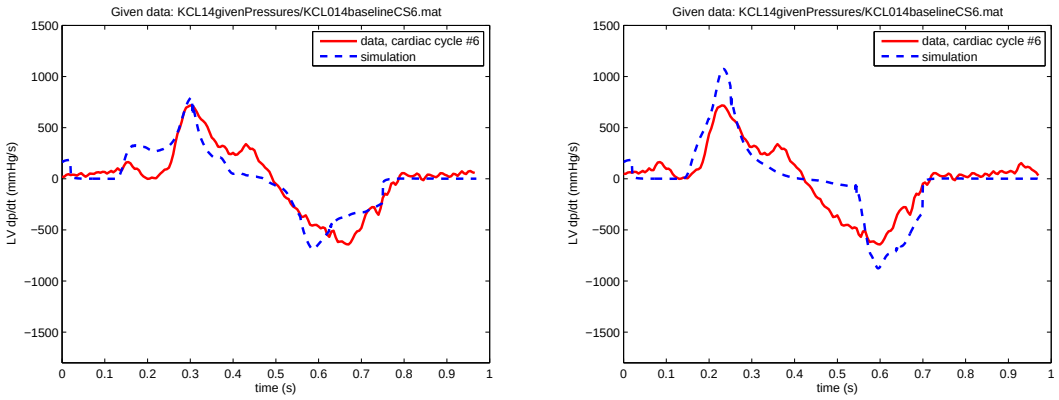

Figure 7.8: KCL014 using the analytical prescription of LBBB-like pattern. The red solid curve represents the measured LV dp/dt in the baseline, the blue dashed curve is the simulated dp/dt using the LBBB-like activation (left, electrical activation according to Figure 7.6), or the synchronous activation with the apex–base propagation (right, electrical activation according to Figure 7.7).

in the model is acceptable with respect to the measurements. In the following section, we will be dealing with detailed patient-specific electrical activation patterns.

7.6 Ensite based patterns

7.6.1 Modeling of the patient-specific electrical activation based on the electrophysiological Ensite data

The electrical activation was obtained by EP measurements of the LV endocardial potentials by means of the Ensite system, see Section 7.2.2. The Eikonal model given by equation (4.7) was used to estimate the depolarization times in the whole myocardium. The Eikonal model was adjusted by researchers at King's College London (KCL) according to [26] and the depolarization times for each part of the myocardium T_d were estimated. It is more difficult to obtain the action potential duration (APD) from the Ensite data, because of a problematic identification of the repolarization T wave. Nevertheless, the repolarization times were estimated in some of the activation patterns of patient KCL009. In all other cases we used the constant APD corresponding to the duration of contraction in the Cine MR images and in the measured LV pressure curves. Thanks to the long repolarization phase – the time period when the electrical activation function u decreases from the maximum back to the minimum value – the differences in real APDs were to some extent smoothed.

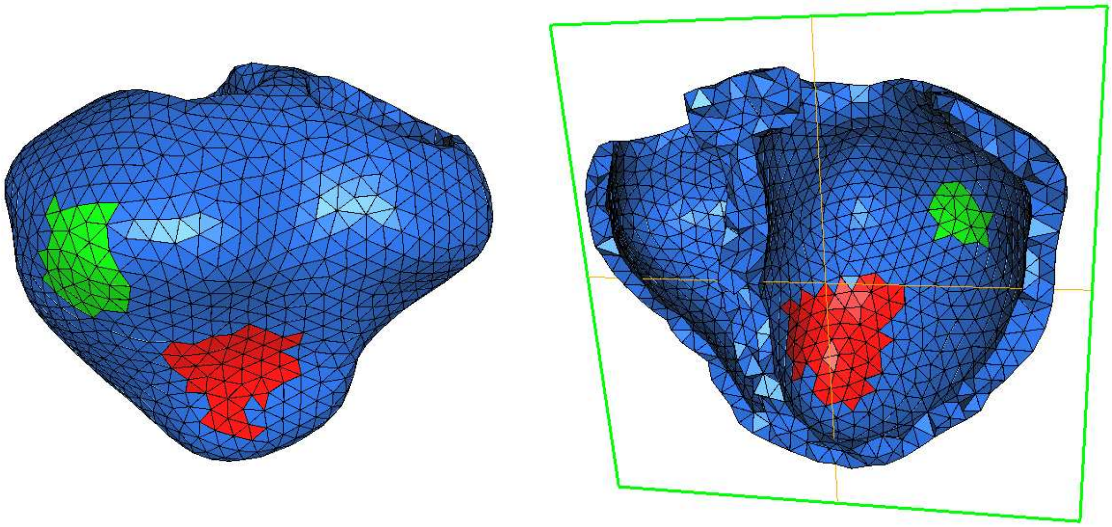

Figure 7.9: KCL009, inferior view on the computational mesh with two infarcted regions (in red and green colors).

7.6.2 KCL009

Baseline (LBBB)

KCL009 is a sixty year old woman with heart failure of class NYHA III. The etiology of the heart failure is a non-ischemic DCM with no flow-limiting disease on coronary angiography although cardiac MRI showed two post-ischemic scars of moderate sizes (in the apical infero-lateral and in the basal infero-lateral segments), see Figure 7.9. The LV ejection fraction was approximately 25%. The surface ECG demonstrated significant conduction disease with a left bundle branch block (LBBB) and a QRS duration of 154 ms.

The model calibration strategy was described in detail in Section 7.4.2. Here, we add a few particular details of the patient-specific set up:

- Duration of plateau of the electrical activation function u: 250 ms for the baseline (see Figure 7.5) and 200 ms for the paced modes[9].
- Contractility is decreased by a factor 2 in AHA 2, 3, 8, 9 (basal and mid-cavity septal segments).
- Passive tissue stiffness is increased by a factor 1.5 in AHA 12, 13, 15, 16 (the thinnest parts of the LV wall).

[9]We identify the action potential duration (APD) with duration of the plateau of u. The cardiac tissue is activated for a longer time period due to a long repolarization phase.

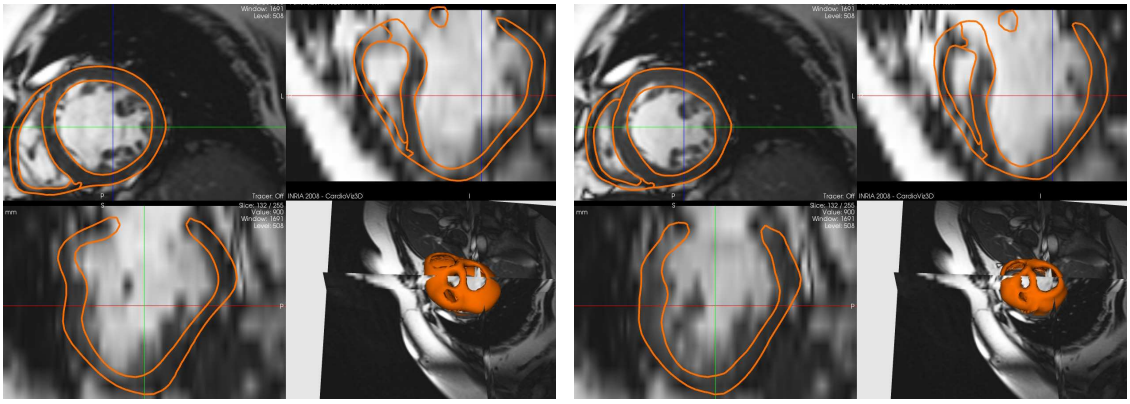

Figure 7.10: KCL009, baseline simulation. Reference segmented image (diastole, on the left) and the end-systolic image as an output of the direct simulation (on the right). Orange color represents contours of the biomechanical model.

activation pattern	max LV dp/dt measured (mmHg/s)	max LV dp/dt simulated (mmHg/s)
baseline	890	930
aai	970	990
dddrv1	1020	1010
dddrv2	1020	960
dddlv	1410	1440
p1triv	1450	1420

Table 7.6: KCL009: Measured and simulated values of max LV dp/dt.

In Figure 7.10 we superposed the simulated mesh contours in the Cine MRI data. The simulated pressure and volume indicators are depicted in Figure 7.11.

Pacing modes

All the model parameters were kept exactly as they had been calibrated in the baseline. For each pacing pattern, we input in the model the electrical activation estimated from the Ensite data. In Figures 7.12, 7.13, 7.14 and 7.15 we compared LV pressure and dp/dt curves predicted by the simulation vs. measured during the EP-procedure. Numerical values of maximum values of the LV dp/dt are listed in Table 7.6.2 and plotted in Figure 7.16.

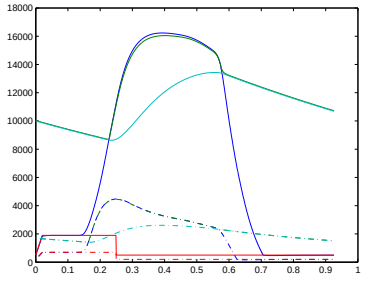

(a) Simulated pressures

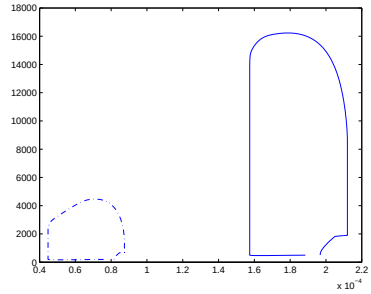

(b) Simulated Pressure–Volume curves

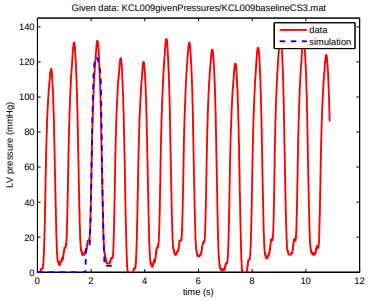

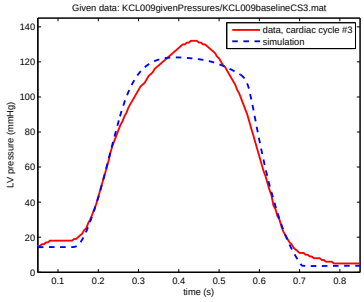

(c) LV pressure in measurement (red line) and in simulation (blue dashed line)

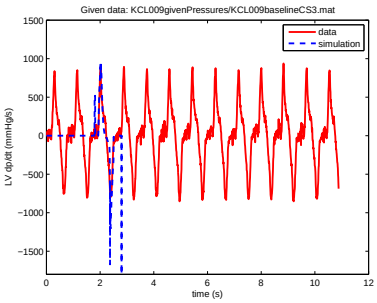

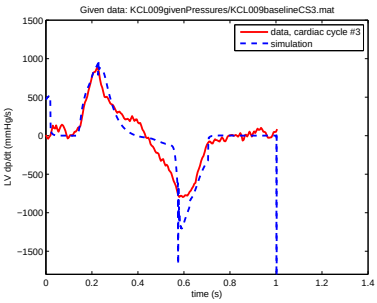

(d) LV dp/dt in measurement (red line) and in simulation (blue dashed line)

Figure 7.11: KCL009: baseline simulation.

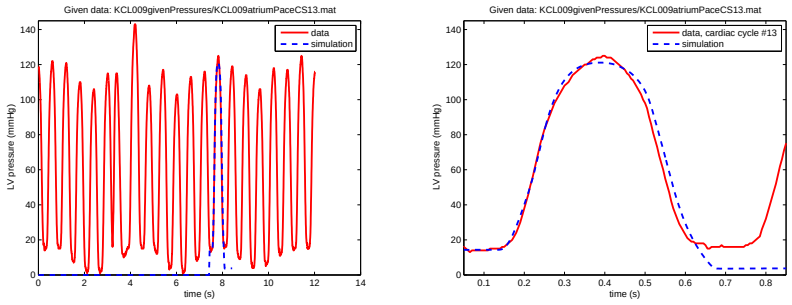

(a) LV pressure in measurement (red line) and in simulation (blue dashed line)

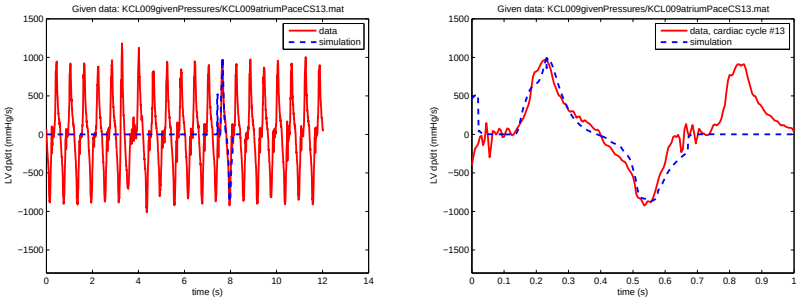

(b) LV dp/dt in measurement (red line) and in simulation (blue dashed line)

Figure 7.12: KCL009: AAI pacing pattern (1 pacing lead placed in the RA).

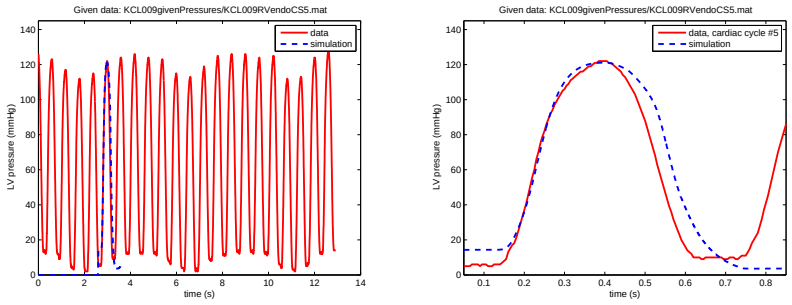

(a) LV pressure in measurement (red line) and in simulation (blue dashed line)

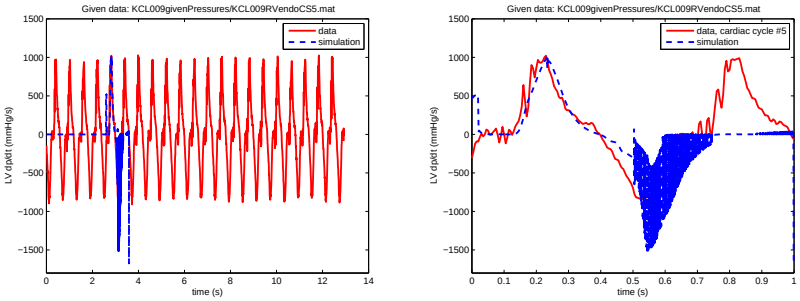

(b) LV dp/dt in measurement (red line) and in simulation (blue dashed line)

Figure 7.13: KCL009: DDDRV (pacing leads placed in the RA and in the RV).

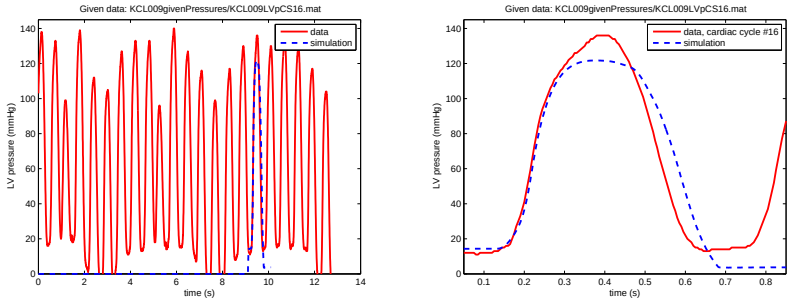

(a) LV pressure in measurement (red line) and in simulation (blue dashed line)

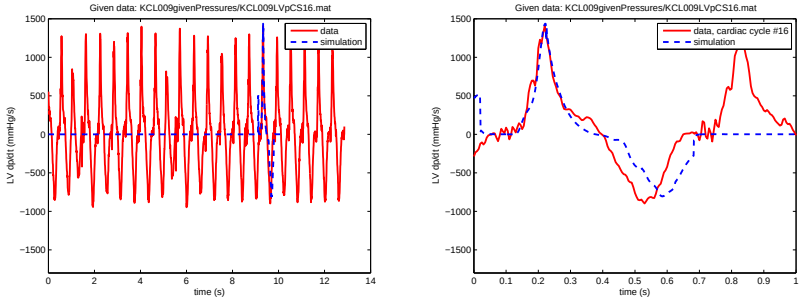

(b) LV dp/dt in measurement (red line) and in simulation (blue dashed line)

Figure 7.14: KCL009: DDDLV pacing pattern (pacing leads placed in the RA and LV endocardium).

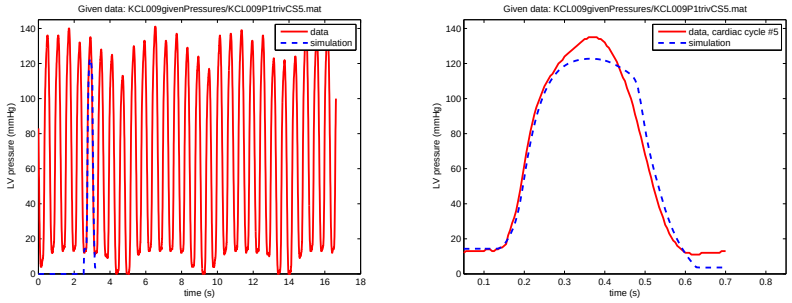

(a) LV pressure in measurement (red line) and in simulation (blue dashed line)

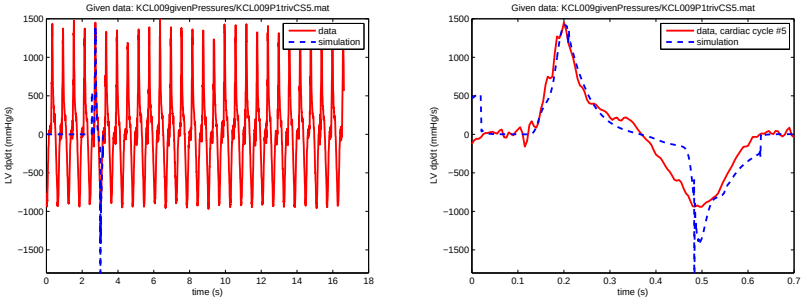

(b) LV dp/dt in measurement (red line) and in simulation (blue dashed line)

Figure 7.15: KCL009: P1TRIV pacing (pacing leads placed in the RA, RV, LV endocardium and a lateral branch of the coronary sinus).

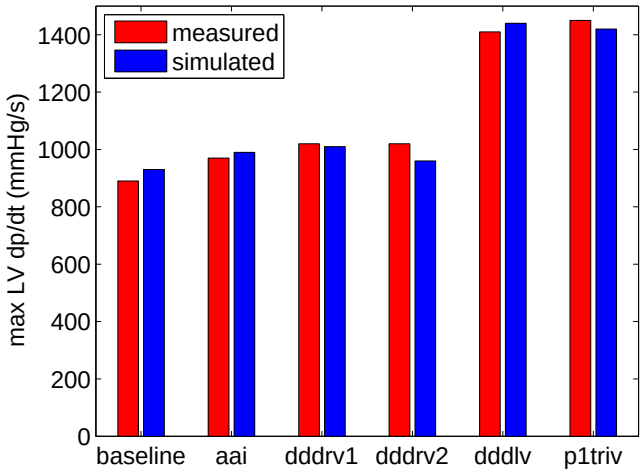

Figure 7.16: KCL009: Comparison of measured and estimated values of max LV dp/dt for all activation patterns.

7.6.3 KCL012

Baseline (LBBB)

The patient KCL012 is a seventy seven year old woman with a developed dilated cardiomyopathy (DCM). She was in NYHA class III heart failure with an LV ejection fraction of 15% and a left bundle branch block (LBBB) with a QRS duration of 200 ms. There was no post-infarct scar in the late-enhancement images but a functional block was observed in the electrophysiological mapping.

In the set up of the patient-specific model we modified in particular the following mechanical parameters of the model:

- Contractility was decreased by a factor 1.5 in the septum since it was visibly less contractile than the LV lateral wall.
- In agreement with [70, Chap. 64], we supposed that the DCM is usually accompanied by interstitial fibrosis. Therefore we increased the passive tissue stiffness by a factor 1.5 in the whole myocardium.

As we can see in Figures 7.17 and 7.18 the simulated local motion and LV pressure correspond well to the measured data (Cine MRI, pressure in the LV cavity). The simulated LV dp/dt slightly overestimates the measured value. All other simulated pressures (the aortic, RV and pulmonary artery pressures) are meaningful with respect to the measured LV pressure and to the known pathology.

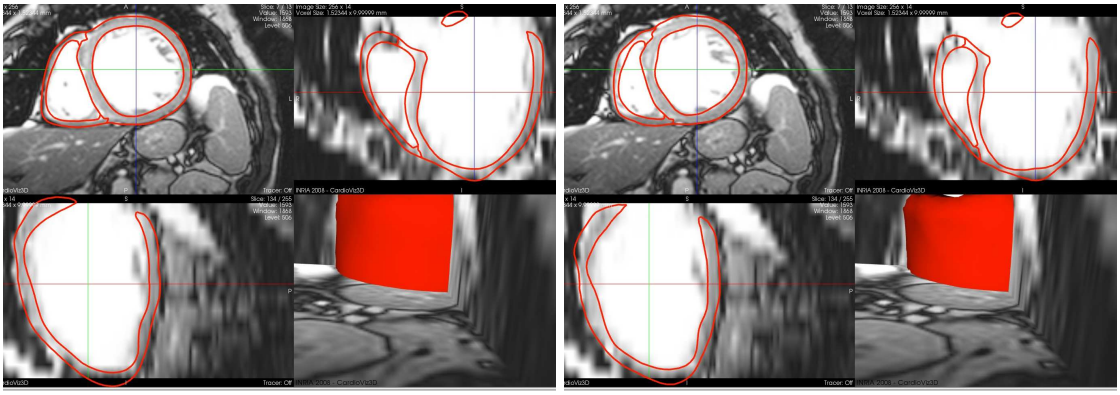

Figure 7.17: KCL012, baseline simulation. Reference segmented image (diastole, on the left) and the end-systolic image as an output of the direct simulation (on the right). The red color represents contours of the biomechanical model.

activation pattern	max LV dp/dt measured (mmHg/s)	max LV dp/dt simulated (mmHg/s)
baseline	640	740
aaai	640	740
BiVsim	950	890
p2dddlv	960	930

Table 7.7: KCL012: Measured and simulated values of max LV dp/dt.

Pacing modes

As in patient KCL009, we kept all the parameters of the model exactly as they had been calibrated in the baseline. For each pacing pattern, we used the electrical activation estimated from the Ensite data as a model input. In Figures 7.19, 7.20 and 7.21 we compared simulated (predicted) LV dp/dt curves with the measured ones. The values of max LV dp/dt are listed in Table 7.6.3 and plotted in Figure 7.22.

7.7 Discussion

7.7.1 Measured pressure values

For each activation pattern, the LV pressure was measured during 7–15 cardiac cycles. In all patients, the maximum pressure value oscillated within the respiratory cycle. Although the max LV dp/dt was more stable comparing with the LV pressure variations in between

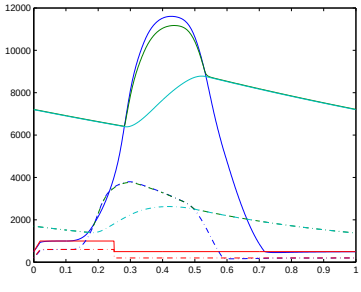

(a) Simulated pressures

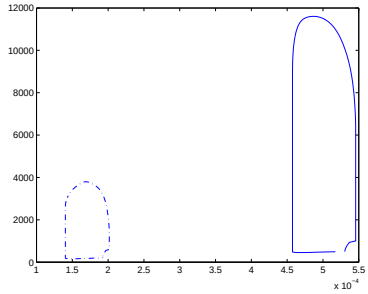

(b) Simulated Pressure–Volume curves

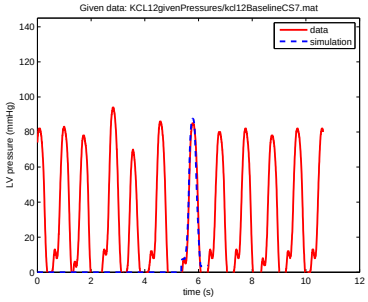

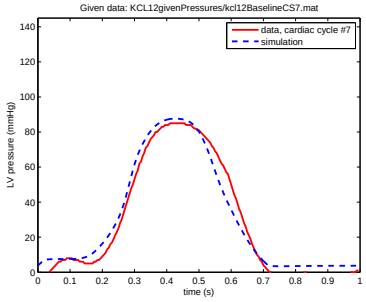

(c) LV pressure in measurement (red line) and in simulation (blue dashed line)

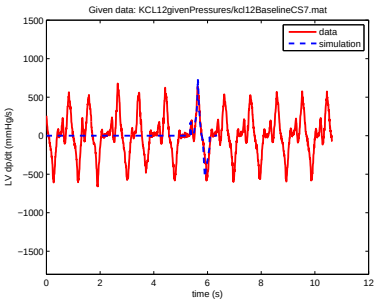

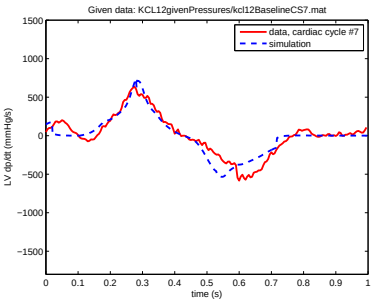

(d) LV dp/dt in measurement (red line) and in simulation (blue dashed line)

Figure 7.18: KCL012: baseline simulation.

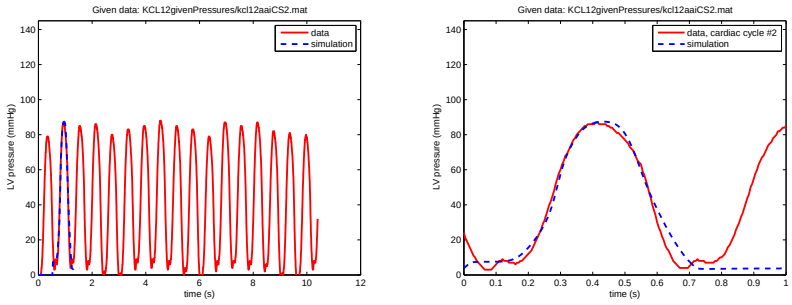

(a) LV pressure in measurement (red line) and in simulation (blue dashed line)

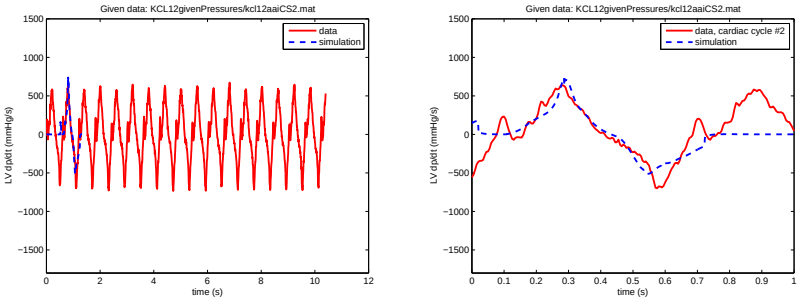

(b) LV dp/dt in measurement (red line) and in simulation (blue dashed line)

Figure 7.19: KCL012: AAI pacing pattern (1 pacing lead placed in the RA).

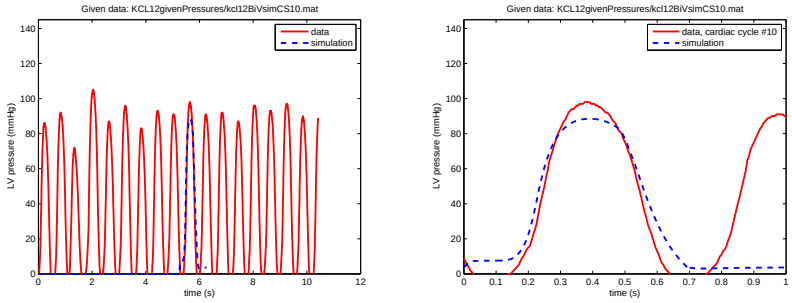

(a) LV pressure in measurement (red line) and in simulation (blue dashed line)

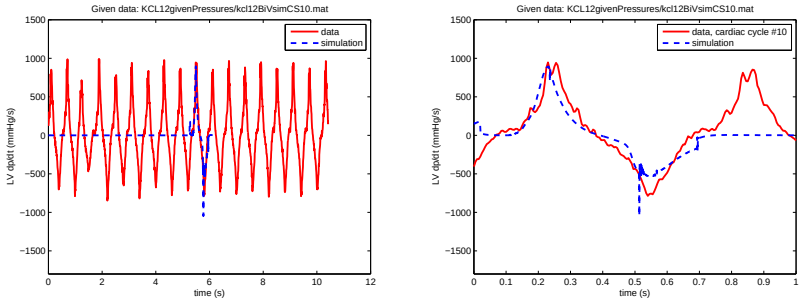

(b) LV dp/dt in measurement (red line) and in simulation (blue dashed line)

Figure 7.20: KCL012: Biventricular pacing (pacing leads placed in the RV endocardium and a lateral branch of the coronary sinus).

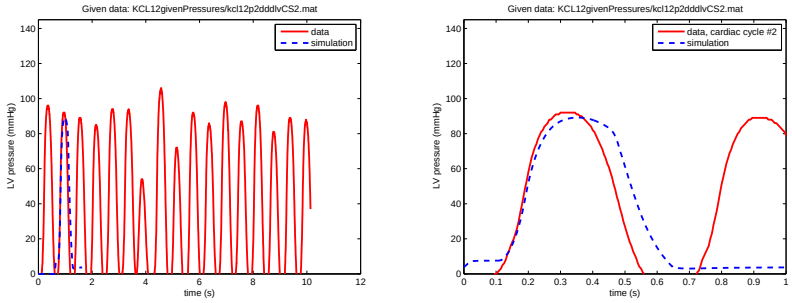

(a) LV pressure in measurement (red line) and in simulation (blue dashed line)

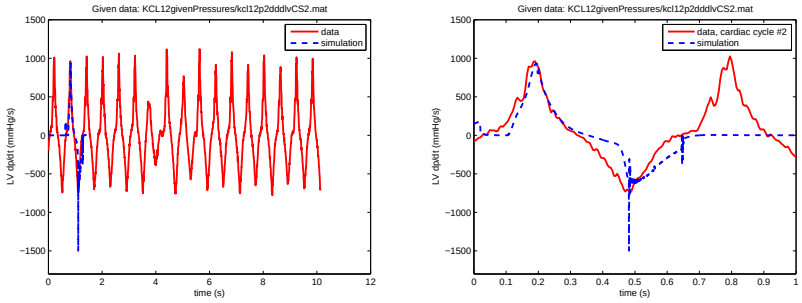

(b) LV dp/dt in measurement (red line) and in simulation (blue dashed line)

Figure 7.21: KCL012: p2dddlv pacing (pacing leads placed in the LV endocardium and a lateral branch of the coronary sinus).

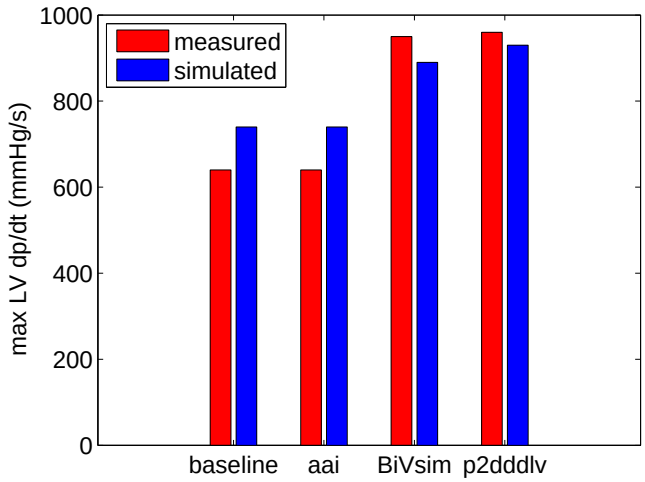

Figure 7.22: KCL012: Comparison of measured and estimated values of max LV dp/dt for all activation patterns.

the cardiac cycles, in some patterns the values varied quite significantly as well. Usually, there were some extrasystoles present in the data. Although they were directly visible in the measurement record, we did not try to detect them automatically. If we wanted to create an average cardiac cycle over several heartbeats, we would have to automatically find the cycles in the expiration and exclude those initiated by the extrasystole. We decided to compare the simulated results with one particular cardiac cycle taken in the expiration phase, that was not initialized by the extrasystole. Then, to see variations in the maximum LV pressure and dp/dt values, we superimposed the simulated curves in the pressure record with all measured cardiac cycles.

The aortic and the RV pressures were not measured during the study. Nevertheless, when adjusting the model we were careful to obtain consistent values for those pressures with respect to the measured LV pressures and to the patient's pathology. It is very likely that for instance the RV pressure may to some extent influence the LV dp/dt and modify the septal flash pattern. An increased RV pressure prevents the septum from returning back into the RV and the septal flash is getting less pronounced. Adjusting the Windkessel models without the measured aortic pressure is also problematic. As we saw in examples of three patients (KCL009, KCL012 and KCL014), the end-systolic LV pressure may vary significantly between two subjects, e.g. according to the level of the heart failure. By increasing the resistance in the Windkessel model, we would increase the end-systolic LV pressure but the LV ejection fraction would decrease. The measured aortic pressure would facilitate the Windkessel model calibration. These are some reasons why we would like to

have the RV and aortic pressures measured in future patients.

7.7.2 Personalization of the biomechanical model

The main mechanical parameters of the model were calibrated manually. Although we projected the nonviable infarcted scar in the computational meshes of the patients with the IHD, the variation of the parameters just between the non-infarcted vs. infarcted part of the heart would not be sufficient. It is caused by the fact that the progression of the IHD over the LV is not uniform and therefore some viable regions may be more kinetic than the others. In the calibration of the passive tissue properties, we assumed that the thin parts of the ventricle had undergone some fibrous remodeling (especially in the DCM patients), therefore we increased the passive tissue stiffness there.

Manual adjustment of the mechanical parameters is a time-demanding process and is subjected to errors in performing the model adjustments. Automatic procedures based on data assimilation techniques (parameter estimation) would be very helpful in this respect. In Chapter 8 we performed an estimation of the contractility parameter in a 'controlled infarct' – the infarct created during an animal experiment. The infarct was special in a sense that it was very extended and the rest of the tissue was completely healthy. Hence, we obtained just two different regions: the infarcted part of the heart and the healthy normokinetic part. The electrical activation was not affected in this case. Although we obtained very encouraging results using those animal data, a direct application of the algorithm on real patients is difficult. The first reason is that the non-infarcted tissue does not have a uniform contractility level. Secondly, the pathological electrical activation needs to be very accurately represented in the model. In the Appendix we will show some promising preliminary results in the estimation of contractility parameters in patient KCL014.

7.7.3 Repolarization times

Estimating the repolarization times from the Ensite data is difficult due to a complicated identification of the repolarization T wave. We used a constant value of APD over the whole myocardium in cases in which the repolarization times could not be extracted from the data. It is known that there are physiological variations of the APD through the wall thickness and also in between segments of the ventricles. If the APD was strictly constant in a LBBB patient with a large offset between the activation of the septum and lateral LV wall, we should see an 'inverse septal flash' in the late systole. The septum should be pushed heavily in the direction of the RV in the time period when the septum is not activated anymore but the LV lateral wall still contracts.

Although we imposed a constant APD we did not observe a pronounced 'inverse septal flash', thanks to the long repolarization phase. In the future, we would like to estimate the repolarization times directly from the Cine MRI using some filtering techniques.

The distribution of repolarization times is important, in order for the model to produce the correct ventricle ejection fraction. This indicator was not measured except for the baseline case (the Cine MRI). Having the estimated repolarization times together with some measurements of the LV ejection fraction at each pacing pattern (e.g. by echocardiography), we could assess the model predictivity also with respect to this global indicator of the heart function.

7.7.4 Analytical activation patterns

The analytical activation patterns did not take into account any local decrease of the conductivity. We only adjusted the direction and velocity of the activation wave propagation, so that the electrical activation would induce the septal flash in the model comparable with the one in the image data. Then, the activation time corresponded approximately to the measured QRSd as well.

We were able to adjust the model so that it represented the baseline activations in patients KCL009, KCL012 and KCL014. When we made the analytical activation more synchronous – by imposing the activation direction along the long axis and increasing the velocity of the propagation – the indicator of max LV dp/dt increased. Moreover, when the timing of the activation in patients KCL009 and KCL012 corresponded to the timing of the re-synchronized patterns, the resulting simulated and measured max LV dp/dt were close to each other. We could have made the analytical patterns even more physiological, e.g. by using two types of propagation velocities – the fast propagation along the given axis and much slower propagation through the ventricle walls. Nevertheless, even with quite simple patterns we were able to set up the patient-specific models accurately.

7.7.5 Patient-specific activation patterns

Simulations with the patient-specific activation patterns obtained by processing the Ensite data were performed for patients KCL009 and KCL012. The predictivity of the model for patient KCL009 was excellent. Therefore we will mainly discuss the results of patient KCL012.

Although the results in patient KCL012 show an increase of the max LV dp/dt in the re-synchronized cases, the simulated max LV dp/dt did not increase sufficiently with respect to the measurements. KCL012 was a patient with an extremely extended DCM (with the LV inner diameter ∼80 mm and the wall thickness in the LV mid-cavity ∼ 8–10 mm) and with a very low LV ejection fraction (∼ 15%). The baseline max LV dp/dt was 680 mmHg/s, which is a very low value. The late-enhancement images did not show any ischemic heart damage, by means of the macroscopic infarctions. Since the function of the LV was severely affected everywhere, it was difficult to distinguish which parts are hypokinetic and which are completely akinetic. Based on our visual observations, we decreased the contractility in the septum.

We saw that the analytical activation patterns represent quite accurately the real activation and the simulated values of max LV dp/dt are very close to the measured ones. In the activation patterns based on the EP mapping, the problem of insufficient max LV dp/dt increase may have arisen from the fact that the estimation of the electrophysiological data was not optimal. The whole pipe-line of the EP data processing consists of several steps and each of them is subjected to some errors, as for example:

- The error in the projection of the measured potentials from the Ensite leads onto the LV endocardium will be larger in more dilated ventricles. The DCM in patient KCL012 was much more developed than in KCL009.
- An error in the XMR registration.
- Modeling errors caused by using a simple EP model (the Eikonal equation).

Finally, we have to point out that the Ensite data themselves include a high level of noise.

7.7.6 Remark: Treppe (Bowditch) effect

The model was calibrated manually for the baseline electrical activation. The heart-rate in the baseline was usually around 60–70/min, while the pacing was performed with the rate of 100/min. It is known that in the healthy heart, the faster stimulation rate increases the myocardium contractility (the so-called Bowditch staircase phenomenon or treppe effect [17], see Figure 7.23). It is probably caused by an accumulation of Ca^{2+} in the sarcoplasm of the cardiomyocytes when the heart-rate increases. We did not take the phenomenon into account, since all our patients had a chronic heart failure. Therefore, for the simulations of the paced activation patterns we we kept all the model parameters as in the baseline – including the tissue contractility – and we only changed the electrical activation.

7.8 Conclusions and perspectives

In this part of the thesis, we showed predictivity of the model with respect to the indicator of max LV dp/dt in patients undergoing cardiac resynchronization therapy (CRT). We were able to set up patient-specific models in the baseline conditions for 8 patients using the analytical activation patterns representing the pathological electrical activation of each patient (the LBBB-like pattern). The models represent the measured Cine MRI data including the timing of the septal flash that was used for calibration of the analytical activation pattern. The simulated LV pressures and LV dp/dt are close to the measured ones.

For two patients, we applied complete patient-specific electrical activation patterns coming from the post-processing of the electrophysiological Ensite data. In the first case, the predictivity of the model was excellent. Although results in the second case were not as accurate, the sensitivity of the predicted LV dp/dt with respect to the pacing patterns was correct.

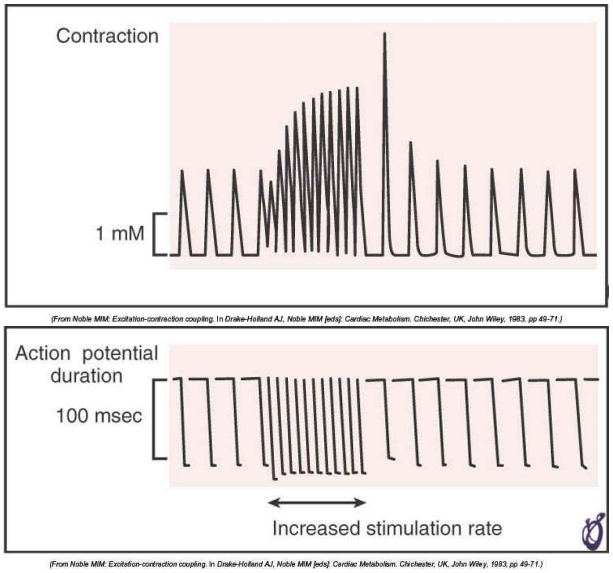

Figure 7.23: An increased heart-rate causes an increase of the force of contraction (Bowditch or treppe effect). From [70].

In the future, we would like to continue in the study and apply the Ensite-based activation patterns on other patients, so that we would fulfill the pre-clinical study. Afterwards, we would like to try to use the model for planning of the CRT before the intervention itself. For each pacing pattern, we would like to evaluate the sensitivity of the LV dp/dt when varying slightly the position of the leads. The modeling of a long-term effect of the CRT would be another challenging step.

The value of max LV dp/dt is established as a clinical indicator of the global LV synchronicity and contractility. It is often used to assess the immediate effect of the CRT mainly since it is easily measured during the CRT implementation. However, it is not certain that the LV dp/dt is the best parameter for assessing neither the short-term, nor the long-term effect of the CRT. The model can provide other mechanical indicators, as for instance the strains and stresses. It is possible that in studying the long-term CRT effects, such quantities – in particular indicators representing local loading of the myocardium – will play an even more important role than the LV dp/dt, and modeling will be crucial in estimating those quantities.

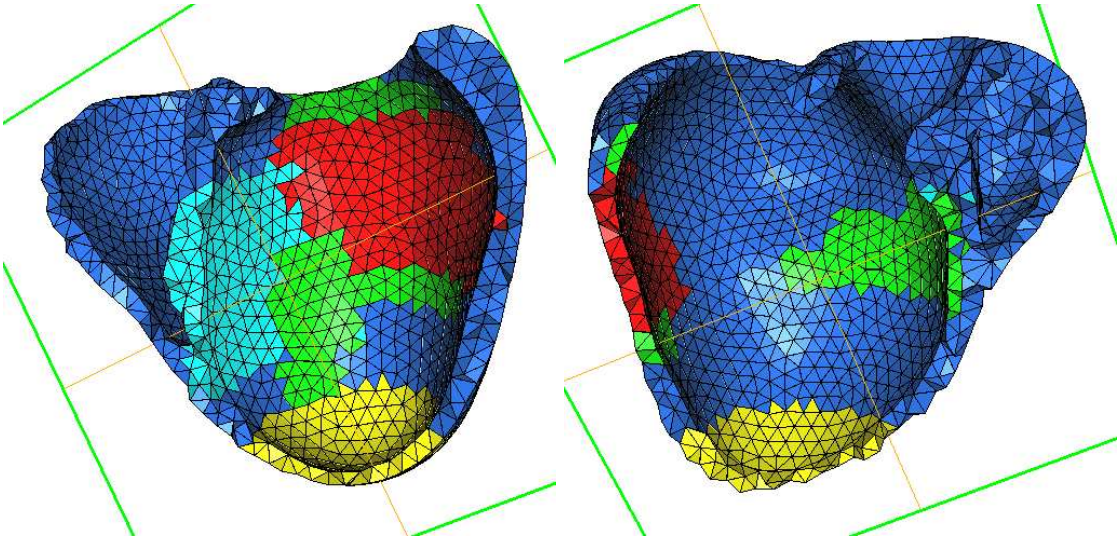

Figure 7.24: Inferior wall view (on the left) and anterior wall view (on the right) of the mesh of KCL014 used for the estimation. The red region corresponds to the transmural infarction, the green to the subendocardial infarction, the yellow to the infarcted apex and the light blue to the hypokinetic septum.

Appendix: Estimation of contractility parameter in KCL014

The case KCL014 is a patient with an IHD with several extended myocardial infarction scars. We projected the non-viable tissue registered from the late-enhancement MR images in the computational mesh and split it into 3 parts: the transmural infarct (TM), the subendocardial infarct (SE) and the infarcted apex. We added a special reference for the septum, which was visibly less kinetic than the rest of the non-infarcted myocardium, see Figure 7.24. We performed an estimation of the contractility parameter with the same set up as in Chapter 8, where all details can be found. As we can see in Figure 7.25, we were successful if the observation surfaces were produced by the direct model itself (synthetic observations). However, when using the segmented real MR images as the observations, the results were inconclusive. The electrical activation pattern could be the main issue, since we used only the simplified analytical prescription of the LBBB-like pattern as in Section 7.5 and we know that the parameter estimation using the real observations (coming from the MR images) is very sensitive to the correct electrical activation pattern.

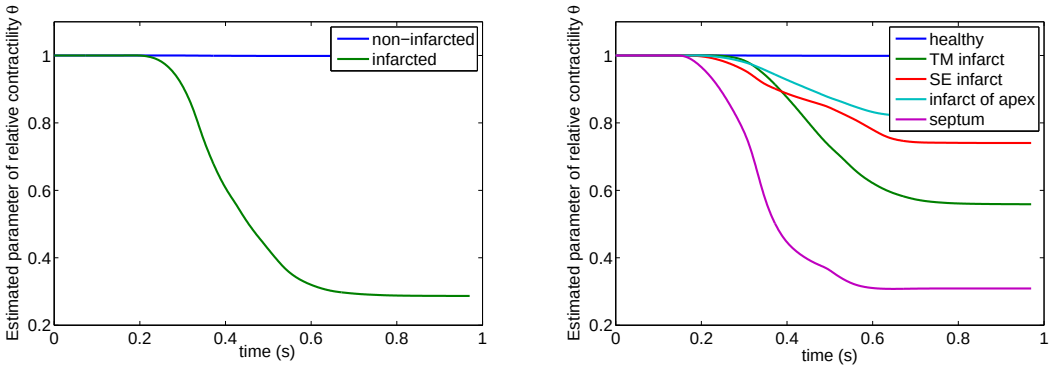

Figure 7.25: Results of estimation of the contractility parameteres using synthetic observations in KCL014.

Chapter 8

Estimation of Tissue Contractility from Cardiac Cine MRI Using the Biomechanical Heart Model

An important part of setting up any biomechanical model is its proper calibration according to the measured data. In order for the model to represent the reality as accurately as possible, the right model parameter values have to be chosen. Some parameter values can be directly connected with the functional state of the modeled system and their abnormal values may be associated with certain diseases. The estimation of such parameters could therefore be used as a diagnostic tool.

In this chapter, we will be using a biomechanical model of the heartbeat described in Chapter 4. This model, even when calibrated manually, can give an important clinical output as shown in Chapter 7. Nevertheless, the goal of this work is to perform an automatic adjustment of a key mechanical property of the model, namely the active tissue contractility. First, the estimated contractility values can improve the model itself. Moreover, they can serve as an indicator of the local heart function, by means of a detection of hypokinetic or akinetic regions in the myocardial tissue as typically arises after a myocardial infarction. To achieve these objectives, we will be using Cine MR image data[1] and data assimilation techniques.

Special data assimilation techniques for parameter estimation in the cardiovascular system were developed in [80], [81] and [79]. For the first application of the algorithms in estimating the contractility parameters using real image data as observations, we would like to use a data set with a pronounced and extended hypokinetic or akinetic region caused by an acute myocardial infarction. At the same time, we would like to test the estimator

[1] Cine MRI stands for a sequence used in cardiac magnetic resonance imaging, that produces 2-dimensional time series images. Usually, the whole ventricle volumes are covered by short axis planes and a few standard long axis projections are acquired as well.

on a healthy data set where the contractility parameters should be quite homogeneous throughout the left ventricle (LV) myocardium. To ensure that the studied pathology (the myocardial infarct) is the only difference between the healthy and the diseased data sets, we decided to design an animal experiment in which a controlled infarction was created. Thanks to this approach, first we obtained all data sets from the same subject. And secondly, we were able to perform some invasive measurements also at the healthy stage, which would be unacceptable for human volunteers.

The animal experiment, including the data acquisition was described in Chapter 6 and Appendix 10 contains the detailed experimental protocol. We also refer to Chapter 6 for the setup and validation of the model in the healthy conditions and after the myocardial infarction. A presentation of Cardiac MRI is given in Section 3.10.1. In the following section we will summarize the experimental data acquisition and the calibration strategy for the healthy and the infarcted hearts.

8.1 Experimental Data and Direct Modeling

8.1.1 Experimental data

The experimental data consist of animal data obtained with a farm pig of 25 kg. The subject was examined and data acquired once in a baseline condition (physiological heartbeat), and 10 and 38 days after the antero-septal infarct creation. The corresponding stages are referred to as baseline, T0+10 and T0+38 in the sequel. The T0+10 data acquisition corresponds to the acute stage of the infarct (edematous necrotic tissue with only slightly diminished wall thickness), while at T0+38 we could already expect – and indeed observed – thinning of the LV wall (caused by resorption of the necrosis and tissue remodeling).

In each of the studied stages (baseline, T0+10 and T0+38), non-invasive MR image data were acquired and pressures in the heart cavities and large vessels were measured. The cardiac MR data consist of Cine MRI, tagged Cine MRI, late enhancement images and phase contrast images. The pressures were measured invasively by means of retrograde catheterization (aortic and left ventricle pressure) and by antegrade catheterization (right atrium, right ventricle, pulmonary artery and pulmonary capillary wedged pressure).

8.1.2 Anatomical model

Anatomical models for each stage were created from the end-diastolic time frames of the Cardiac MR images, according to Section 4.4.1. Fiber directions were prescribed using the values of angles between the short axis plane and the fibers on the epicardium and endocardium -60/60 degrees in LV, and -50/50 degrees in RV. The non-viable tissue in the infarcted stages was segmented from the late enhancement images and projected in the volumic meshes. The left ventricle of each stage was also subdivided into 6 volume regions – which correspond in their upper third to the basal segments of the standard 17-segment

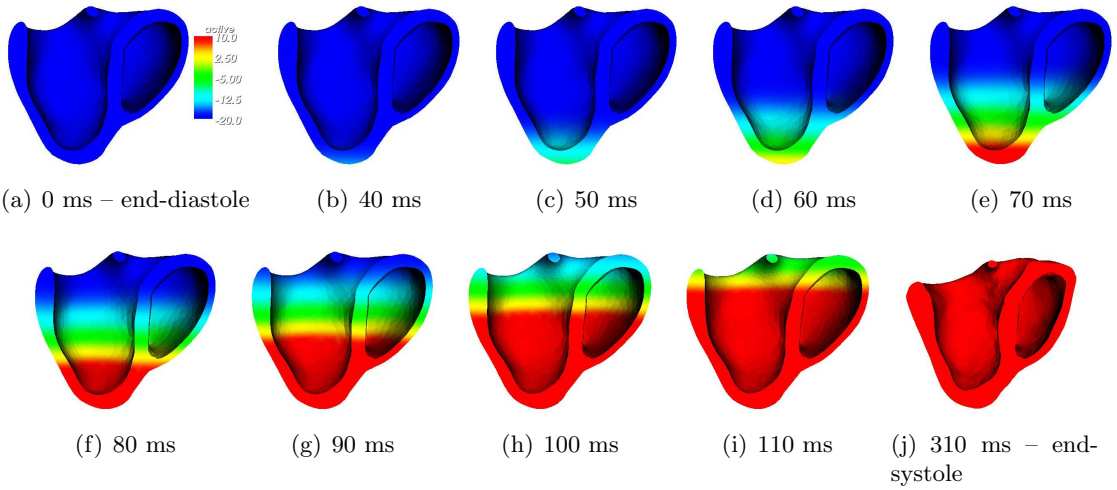

(a) 0 ms – end-diastole (b) 40 ms (c) 50 ms (d) 60 ms (e) 70 ms

(f) 80 ms (g) 90 ms (h) 100 ms (i) 110 ms (j) 310 ms – end-systole

Figure 8.1: Analytical prescription of the electrical activation at the baseline stage: the red activation planar wave propagates from the apex to the base. The activation offset between the apex and the base corresponds to the measured QRSd.

subdivision of the left ventricle proposed by the American Heart Association (AHA) in [21]. The details about this subdivision is given in Section 8.5.1. The 2-region mesh (with the infarcted and the non-infarcted part) and the subdivision of the LV into 6 regions will be used to estimate the contractility parameters in these regions.

8.1.3 Direct modeling

Manual calibration of the healthy heart (baseline stage)

A direct model of the healthy heart was set up by a manual adjustment of the main mechanical parameters of the model, e.g. the active properties (represented by tissue contractility), the passive properties (tissue stiffness). These parameters were kept constant over the whole myocardium. The boundary conditions of the model were prescribed according to Section 4.2.5. We used visco-elastic boundary conditions given by form (4.13) applied on the base of the ventricles (area around the valves) and on the area around the heart apex. The boundary conditions stiffnesses were adjusted so that we preserved the motion of the base of the heart, as seen in the long axis projections of the Cine MR images, and we prevented the apex from displacing. Therefore the stiffness of the boundary condition applied on the apex was higher than for the the boundary condition applied on the base. An additional visco-elastic boundary condition representing a contact between the anterior heart wall with the thoracic cage was used. This boundary condition stiffness was of the

same order as for the apex. Finally, the Windkessel models parameters were adjusted so that the simulated ventricle and arterial pressures would be close to the measured values.

In the direct simulations and also in the estimations we used the following simple electrical activation pattern: the depolarization times were prescribed analytically by a planar wave propagating from the apex to the base of the heart along the long axis (see Figure 8.1). The propagation velocity was adjusted so that the whole myocardium would be activated in a time period corresponding to the measured QRS duration. The action potential duration in the simulation was kept constant over the whole myocardium, and was adjusted according to the Cine MR images and the processed phase contrast data, which quite accurately reflect the timing of valves opening and closure.

Modeling of the infarct at stages T0+10 and T0+38

An acute myocardial infarction is characterized by a sudden drop of contractility in the affected part (see [70, Chap. 50]). At stage T0+10 and even more so at stage T0+38, we can observe in the image data a visibly weaker contraction of the antero-septal part of the left ventricle. The constant parameter of contractility in the whole myocardium – as was calibrated for the baseline – applied at the infarcted stages causes the infarcted region to be much more kinetic in the simulations than in the images and the simulated pressures in the left ventricle overestimate the measured pressure curves. By decreasing the contractility in the infarcted region, the direct model gets closer to the measured image and pressure data.

Conclusion of the direct modeling

The comparison of the direct model v.s. measured data showed that the biomechanical model is capable of representing both the healthy heartbeat, and the infarcted heart (see [22]). The infarct can be modeled by modifying the contractility parameter (the parameter most directly related to the pathology type) and only in the affected region. The model shows a very good predictivity with respect to the global ventricle volumes and local kinematics of the wall of the left ventricle, in this particular pathology.[2]

8.2 Introduction to state and joint state-parameter estimations

Even though we showed in Chapters 6 and 7 that the direct model can be set up manually with very good results with respect to the measured image and pressure data, the goal of this part of the thesis is to automatically correct the direct model by means of *state*

[2]It is a very particular pathology indeed, since we created a large akinetic region (the infarct) whereas the non-infarcted tissue remained completely healthy. Moreover, the non-infarcted part may have reacted by an hypertrophy to compensate for the decreased heart effectivity.

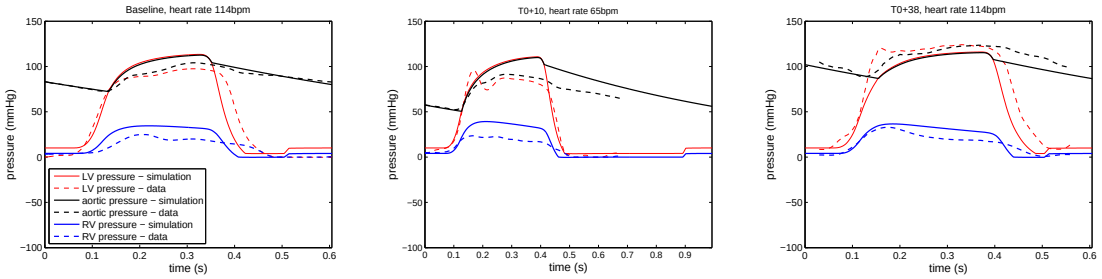

Figure 8.2: Comparison of output pressures of the direct model (solid lines) and the measured values (dashed lines) for each stage of the infarction.

estimation and to estimate some crucial mechanical parameters by means of *joint state-parameter estimation*. The estimation of the state – or of the state and some parameters – is also known as *data assimilation*.

The model used for the estimation process is to some extent a simplification of the direct model described in Chapter 4. Although we use the same material laws, the ventricle pressures are not taken as unknowns of the problem anymore. Their prescription is based on an output pressure value of the direct model. As we can see in Figure 8.2, the measured and the simulated cavity pressures obtained by the direct modeling are very similar. We may think of using the simulated pressures as a regularization of the measured ones. By such an approach we also avoid difficulties with an exact synchronization of the measured pressures with the timing of the electrical activation in the model, e.g. at changes of the cardiac cycle phases (openings and closures of the valves).

8.2.1 Formulation of the problem

The discretized problem (4.19) introduced in Section 4.2.6 can be re-written as the following first order system:

$$\begin{cases} \dot{X} = A(X, \theta, t), \\ X(0) = X_0 + \zeta_X, \\ \theta(0) = \theta_0 + \zeta_\theta, \\ Z(t) = H(X(t)) + \chi, \end{cases} \tag{8.1}$$

with $X = (Y \ \dot{Y})^T$ being the state of the system, where Y and $\dot{Y}$ represent the unknown displacement and velocity vectors of degrees of freedom (DOFs). In the dynamical system given by (8.1), $X(0)$ represents the unknown initial condition with its a-priori knowledge X_0. The θ variables are the unknown parameters in the model with their a-priori knowledge given by θ_0. In our case, the vector θ represents relative contractility values given for each volume region of the left ventricle. The quantities ζ_X and ζ_θ are uncertainties in the initial

condition (in the state) and in the unknown parameters and both need to be estimated during the joint state-parameter estimation. The state and the parameters are estimated using observations $Z(t)$, which are some measurements of the states of the system at time t. The observation $Z(t)$ is associated with the corresponding state $X(t)$ via an observation operator H. The variable χ represents a white noise introduced by the measurement procedure.

In case there is no uncertainty in the parameters θ, the system (8.1) can be written in the form

$$\begin{cases} \dot{X} = A(X,t), \\ X(0) = X_0 + \zeta_X, \\ Z(t) = H(X(t)) + \chi, \end{cases} \tag{8.2}$$

and we only need to perform the state estimation.

8.2.2 Observations and observation operator

The observation operator H is a mapping between the model $X(t)$ and the measured data $Z(t)$. In practice, the measured data are obtained in discrete time snapshots k with a sampling rate ΔT. We can define the measurement in the continuous time t for example by linear interpolation in the following manner:

$$Z(t) = \alpha_k(t) Z_k + (1 - \alpha_k(t)) Z_{k+1}, \quad \text{with} \quad \alpha_k(t) = \frac{(k+1)\Delta T - t}{\Delta T}, \tag{8.3}$$

where $Z_k = Z(k\Delta T)$ and $t \in [k\Delta T, (k+1)\Delta T]$.

The observation operator H can be linear, for example directly given by measured displacements or velocities of certain points in the computational domain (e.g. when using post-processed tagged MR images). In general, the observation operator H is a nonlinear mapping between the model and the measured data. By H' we denote the adjoint operator to H.

8.2.3 Classical assimilation techniques

There are two general approaches for data assimilation – the *variational* and the *sequential* one. We are aiming at estimating the initial condition $X(0) = X_0 + \zeta_X$ and the unknown parameter $\theta = \theta_0 + \zeta_\theta$ in the problem given by (8.1) or just the initial condition $X(0) = X_0 + \zeta_X$ in problem (8.2).

Variational estimation

In the variational approach, we need to minimize a functional of the following form:

$$J(\xi_X, \xi_\theta) = \frac{1}{2} \int_0^T ||Z(t) - H(X(\xi_X, \xi_\theta, t))||^2_{W^{-1}} dt + \frac{1}{2} ||\xi_X||^2_{P^{-1}_{0,XX}} + \frac{1}{2} ||\xi_\theta||^2_{P^{-1}_{0,\theta\theta}}, \tag{8.4}$$

where the trajectory $X(\xi_X, \xi_\theta, t)$ satisfies

$$\begin{cases} \dot{X} = A(X, \theta, t), \\ X(0) = X_0 + \xi_X, \\ \theta(0) = \theta_0 + \xi_\theta. \end{cases} \tag{8.5}$$

The selection of the norms $||\cdot||_{W^{-1}}$ and $||\cdot||_{P_{0,\cdot\cdot}^{-1}}$ in (8.4) is driven by the confidence in the accuracy of observations (the first term of (8.4)) and by the confidence in the a-priori knowledge of the initial condition given by X_0, and in the parameters given by θ_0.

Among the difficulties of the variational approach we should mention the need to compute the adjoint operator and the gradient of (8.4). Each iteration of the assimilation procedure then implies running the whole direct model in the forward and the backward sense (the adjoint problem), to finally obtain the gradient $dJ(\xi_X, \xi_\theta)$ of the system used in the optimization algorithm. There are heavy associated computational and storage costs.

Sequential estimation (filtering)

In sequential estimation (filtering), the model is corrected using the observations during one simulated cardiac cycle and the estimated state $\hat{X}$ – the so-called *observer* – is obtained. The general form for obtaining the corrected state using a filter K_X in problem (8.2), in which we assume no uncertainty in the parameters θ, is as follows:

$$\begin{cases} \dot{\hat{X}} = A(\hat{X}) + K_X(Z - H(\hat{X})), \\ \hat{X}(0) = X_0. \end{cases} \tag{8.6}$$

In the case of the joint state-parameter estimation given by system (8.1), we can introduce the following formalism in order to obtain the system of the form (8.2):

$$X^e = \begin{pmatrix} X \\ \theta \end{pmatrix}, \quad X_0^e = \begin{pmatrix} X_0 \\ \theta_0 \end{pmatrix}. \tag{8.7}$$

Then, the joint state-parameter estimation turns into a state estimation for the *augmented state* X^e:

$$\begin{cases} \dot{X}^e = \begin{pmatrix} \dot{X} \\ \dot{\theta} \end{pmatrix} = \begin{pmatrix} A(X, \theta, t) \\ 0 \end{pmatrix}, \\ X_0^e = \begin{pmatrix} X_0 \\ \theta_0 \end{pmatrix} = \begin{pmatrix} X_0 \\ \theta_0 \end{pmatrix} + \begin{pmatrix} \zeta_X \\ \zeta_\theta \end{pmatrix}, \\ Z^e = (H \;\; 0) \begin{pmatrix} X \\ \theta \end{pmatrix} + \begin{pmatrix} \chi \\ 0 \end{pmatrix}, \end{cases} \tag{8.8}$$

and the observer $\hat{X}^e$ has a form analogous to (8.6).

As a filter K_X in (8.6), we could consider the optimal (*Kalman*) filter (see [58], [59]). Unfortunately, computing the Kalman filter requires handling a covariance matrix P which is full and of the same size as the state, which is practically unrealizable.

8.2.4 Physical filters

Considering the difficulties in applying Kalman filtering in large systems, we use alternative filters that are based on effective feedback control. If the operators A and H are linear, by substituting the error $\tilde{X} = X - \hat{X}$ in (8.6), we obtain

$$\begin{cases} \dot{\tilde{X}} = (A - K_X H)\tilde{X} - K\chi, \\ \tilde{X}(0) = \zeta_X. \end{cases} \tag{8.9}$$

We aim at $\tilde{X} \to 0$ rapidly. This problem is transformed in the problem of stability of the operator $A - K_X H$ at the critical point 0. According to the theory of stability (see [50], [33]), we need to choose the filter K_X so that the eigenvalues of the operator $(A - K_X H)$ have negative real part. This so-called *Luenberger asymptotic observer* was introduced in [71] and the following filters are based on this approach.

Direct velocity feedback (DVF)

Assuming our observations consist of measured velocities, we can apply forces proportional and opposed to the velocity errors, directly at the measured locations. This standard technique in the control of mechanical structures is called *direct velocity feedback* (DVF, see [89], [29]). To present this method, let us assume that our problem is linear and given by the following equation:

$$M\ddot{Y} + C\dot{Y} + KY = F, \tag{8.10}$$

with M, C, K being the mass, damping and stiffness matrices, Y the unknown displacement vector for DOFs as in (4.17) and we aim at correcting the state using the observations (measured velocities). According to [80], the filter K_X can be simply given by

$$K_X = \begin{pmatrix} 0 \\ \gamma H' M^{-1} \end{pmatrix}, \tag{8.11}$$

with a parameter $\gamma > 0$. Then the observer for the linear model given by the equation (8.10) is:

$$M\ddot{\hat{Y}} + C\dot{\hat{Y}} + K\hat{Y} = F + \gamma H'(Z - H\dot{\hat{Y}}), \tag{8.12}$$

or equivalently

$$M\ddot{\hat{Y}} + (C + \gamma H'H)\dot{\hat{Y}} + K\hat{Y} = F + \gamma H'Z. \tag{8.13}$$

The positive factor $\gamma H'H$ on the left hand side of (8.13) ensures the dissipative effect of the filter. The gain parameter γ governs the effectivity of the state estimator. The

optimal value of γ for the linear problem (8.10) can be derived by considering the following quadratic eigenvalue problem (QEP):

$$\begin{pmatrix} 0 & K \\ -K & -C-\gamma(H'H) \end{pmatrix} V = \lambda \begin{pmatrix} K & 0 \\ 0 & M \end{pmatrix} V. \tag{8.14}$$

The parameter γ stabilizes the original problem by shifting the eigenvalues solutions of (8.14) towards the negative real plane. A detailed analysis of the damping properties of DVF filter K_X is in [80].

In the joint-state parameter estimation in system (8.1), we can combine the approach of an augmented state formulation as introduced by (8.7) with an application of the DVF filter for the state estimation. Therefore the augmented observer will have the following form:

$$\hat{X}^e = \begin{pmatrix} \hat{X} \\ \hat{\theta} \end{pmatrix}, \tag{8.15}$$

where $\hat{X}$ denotes the state observer for a given parameters θ computed by using the 'cheap' state filter based on DVF, and the classical Kalman filtering is reduced only on the space of the parameters θ. A detailed presentation of this extension for the joint state-parameter estimation is also presented in [80] and an extension for the nonlinear problems by means of the *reduced-order unscented Kalman filtering* (UKF) is in [79]. We note that the UKF approach is highly parallelizable and the final parameter estimation in n regions is obtained by $n+1$ independent computations, each of them comparable with the direct simulation.

Since our observations do not consist of measured velocities in general, we cannot directly use the DVF approach. In the following paragraph, we describe a generalized observation operator based on measuring distances between the surfaces of estimator and the observations (represented by the surfaces obtained from Cine MRI), and the estimation procedure using such an observation operator.

Distance discrepancy operator

In our problem, the estimation process is performed only in the left ventricle. We take the endocardial and epicardial surfaces of the left ventricle obtained by segmenting the Cine MR images as the observations. Such a choice may be limiting with respect to the observability of the intra-myocardial parts and also the wall motion tangential to the surfaces cannot be observed. However, data needed for creating such observations are available for any examined subject.[3] We denote the surfaces segmented from the k-th time frame image by S_{LVendo_k} and S_{LVepi_k}, and $S_k = S_{LVendo_k} \cup S_{LVepi_k}$. The segmentation of the contours is difficult in regions around the valves (above AHA segments 1–6) and around

[3]Typically, we need dynamic MR or CT image data covering the whole volume of the ventricles. These type of image data are becoming common in clinical practice. In our case, we used multiple 2D acquisitions of Cine MRI taken in short axis views.

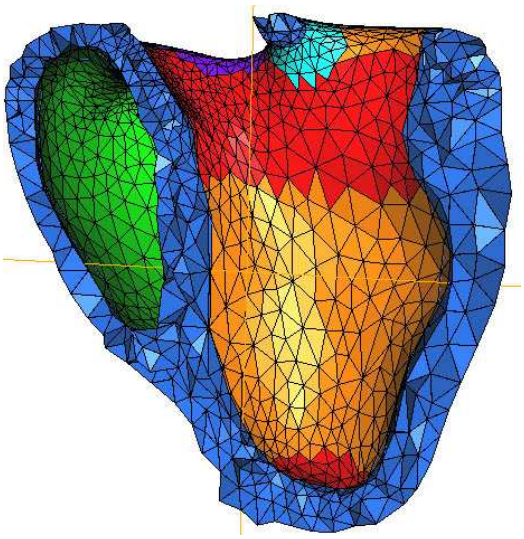

(a) Computational mesh, view from the anterior side. The endocardial surface of the LV used for the estimation $\partial\hat{\Omega}_{OBSendo}$ is in orange color. The red part of the LV endocardium was considered to be non-observable. Similarly, a part of the LV epicardial surface was selected (including RV endocardium of the septum).

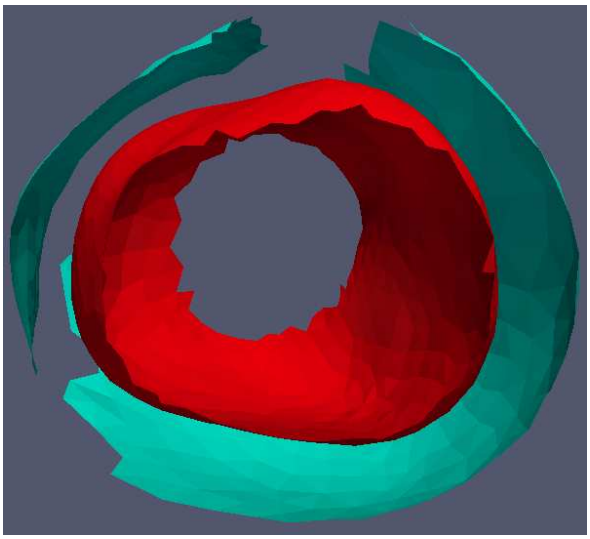

(b) Example of synthetic observations – parts of LV endocardial (in red) and epicardial (in blue) surfaces viewed from top. The surfaces were produced directly by the model. They were truncated in the same way as the real MR observations.

Figure 8.3: Computational mesh and examples of synthetic observations.

the apex because of the low resolution of the short axis Cine MR images and the anatomical complexity at these locations, as discussed in Section 4.4.1. Therefore, we perform the estimations only in the parts of the left ventricle corresponding to AHA segments 1–16 using the parts of LV endocardial and epicardial surfaces adjacent to those regions, see Figure 8.3(a). We denote these surfaces of the estimator by $\partial\hat{\Omega}_{OBSendo}$ and $\partial\hat{\Omega}_{OBSepi}$ (the observable parts of LV endocardial and epicardial surfaces), $\partial\hat{\Omega}_{OBS} = \partial\hat{\Omega}_{OBSendo} \cup \partial\hat{\Omega}_{OBSepi}$.

Using the observations as described above, we introduce the discrepancy operator given by measuring distances between the surfaces of the estimator $\partial\hat{\Omega}_{OBS}$ and the observations S_k. Let the k-th reference surface correspond to time t of the simulation. Then the state matches the given observation if

$$\mathrm{dist}(x_t, S_k) = 0 \quad \forall x_t \in \partial\hat{\Omega}_{OBS}, \tag{8.16}$$

where $\mathrm{dist}(x_t, S_k)$ stands for the signed distance of a point x_t to surface S_k and

$$\mathrm{dist}(x_t, S_k) = \begin{cases} \mathrm{dist}(x_t, S_{LVendo_k}) & \text{if} \quad x_t \in \partial\hat{\Omega}_{OBSendo}, \\ \mathrm{dist}(x_t, S_{LVepi_k}) & \text{if} \quad x_t \in \partial\hat{\Omega}_{OBSepi}. \end{cases} \tag{8.17}$$

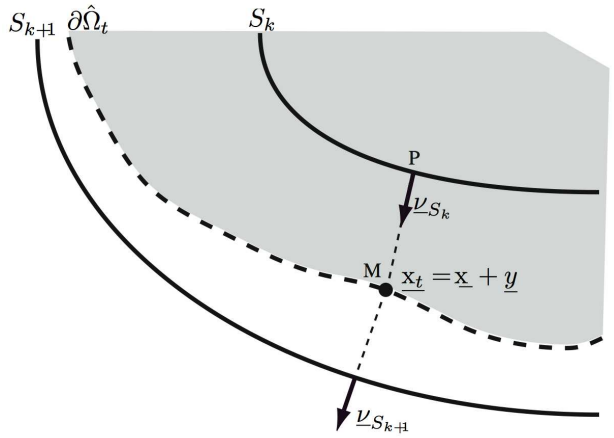

Figure 8.4: Projection of simulated contour $\partial\hat{\Omega}_t$ on segmented surfaces S_k and S_{k+1}.

We can extend the distance operator on the full finite element model and denote it by $\text{dist}(\hat{X}^d, S_k)$. Then, the condition $\text{dist}(\hat{X}^d, S_k) = 0$ can be directly compared with the usual measurement matching condition, i.e. $Z - H(\hat{X}) = 0$, and the distance operator represents an extension of the the observation quantity $Z - H(\hat{X})$ that we call discrepancy operator. By interpolation, we can obtain the discrepancy operator for any simulated time t ([81]):

$$W_d(\hat{X}^d, t) = \alpha_k(t)\,\text{dist}(\hat{X}^d, S_k) + (1-\alpha_k(t))\,\text{dist}(\hat{X}^d, S_{k+1}),\ \ \forall t \in [k\Delta T, (k+1)\Delta T], \quad (8.18)$$

with $\alpha_k(t)$ defined as in (8.3).

Schur displacement feedback (SDF)

Compared to DVF where the observed velocities are used for the model correction, in the state estimation based on the Schur displacement feedback (SDF) we can directly use the displacements as observations. We will demonstrate the SDF method on a simple linear problem given by (8.10). We introduce the notation $X = (X^d\ X^v)^T$, where X^d and X^v represent the displacement and velocity vectors of DOFs. Then, using the filter

$$K_X = \begin{pmatrix} \gamma K^{-1} H' \\ 0 \end{pmatrix}, \quad (8.19)$$

with a parameter $\gamma > 0$, the observer of (8.10) can be written in the following form ([81]):

$$\begin{cases} K\dot{\hat{X}}^d = K\hat{X}^v + \gamma H'(Z - H\hat{X}^d), \\ M\dot{\hat{X}}^v + C\hat{X}^v + K\hat{X}^d = F. \end{cases} \quad (8.20)$$

The corresponding quadratic eigenvalue problem (QEP) has the following form:

$$\begin{pmatrix} \gamma H'H & K \\ -K & -C \end{pmatrix} V = \lambda \begin{pmatrix} K & 0 \\ 0 & M \end{pmatrix} V. \tag{8.21}$$

By analyzing the QEP, we can find the optimal value of the gain γ (see [81]):

$$\gamma_{opt} = \sqrt{2}\omega_0 + \text{h.o.t.}, \tag{8.22}$$

where ω_0 is the lowest eigenfrequency of QEP (8.21).

Considering our type of observations and the discrepancy operator W_d given by (8.18), System (8.20) turns into ([81]):

$$\begin{cases} K\dot{\hat{X}}^d = K\hat{X}^v - \gamma \left(\frac{\partial W_d}{\partial Y}\right)' W_d(\hat{X}_d, t), \\ M\dot{\hat{X}}^v + C\hat{X}^v + K\hat{X}^d = F, \end{cases} \tag{8.23}$$

with the following variational term associated to $\left(\frac{\partial W_d}{\partial Y}\right)' W_d(\underline{x}_t, t)$:

$$\int_{\Gamma_m} \text{dist}(\underline{x} + \underline{y})(\underline{\nu}_{S_k} \cdot \delta\underline{y}) dS, \tag{8.24}$$

with the notation according to Figure 8.4.

The effective joint state-parameter estimation for the original non-linear problem (8.1) is based on the application of reduced-order unscented Kalman filtering (UKF) on an augmented system with the state estimator based on SDF, in the same way as was presented for DVF.

In the following parts, we will be dealing with the application of the estimation methods described above, namely the estimation based on the SDF and the measurement of distances between the contours of the model and observations. The input data were acquired during the animal experiment and we will be using the pre-calibrated direct model representing the baseline stage. We emphasize that – by construction of the filtering procedure – the estimated parameter values plotted in the following sections evolve during the simulation period – corresponding to a complete heartbeat in our case – and of course the actual estimation is achieved with the final values.

8.3 State estimation

The data obtained at the baseline stage come from a healthy subject without any cardiac pathology. We can assume that the contractility parameter will not significantly vary over the myocardium of the left ventricle. Indeed, we saw in Chapter 6 that a direct model with constant contractility simulates the healthy stage adequately. We are going to correct the

direct model representing the baseline stage using the observation surfaces by means of the state estimation.

As discussed in Section 8.2.4, to perform the state estimation we apply corrections based on the computed distances between the simulated and measured surfaces, both for the endocardial and epicardial contours (Schur displacement feedback, SDF). As the efficiency of the state filter is conditioned by the gain γ, we will test and compare the resulting corrected simulations when using the following values of γ:

- the optimal value γ_0 with respect to the state estimator by means of an analysis of the eigenvalues and eigenfrequencies of QEP of the linearized problem (8.21), see [81].
- an increased value $\gamma = 8\gamma_0$.
- an intermediate value $\gamma = 20\gamma_0$.
- a large value $\gamma = 40\gamma_0$.

In Figure 8.5, we superposed the contours of the direct (non-corrected) model, the contours of the corrected models, as well as the observation surfaces in the MR image data. In Figure 8.6 we plot distance errors between the simulated and segmented surfaces for LV subdivided into 6 regions according to Section 8.5.1. The resulting distance errors are summarized in Table 8.1. As we can see, the state estimator becomes effective when the value of γ is greater than $8\gamma_0$. For the lower values, the estimated model is almost identical to the direct model. The reason why the 'optimal value' of γ is not sufficient for the corrections is that γ_0 was computed using the spectral analysis – which pertains to the linear problem – whereas our problem is highly nonlinear. A second reason may be errors in the observations (e.g. due to noise in the data or segmentation errors). However, a strong correction by using a high value of the gain γ can induce some non-physical behaviour, for example incorrect high stresses. The strong state estimator may also influence the estimation of parameters in the joint state-parameter estimation, as will be presented later. Note also in Figure 8.5 that the error in the direct model is rather large in the beginning of the diastole (time $\sim$400 ms). One reason comes from the fact that we used a constant value of the action potential duration. This is why – although the activation onset corresponds quite well to the Cine MRI data – the onset of the relaxation does not sufficiently fit the data.

8.4 Adjustment of the joint state-parameter estimator

The joint state-parameter estimator will be set up using the mesh of the stage T0+38 subdivided into 2 volumic regions – the infarcted and the non-infarcted parts. The estimations will be initialized by constant contractility over the whole myocardium ($\theta_{init} = 1$ in each volume region), using the same contractility value as in the direct model of the baseline

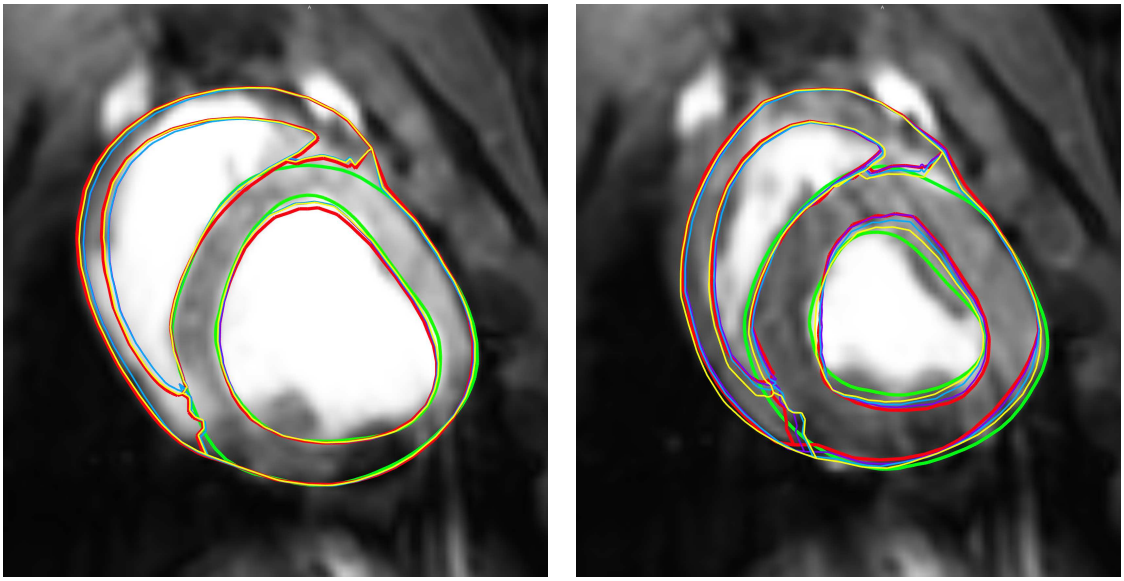

(a) End-diastole (b) End-systole

Figure 8.5: State estimation at the baseline stage. With increasing values of the state estimation gain γ, the corrected model is approaching the observations (in green). Colors correspond to γ values $8\gamma_0$ (purple color, almost completely hidden by the red contour of the direct model), $20\gamma_0$ (light blue) and $40\gamma_0$ (in yellow).

Region	1	2	3	4	5	6
Direct model	2.2 / 1.2	2.8 / 1.4	1.9 / 3.7	3.1 / 4.1	2.8 / 2.7	2.3 / 2.6
StateEstim γ_0	2.5 / 0.9	3.0 / 1.2	1.9 / 3.8	2.6 / 3.7	3.0 / 2.3	2.4 / 2.4
StateEstim $8\gamma_0$	1.7 / 0.9	2.5 / 1.2	1.7 / 3.2	2.1 / 3.2	2.7 / 2.3	1.8 / 2.2
StateEstim $20\gamma_0$	1.1 / 0.8	1.8 / 1.0	1.7 / 2.2	2.0 / 2.4	2.1 / 2.0	1.7 / 1.8
StateEstim $40\gamma_0$	0.9 / 0.7	1.2 / 0.7	0.8 / 1.3	1.4 /1.4	1.4 /1.4	1.3 / 1.2

Table 8.1: Distance errors (in millimeters) for the LV **endocardial / epicardial** surfaces at the baseline stage in the direct simulation and in the state estimation. The surfaces were divided into 6 parts according to the volumic mesh subdivision, and the mean distance from the observation was computed for each observation step. The values in the table are maxima of the mean errors for each region over the whole cardiac cycle.

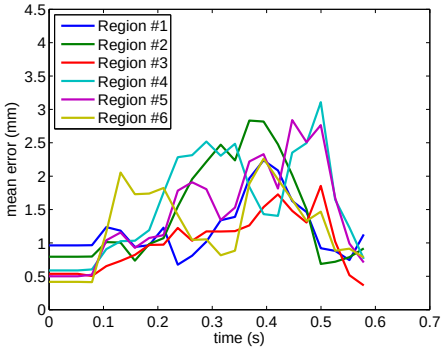

(a) Direct model, endocardial error

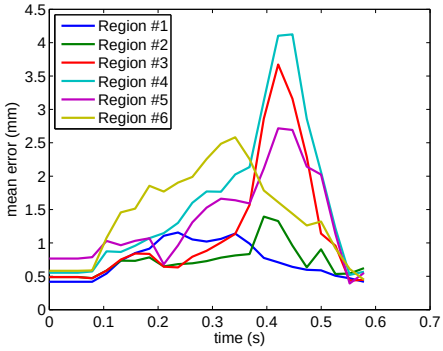

(b) Direct model, epicardial error

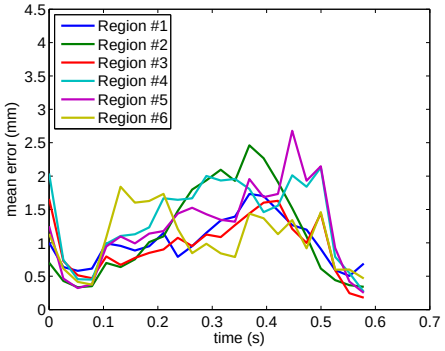

(c) State estimation, $\gamma = 8\gamma_0$, endocardial error

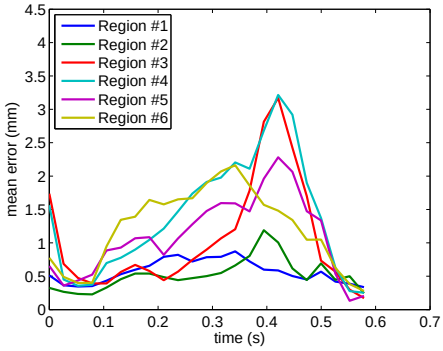

(d) State estimation, $\gamma = 8\gamma_0$, epicardial error

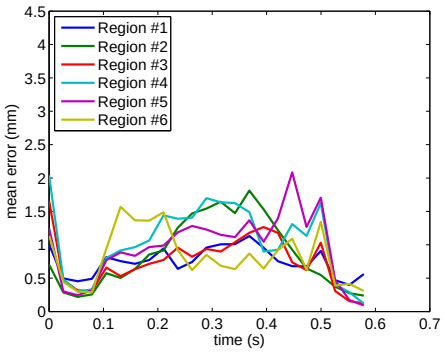

(e) State estimation, $\gamma = 20\gamma_0$, endocardial error

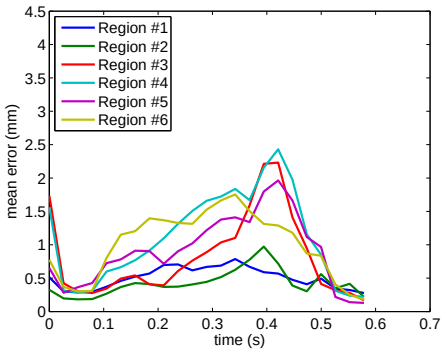

(f) State estimation, $\gamma = 20\gamma_0$, epicardial error

Figure 8.6: Mean error over the LV endocardial and epicardial surface regions at the baseline stage during the cardiac cycle. The errors were computed for the direct model and for the model corrected by the state estimator with increasing the values of gain γ.

stage. The direct model with the constant contractility cannot represent the hypokinetic infarcted part of the stage T0+38, as was discussed in Section 8.1.3. This will be corrected by the joint state-parameter estimator. For preliminary adjustments of the estimator, we will be using synthetic observations produced by the direct model itself. More detailed adjustments will be performed using real Cine MR image data.

8.4.1 Estimation using synthetic observations

The synthetic observations were obtained from the direct model of the heartbeat by reducing the contractility in the infarcted part by a factor 4. The endocardial and epicardial surfaces were exported with a temporal resolution of 26 ms (Δt^{obs}) which corresponds to that of the Cine MRI at stage T0+38. See Figure 8.3(b) for an example of such surfaces.

The confidence in the observations is given by

$$J_T = \int_0^T ||Z(t) - H(X(\xi_X, t))||^2_{W^{-1}} dt, \tag{8.25}$$

which has the discrete form

$$J_n = \sum_{k=0}^{n} (Z(t_k) - H(X(t_k)))^T W_k^{-1} (Z(t_k) - H(X(t_k))), \tag{8.26}$$

where $\{t_k\}_{k=0}^n$ corresponds to the time discretization of the simulation. The covariance W_k^{-1} depends on the time discretization step $\Delta t^{sim} = t_k - t_{k-1}$ in the following way:

$$W^{-1}\Delta t^{sim} = W_k^{-1}, \quad \text{hence} \quad W = W_k \Delta t^{sim}. \tag{8.27}$$

We assume that the expected spatial errors in the observations given by the covariance W_{obs} have white noise characteristics and the covariances corresponding to each observation time step are independent. Therefore,

$$W = \Delta t^{obs} W_{obs}, \tag{8.28}$$

where Δt^{obs} is the time step of the observation snapshots. Then, if we want to define discrete criteria (8.26) we need to have according to (8.27) and (8.28)

$$\Delta t^{sim} W_k = \Delta t^{obs} W_{obs}. \tag{8.29}$$

In our case, $\Delta t^{obs} \sim 26$ ms and $\Delta t^{sim} \sim 1$ ms. We tested the following values of W_k:

- $W_k = 10^{-6}$ mm^2, for the level of expected noise in the observations $W_{obs} \sim (0.25 \text{ mm})^2$
- $W_k = 10^{-5}$ mm^2, for the level of expected noise in the observations $W_{obs} \sim (0.60 \text{ mm})^2$

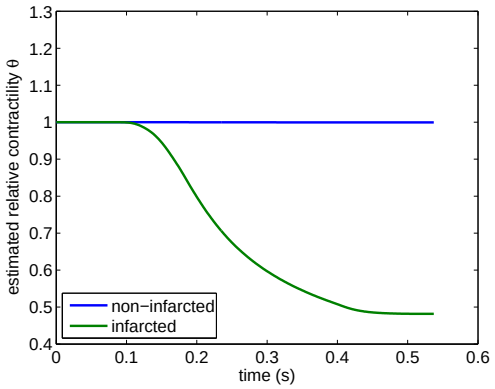

(a) $W_k = 10^{-6}$ mm^2, $P_{0,\theta\theta} = \frac{1}{2}\mathrm{diag}(10^{-3}, 1)$

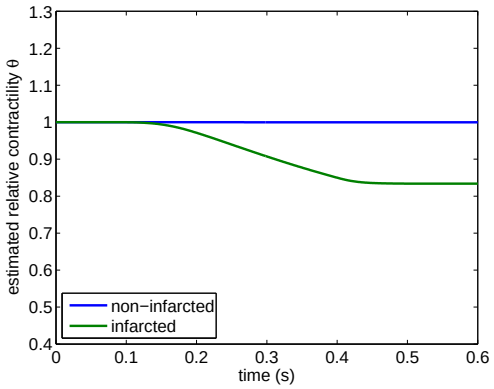

(b) $W_k = 10^{-5}$ mm^2, $P_{0,\theta\theta} = \frac{1}{2}\mathrm{diag}(10^{-3}, 1)$

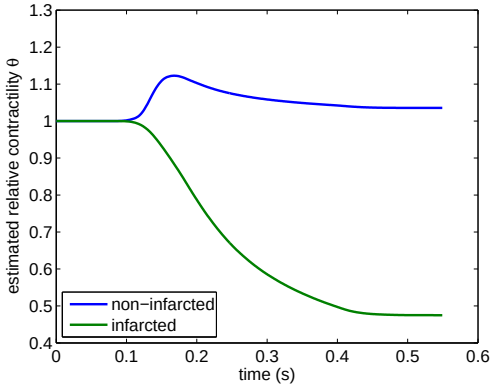

(c) $W_k = 10^{-6}$ mm^2, $P_{0,\theta\theta} = \frac{1}{2}\mathbf{1}$

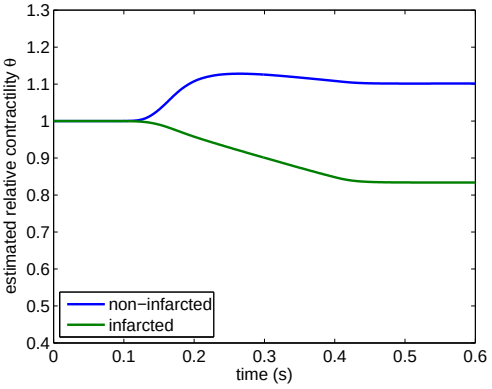

(d) $W_k = 10^{-5}$ mm^2, $P_{0,\theta\theta} = \frac{1}{2}\mathbf{1}$

Figure 8.7: Parameter of relative contractility θ estimated in a 2-region mesh of stage T0+38 with the non-infarcted and the infarcted region using synthetic observations.

Figure 8.7 shows that by increasing the level of expected noise, the sensitivity of the estimator decreases. At the same time, we either fixed the contractility value in the non-infarcted tissue (using a low value corresponding to the healthy tissue in the covariance matrix $P_{0,\theta\theta}$) or we used the unit covariance matrix (in order not to fix the contractility anywhere). As we can see also in Figure 8.7, the two choices of the covariance matrix did not substantially change the results.

8.4.2 Estimation using real MR images as observations

In this section, we focus on some other issues in the setup of the joint state-parameter estimator, in order to detect the infarcted (hypokinetic) regions in the left ventricle, without any a-priori knowledge. From now on, we will be using *real observations* obtained by segmenting the Cine MR images, as was discussed in Section 8.2.4. We will keep the value of expected noise $W_k = 10^{-6}$ and we will be using the unit covariance.

Passive tissue stiffness

From the histological analysis of the infarcted stages we should assume that the passive tissue stiffness would vary between the infarcted and the non-infarcted regions. Due to the remodeling of the antero-septal part of the apex at stage T0+38 by means of a thinning of the akinetic wall and replacement of the myocardium by fibrous tissue, we may expect an increase of the passive tissue stiffness at this location. However, the edematous recent infarct at stage T0+10 can be associated with a decreased passive tissue stiffness.

In this work, we are not focusing on estimating the passive tissue properties. Since we would like to find the infarcted region without any a-priori knowledge of its location we will keep the value of the passive tissue stiffness constant in the whole myocardium and for all 3 stages.

Nevertheless, in Figure 8.8 we tested the impact of the actual value of the passive tissue stiffness on the estimation of the system. A very high value of the tissue stiffness prevents the myocardium from contracting and the difference between displacements when varying the contractility is getting lower. Hence, the observability of the infarct decreases. For this reason, we would rather be using a lower value of the stiffness. However, the thin wall infarcted tissue may tend to bulge, especially if the modeled tissue stiffness is lower than the actual correct value. In our case, the bulging will be prevented by boundary conditions representing a contact with the surrounding tissues (thoracic cage).

Gain of the state estimator γ

As in Section 8.3, we performed the state estimation – and further the joint state-parameter estimation – first using the optimal state estimator gain γ with respect to the state estimator by means of an analysis of eigenvalues and eigenfrequencies of the linearized problem ($\gamma = \gamma_0$), and also with larger gains ($8\gamma_0$, $20\gamma_0$ and $40\gamma_0$).

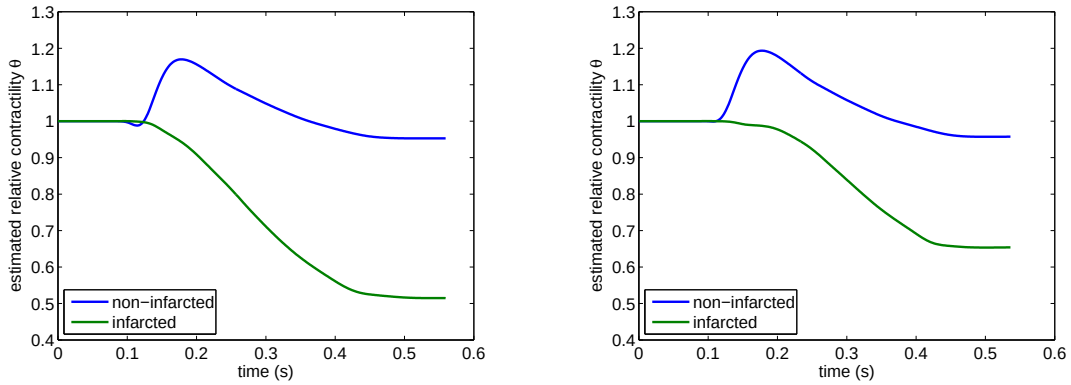

(a) T0+38, the passive tissue stiffness as in Table 8.2

(b) T0+38, increased passive tissue stiffness (multiplied by factor 2)

Figure 8.8: Parameter of relative contractility θ estimated in a 2-region mesh of stage T0+38 with the non-infarcted and the infarcted region using real observations. The observability of the infarct is reduced if the stiffer tissue is assumed.

We compared the direct (uncorrected) simulation performed with constant contractility values, either with the correction just by the state estimator or by the state-parameter estimator. In Figure 8.9(a), we can see separately the role of each of them. Depending on the gain of the state estimator, the model either gets closer to the observations (for the large state estimator gain γ) or stays almost exactly at the position of the direct model. When performing the joint state-parameter estimation, the model is well corrected even if the low gain γ is used, as illustrated in Figure 8.9(b).

Figure 8.10 shows that no matter which value of γ was used, the contractility parameters were well retrieved. To assess which value of γ is the best, we will have to perform further tests on a more refined subdivision of the left ventricle.

Finally, in Figure 8.11 we can see a comparison of the contractility estimation in the 2-region meshes for the infarcted stages (T0+10 and T0+38), using settings of the estimator according to Table 8.2. The same parameters of the estimator will be used in all the following estimations, with the exception of testing several values of the state estimator gain γ.

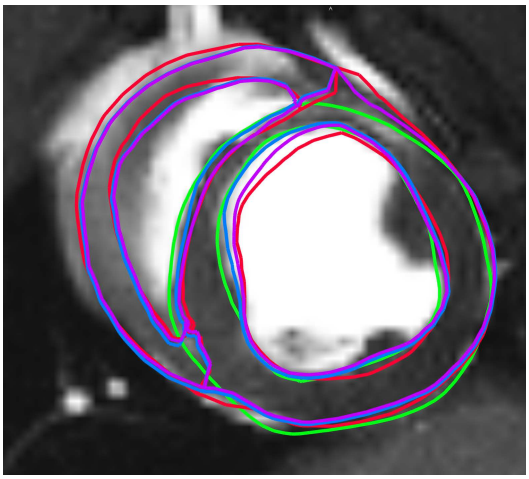

(a) Comparison of the state estimation in purple and the joint state-parameter estimation (in blue). $\gamma = 20\gamma_0$, in both cases.

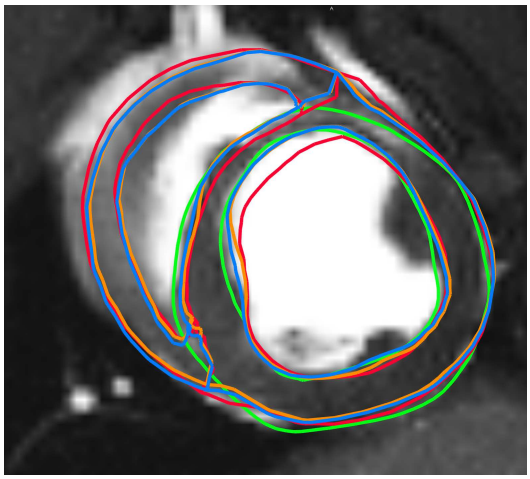

(b) Comparison of the joint-state parameter estimation using the gain γ with an optimal value wrt. state estimator ($\gamma = \gamma_0$, in orange) and $\gamma = 20\gamma_0$ (in blue).

Figure 8.9: End-systolic image at stage T0+38. Direct model with constant contractility in red, observations (the segmented surfaces) are in green.

Parameter	Value	Note
γ	$20\gamma_0$	state estimator gain
W_k (mm^2)	10^{-6}	level of expected noise in the observations
$P_{0,\theta,\theta}$	$\frac{1}{n}\mathbf{1}$	an identity covariance matrix
κ_1 (Pa)	$5 \cdot 10^3$	constant passive tissue stiffness in the myocardium
κ_2 (Pa)	40	constant passive tissue stiffness in the myocardium
bulk modulus (Pa)	$5 \cdot 10^5$	constant passive tissue stiffness in the myocardium

Table 8.2: Setup of the joint state-parameter estimator used for automated detection of the hypokinetic regions of the left ventricle. Parameter γ_0 stands for the optimal gain of the state estimator discussed in Section 8.3, parameter n stands for the number of regions in which the unknown parameter is to be estimated and $\mathbf{1}$ is a unit matrix of size n.

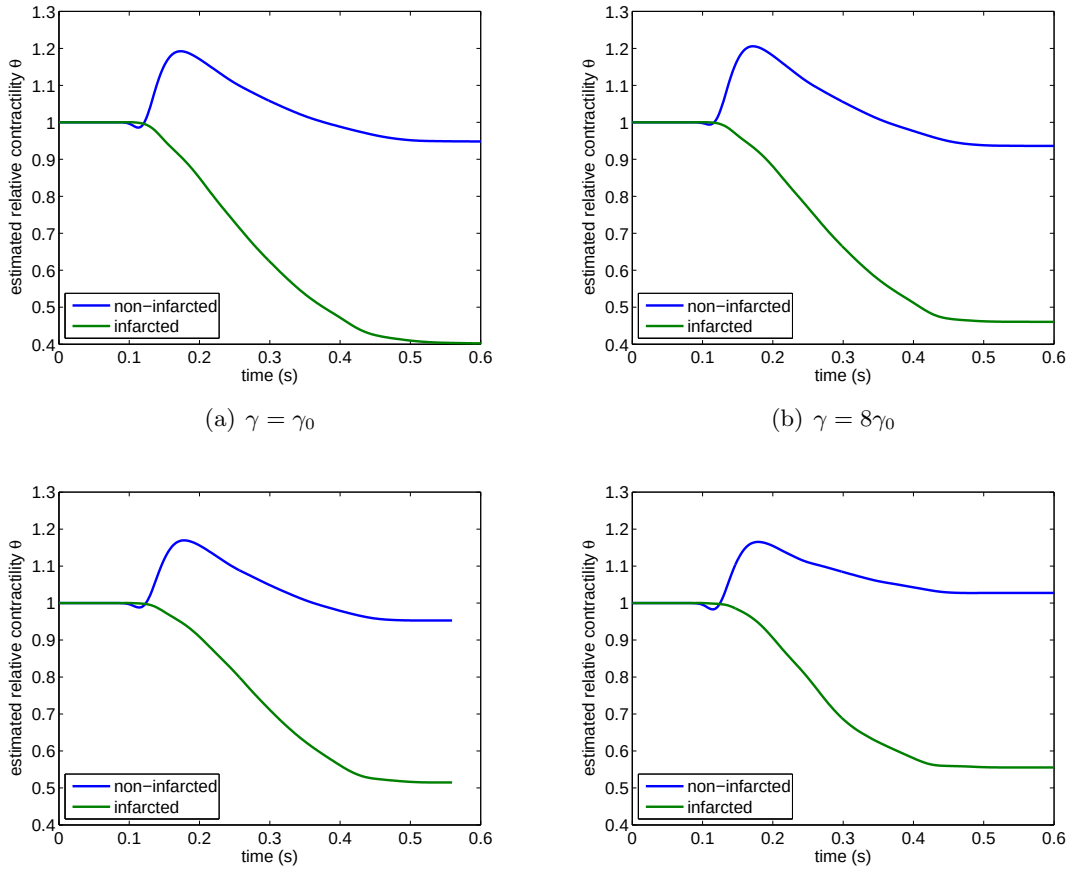

(a) $\gamma = \gamma_0$ (b) $\gamma = 8\gamma_0$

(c) $\gamma = 20\gamma_0$ (d) $\gamma = 40\gamma_0$

Figure 8.10: Parameter of relative contractility θ estimated in a 2-region mesh of stage T0+38 with the non-infarcted and the infarcted region using real observations, with different values of the state estimation gain γ.

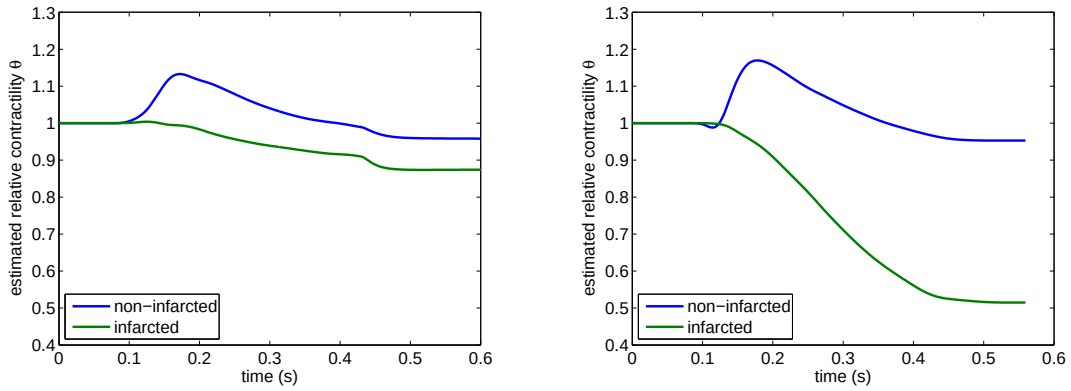

(a) T0+10 (b) T0+38

Figure 8.11: Parameter of relative contractility θ estimated in a 2-region mesh of stages T0+10 and T0+38 with the non-infarcted and the infarcted region using real observations.

8.5 Automatic contractility personalization and detection of hypokinetic regions

In this section we will try to retrieve contractility parameters using a general subdivision of the left ventricle myocardium that does not take into account the infarct location. The objectives are twofold. First, the parameter estimation provides an automatic personalization of the model, which enables further applications for predictive purposes as in therapy planning. Secondly, the estimated parameters may help to localize and quantify the infarcted region automatically with respect to the ventricle subdivision.

8.5.1 Subdivision of the myocardium

We created computational meshes with 6(+1) volumic regions in the following way: First, the left ventricle was truncated by two short-axis planes that detached the apical and the basal parts of the left ventricle in which the observations are missing. These parts of the left ventricle together with the myocardium of the right ventricle form a volumic region #0 that will be considered as a *non-observable region*. Then, the observable left ventricle myocardium was divided into 6 circumferential regions. These regions correspond in their upper third to the basal segments of the standard 17-segment LV subdivision according to AHA ([21]). See Figure 8.12 and Table 8.3 for the subdivision of the meshes into 6(+1) regions. Tables 8.4 and 8.5 show the proportion of tissue marked by the late enhancement in each region.

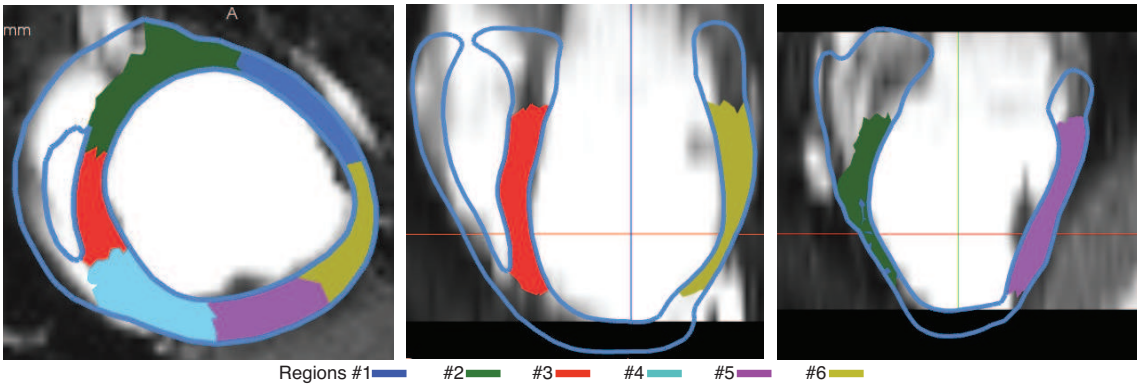

Figure 8.12: Mesh of T0+38 subdivided into 6(+1) volumic regions. The part of myocardium not filled with color represents the *non-observable regions* with the volumic reference #0.

Region	AHA segments	Note
0	–	all parts without observations (RV, apex and base of the LV around valves)
1	1+7+extension to the apex	anterior part of the LV
2	2+8+extension to the apex	antero-septal part of the LV
3	3+9+extension to the apex	infero-septal part of the LV
4	4+10+extension to the apex	inferior part of the LV
5	5+11+extension to the apex	infero-lateral part of the LV
6	6+12+extension to the apex	antero-lateral part of the LV

Table 8.3: The 6(+1)-region mesh subdivision based on the circumferential subdivision of the left ventricle according to AHA.

Region	Name of the region	volume of the region	proportion of the infarct
0	non-observable	152mL	2%
1	anterior	12mL	36%
2	antero-septal	14mL	53%
3	infero-septal	12mL	19%
4	inferior	15mL	0%
5	infero-lateral	11mL	0%
6	antero-lateral	11mL	3%

Table 8.4: Relative extent of the infarct for each region in the 6(+1)-region mesh of T0+10.

Region	Name of the region	volume of the region	proportion of the infarct
0	non-observable	121mL	3%
1	anterior	11mL	45%
2	antero-septal	15mL	64%
3	infero-septal	10mL	20%
4	inferior	16mL	0%
5	infero-lateral	12mL	0%
6	antero-lateral	13mL	0%

Table 8.5: Relative extent of the infarct for each region in the 6(+1)-region mesh of T0+38.

8.5.2 Joint state-parameter estimation at baseline, T0+10 and T0+38 stages using a 6(+1)-region mesh subdivision

The subdivision of the observable tissue was performed according to Section 8.5.1. We used the setup of the estimator according to Table 8.2. In Section 8.4.2 we have found that the estimated contractility parameters did not markedly depend on the value of the state estimator gain γ when using the 2-region mesh subdivision of the stage T0+38. We tried the same type of estimations using the 6(+1)-region subdivision.

Figure 8.13 shows estimation results for all the stages using 3 values of the state estimator gain γ. On the first sight we can see that a lower value of γ increases the sensitivity of the parameter estimator – the spread of the parameter values is larger than for the higher γ values. However, by analyzing in detail some artifacts in the parameter estimation, this test shows some important aspects of the state estimation and gives us some clues how to tune the gain γ.

The state estimator tends to compensate for the discrepancy between the model and the observations, given e.g. by modeling errors. If the state estimator is weak and the model is far from the observed surfaces, the parameter estimator tries to correct the model. Since the parameter estimator may be correcting mainly for instance the modeling errors, the true parameter values may be masked by those corrections. Figure 8.13(i) shows a decrease of contractility in region #5, caused by the relaxation that is not perfectly synchronous between the model and the data. This little discrepancy can be corrected by the stronger state estimator.

However, a strong state estimator may correct the model to such an extent that the parameter estimator does not detect any need for other corrections, namely this would correspond to a loss of observability. Even more, Figure 8.14 demonstrates that excessive correction by the state estimator can cause some non-physiological tissue displacements, that may affect the estimated parameters.

For the real observations, the best results were obtained using the intermediate value $\gamma = 20\gamma_0$, as can be seen in the middle column of Figure 8.13. In the baseline case, the contractility values do not vary more than by 10%. At stage T0+38 the lowest values

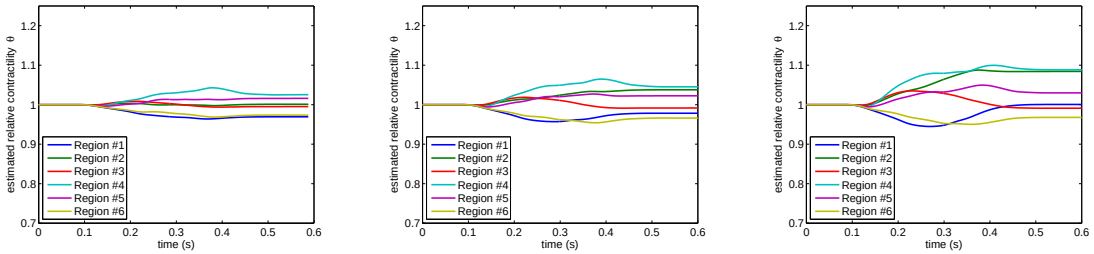

(a) Baseline, $\gamma = 40\gamma_0$ (b) Baseline, $\gamma = 20\gamma_0$ (c) Baseline, $\gamma = 8\gamma_0$

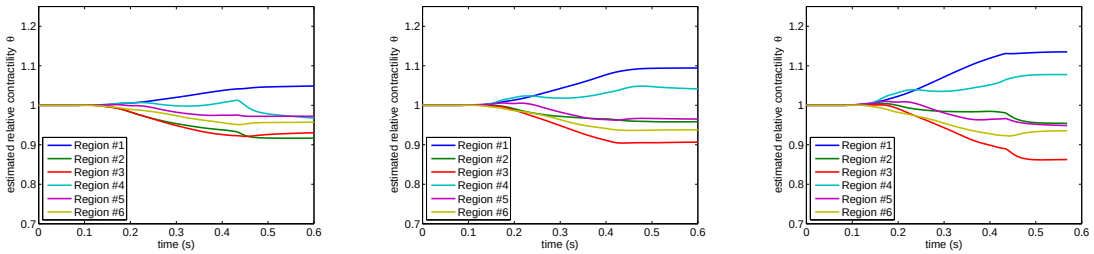

(d) T0+10, $\gamma = 40\gamma_0$ (e) T0+10, $\gamma = 20\gamma_0$ (f) T0+10, $\gamma = 8\gamma_0$

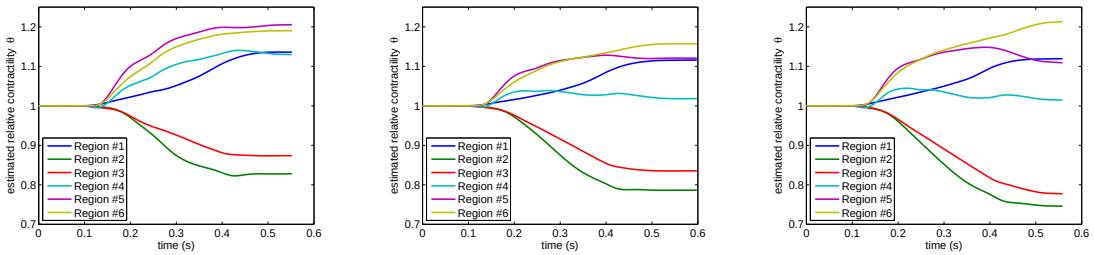

(g) T0+38, $\gamma = 40\gamma_0$ (h) T0+38, $\gamma = 20\gamma_0$ (i) T0+38, $\gamma = 8\gamma_0$

Figure 8.13: The 6(+1)-region subdivisions for each stage, using several values of the state estimation gain γ and real observations.

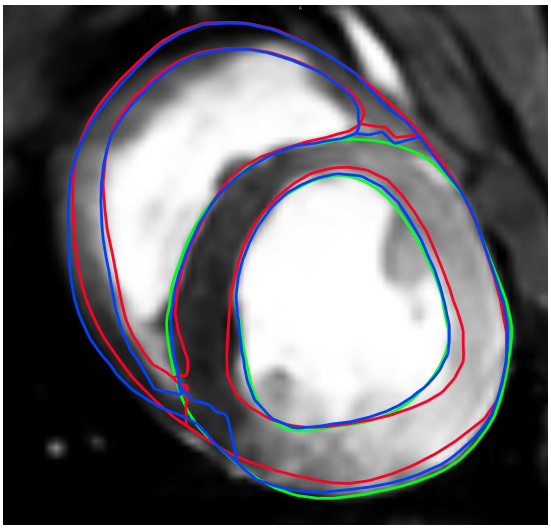

(a) The blue contour with excessive correction of the state on the inferior wall around the attachment of the left ventricle and the right ventricle in the early diastole (region #4).

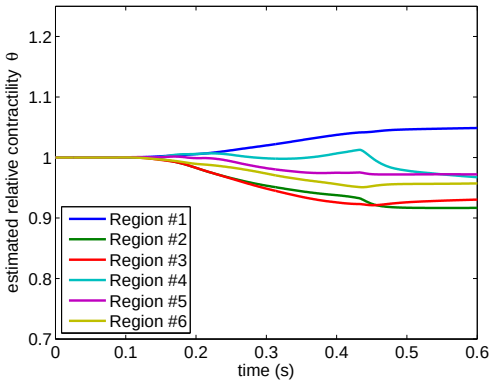

(b) A sudden drop of estimated contractility in region #4 in the early diastole (t ∼430ms).

Figure 8.14: Non-physiological deformation when using overly large value of the state estimator gain ($\gamma = 40\gamma_0$).

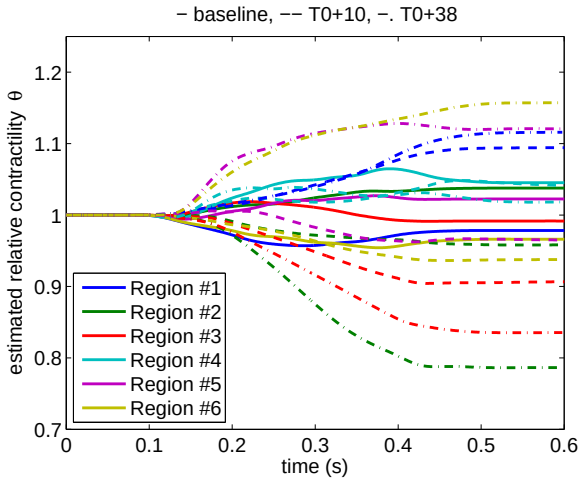

Figure 8.15: Comparison of the estimated contractility parameters for the baseline (solid line), T0+10 (dashed line) and T0+38 (dash-dot line) for $\gamma = 20\gamma_0$ using real observations. Note a narrow range of the contractility values for the baseline stage, and a wide range for the infarcted stages with the lowest values in regions #2 and #3 (infarcted zone) and the highest values in regions #5 and #6 (healthy – lateral LV wall).

of contractility are located in regions #2 and #3 that correspond to the actual infarcted regions. The lateral wall of the left ventricle situated opposite to the infarction (regions #5 and #6), contracts even more – which may be caused by a compensation hypertrophy.

Figure 8.15 illustrates that the contractility values are quite comparable in between the baseline stage and T0+10, except for regions #2 and #3. In both affected regions, we observe a drop of contractility of the order of 10%. At stage T0+38, we can see an even more pronounced drop of contractility in the same regions and a large increase of contractility in regions #5 and #6.

Finally, in Figure 8.16 we compare the joint state-parameter estimation using either the synthetic or the real observations at stage T0+38 with $\gamma = 20\gamma_0$. The synthetic observations are perfect surfaces with respect to the model and the resulting estimated parameters are very accurate. Nevertheless, we obtained similar results when using the the real observations created from the Cine MR images.

8.6 Simulations with estimated values of contractility

As a direct validation of the contractility parameters estimated in Section 8.5.2, we performed direct simulations of the stage T0+38 using the estimated parameter values. In Figure 8.17 we compare the direct model with constant contractility, the joint-state param-

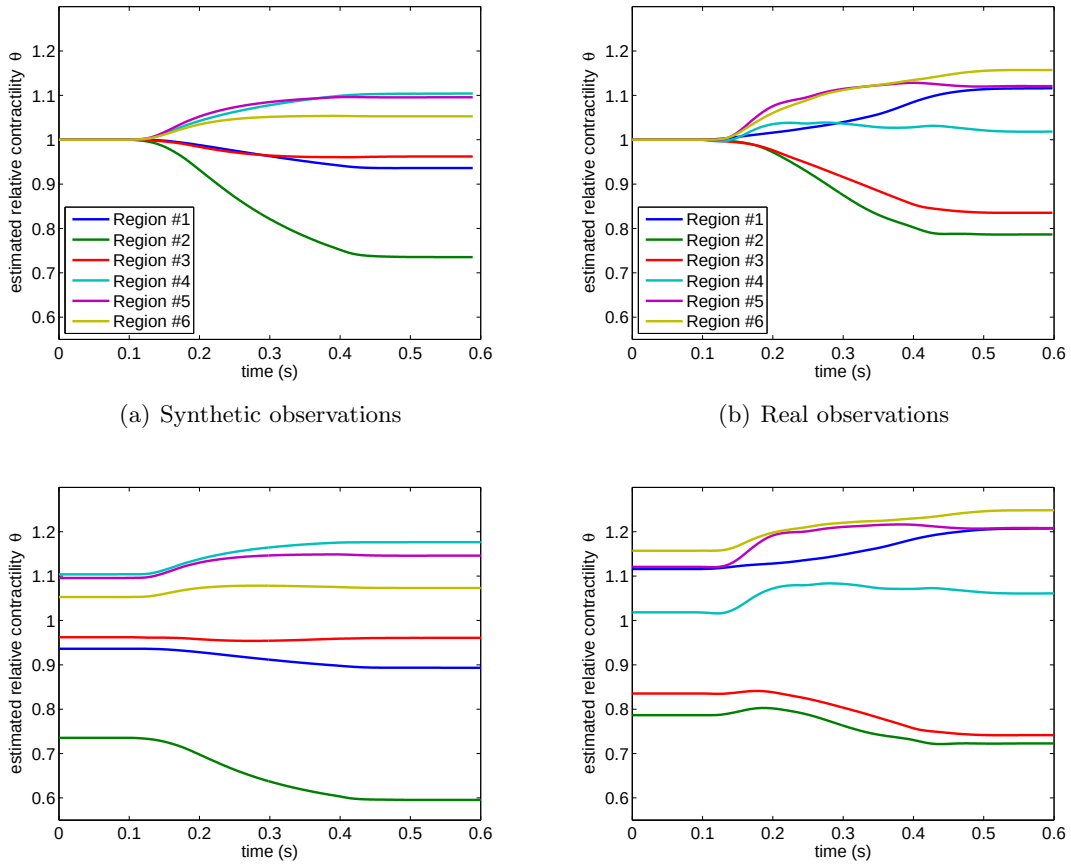

(a) Synthetic observations

(b) Real observations

(c) Synthetic observations, 2nd run of estimation

(d) Real observations, 2nd run of estimation

Figure 8.16: The 6(+1)-region subdivisions of stage T0+38, using either synthetic or real observations. $\gamma = 20\gamma_0$. The second run of estimation was initialized by contractility values θ obtained during the first run.

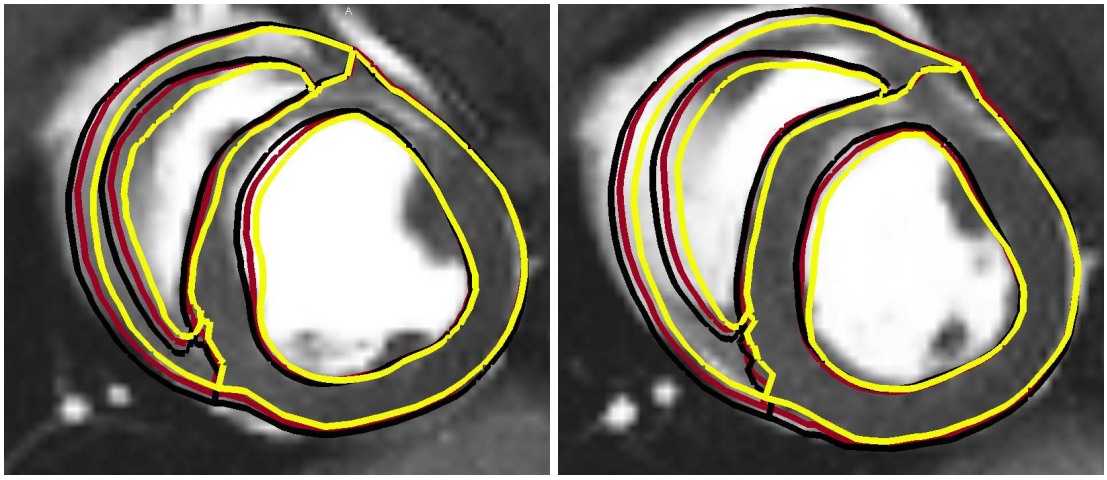

Figure 8.17: Two slices of the end-systolic phase at stage T0+38. Comparison of direct model with constant contractility (yellow contour), direct model using the estimated values of contractility (red) and joint state-parameter estimation (black).

eter estimation and finally the direct model using the estimated contractility parameters. As expected, the best results were obtained by the joint state-parameter estimation. Although the direct model with the estimated contractility parameters does not completely coincide with observations, the estimated parameters clearly correct the direct model in the right direction and push it closer to the observed surfaces.

8.7 Electrical activation

In the previous simulations we used the simple analytically prescribed electrical activation pattern in which the depolarization times were given by a planar wave propagating from the apex to the base of the heart along the long axis, as shown in Figure 8.1. The propagation velocity was adjusted so that the whole myocardium is activated in a time period corresponding to the measured QRS duration. The action potential duration in the simulation was kept constant over the whole myocardium, and was adjusted according to the Cine MRI data.

We tried to modify the activation pattern, so that it would become even more physiological. The analytically prescribed planar wave propagates from the apex to the base while activating only the subendocardial part of the myocardium. The transmural propagation is represented by the traveling wave with a lower propagation velocity. The two velocities are adjusted in the baseline case so that the periods for the wave propagation would correspond to the physiological situation, in particular:

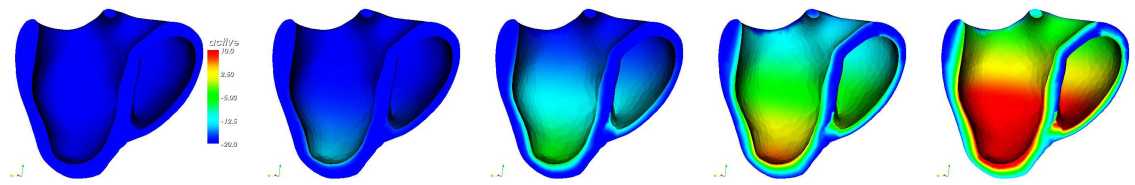

(a) 0 ms – end-diastole (b) 30 ms (c) 40 ms (d) 50 ms (e) 60 ms

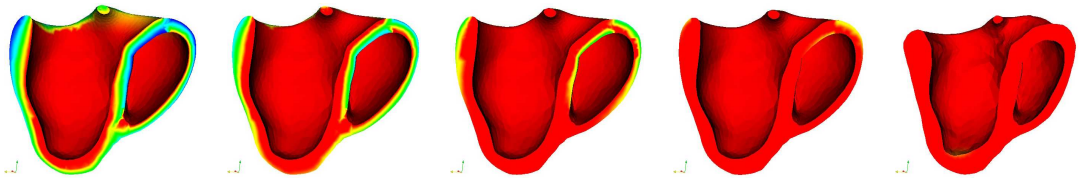

(f) 70 ms (g) 80 ms (h) 90 ms (i) 100 ms (j) 300 ms – end-systole

Figure 8.18: Analytical prescription of the electrical activation at the baseline stage: the planar wave activating the subendocardial part propagates fast from the apex to the base, together with the slow transmural propagation.

- the period of the activation of the whole endocardium is $\sim$ 30–35 ms.
- the period for the endocardium–epicardium propagation is $\sim$ 30–35 ms.
- the whole myocardium is activated in $\sim$70–80 ms, which corresponds to the measured QRS duration.

Figure 8.18 shows the electrical activation pattern for the baseline stage prescribed according the these constraints.

We compared the direct simulations and also the joint state-parameter estimations for each stage using the two types of electrical activation. We observed that the new electrical activation changes the direct model only in a few details and Figure 8.19 shows that also the estimated contractility parameters are nearly the same. It means that if the simplified electrical activation is well adjusted with respect to the measured QRS duration and the initiation of the contraction according to the Cine MRI data, and in case there are no serious blocks in the activation propagation, the more physiological transmural propagation does not substantially change the resulting model and we can keep using the simpler activation pattern.

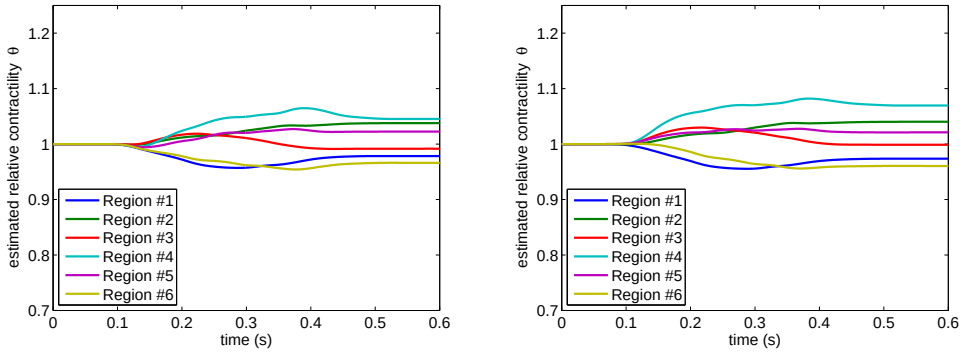

(a) Baseline

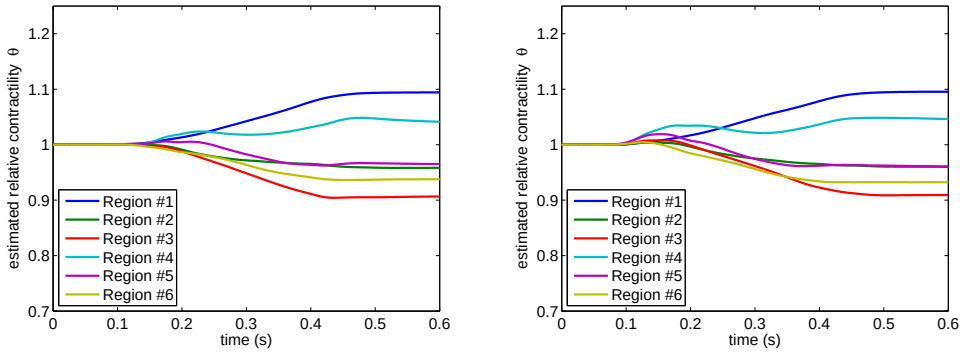

(b) T0+10

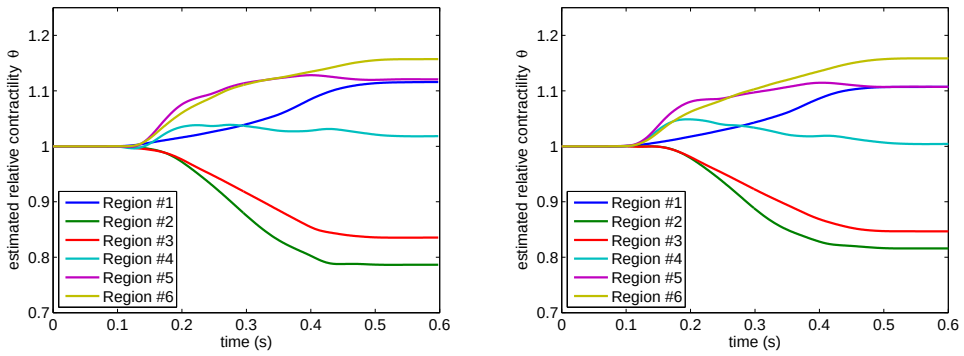

(c) T0+38

Figure 8.19: Comparison of two analytical electrical activation patterns: simple planar apex–base wave (the left column) and planar apex–base wave combined with a slow transmural conduction (the right column). The 6(+1)-region mesh subdivisions, $\gamma = 20\gamma_0$, using real observations.

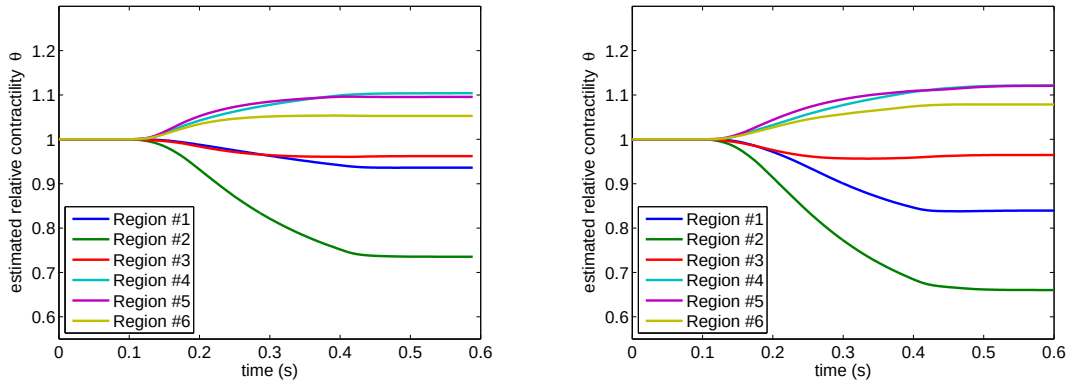

(a) Visco-elastic boundary condition

(b) Sliding boundary condition

Figure 8.20: The 6(+1)-region subdivisions for the stage T0+38 using synthetic observations and applying two types of boundary conditions applied on the anterior wall. $\gamma = 20\gamma_0$.

8.8 A contact boundary condition

The visco-elastic boundary conditions given by (4.13) applied on the anterior wall prevent to some extent the anterior wall from thickening. The hypokinesis of the anterior wall is corrected by the state-parameter estimator. Unfortunately, the parameter estimator causes an increase of the estimated parameter of contractility in region #1, although a large part of region #1 is infarcted, see Figure 8.24 (c) and (e). This is a typical example of a modeling error and of the correction of this error by an inadequate modification of the parameters. For this reason, we will test a new type of the boundary condition – which enables sliding of the epicardial surface of the anterior wall along the pericardium. This boundary condition is given by (4.14).

By implementing such a type of boundary condition, we obtain the physiological thickening of the anterior wall in the direct model. As we can see in Figure 8.20, the estimation using the synthetic observations (the same as in Section 8.5.2), gives very good results including region #1. However, before applying the model with the new boundary conditions to the joint state-parameter estimations using the real data, we would need to re-calibrate the model so that it would correspond adequately to the Cine MRI data. Figures 8.21 and 8.22 show that although the new boundary conditions corrected one modeling error (the thickening of the LV anterior wall), some other modeling errors were introduced.

The anterior wall has become more kinetic after applying the sliding boundary condition. At the same time the more contractile anterior wall prevents the inferior wall inward motion, as we can see in Figure 8.21. The estimator corrects this discrepancy by increasing the contractility value in the inferior and infero-lateral wall (regions #4 and #5), as can

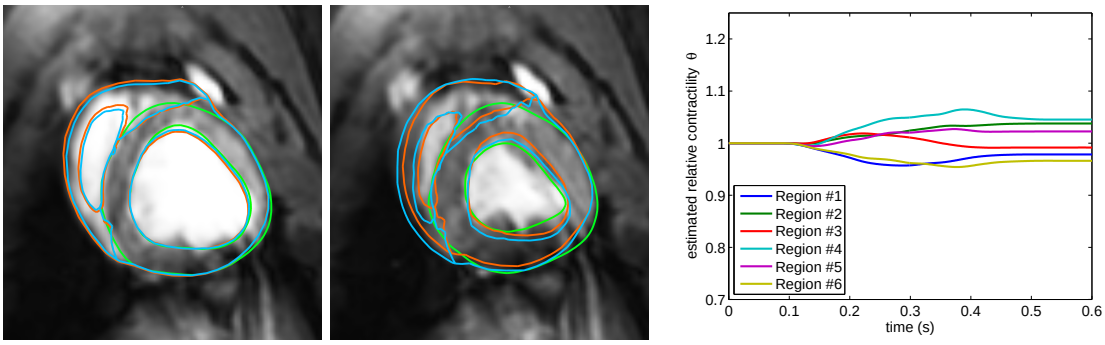

(a) Baseline, visco-elastic boundary condition

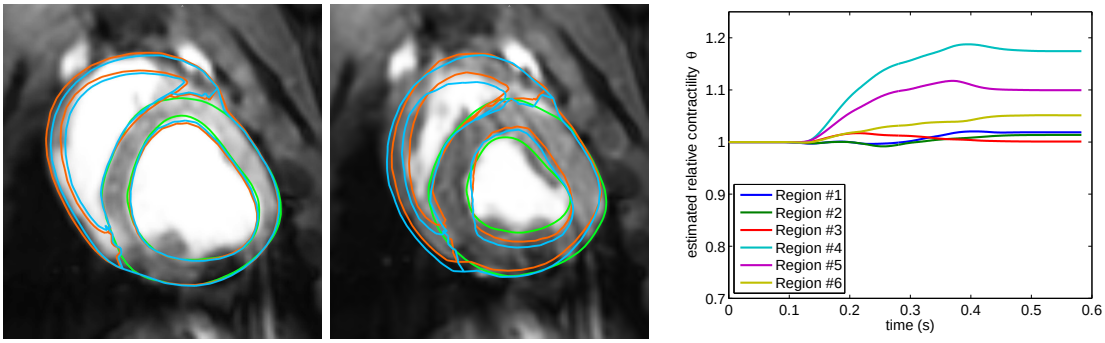

(b) Baseline, sliding boundary condition

Figure 8.21: Comparison of direct models at the baseline stage in 2 MRI slices using the following boundary conditions applied on the anterior wall: the visco-elastic (in orange) and the sliding boundary condition (in blue). The observations are in green. The end-diastolic images are on the left, the end-systolic images on the right. The plots shows the estimated contractility parameters for each type of boundary condition.

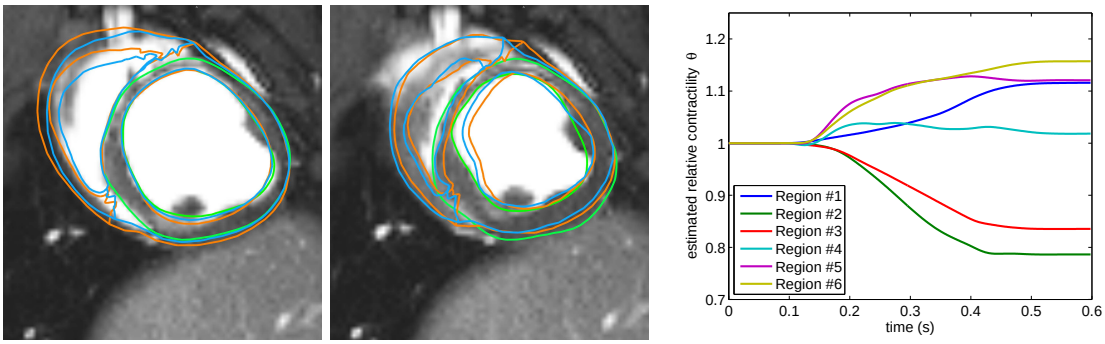

(a) T0+38, visco-elastic boundary condition

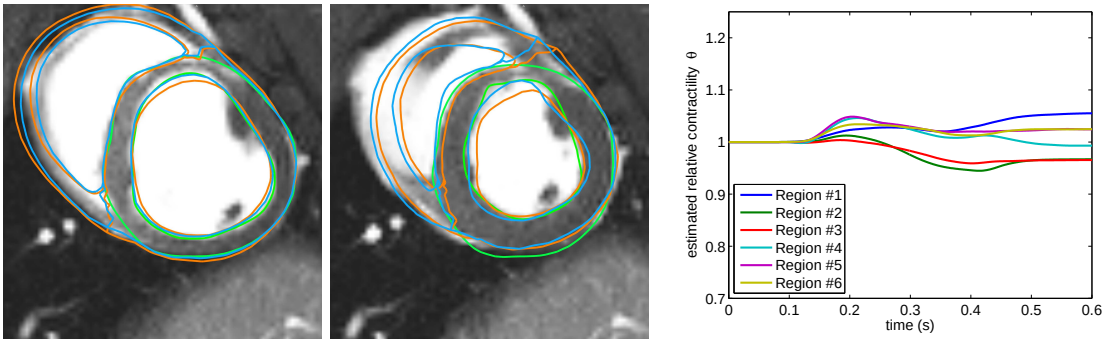

(b) T0+38, sliding boundary condition

Figure 8.22: Comparison of direct models for stage T0+38 in 2 MRI slices using the following boundary conditions applied on the anterior wall: the visco-elastic (in orange) and the sliding boundary condition (in blue). The observations are in green. The end-diastolic images are on the left, the end-systolic images on the right. The plots shows the estimated contractility parameters for each type of boundary condition.

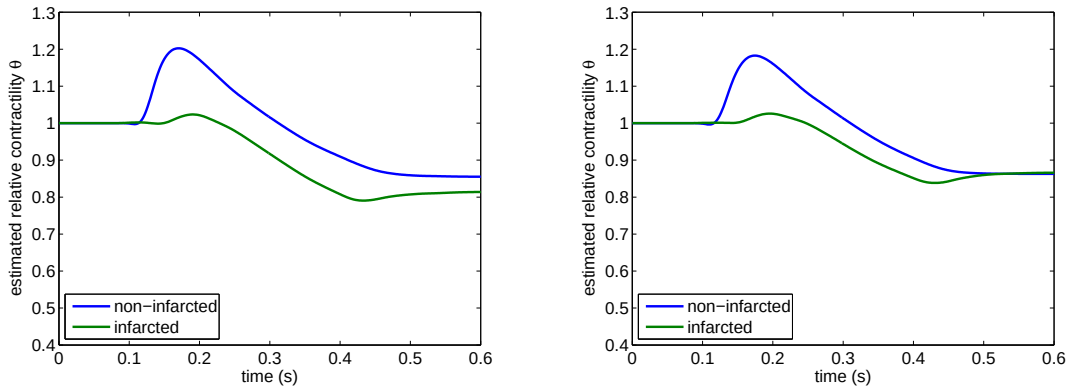

(a) $\gamma = 8\gamma_0$ (b) $\gamma = 20\gamma_0$

Figure 8.23: Contractility parameter θ estimated in a 2-region mesh for the stage T0+38 with the non-infarcted and the infarcted region using the boundary condition that enables sliding of the anterior wall along the pericardium and real observations.

be seen in the plot of the estimated parameters in the same figure.

Figure 8.22 shows a comparison of direct simulations at the stage T0+38 using either the visco-elastic or the sliding boundary conditions. In both cases, the tissue contractility was set to a constant value since we did not aim at modeling the infarct at this time. While the septum is well kinetic when using the visco-elastic boundary condition, it is hypokinetic when the sliding boundary condition is applied. This is most probably an indirect effect of the irregularities of the contact surfaces that prevent the surfaces from free sliding in any direction. Then, the septum seems to be hypokinetic and the estimator does not need to correct the contractility value e.g. in the infarcted region #2 (the antero-septal part of the LV).

As we have shown, without any model re-calibration the direct model is not sufficiently accurate. It finally causes that the parameter estimator is less sensitive, when using the real observations. Nevertheless, we performed the join state-parameter estimations at each stage of the infarction in order to see the behavior of the estimator when using such a preliminary model. Figure 8.23 shows that the estimator fails using the 2-region subdivision. In the 6(+1)-region subdivision, the estimator recognizes the decreased contractility in regions #2 an #3, but it fails in the estimation in some other regions, see Figure 8.24.

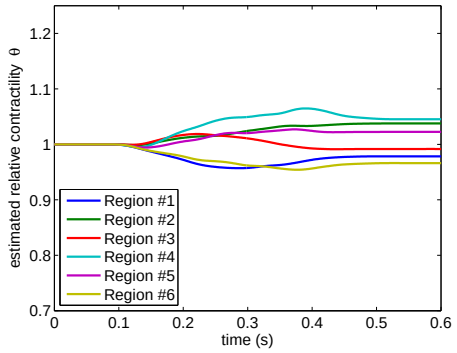

(a) Baseline, visco-elastic boundary condition

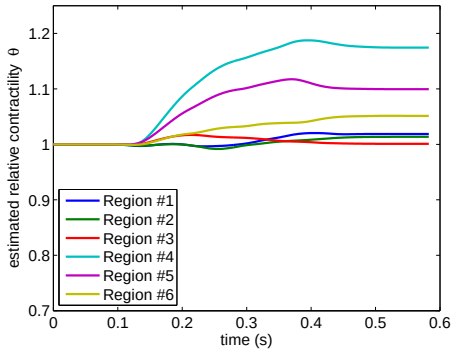

(b) Baseline, sliding boundary condition

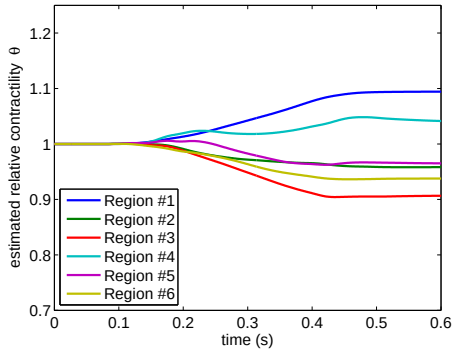

(c) T0+10, visco-elastic boundary condition

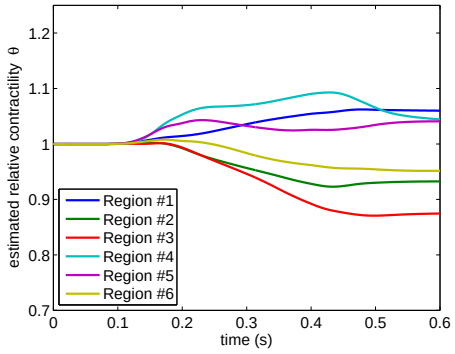

(d) T0+10, sliding boundary condition

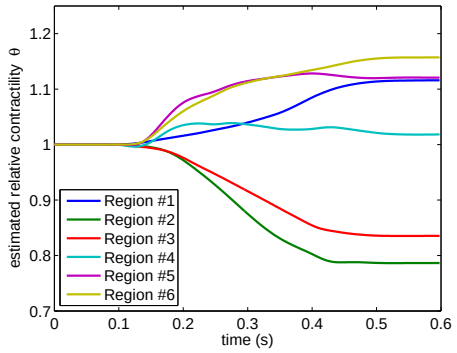

(e) T0+38, visco-elastic boundary condition

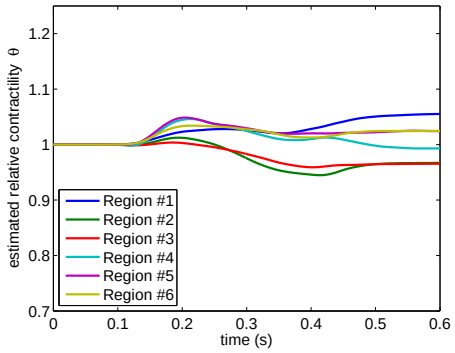

(f) T0+38, sliding boundary condition

Figure 8.24: The 6(+1)-region subdivisions for each stage, two different types of boundary condition representing the contact of the anterior wall with the thoracic cage. $\gamma = 20\gamma_0$, real observations.

8.9 Discussion

8.9.1 Modeling error

An important part of the estimator setup is a pre-calibration of the direct simulation. The model can be pre-calibrated using constant mechanical parameters over the myocardium, but it must behave as in the observations in the following aspects:

- The initial geometry needs to be as close as possible to the observation, in order to reduce the initial error. This is why the computational mesh used for the joint state-parameter estimation was created from the original segmented mesh, and corrected by running the state estimator with a large gain γ, during one cardiac cycle. Hence, the estimation procedure was used for image processing purposes. Figure 8.25 shows a comparison of the original initial mesh, the corrected mesh by means of the state estimation with a large gain γ and the observation surfaces. Such a corrected mesh was used for the joint state-parameter estimations afterwards.

- The initiation of the model contraction and of its relaxation needs to be as synchronous with the observations as possible. Any offset in the electrical activation of the model can cause sudden changes of the estimated parameters in any direction. The electrical activation pattern is often impaired by the myocardial infarction. Any large dyssynchrony in the contraction (for instance the pronounced septal flash in left bundle branch block) has to be taken into account in the model activation. In our case, the ECG obtained for each stage of the study showed no irregularity and the contractions were visibly synchronous. For this reason, we were able to keep using the same – physiological – electrical activation pattern in all stages.

- The timing of the prescription of the ventricle pressures needs to be compatible with the electrical activation imposed in the model. This was managed by exporting the pressure values from the direct model. The exported pressure curves were close to the measured pressures. We thus avoided any problem in the synchronization between the pressure and the electrical activation in the model.

- The adjustment of correct boundary conditions is a difficult problem. The atria and the attachment to the large vessels have to be replaced in the model. This is achieved by using visco-elastic boundary conditions. In addition, we need to represent the contact of the heart with the surrounding structures (mainly the thoracic cage and the diaphragm). For this, we first used the same type of visco-elastic boundary condition as for the base and the apex of the heart. Unfortunately, this type of boundary condition applied on the anterior wall (part of region #1) to some extent prevented its contraction. The hypokinesis of the region was corrected by the state-parameter estimator, but it caused an increase of the estimated contractility parameter in region #1, see Figure 8.24(c) and (e). For this reason, we lost the

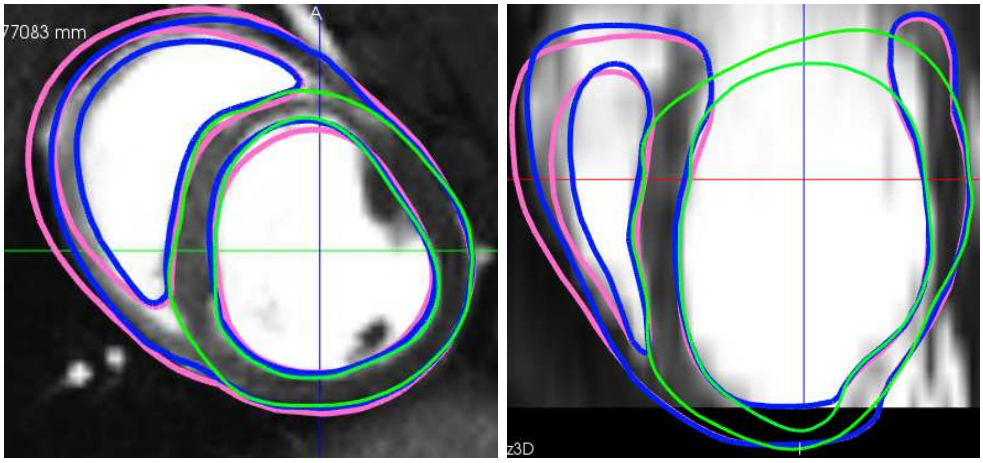

Figure 8.25: Comparison of the original initial mesh (pink color) and the mesh obtained by running the state estimation with a large gain γ (blue color) with the observations (in green). Since the corrected mesh is closer to the observations than the original mesh, the initial error was reduced.

sensitivity in the parameter estimator for region #1. By implementing a new type of boundary condition that enables the sliding of a part of the epicardium along the parietal pericardium, we obtained physiological thickening of the anterior wall in the direct modeling. However, on the whole the direct model was not as good as the model with the previous, less physiological, boundary conditions. It is known that such boundary conditions require very smooth surface meshes to allow adequate sliding. If the sliding is prevented due to some surface irregularities, the correction of estimator may induce some incorrect behavior. We saw in Figures 8.21 and 8.22 some issues that would need to be solved in the direct model before using the contact (sliding) boundary conditions in the estimations. The second column of Figure 8.24 shows that the parameter estimator was less sensitive and in some regions indeed failed. It demonstrates that even when changing only the boundary conditions the model needs to be well re-calibrated in all aspects. Nevertheless, even though the re-calibration was not optimal, the estimator recognized the decreased contractility in regions #2 and #3 at the infarcted stages.

8.9.2 Synthetic observations

The synthetic data consisted of the LV endocardial and LV epicardial surfaces, truncated in the same way as for the estimations using the real data. The synthetic data were produced by the direct model with the contractility reduced by a factor 4 in the infarcted region.

We did not add any noise in the synthetic observations.

When performing the estimation with the mesh subdivided into the non-infarcted and the infarcted region, we could expect that the estimated contractility parameter θ may reach the value 0.25 – the value used for creating the synthetic observations. However, the minimum estimated parameter θ was around 0.5. The estimated contractility may decrease further if performing a second run of estimation process, with θ initialized by the values obtained during the first run. In such a case, we obtained the value of 0.3. We still did not reach the value of 0.25, probably because of the limited observability caused by the fact that the observations are available only for the parts of the LV endocardial and epicardial surfaces, which is why we miss any information about the intramyocardial parts. Some additional tagged MR images, when adequately post-processed, could provide crucial information about the inner part of the myocardial wall.

When running the estimation with the left ventricle subdivided into 6 regions, we retrieved the contractility parameters in a good agreement with the late enhancement proportions in regions #2–6. The contractility was overestimated in region #1, which was explained by the modeling error caused by the artificial visco-elastic boundary conditions applied on the anterior wall. The correctly estimated contractility values in regions #2–6 show that the infarcted part is well observable using our estimation approach.

8.9.3 Cine MRI observations (the real data)

The estimated contractility parameters in the baseline did not vary more than by 10%, as expected for a healthy heart.

At stage T0+10, the ventricle does not show any evidence of remodeling in the form of infarcted wall thinning. Visually, except for 1–2 slices, we can hardly find an akinetic part and the hypokinetic parts of the LV wall are quite small. The variations of estimated contractility parameters between the healthy and the infarcted regions are lower than at stage T0+38. As in the case of synthetic observations, the reason may be due to limitations in the observations, and missing information from the inside part of the LV wall. Another reason may be the incomplete calibration of some other mechanical parameters, e.g. the passive tissue stiffness. Although there will be an increase of the tissue stiffness in the infarct at stage T0+38 (the fibrous tissue), the stiffness may be reduced at stage T0+10 due to tissue edema (and the acute inflammation that accompanies the infarction). In Figure 8.8 we showed that a lower passive tissue stiffness makes the estimator more sensitive for detecting the parameters. However, we would not like to use an a-priori knowledge of the infarct location by means of modifying the tissue stiffness in the infarct regions. Later on, we could perform estimations of both parameters – the contractility and the passive tissue stiffness.

Although the tissue marked by the late enhancement is quite large, the hypokinetic region does not seem to be as extended at stage T0+10 as in the last stage. It can be due to the fact that the late enhancement in a very recent infarct overestimates the final

infarct extension. Each of our 6 regions is relatively large and their infarcted part may be comparable with the volume of the healthy part of the region. In such a case, the estimator would not really be able to detect large changes in the contractility. The subdivision into smaller regions could help in the detection.

At the final stage (T0+38), the hypokinetic and akinetic regions are very extended, especially in the septal regions (regions #2 and #3), where the contractility parameters drop, while they rise in other regions. The increase in the opposite regions could be caused by a hypertrophy of the non-infarcted parts. First, the animal grew between the acquisition of the baseline stage and the stage T0+38, and the increased contractility could be just attributed to a normal growth. In addition, the non-infarcted part could have undergone a compensatory hypertrophy – the decreased performance of the heart causes the hypertrophy of the healthy myocardium. We cannot distinguish between those two explanations.

In both infarcted stages, the contractility was overestimated in region #1, for the same reasons as in the case of synthetic observations (the modeling error).

When running the direct model of infarcted stages using the estimated parameters, the resulting simulation does not completely correct the direct model with constant values of contractility. By adding the state estimator that was used during parameter estimation, we obtained excellent results. Therefore, whereas the estimated parameters behaved as could be expected for the increased or the decreased contractility, the estimated values in the infarcted v.s. non-infarcted parts were not sufficient to correct the direct model completely without any state correction. It is a similar situation as in the estimation with the synthetic observations, where we did not retrieve the reference contractility value. The reason can most probably be attributed to the limitations in the observations that we are using (the endocardial and epicardial surfaces), to the modeling errors discussed above and to the partial corrections performed by the state estimator during the joint state-parameter estimation.

8.10 Conclusions and perspectives

In this chapter, we successfully applied the methodology of the sequential joint-state parameter estimation with real cardiac Cine MRI data. We were able to detect myocardial infarction in several stages, while in the healthy stage the estimated contractility values were nearly constant over the myocardium of the left ventricle. The estimator is very sensitive if the diseased region is akinetic or dyskinetic. For small hypokinetic regions, the estimator is less effective, at least with the observations coming from the Cine MR images.

For our future work, we can apply the algorithm on even more detailed subdivisions of the mesh (e.g. a 17-segment AHA subdivision of the left ventricle). After post-processing the tagged MRI data, we could use a combination of observations coming from the endocardial and epicardial surfaces, and from the inner part of the myocardium as well. We

can either consider directly extracting the myocardium displacements from the tagged MR images, or applying in a straightforward manner the estimator used in this work based on measuring distances between the simulated and observed surfaces. In addition to the endocardial and epicardial surfaces from the Cine MR images, we would use surfaces representing the tag planes in the tagged MR images.

Another challenging goal would be an estimation of the contractility parameters in human patients with extended myocardial infarction – including patient-specific electrical activation patterns. Concurrently, we can work on improvements of the direct model, e.g. by prescribing more physiological boundary conditions. Finally, some other mechanical parameters could be estimated, for instance the passive tissue stiffness or directly some parameters of the electrical activation.

Chapter 9

Conclusions and perspectives

Each chapter of the applied modeling part contains conclusions of the performed work and possible perspectives. Here, we will conclude the main achievements of the PhD study in short paragraphs that are transverse to the chapters topics. Then, we will suggest what the future work related to the thesis could be.

9.1 Work realized

Experimental part

We performed ambitious experiments with big animals during which we obtained non-invasive image data and invasive pressure data of two healthy hearts. In one of the subject, we acquired the same data sets as in the baseline also after creating a controlled myocardial infarction. The animal data were applied in Chapter 6 – in which a validation study was performed and a strategy for adequately modeling an infarct was verified – and in Chapter 8, in which state and joint state-parameter estimations using real image data were performed. A side-effect of these experiments was the optimization of various MR sequences used in Cardiac MRI at Henri Mondor Hospital in Créteil, France.

Validation studies

In Chapter 5 we validated the model at a 1D level using experimental data of fiber contraction. We showed that the model is able to reproduce the experiments. We observed some non-physiological phenomena caused by inadequate values of several parameters. We were able to avoid some of them by readjusting the parameters related to these effects.

A validation of the full 3D heart model was performed in Chapter 6. We showed that our biomechanical model can be personalized and calibrated to accurately reproduce the pressures and motion measured in a healthy subject. Then, by changing only the parameters directly related to the state of myocardial infarction (contractility and stiffness

in the infarcted area) we demonstrated that we can also adequately represent the behavior of the acutely infarcted heart.

Patient-specific modeling

We showed that we are able to adjust the model so that it can represent healthy hearts, hearts with a controlled myocardial infarction and hearts of real patients with ischemic heart disease or dilated cardiomyopathy. In the case of healthy hearts we can use the constant values of mechanical parameters in the whole myocardium. For the controlled infarct, we need to modify the mechanical parameters only in the infarcted region (as was discussed in the previous paragraph). The personalization is substantially more difficult if we need to set up the model of a real patient – as was performed in Chapter 7. Since the ventricles may consist of healthy zones, completely akinetic or dyskinetic parts, and regions of several levels of hypokinesis, we need to adjust the mechanical parameters locally.

The setup of these patient-specific models can be performed manually – without any automatic feedback. We demonstrated that this strategy is feasible and the manual adjustment was effective in first clinical applications. The automatic personalization will be discussed in the paragraph related to joint state-parameter estimation.

Model predictivity

In Chapter 6 we showed the model predictivity by means of the volume changes (ejection fraction) and local kinematics caused by an acute myocardial infarction. In the preclinical study with patients undergoing cardiac resynchronization therapy (CRT) performed in Chapter 7, we demonstrated the model predictivity with respect to a global indicator of tissue contractility – max LV dp/dt. This preliminary clinical validation showed that the modeling of CRT procedures is a very promising approach as an assistance to medical therapy planning, in order to pre-operatively optimize the procedure in a patient-specific framework.

State and joint state-parameter estimation using real data

In Chapter 8, we demonstrated that the simulations can be corrected by means of the state estimation, using observations coming from Cine MR images (endocardial and epicardial contours). The algorithms developed by the MACS team proved to be efficient also in the joint state-parameter estimation. When using the same type of observations, the data assimilation procedure succeeded in the detection of the controlled myocardial infarction in the animal heart. The estimation of the contractility parameters failed for real clinical cases in which the contrast between the non-infarcted and infarcted tissue is not so pronounced and the electrical activation of the model must be jointly personalized in detail with respect to the activation propagation in the patient's heart.

Co-operations with clinical partners

During the PhD study, we extended interesting co-operations with Henri Mondor Hospital in Créteil and with Hospital Bicêtre, both in France. During the animal campaign, an important role played my personal co-operation with Institute for Clinical and Experimental Medicine (IKEM) Prague, Czech Republic, that showed to be open for further joint projects as well. Thanks to the preclinical study related to CRT modeling, we strengthened our relation with the Department of Imaging Sciences of King's College London and St. Thomas' Hospital in London, UK.

9.2 Perspectives

Animal data

The data acquired during the animal experiments served already in several projects – in the validation study, infarct modeling and in the infarct detection by means of joint state-parameter estimation. Until now, we have not used tagged MRI that are available for each data set, except in visual comparison with the model outputs. This type of data could be used for further validations or in estimation procedures.

Model improvements

In Chapter 8 we performed a preliminary test of more physiological boundary conditions representing the contact of epicardial part of ventricles with surrounding structures (thorax, diaphragm). By solving some issues in the setup of these boundary conditions, we may improve both direct models and the estimation procedures.

In co-operation with other groups, we may use more realistic electrical activation patterns. In Chapter 8 we showed that for physiological activation we can keep using simplified analytically prescribed patterns with correct timing with respect to the available data (Cine MRI, ECG) and we can obtain good results both in the direct simulations and in the estimations. However, in a dyssynchronous contraction – which is often the case for patients – the estimation process is sensitive to the activation pattern and we need to personalize it adequately.

We can further explore some parts of the model using the 1D implementation – in particular material laws and implementation of the Frank–Starling mechanism – that are likely to improve simulation results with the fiber, and the model itself. We may also design our own experiment in order to obtain exactly the type of data that we need.

The modeling of fully coupled mechano-electrical feedback can be interesting from the pre-clinical point of view, e.g. in explaining some physiological phenomena or in future testing of some pharmacological and non-pharmacological treatment of arrhythmias.

In some diseases, the modeling of the RV behavior would be of a great importance. We can mention the arrhythmogenic right ventricle dysplasia (ARVD) and some congen-

ital heart diseases as examples in which modeling may help in a diagnosis process, or to predict the future evolution, and propose a good timing for the treatment. In our anatomical models, the thickness of the RV is often overestimated – due to difficulties in the mesh creation of this thin structure. We can consider shell elements for this part of the computational mesh.

The modeling of fluid-structure interaction in the heart requires intensive computing. Therefore a targeted clinical motivation is crucial. The modeling of valve disorders or some congenital heart diseases (in order to suggest a good planning of surgery e.g. in some septal defects) could be of clinical interest.

We may consider the validation of perfusion models being developed by the MACS and REO teams at INRIA (see [24]). Although obtaining the truly quantitative perfusion data from MRI is very challenging, we can investigate the possibilities both of quantitative and semi-quantitative perfusion data, or suggest an in vitro experiment that would provide required data.

Clinical applications

The first objective is to fulfill the preclinical study started in the co-operation with St.Thomas' Hospital and King's College London. We should study in detail the sensitivity of the estimated max LV dp/dt values e.g. depending on the position of the pacing leads. The challenging work is to apply the model before the CRT implantation itself, which would be the next step for the therapy planning.

We should follow-up the patients included in the study in order to observe long-term CRT effects. In fact, these effects are likely to be directly related to the pathology itself – the chronic heart failure (CHF). Due to a high prevalence and a poor prognosis of CHF, it is a topic of high importance in clinical practice and another modeling challenge. In most aspects of long-term modeling, we should couple the systemic and pulmonary circulations. By adding some regulatory circuits (e.g. long-term pressure and fluid controls by kidneys), we could model some phenomena particularly important in CHF.

We can consider using some other indicators computed by the model (e.g. strains and stresses) to better understand some processes as for instance the already mentioned long-term CRT effects or the remodeling of the myocardium after the infarction. For example Figure 9.1 shows the distribution of wall stresses in the model in which the contractility was decreased in a region corresponding to one particular AHA segment in order to represent an infarct.

Parameter estimation

We should continue the work started in Chapter 8 on the joint state parameter-estimation using real data. The subdivision of LV into 17 AHA segments would be a natural continuation. Using richer observations – by post-processing tagged MRI data – could increase

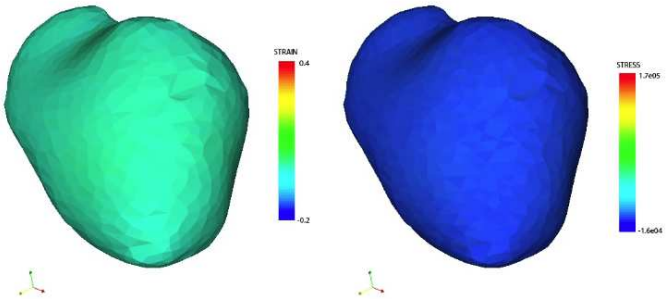

(a) End-diastole

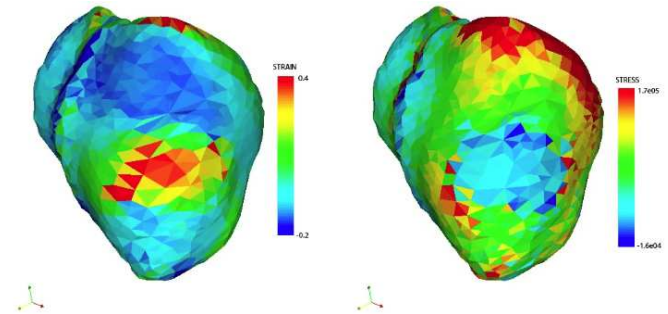

(b) End-systole

Figure 9.1: Model with artificially decreased contractility in a part of the anterior wall. We plot the circumferential strain (left) and the first eigenvalue of Cauchy stress tensor (right). Note the low stress values in the akinetic zone and the stress concentrations around.

the observability of the infarct. We may think about estimating some other mechanical parameters from the real data – as for instance the passive tissue stiffness.

We mentioned an idea to validate the perfusion model [24] using MRI. We can also think the other way around. Once the perfusion model is validated – using any experimental setup – it may be used to quantify the myocardial perfusion locally from the MR perfusion data, by means of data assimilation techniques.

In Chapter 7, we showed that analytical activation patterns prescribed by using some typical signs in the images can represent the electrical activation quite accurately, including those particular patients with LBBB in the CRT study. This illustrates that the estimation of some electrical parameters from image data is very promising. An approximate depolarization times obtained in a non-invasive way – by using a biomechanical model – could provide for instance some indices of dyssynchrony that could be of great importance for patients with some diseases affecting the electrical activation. Indeed, for example ARVD in the initial stages often does not show any pronounced morphological signs but sudden death due to ventricle fibrillation may occur. The contraction dyssynchrony is unfortunately hard to precisely assess with the naked eye in images, but some quantitative indices could be a clue for a timely diagnosis.

9.3 Final conclusions

Research in the field of biomechanical modeling – and this thesis in particular – shows that modeling is extremely promising in the clinical environment. The cardiovascular system is a prototype example. Thanks to a long tradition of the cardiac modeling, some sophisticated models were already created and they are waiting for their right applications. However, the thesis also shows that – as in any branch of research – at each step of our learning, there will be new questions coming in. Fortunately, we will have a chance to reply to some of them.

Chapter 10

Appendix: Animal data acquisition

During planning of the animal experimental campaign, the following experimental protocol was created.

10.1 Introduction

The objectives of this interdisciplinary work are to validate mathematical models of the heartbeat developed by INRIA[1] (project MACS[2]) and to bring new pathophysiological consequences that come along with the formation and acute stage of myocardial infarction, including mathematical modeling of the tissue remodeling in the first days and weeks after coronary artery occlusion.

A source of data for the mathematical model will be an animal (a young farm pig) with a controlled myocardial infarction. The animal will be examined and data acquired before creation of the infarct (healthy animal) and at regular intervals afterwards, so that the possible remodeling of the myocardial tissue will be observed.
The following notation will be used:

[1] The French National Institute for Research in Computer Science and Control, `http://www.inria.fr/index.en.html`

[2] `http://www-c.inria.fr/MACS/`

LA	left atrium
RA	right atrium
LV	left ventricle
RV	right ventricle
MR, MRI	magnetic resonance, magnetic resonance imaging
GE	gradient echo
PC MRI	phase contrast MRI
bSSFP	balanced steady state free precession (also known as TrueFISP)
FLASH	GE sequence with gradient spoiling (fast low-angle shot)
IR, STIR	inversion recovery, short tau inversion recovery (a fat suppression sequence)
DTI	diffusion tensor imaging
CT	computerized tomography
TDI	tissue Doppler imaging
LAFB	left anterior fascicular block
LBBB	left bundle branch block

10.2 Mathematical model

A mathematical model was developed by INRIA within the CardioSense3D[3] initiative. The heart is modeled as a 3D viscoelastic material with 1D active component representing the contraction of muscle fibers. The mathematical model including the numerical solution is fully described in [95].

The geometry is obtained by the segmentation of cardiac data acquired by the magnetic resonance imaging (MRI) or by the computerized tomography (CT). A diastolic time frame image preceding the atrial contraction is taken as a reference configuration of the heart (stress-free configuration). Segmentation of the left and right heart ventricles in this particular time-frame image is performed using the software CardioViz3D ([107]) being developed by INRIA, project Asclepios[4]. Afterwards, the computational mesh is built in the segmented geometry using tools developed by INRIA, in particular in project Gamma[5].

The active contraction consists of 1D deformation of the myocardial fibers. This contraction is triggered by an electrical activation. As an example, the electrical activation can be prescribed by defining the onset and the duration of the action potential for each node of the computational mesh. Full electrical activation of the heart (based on the modeling of transmembrane ionic flows and spread of the action potential from cell to cell) is also modeled by INRIA, project REO[6] (see [15]).

The main parameters of the model are calibrated so that the initial geometry (given by the only segmented time-frame) deforms during the heartbeat in correspondence with

[3] http://www-sop.inria.fr/CardioSense3D/

[4] http://www-sop.inria.fr/asclepios/

[5] http://www.inria.fr/recherche/equipes/gamma.en.html

[6] http://www-rocq.inria.fr/REO/

the acquired image data. The main parameters of the model are material properties which consist of active components (given by the contractility and direction of the myocardial fibers) and passive components (e.g. the tissue stiffness, elastic properties, viscosity). Some other crucial indicators are the pressures in the heart chambers, pressures in the systemic and pulmonary circulations, flow through the valves, etc. Varying the parameters we can represent typical cardiac physiological and pathophysiological states such as:

- Change of inotropy – this can be achieved by varying the contractility of the myocardial fibers. By this approach, global or local systolic dysfunctions can be modeled. Cardiac effects of positive/negative inotropic agents can be studied as well.
- Change of chronotropy (heart rate) – by varying the duration of the systole and diastole (directly on the cellular level – by changing the duration of the action potential on membranes of myocardial cells).
- Change of dromotropy (velocity of the conduction of the electrical activation) and the whole electrical activation scheme (modeling of disorders of the heart electrical conduction system).
- Diastolic dysfunction – by varying parameters of the passive component of the tissue.
- Change of resistance and capacitance of ventricle outflow tracts, large arteries or pulmonary and peripheral circulation, which can serve as models of valvular diseases (stenosis or regurgitation) or models of systemic or pulmonary hypertension (with possible study of the effect of treatment/non-treatment on the heart function).
- Change of the electrical activation scheme – as a model of conduction system disorders and effect of the treatment, e.g. by cardiac resynchronization therapy (CRT).
- Change of the fiber directions (e.g. study of possible consequences in the hypertrophic cardiomyopathy).
- Congenital heart diseases (using the actual geometry of the particular pathology).

10.3 Measured data

10.3.1 Cardiac MRI

The main source of data is Cardiac MRI. By this imaging modality we will acquire data necessary for the model creation and calibration. The model will be entirely specific to the examined subject. During the same acquisition sessions we will also obtain the main data for the validation of the mathematical model.

Cardiac MRI will be performed on MR system Philips Achieva 3.0 T at Henri Mondor hospital[7] in Créteil in a collaboration with A. Rahmouni and J.F. Deux and with the participation of J. Garot (Centre Hospitalier Jacques Cartier, Massy).

Data needed for creation and validation of the mathematical model

- **CINE MRI** enables to cover the whole organ with very good spatial resolution and capture the whole cardiac cycle in a good temporal resolution. It gives us the first knowledge about the anatomy and kinematics of the heart. The heart geometry (computational mesh) will be built from the diastolic time-frame image preceding the atrial contraction. For the model calibration, we use global indicators derived from the CINE MR images (typically evolution of the LV and RV volumes during the cardiac cycle) and local indicators of the heart kinematics (thickening of each AHA segment[8] during the cardiac cycle, longitudinal displacement of the fibrous rings of atrioventricular and semilunar valves and information about fixation of the apex). Electrical activation of the heart will be built in the correspondence with CINE MR images of high temporal resolution (obtained typically by using non-cartesian trajectories of the data acquisition).

- **Tagged MRI** in which the tissue magnetization is modulated in a regular grid so that the 'tagged' part of the volume does not give any MR signal (and that is why it appears black in the MR images)[9]. The grid follows the deformation of the heart during the cardiac cycle. By extraction of the grid nodes we are able to measure actual local deformations of the heart wall. The displacement fields coming from the tagged MR CINE images will serve as a source of data for the validation of the mathematical model.

- **First pass of the contrast agent** with an infusion of adenosin[10] will give us very good information about the perfusion of the myocardium. The imaging slices will be focused with respect to the infarcted tissue.

- **Late enhancement** are necessary data for the quantification of the infarcted tissue. The late enhancement images will be a source of information about the infarct extension, together with the perfusion data and kinematical CINE (which will inform us about local myocardial hypokinesis).

[7] `http://chu-mondor.aphp.fr/`

[8] Division of the ventricles into circumferential segments according to the American Heart Associations, see [21].

[9] The so called SPAMM technique – SPatial Modulation of Magnetization.

[10] The stress induced by dopamin will not be performed for the reason to avoid ventricular tachyarrhytmias which often appear in this animal species after the myocardial infarction.

Optional data coming from cardiac MRI

- **Phase contrast imaging (PC MRI)** will be used for estimation of flow in the ascending aorta, pulmonary trunk and through tricuspidal and mitral valve (only the component of velocity vector which is parallel to the direction of flow will be measured). The flow information is needed especially if some of the pressure data are missing (see Section 10.3.2).
- **T2 STIR**[11] can give us information about the extension of edematous tissue (which has high signal on T2-weighted images due to increased free water contents) in the acute stage of the myocardial infarct. The edematous tissue may correspond to the region with the decreased tissue stiffness in an acute stage of the infarct.
- **Diffusion tensor imaging (DTI)** will give us the directions of the myocardial fibers to be prescribed in the mathematical model. DTI data will be acquired only in the last imaging session since it needs to be performed on a non-beating heart.

10.3.2 Pressure data

Pressure conditions are necessary for the model calibration. The pressure data needs to be estimated approximately in the same time as the image acquisition takes place, so that the pressure data would correspond to the state of the anesthetized animal during the imaging. Since we expect evolution of the pressures along the development of the myocardial infarct, we need to get pressure data in each image acquisition session. The missing pressure data can be to some extent substituted by the inflow/outflow information (see Section 10.3.1) and / or by the usage of typical physiological values with respect to the known pathology. For optimal calibration of the model, the following pressure data are needed:

- RA pressure
- RV pressure
- Pressure in the pulmonary artery
- LA pressure
- LV pressure
- Aortic pressure

The RA, RV, pulmonary artery pressure and pulmonary capillary wedged pressure (PCWP, as a reflection of the LA pressure) will be measured using the Swan-Ganz catheter. A high fidelity catheter will be used for direct measurement of the aortic and LV pressure.

[11] T2 weighted images with an additional 180^{o} pulse (Short Tau Inversion Recovery) which nullifies MR signal from fat.

10.3.3 Electrocardiography and echocardiography

A few 2D echocardiography[12] loops will be obtained in standard projections (4-chamber view, 2-chamber view, several short axis views) and the flow data through all the heart valves (using pulse and continuous Doppler imaging).

For the proper calibration of the model we need to obtain a correct electrical activation of the heart. For the right timing of the systole and diastole we will use the 2D echocardiograhic data and the Doppler data with the recorded one lead ECG curve. Velocity of the propagation of the electrical activation will be adjusted according to the width of QRS complex.

Optional: The longitudinal motions of the lateral, septal, anterior and posterior parts of the fibrous rings of AV valves can be measured by the tissue Doppler imaging (TDI). The TDI data would be used for the calibration of the boundary conditions in the model.

10.4 Principal objectives

On INRIA's side, there are two principal objectives. These are the validation of the model representing a physiological heart and the modeling of the myocardial infarction (with the perspective to build a model of tissue remodeling after the myocardial infarction).

10.4.1 Validation of the physiological heart model

In the first stage, we will perform direct simulations without an a-priori knowledge of the detailed displacement fields. The input data will be: Stress-free geometry obtained from one particular time frame image of CINE MRI, volumes of the ventricles during cardiac cycle, wall thickening in each AHA segment (both obtained from CINE MRI) and pressure data. Doppler flow data and TDI will be used for better calibration of the model. Then, the simulations will be compared with displacement fields extracted from the tagged MRI data.

10.4.2 Direct simulations of the infarcted heart

The goal of this part is to perform direct simulations of the infarcted heart based on the geometry of the infarcted heart and with the knowledge of the extension of the infarct and the location and the level of the tissue hypocontractility. The model will be validated in the same manner as in Section 10.4.1 using the detailed displacement fields extracted from the tagged MRI data.

[12] For transthoracic echocardiography in minipigs, see [61].

10.4.3 Remodeling of the heart

Using the geometry of a healthy animal (before the infarction) and the data concerning the extension of the infarcted tissue, we would like to predict a geometry of the heart N-days after the coronary artery occlusion (mathematical model of the acute stage of myocardial infarct). The validation will be based on the tagged MRI data coming from N-days after the coronary artery occlusion.

10.5 Detailed protocol of the data acquisition

10.5.1 Examination of healthy animals, creation of the infarct

Young farm pigs will be taken as an animal model. 1–3 days before creation of the infarct the animals will be examined according to the imaging protocol described in Section 10.5.3.

In Day 0 the controlled occlusion of the left anterior descending coronary artery (LAD) will be performed by a balloon catheter. The occlusion will last 120 minutes. By shorter occlusion we would protect the animals from fatal arrhytmias but instead of the truly infarcted tissue we would be more likely to obtain myocardial stunning (see [63]). For the detailed description of the animal model see [42].

10.5.2 Follow-up of the animals

The animals will be examined by the imaging protocol described in Section 10.5.3 in the following days after the coronary artery occlusion:

- Day 2: Hyperacute reaction on the occlusion.
- Day 16: Acute stage of the myocardial infarction.
- Day 30: 'Later acute' stage of the myocardial infarction.

10.5.3 Examination protocol

Cardiac MRI

The most of the measurements will be performed in induced breath-hold, true 3D data will be acquired using the breath navigator. If more slices will be acquired, then multislice scan mode is to be used. **To reduce MR susceptibility artifacts, each instrument used for the intubation or the catheterization must be from the MR compatible material.**

- CINE TFE[13] (segmented FLASH), retrospective triggering, slice thickness: 7 mm, measured voxel size: 1.2 x 1.5 x 7.0 mm, SENSE = 1 (no parallel imaging), Trigger Delay = minimal (time delay between the detection of the R-peak of the QRS complex and start of the acquisition), phase percentage 80% (echo sharing)
  - short axis view: 10–15 slices covering the whole heart from the apex to the base (with no gap between the imaging slices)
  - long axis view – 4-chamber projection: 5-8 slices of 4-chamber projections covering the whole heart volume (standard 4-chamber view + parallel slices with no gap between the slices
  - long axis view – 2-chamber projection in LV: 3-5 parallel slices
  - long axis view – 3-chamber projection: 3 parallel slices
  - long axis view – 2-chamber projection in RV: 1 slice
  - *Optional:* Non-cartesian data acquisition (radial or spiral) used either for acquisition of all the preceding CINE MR images or at least in some projections (e.g. 5 short axis views, the 4-chamber and the 2-chamber view).
- Full 3D dataset of the morphological data in the diastole using breath navigator (according to the protocol discribed in [44]). Spatial resolution: 1.0x1.0x3 mm (interpolated to 0.5x0.5x1.5 mm), with TD corresponding to the diastole preceding atrial contraction.
- TFE + SPAMM (tagged data), the same voxel size as in the CINE MRI to be used, 2D grids inclined 45° to the axes of the imager, tag spacing 7.0 mm, TD = minimal, SENSE = 1, maximal water-fat shift, field of view as small as possible. The following positions will be copied from the preceding CINE MRI:
  - short axis view: 10–15 slices covering the whole heart from the apex to the base (with no gap between the imaging slices)
  - long axis view – standard 4-chamber projection
  - long axis view – standard 2-chamber projection in LV
  - long axis view – standard 3-chamber projection
  - long axis view – 2-chamber projection in RV
- Dark blood technique: T2 STIR in the short axis and 4-chamber view (respectively the slices focused on the pathology)

[13] Turbo Field Echo on Philips. The offset frequency for bSSFP sequence (the so-called delta TrueFISP frequency on Siements) is a sequence parameter that cannot be changed in the user mode on Philips Achieva 3.0 T. Since it is crucial for the optimal quality of bSSFP CINE images at 3.0 T field, we are acquiring the segmented FLASH images (TFE).

- First pass of the contrast agent: Snapshot FLASH sequence focused on the pathology
- Late enhancement: segmented FLASH (or bSSFP) sequence with inversion recovery pulse, slice thickness: 7.0 mm, measured voxel size: 1.2 x 1.5 x 7.0 mm (1 slice per single breath-hold) with both types of reconstruction:
  - magnitude-reconstructed images
  - phase-sensitive images (if supported by the MR system).
- *Optional:* Late enhancement – acquisition of a full 3D dataset (using a breath navigator)
- PC MRI – a component of the velocity parallel to the flow in the following locations:
  - aortic valve
  - pulmonary valve
  - mitral valve
  - tricuspidal valves
- DTI – in the last imaging session (on the non-beating heart) with the reconstruction of the myocardial fibers; spatial resolution: 2.0 x 2.0 x 2.0 mm, 15 diffusion direction + B0 image, EPI sequence with SENSE = 2, good magnetic field shimming and as low number of the lines in the phase encoding direction as possible)

Pressure data

- Antegrade catheterization using the Swan-Ganz catheter:
  - inferior (superior) caval vein pressure
  - RA pressure
  - RV pressure
  - pressure in the pulmonary trunk
  - pulmonary capillary wedged pressure
- Retrograde catheterization using the high fidelity catheter:
  - arterial pressure (after entering the arterial system)
  - aortic pressure
  - LV pressure

Echocardiography

- 2D mode: recording of heartbeat kinematics with one lead ECG at the same time in the following projections:
  - long axis view – 4-chamber projection in LV
  - long axis view – 2-chamber projection in LV
  - long axis view – 2-chamber projection in RV
  - short axis view – 1-3 slices
- Pulse (continuous) Doppler imaging in:
  - mitral valve
  - LVOT, resp. flow in ascending aorta
  - tricuspidal valve
  - RVOT, resp. flow in the pulmonary trunk
  - caval veins, pulmonary veins
- Tissue Doppler Imaging – fibrous rings of tricuspidal and mitral valves (lateral, anterior, septal and posterior part of the rings)

In the last session, cardiac MRI will be performed as the last imaging technique with final DTI on a non-beating heart. The histological verification of the infarct extension may be performed later on.

10.6 Data processing

Three months after the data have been collected, the INRIA researchers will deliver a synthetic technical report to summarize the preliminary results obtained when using the data in the simulations. The conclusions of this report will include an assessment of the perspectives regarding potential further experimental campaigns.

Bibliography

[1] W.T. Abraham, W.G. Fisher, A.L. Smith, D.B. Delurgio, A.R. Leon, E. Loh, D.Z. Kocovic, M. Packer, A.L. Clavell, D.L. Hayes, M. Ellestad, and J. Messenger. Cardiac resynchronization in chronic heart failure. N Engl J Med, 346(24):1845–1853, 2002.

[2] J. Aguado-Sierra, R.C.P. Kerckhoffs, F. Lionetti, D. Hunt, C. Villongco, M. Gonzales, S.G. Campbell, and A.D. McCulloch. Patient-Specific Modeling of the Cardiovascular System. Springer, 2010.

[3] R. Aliev and A. Panfilov. A simple two-variable model of cardiac excitation. 3(7):293–301, 1996.

[4] L. Axel and L. Dougherty. Improved method of spatial modulation of magnetization (SPAMM) for MRI of heart wall motion. Radiology, 172:349–350, 1989.

[5] L. Axel and L. Dougherty. MR imaging of motion with spatial modulation of magnetization. Radiology, 171:841–845, 1989.

[6] F. Balleux-Buyens, O. Jolivet, J. Bittoun, and A. Herment. Velocity encoding versus acceleration encoding for pressure gradient estimation in MR haemodynamic studies. Phys. Med. Biol., 51:4747–4758, 2006.

[7] K.-J. Bathe. Finite Element Procedures. Prentice-Hall, 1996.

[8] G.W. Beeler and H. Reuter. Reconstruction of the action potential of ventricular myocardial bers. Journal of Physiology, 268:177–210, 1977.

[9] J.W. Belliveau, D.N. Kennedy, R.C. McKinstry, B.R. Buchbinder, R.M. Weisskoff, M.S. Cohen, J.M. Vevea, T.J. Brady, and B.R. Rosen. Functional mapping of the human visual cortex by magnetic resonance imaging. Science, 254:716–719, 1991.

[10] M.A. Bernstein, K.F. King, and X.J. Zhou. Handbook of MRI pulse sequences. Elsevier, 2004.

[11] O. Bernus, R. Wilders, C.W. Zemlin, H. Verschelde, and A.V. Panfilov. A computationally efcient electrophysiological model of human ventricular cells. Am J Physiol Heart Circ Physiol, 282:2296–2308, 2002.

[12] J. Bestel, F. Clément, and M. Sorine. A biomechanical model of muscle contraction. In Lectures Notes in Computer Science, volume 2208. Eds W.J. Niessen and M.A. Viergever, Springer-Verlag, 2001.

[13] J. Bogaert, S. Dymarkowski, and A.M. Taylor. Clinical Cardiac MRI. Springer, 2005.

[14] M. Boulakia, M.A. Fernández, J.-F. Gerbeau, and N. Zemzemi. Towards the numerical simulation of electrocardiograms. In F.B. Sachse and G. Seemann, editors, Functional Imaging and Modeling of the Heart, number 4466 in Lecture Notes in Computer Science, pages 240–249. Springer-Verlag, 2007.

[15] M. Boulakia, M.A. Fernández, J.-F. Gerbeau, and N. Zemzemi. Direct and inverse problem in electrocardiography. In P. George T.E. Simos and Ch. Tsitouras, editors, Numerical Analysis and Applied Mathematics, pages 113–118. American Institute of Physicsg, 2008.

[16] Y. Bourgault, Y. Coudière, and C. Pierre. Existence and uniqueness of the solution for the bidomain model used in cardiac electrophysiology. Nonlinear Analysis: Real World Applications, 10(1):458–482, 2009.

[17] H.P. Bowditch. Über die Eigenthüemlichkeiten der Reizbarkeit, welche die Muskelfasern des Herzens zeigen. Verh. K Sachs Gen Wochenschr Leipzig Math Phys Cl, 23:652–669, 1871.

[18] M.R. Bristow, L.A. Saxon, J. Boehmer, S. Krueger, D.A. Kass, T. De Marco, P. Carson, L. DiCarlo, D. DeMets, B.G. White, D.W. DeVries, and A.M. Feldman. Cardiac-resynchronization therapy with or without an implantable defibrillator in advanced chronic heart failure. N Engl J Med, 350(21):2140–2150, 2004.

[19] F. Buyens, O. Jolivet, A. De Cesare, J. Bittoun, A. Herment, J.-P. Tasu, and E. Mousseaux. Calculation of left ventricle relative pressure distribution in MRI using acceleration data. Magnetic Resonance in Medicine, 53:877–884, 2005.

[20] O. Cazorla, Y. Wu, T.C. Irving, and H. Granzier. Titin-based modulation of calcium sensitivity of active tension in mouse skinned cardiac myocytes. Circ. Res., 88:1028–1035, 2001.

[21] M.D. Cerqueira, N.J. Weissman, and Dilsizian V. et al. Standardized myocardial segmentation and nomenclature for tomographic imaging of the heart: A statement of healthcare professionals from the cardiac imaging comittee of the council on clinical cardiology of the american heart association. Circulation, 105:539–542, 2002.

[22] R. Chabiniok, D. Chapelle, P.F. Lesault, A. Rahmouni, and J.F. Deux. Validation of a biomechanical heart model using animal data with acute myocardial infarction. In CI2BM09 - MICCAI Workshop on Cardiovascular Interventional Imaging and Biophysical Modelling, London, UK, 2009.

[23] D. Chapelle, M.A. Fernández, J.F. Gerbeau, P. Moireau, and N. Zemzemi. Numerical simulation of the electromechanical activity of the heart. In Proceedings of Functional Imaging and Modeling of the Heart 2009 (FIMH'09), volume 5528 of LNCS.

[24] D. Chapelle, J.-F. Gerbeau, J. Sainte-Marie, and I. Vignon-Clementel. A poroelastic model valid in large strains with applications to perfusion in cardiac modeling. Computational Mechanics, 46:91–101, 2009. doi:10.1007/s00466-009-0452-x.

[25] D. Chapelle, P. Le Tallec, P. Moireau, and M. Sorine. An energy-preserving muscle tissue model: formulation and compatible discretizations. International Journal of Multiscale Computational Engineering, 2011. in Press.

[26] P. Chinchapatnam, K.S. Rhode, M. Ginks, C.A. Rinaldi, P. Lambiase, R. Razavi, S. Arridge, and M. Sermesant. Model-based imaging of cardiac apparent conductivity and local conduction velocity for diagnosis and planning of therapy. IEEE Transactions on Medical Imaging, 27(11):1631–1642, 2008.

[27] P.G. Ciarlet. Mathematical Elasticity, Vol. I : Three-Dimensional Elasticity. Studies in Mathematics and its Applications. North Holland, 1988.

[28] J.G. Cleland, J.C. Daubert, E. Erdmann, N. Freemantle, D. Gras, L. Kappenberger, and L. Tavazzi. The effect of cardiac resynchronization on morbidity and mortality in heart failure. N Engl J Med, 352(15):1539–1549, 2005.

[29] M. Collet, V. Walter, and P. Delobelle. Active damping of a micro-cantilever piezocomposite beam. Journal of Sound and Vibration, 260(3):453–476, 2003.

[30] P. Colli Franzone, L. Guerri, and S. Rovida. Wavefront propagation in activation model of the anisotropic cardiac tissue: Asymptotic analysis and numerical simulations. J. Math. Biol., 28(2):121–176, 1990.

[31] E.J. Crampin, M. Halstead, P. Hunter, P. Nielsen, D. Noble, N. Smith, and M. Tawhai. Computational physiology and the physiome project. Experimental Physiology, 89:1–26, 2004.

[32] K. Djabella and M. Sorine. Differential model of the excitation-contraction coupling in a cardiac cell for multicycle simulations. In EMBEC'05, volume 11, pages 4185–4190, Prague, 2005.

[33] P. Drábek and J. Milota. Methods of Nonlinear Analysis: Applications to Differential Equations. Birkhäuser Verlag, 2007.

[34] E.P. Durand, O. Jolivet, E. Itti, J.-P. Tasu, and J. Bittoun. Precision of magnetic resonance velocity and acceleration measurements: Theoretical issues and phantom experiments. Journal Of Magnetic Resonance Imaging, 13:445–451, 2001.

[35] M. Ethier and Y. Bourgault. Semi-implicit time-discretization schemes for the bidomain model. SIAM J. Numer. Anal., 46(5):2443–2468, 2008.

[36] F. Fenton and A. Karma. Vortex dynamics in three-dimensional continuous myocardium with fiber rotation: Filament instability and fibrillation. Chaos, 8:20–47, 1998.

[37] R. Fitzhugh. Impulses and physiological states in theoretical models of nerve membrane. Biophys. J., (1):445–465, 1961.

[38] L. Formaggia, A. Quarteroni, and A. Veneziani. Cardiovascular Mathematics. Springer-Verlag, Milano, 2009.

[39] J. Frahm, A. Haase, and D. Matthaei. Rapid NMR imaging of dynamic processes using the FLASH technique. Magn Reson Med, 3:321–327, 1986.

[40] J. Frahm, A. Haase, and D. Matthaei. Rapid three-dimensional MR imaging using the FLASH technique. J Comput Assist Tomogr, 10:363–368, 1986.

[41] P.J. Frey and P.-L. George. Mesh generation application to finite elements. Wiley, London, 2008.

[42] J. Garot, T. Unterseeh, E. Teiger, S. Champagne, B. Chazaud, R. Gherardi, L. Hittinger, P. Guéret, and A. Rahmouni. Magnetic resonance imaging of targeted catheter-based implantation of myogenic precursor cells into infarcted left ventricular myocardium. Journal of the American College of Cardiology, 41(10):1841–1846, 2003.

[43] J.-F. Gerbeau and V. Martin. Blood flow simulation and magnetohydrodynamics effects in MRI. In preparation.

[44] B. Giorgi, S. Dymarkowski, F. Maes, M. Kouwenhoven, and Bogaert J. Improved visualization of coronary arteries using a new three-dimensional submillimeter MR coronary angiography sequence with balanced gradients. American J. Roentgenology, 179(4):901–910, 2002.

[45] T. Grobner. Gadolinium – a specific trigger for the development of nephrogenic fibrosing dermopathy and nephrogenic systemic fibrosis? Nephrol Dial Transplant, 21(4):1104–1108, 2006.

[46] A.C. Guyton and J.E. Hall. Textbook of medical physiology, 10th edition. Saunders, 2010.

[47] A. Haase. Snapshot FLASH MRI. Applications to T1, T2, and chemical-shift imaging. Magn Reson Med, 13(1):77–89, 1990.

[48] A. Haase, J. Frahm, W. Hanicke, and D. Matthaei. ^{1}H NMR chemical shift selective (CHESS) imaging. Phys. Med. Biol., 30:341–344, 1985.

[49] A. Haase, J. Frahm, D. Matthaei, W. Hänicke, and K.D. Merboldt. FLASH imaging: rapid NMR imaging using low flip angle pulses. J Magn Res, 67:258–266, 1986.

[50] W. Hahn. Stability of motion. Springer Verlag, 1967.

[51] L.D. Hall, S. Sukumar, and S.L. Talagala. Chemical-shift-resolved tomography using frequency-selective excitation and suppression of specific resonances. Journal Of Magnetic Resonance Imaging, 56(2):275–278, 1984.

[52] A.V. Hill. The heat of shortening and the dynamic constants in muscle. Proc. Roy. Soc. London (B), 126:136–195, 1938.

[53] P. Hunter. Finite element analysis of cardiac muscle mechanics. PhD thesis, University of Oxford, 1975.

[54] A.F. Huxley. Muscle structure and theories of contraction. In Progress in Biophysics and Biological Chemistry, volume 7, pages 255–318. Pergamon press, 1957.

[55] A.F. Huxley and R. Niedergerke. Structural changes in muscle during contraction. interference microscopy of living muscle bres. Nature, 173:971–973, 1954.

[56] H.E. Huxley and J. Hanson. Changes in the cross-striations of muscle during contraction and stretch and their structural interpretation. Nature, 173:973–976, 1954.

[57] H. Ismail and A.N. Makaryus. Predictors of response to cardiac resynchronization therapy: the holy grail of electrophysiology. Int J Cardiovasc Imaging, 26:197–198, 2010.

[58] R.E. Kalman. A new approach to linear filtering and prediction problems. ASME Trans – J Basic Eng, 82(Series D):35–45, 1960.

[59] R.E. Kalman and R.S. Bucy. New results in linear filtering and prediction theory. ASME Trans – J Basic Eng, 83(Series D):95–108, 1961.

[60] J. Keener and J Sneyd. Mathematical Physiology. Springer, 1998.

[61] E.K. Kerut, C.M. Valina, T. Luka, K. Pinkernell, P. Delafontaine, and E.U. Alt. Technique and imaging for transthoracic echocardiography of the laboratory pig. Echocardiography, 21(5):439–442, 2004.

[62] Y. Kinouchi, H. Yamaguchi, and T.S. Tenforde. Theoretical analysis of magnetic field interactions with aortic blood flow. Bioelectromagnetics, 17(1):21–32, 1996.

[63] R.A. Kloner and R.B Jennings. Consequences of brief ischemia: Stunning, preconditioning, and their clinical implications, part 1. Circulation, 24(104):2981–2989, 2001.

[64] P.C. Lauterbur. Image formation by induced local interactions: Examples of employing nuclear magnetic resonance. Nature, 242:190–191, 1973.

[65] D. Le Bihan, E. Breton, D. Lallemand, P. Grenier, E. Cabanis, and M. Laval-Jeantet. MR imaging of intravoxel incoherent motions: application to diffusion and perfusion in neurologic disorders. Radiology, 161(2):401–407, 1986.

[66] D. Le Bihan, C. Poupon, A. Amadon, and F. Lethimonnier. Artifacts and Pitfalls in Diffusion MRI. J. Magn. Reson. Imaging, 24:478–488, 2006.

[67] P. Le Tallec. Numerical methods for nonlinear three-dimensional elasticity. In P.G. Ciarlet and J.-L. Lions, editors, Handbook of Numerical Analysis, volume 3. Elsevier, 1994.

[68] J. Lee and N.P. Smith. Theoretical modeling in hemodynamics of microcirculation. Microcirculation, 15(8):730–745, 2008.

[69] M.H. Levitt. Spin Dynamics: Basics of Nuclear Magnetic Resonance. Wiley, 2002.

[70] P. Libby, R.O. Bonow, D.L. Mann, and D.P. Zipes. Braunwald's Heart Disease: A Textbook of Cardiovascular Medicine, 8th edition. Saunders, 2008.

[71] D.G. Luenberger. An introduction to observers. IEEE Transactions on Automatic Control, 16:596–602, 1971.

[72] C.-H. Luo and Y. Rudy. A model of the ventricular cardiac action potential: depolarization, repolarization, and their interaction. Circulation Research, 68:1501–1526., 1991.

[73] C.-H. Luo and Y. Rudy. A dynamic model of the cardiac ventricular action potential: I. simulations of ionic currents and concentration changes. Circulation Research, 74:1071–1096, 1994.

[74] D.A. MacDonald. Blood Flow in Arteries. Edward Harold Press, 1974.

[75] P. Mansfield. Multi-planar image formation using NMR spin-echos. J. Phys. C: Solid State Physics, 10:L55–L58, 1977.

[76] M.V. McConnell, V.C. Khasgiwala, and B.J. Savord. Prospective adaptive navigator correction for breath-hold MR coronary angiography. Magn Reson Med, 37(1):148–152, 1997.

[77] C.C. Mitchell and D.G. Schaeffer. A two-current model for the dynamics of cardiac membrane. Bulletin Math. Bio., 65:767–793, 2003.

[78] P. Moireau. Filtering based data assimilation for second order hyperbolic PDE. Applications in cardiac mechanics. PhD thesis, Ecole Polytechnique, 2008.

[79] P. Moireau and D. Chapelle. Reduced-order Unscented Kalman Filtering with application to parameter identification in large-dimensional systems. COCV, 2010. Published online, doi:10.1051/cocv/2010006.

[80] P. Moireau, D. Chapelle, and P. Le Tallec. Joint state and parameter estimation for distributed mechanical systems. Computer Methods in Applied Mechanics and Engineering, 197:659–677, 2008.

[81] P. Moireau, D. Chapelle, and P. Le Tallec. Filtering for distributed mechanical systems using position measurements: Perspectives in medical imaging. Inverse Problems, 25(3):035010 (25pp), 2009. doi:10.1088/0266-5611/25/3/035010.

[82] P. Moireau, N. Xiao, M. Astorino, C.A. Figueroa, D. Chapelle, C.A. Taylor, and J.-F. Gerbeau. External tissue support and fluid-structure simulation in blood flows. Submitted to: Biomechanics and Modeling in Mechanobiology.

[83] M.E. Moseleym, Y. Cohen, J. Kucharczyk, J. Mintorovitch, H.S. Asgari, M.F. Wendland, J. Tsuruda, and D. Norman. Diffusion-weighted MR imaging of anisotropic water diffusion in cat central nervous system. Radiology, 176(2):439–445, 1990.

[84] F.H. Netter. Atlas of Human Anatomy, 10th edition. Saunders, 2000.

[85] S. Nordmeyer, E. Riesenkampff, G. Crelier, A. Khasheei, B. Schnackenburg, F. Berger, and T. Kuehne. Flow-sensitive four-dimensional cine magnetic resonance imaging for offline blood flow quantification in multiple vessels: A validation study. Journal of Magnetic Resonance Imaging, 32(3):677–683, 2010.

[86] S. Ogawa, T.M. Lee, A.S. Nayak, and P. Glynn. Oxygenation-sensitive contrast in magnetic resonance image of rodent brain at high magnetic fields. Magnetic Resonance in Medicine, 14:68–78, 1990.

[87] C.M. Otto. Textbook of Clinical Echocardiography, 4th edition. Saunders, 2004.

[88] J.-M. Peyrat, M. Sermesant, X. Pennec, H. Delingette, C.Y. Xu, E.R. McVeigh, and N. Ayache. A computational framework for the statistical analysis of cardiac diffusion tensors: Application to a small database of canine hearts. IEEE Transactions on Medical Imaging, 26(11):1500–1514, 2007.

[89] A. Preumont. Vibration Control of Active Structures: An Introduction, 2nd edition. Kluwer Academic Pub, 2002.

[90] A.J. Pullan, M.L. Buist, and L.K. Cheng. Mathematically modelling the electrical activity of the heart: From cell to body surface and back again. World Scientific Publishing Co. Pte. Ltd., Hackensack, NJ, 2005.

[91] K. Rhode, M. Sermesant, D. Brogan, S. Hegde, J. Hipwell, P. Lambiase, E. Rosenthal, C. Bucknall, S. Qureshi, J. Gill, R. Razavi, and D. Hill. A system for real-time XMR guided cardiovascular intervention. IEEE Transactions on Medical Imaging, 24(11):1428–1440, 2005.

[92] Y. Rouchdy, J. Pousin, J. Schaerer, and P. Clarysse. A hyperelastic deformable template for cardiac segmentation in MRI. In Proceedings of Functional Imaging and Modeling of the Heart 2007 (FIMH'07), volume 4466 of LNCS, pages 443–452, Salt Lake City, 2007.

[93] G.D. Rubin and N.M. Rofsky. CT and MR Angiography: Comprehensive Vascular Assessment. Lippincott Williams & Wilkins Publishers, 2008.

[94] F.B. Sachse. Computational Cardiology: Modeling of Anatomy, Electrophysiology, and Mechanics. Springer-Verlag, 2004.

[95] J. Sainte-Marie, D. Chapelle, R. Cimrman, and M. Sorine. Modeling and estimation of the cardiac electromechanical activity. Computers & Structures, 84:1743–1759, 2006.

[96] J. Schaerer, C. Casta, J. Pousin, and P. Clarysse. A dynamic elastic model for segmentation and tracking of the heart in mr image sequences. Medical Image Analysis, 14(6):738–749, 2010.

[97] M. Sermesant, F. Billet, R. Chabiniok, T. Mansi, P. Chinchapatnam, P. Moireau, J.M. Peyrat, K. Rhode, M. Ginks, P. Lambiase, S. Arridge, H. Delingette, M. Sorine, A. Rinaldi, D. Chapelle, R. Razavi, and N. Ayache. Personalised electromechanical model of the heart for the prediction of the acute effects of cardiac resynchronisation therapy. In Proceedings of Functional Imaging and Modeling of the Heart 2009 (FIMH'09), volume 5528 of LNCS, pages 239–248, June 2009.

[98] M. Sermesant, R. Chabiniok, P. Chinchapatnam, T. Mansi, F. Billet, P. Moireau, J.-M. Peyrat, K.C.L. Wong, J. Relan, K. Rhode, M. Ginks, P. Lambiase, H. Delingette, M. Sorine, A. Rinaldi, D. Chapelle, R. Razavi, and N. Ayache. Personalised macroscopic electromechanical model of the heart for the prediction of the acute effects of pacing in cardiac resynchronisation therapy. In preparation.

[99] M. Sermesant, P. Moireau, O. Camara, J. Sainte-Marie, R. Andriantsimiavona, R. Cimrman, D.L. Hill, D. Chapelle, and R. Razavi. Cardiac function estimation from MRI using a heart model and data assimilation: advances and difficulties. Med. Image Anal., 10(4):642–656, 2006.

[100] N. Smith. A computational study of the interaction between coronary blood flow and myocardial mechanics. Physiol Meas, 25(4):863–877, 2004.

[101] S. Standring. Gray's Anatomy. Churchill Livingstone, 2008.

[102] E.O. Stejskal and J.E. Tanner. Spin diffusion measurements: Spin echoes in the presence of a time-dependent field gradient. The Journal of Chemical Physics, 42(1):288–292, 1965.

[103] N. Stergiopulos, B.E. Westerhof, and N. Westerhof. Total arterial inertance as the fourth element of the windkessel model. Am J Physiol Heart Circ Physiol, 276:81–88, 1999.

[104] J. Sundnes, G.T. Lines, X. Cai, B.F. Nielsen, K.-A. Mardal, and A. Tveito. Computing the electrical activity in the heart. Springer-Verlag, 2006.

[105] J.-P. Tasu, E. Mousseaux, P. Colin, M.S. Slama, O. Jolivet, and J. Bittoun. Estimation of left ventricular performance through temporal pressure variations measured by MR velocity and acceleration mappings. Journal Of Magnetic Resonance Imaging, 16:246–252, 2002.

[106] K. Ten Tusscher, D. Noble, P. Noble, and A. Panlov. A model of the human ventricular myocyte. American Journal of Physiology – Heart and Circulatory Physiology, 286:1573–1589, 2004.

[107] N. Toussaint, T. Mansi, H. Delingette, N. Ayache, and M.: Sermesant. An integrated platform for dynamic cardiac simulation and image processing: Application to personalised tetralogy of Fallot simulation. In Proc. Eurographics Workshop on Visual Computing for Biomedicine (VCBM). Delft, The Netherlands, 2008.

[108] N. Toussaint, C.T. Stoeck, M. Sermesant, S. Kozerke, and P.G. Batchelor. Three-dimensional prolate spheroidal extrapolation for sparse DTI of the in-vivo heart. In Book of Abstracts, International Society in Magnetic Resonance in Medicine, Sockholm, June 2010 (ISMRM'10), 2-7 June 2010.

[109] S. Uribe, P. Beerbaum, T.S. Sørensen, A. Rasmusson, R. Razavi, and T. Schaeffter. Four-dimensional (4D) flow of the whole heart and great vessels using real-time respiratory self-gating. Magnetic Resonance in Medicine, 62(4):984–992, 2009.

[110] J. Weis and P. Boruta. Introduction to magnetic resonance. GOEN, 1998. (In Slovak).

[111] G.E. Wesbey, C.B. Higgins, M.T. McNamara, B.L. Engelstad, M.J. Lipton, R. Sievers, R.L. Ehman, J. Lovin, and R.C. Brasch. Effect of gadolinium-DTPA on the magnetic relaxation times of normal and infarcted myocardium. Radiology, 153:165–169, 1984.

[112] K.C.L. Wong, F. Billet, T. Mansi, R. Chabiniok, M. Sermesant, H. Delingette, and N. Ayache. Cardiac motion estimation using a proactive deformable model: Evaluation and sensitivity analysis. In STACOM MICCAI Workshop on Statistical Atlases and Computational Models of the Heart: Mapping Structure and Function, Beijing, China, 2010.

[113] E.X. Wu, Y. Wu, J.M. Nicholls, J. Wang, S. Liao, S. Zhu, C.-P. Lau, and H.-F. Tse. MR diffusion tensor imaging study of postinfarct myocardium structural remodeling in a porcine model. Magnetic Resonance in Medicine, 58:687–695, 2007.

[114] K.C. Wu and J.A.C. Lima. Noninvasive imaging of myocardial viability: Current techniques and future. Circ. Res., 93:1146–1158, 2003.

[115] M.-T. Wu, W.-Y. I. Tseng, M.-Y. M. Su, C.-P. Liu, K.-R. Chiou, V.J. Wedeen, T.G. Reese, and C.-F. Yang. Diffusion tensor magnetic resonance imaging mapping the fiber architecture remodeling in human myocardium after infarction: Correlation with viability and wall motion. Circulation, 114:1036–1045, 2006.

[116] G.H. Zahalac. A distribution-moment approximation for kinetic theories of muscular contraction. Mathematical Biosciences, 114:55–89, 2006.

[117] E.A. Zerhouni, D.M. Parish, W.J. Rogers, A. Yang, and E.P. Shapiro. Human heart: tagging with MR imaging – a new method for noninvasive assessment of myocardial motion. Radiology, 169(1):59–63, 1988.